EXPERIMENTAL AND COMPUTATIONAL INVESTIGATION OF GRAVITY SEPARATION IN A VERTICAL FLASH TANK SEPARATOR

A Thesis submitted by

Raid Ahmed Mahmood

For the award of

Doctor of Philosophy

2018

Dedication

Every challenging work needs self efforts as well as guidance of people especially those who are very close to our heart.

My humble effort, I dedicate to my loving,

Father and Mother

Whose affection, endless love, support, encouragement and prayer of day and night make me able to get such success and honor.

My family

With special thanks to my son Abdullah, I can't imagine how much pain you endured while you received the chemical treatment and fought the illness. My son Mahmood, my daughter Aeyah and my wife Iman each of whom has a special place in my heart.

Brothers and sisters

I am really grateful to all of you. I could not imagine my life without you.

Abstract

Vapour injection through flash tank separation is an effective way to enhance the coefficient of performance (COP) and increase the capacity of air conditioning and refrigeration systems. In refrigeration systems which use the vapour injection technique, the flash tank feeds the evaporator with refrigerant liquid and the vapour is delivered to the compressor. Hence, the vertical flash tank is an important component that can be used to improve the performance of air conditioning and refrigeration systems. Semi-empirical design methods based on settling theory can be used for flash tank design, but the approach does not offer precise sizing data or an accurate assessment of likely performance under different operation conditions. Therefore, this thesis assesses the usefulness of CFD in flash tank design, and this is achieved through experiments and simulations on a range of relevant configurations using water as the working fluid. A new experimental facility was built and five different models of the vertical separator were used to investigate the effect of the aspect ratio (H/D) on the liquid separation efficiency for a range of mass flow rates from 2.1 to 23.4 g/s. The internal diameter of the separator in each case was 50 mm. The separation tank was fed with two-phase flow generated using an expansion device and a length of horizontal pipe of diameter 25 mm. The two-phase flow developed gradually after the expansion device, reaching the developed region at about 165 cm downstream.

For the vertical tank without enhancement options, the highest value of the liquid separation efficiency of 0.96 was achieved using the highest height separator (H=250 mm) at the maximum mass flow rate 23.4 g/s. The separation efficiency increased with increasing inlet mass flow rate. In order to improve the liquid separation efficiency of the vertical separator, four enhancement options for the design were proposed: an extractor, a change in the inlet flow direction, a change in the position of the inlet pipe

and a combination of the extractor and the change of the flow direction. The highest liquid separation efficiency of 0.99 was achieved by the last option at the maximum flow rate of 23.4 g/s. Empirical correlations were developed in horizontal pipe and vertical flash tank separator cases to predict the expansion length, void fraction and liquid separation efficiency. The range of the non-dimensional two-phase flow parameters covered by this study was: Reynolds number from 450.45 to 3246, Weber number from 0.005 to 0.72, and Froude number from 0.06 to 7.86.

CFD simulations were performed to simulate the two-phase flow within the horizontal tube which formed the inlet to the vertical separator, and the vertical separator itself. The simulations adopted the pressure based solver using the Eulerian-Eulerian multiphase model. In the horizontal tube case, the numerical results underestimated the expansion length in the experimental results with the simulated expansion length being an average of 8 % lower than the experimental observations. In the vertical tank separator case, the numerical results also underestimated the liquid separation efficiency in the experimental results with an average difference of the liquid separation efficiency of between 1 % and 2 %.

Based on the assessment of the CFD against the experiments of the present work, future applications of CFD in flash tank design should achieve liquid separation efficiency results that reflect the physical reality to within a few percent for operating conditions comparable to the present work. It is concluded that CFD can reliably be used for vertical flash tank design optimisation at least for stratified inlet flow conditions.

Certification of Thesis

This thesis is entirely the work of Raid Ahmed Mahmood except where otherwise acknowledged. The work is original and has not previously been submitted for any other award, except where acknowledged.

Principal Supervisor: Professor David Buttsworth

Associate Supervisor: Dr.Ray Malpress

Associate Supervisor: Dr.Ahmad Sharifian

Student and supervisors signatures of endorsement are held at the University.

Acknowledgments

First of all, I would like to thank My God and say Alhamdulillahi Rabbil Aalameen for getting healing for my son who was diagnosed with childhood cancer. It was a really hard challenge during the medical treatment.

I would like to express my sincere gratitude to my supervisor Professor David Buttsworth for the continuous support of my Ph.D study and related research, for his patience, motivation, and immense knowledge. His guidance helped me all the time. His insight and enthusiasm proved invaluable in the pursuit of new ideas and in the preparation of this thesis.

I would also like to thank Dr. Ray Malpress for his great technical support in the lab. My appreciation also goes to the technical staff in the Engineering workshop at University of Southern Queensland for their support, without their expertise and experience my conceptual ideas could never have been transformed into successful working realities.

I would like to thank my parents for their emotional and blessed support. All the support they have provided me over the years was the most precious gift that anyone has ever given me. My sincere thanks go to my wife for her encouraging me to finish up my study. I would also like to acknowledge the support of the Australian Commonwealth Government for giving me an opportunity to complete this work.

Raid Ahmed Mahmood

University of Southern Queensland
October 2018

Contents

Dedication **i**

Abstract **i**

Acknowledgments **iv**

List of Figures **xiv**

List of Tables **xxvii**

Notation **xxx**

Acronyms & Abbreviations **xxxv**

Chapter 1 Introduction **1**

1.1 Value of flash tank separators 1

1.2 Features of gravity separation 4

1.3 Design and optimisation challenge 7

1.4 Water as a refrigerant 8

1.5 Objectives of the thesis 8

1.6 Overview of the thesis 10

Chapter 2 Literature review **12**

2.1 Introduction 12

2.2 Configuration of vertical separators 12

2.3 Flash tanks in vapour compression refrigeration systems 13

2.4 Performance of vertical gas-liquid separators 19

2.5 Vertical flash tank design using settling theory 23

2.6 CFD studies of separators 28

2.7 Conclusion 30

Chapter 3 Basic definitions and terminology of two-phase flow **32**

3.1 Introduction 32

3.2 Definition of two-phase flow 32

3.3 Vapour quality 33

3.4 Volume flow rate 34

3.5 Mass flux 35

3.6 Velocities 35

3.6.1 Average Local Velocity 35

3.6.2 Superficial Velocity 36

3.7 Void fraction in two-phase flow 37

3.8 Two-phase flow regimes in a horizontal tube 39

3.9 Two-phase flow regimes maps 43

3.10 Equations for regime transitions 47

3.11 Two-phase pattern map for water 50

3.12 Non-dimensional two-phase flow numbers 51

3.13 Conclusion 53

Chapter 4 Experimental apparatus 54

4.1 Introduction 54

4.2 Apparatus layout 55

4.3 Vacuum Condenser 58

4.4 Expansion device 64

4.5 Test sections 67

4.5.1 Horizontal tube 68

4.5.2 Vertical flash tank separator 70

4.6 Vacuum pump 72

4.7 Coil heat exchanger 73

4.8 Adiabatic enclosure 75

4.9 Flow visualisation technique 77

4.10 Instruments 78

4.10.1 Overview 78

4.10.2 Mass flow rate meters 79

4.10.3 Pressure transducers 80

4.10.4 Temperature sensors 80

4.10.5 Data Acquisition 81

4.11 Analysis of Experimental uncertainty 81

4.12 Operating conditions 83

4.13 Conclusion 85

Chapter 5 CFD Simulation **86**

5.1 Introduction 86

5.2 CFD Two-phase flow modelling approaches 87

5.3 Computational domains 89

5.3.1 Horizontal tube 89

5.3.2 Vertical flash tank 90

5.4 Boundary conditions 91

5.4.1 Horizontal tube 91

5.4.2 Vertical flash tank 92

5.5 Mesh independence study 93

5.5.1 Mesh quality 93

5.5.2 Horizontal pipe 93

5.5.3 Vertical flash tank 96

5.6 High performance computing facility 97

5.7 Convergence 98

5.8 CFD solver setting 99

5.9 Conclusion 100

Chapter 6 Two-phase flow development after expansion in a horizontal pipe 101

6.1 Introduction 101

6.2 Development of two-phase flow after the expansion device 102

6.3 Expansion length 109

6.4 Liquid height in the developed region 112

6.5 Void fraction analysis 113

6.6 Local velocity and slip ratio 115

6.7 Dimensionless Parameters 116

6.8 Empirical correlation to identify the expansion region in a horizontal pipe. 121

6.9 CFD simulation results 123

6.9.1 Two-phase flow development on the bottom of the pipe 123

6.9.2 Liquid height in developed region 128

6.10 Length to fully-developed region 130

6.11 Conclusion 132

Chapter 7 Two-phase flow in a vertical flash tank 133

7.1 Introduction 133

7.2 Performance of the vertical flash tank 134

7.3 Flow behaviour inside the vertical tank 135

7.3.1 Experiments 135

7.3.2 Numerical simulation 141

7.4 Comparison of numerical and experimental results 141

7.4.1 Effect of the mass flow rate 141

7.4.2 Effect of the height 145

7.4.3 Vapour quality at the vapour outlet 146

7.5 Effect of d/D ratio 148

7.6 Empirical correlation 151

7.7 Conclusion 156

Chapter 8 Enhancement of a vertical flash tank separator 157

8.1 Introduction 157

8.2 Performance enhancement techniques 158

8.3 Enhancement options 159

8.4 Procedure of the CFD assessment 159

8.5 Experimental arrangement 159

8.5.1 Inlet pipe supporter 160

8.5.2 Operating conditions and measurements 161

8.6 Design enhancements 161

8.6.1 Extractor at the gas outlet of the VFT-V5 161

8.6.2 Inlet moved inside separator 166

8.6.3 Change the direction of inlet flow 169

8.6.4 Extractor at the outlet of VFT-V5-OD 172

8.7 Comparison with the VFT-V5 baseline 175

8.7.1 Liquid separation efficiency 175

8.7.2 Vapour quality at the gas outlet 177

8.7.3 Flow behaviour inside the separator 178

8.8 Conclusion 180

Chapter 9 Conclusions **181**

9.1 Description of work 181

9.2 Outcomes 182

9.2.1 Two-phase flow in a horizontal pipe 182

9.2.2 Liquid separation efficiency in the flash tank before enhancement 183

9.2.3 Enhancement of vertical separator 184

9.3 Summary of conclusions 185

9.4 Future work 185

References **186**

Appendix A Drawings and design of apparatus **199**

A.1 Condenser design and assembly 199

A.2 Expansion device design 206

A.2.1 Description of expansion device design 206

A.2.2 Connection of the expansion device 208

A.2.3 Pipe supporter clamp 209

A.3 Vertical flash tank separator 211

A.4 Experiment of a vertical separator 213

Appendix B Instrument calibration **214**

B.1 Pressure Transducer 214

B.2 RTD calibration check 216

B.3 Mass flow rate calibration 217

Appendix C Experimental procedures **218**

C.1 Procedures for horizontal pipe 218

C.2 Procedures for flash tank 220

Appendix D Vapour quality calculation **221**

Appendix E Calculation for flow pattern map **222**

Appendix F Uncertainty analysis **225**

F.1 Quantification of random errors — horizontal pipe 225

F.2 Quantification of random errors — flash tank 227

F.3 Uncertainty in measured parameters — horizontal pipe 228

F.4 Uncertainty in vapour quality — horizontal pipe 229

F.5 Uncertainty in void fraction — horizontal pipe 230

F.6 Uncertainty in separation efficiency and quality — flash tank 230

Appendix G Flash tank sizing calculation **233**

Appendix H Fluent 17.1 key equations **235**

H.0.1 Governing two-phase equations solved by fluent 235

H.0.2 Turbulence model 239

Appendix I Experimental results **243**

I.1 Horizontal pipe experiments 243

I.2 Vertical flash tank experiments 244

I.3 Enhancement design options of the vertical flash tank experiments . . . 245

List of Figures

1.1 Schematic and P-h diagram of single stage compression refrigeration vapour injection system. (A) With a flash tank separator; (B) without a flash tank separator (Hanfei and Hrnjak 2012). 2

1.2 Schematic and P-h diagram of two stage vapour injection by using flash tank (Jang et al., 2010). 3

1.3 Schematic of the flash tank connection details in a refrigeration system (Hrnjak 2011). 5

1.4 Effect of inlet mass flow rate on the two-phase flow behaviour inside a vertical separator (Hrnjak 2011). 5

1.5 Different droplets size behaviour in a gravity separator (GPSA 2004). . 6

1.6 Vertical gravity separator showing a mist extractor (Arnold and Stewart 1998). 6

2.1 Flash tank in a two stage vapour compression system (Elbel and Hrnjak 2004). 14

2.2 Vapour injection effect: (A) COP variation with compressor frequency, (B) power consumption variation with frequency (Heo et al. 2010). . . 15

2.3 Vapour compression cycle with multi injection ports: (A) Schematic of multi injection system, (B) P-h diagram of system (Mathison et al. 2011). 15

2.4 Schematic of two stage vapour injection, a) Flash tank separator system, b) Internal heat exchanger system (Jang et al. 2010). 17

2.5 Heat pump system with flash tank: a) Schematic diagram of system, b) p-h diagram of heat pump system (Ma and Zhao 2010). 18

2.6 Flash tank and sub-cooler vapour injection air source heat pump (Heo et al. 2011). 19

2.7 Variation of liquid separation efficiency with inlet quality and mass flow rate for inlet diameter of 8.7 mm and body diameter 18.3 mm of T-junction gravity separator (Hanfei and Hrnjak 2012). 20

2.8 Photographs of flow at inlet quality 15 % and varied mass flow rates (Hanfei and Hrnjak 2012). 20

2.9 Variation of liquid separation efficiency with inlet quality and inlet inclination angles at 30 g/s (Hanfei and Hrnjak 2012). 21

2.10 Photographs of flow showing effect of inlet inclination angle on the flow behaviour inside the vertical separator at 30 g/s mass flow rate and 15 % vapour quality (Hanfei and Hrnjak 2012). 21

2.11 Schematic of the heat pump system with flash tank investigated by Xu et al. (2011). 22

2.12 Typical flow patters in the horizontal tube inlet of a T-junction for different flow regimes: (A) Slug flow $G = 100$ kg/m^2·s, $x_{in} = 0.073$, (B) Stratified-wavy flow $G = 100$ kg/m^2·s, $x_{in} = 0.463$, (C) Intermittent flow $G = 400$ kg/m^2·s, $x_{in} = 0.372$, (D) Annular flow $G = 600$ kg/m^2·s, $x_{in} = 0.372$ (Zheng 2016). 23

2.13 Drag coefficient values for the rigid spheres (GPSA 2004). 26

3.1 Cross sectional void fraction 37

3.2 Comparison of the logarithmic mean void fraction $\alpha_{LM\epsilon}$ with the Rouhani and Alxelsson void fraction α_{NH} and homogeneous void correlation α_H for R410A in circular tube with inside diameter d= 8 mm at mass flux G=400 kg/m^2·s, saturation temperature T=40 ℃ (El Hajal et., 2003) . 39

3.3 Two-phase flow regimes during the evaporation process in a horizontal tube (Collier and Thome, 1994). 40

3.4 Flow regime classifications in a horizontal pipe at high void fraction (Dobson, 1994) 42

3.5 Flow regime classifications in a horizontal pipe at low void fraction (Dobson, 1994) 43

3.6 Air-water two-phase flow pattern map for horizontal flow in tube by Baker (1954). 44

3.7 Air-water two-phase flow pattern map for horizontal flow in a tube by Mandhane et al. (1974). 45

3.8 Two-phase flow pattern map for R410A at T_{sat}=5 ℃ in a 13.84 mm diameter horizontal tube by Kattan et al. (1998). 46

3.9 Flow pattern map for R22 at $T_{sat} = 5^oC$ in the 13.84 mm test section diameter, evaluated at 100 kg/m^2.s and 2.1 kW/m^2 by Wojtan et al. (2005). 47

3.10 Stratified angle in two-phase flow (Thome 2003). 47

3.11 Two-phase regimes map for water according to the equations presented in section 3.10 for d= 25 mm and saturated conditions at 23 ℃. 50

4.1 Schematic diagram of the expansion device and horizontal pipe experimental apparatus. 56

4.2 Schematic diagram of the vertical tank separator experimental apparatus. 56

4.3 Photograph of the horizontal pipe experiment arrangement. 57

4.4 Photograph of the vertical separator experiment arrangement. 57

4.5 Schematic diagram of the condenser configuration and connection details of the condenser. 59

4.6 Arrangement of the brass hose fittings around the PVC pipe. 59

4.7 Details of the flange combination connection to hold and seal the PVC and brass pipes (test section connection side). 60

4.8 Section view of the condenser (upstream test section connection side). . 61

4.9 Photograph of the condenser water pump. 62

4.10 Photograph of the condenser flanges and connections on the vacuum pump side. 63

4.11 Photograph of the condenser flanges and connections on the test section side. 63

4.12 Geometry of the expansion device and its section view. 64

4.13 Short control volume for analysis of the expansion device (a) Total length of the hole (b) Segment in two-phase region. 65

4.14 Configuration of the expansion device connection with the horizontal pipe test section. 68

4.15 Connection details at the inlet of the horizontal pipe. 69

4.16 Horizontal transparent acrylic pipe and special clamp. 70

4.17 Photograph of the vertical flash tank separator. 71

4.18 Arrangement of the vertical flash tank separator. 72

4.19 Connection of the vacuum pump with the condenser. 73

4.20 Photograph of the coil heat exchanger arrangement. 74

4.21 Adiabatic enclosure arrangement in the experiments: (a) Horizontal tube, (b) Vertical flash tank. 76

4.22 Photograph of the adiabatic enclosure around the horizontal tube. . . . 77

4.23 Photograph of cover and heat gun technique to control separator wall temperature. 78

4.24 Arrangement of the measurement instruments and experimental apparatus in the vertical separator case. 79

5.1 Computational domain of the horizontal tube geometry. 89

5.2 Computational domain of the vertical flash tank geometry. 90

5.3 Horizontal tube mesh with inflation near the wall for the 199356 element mesh case. 94

5.4 Assessment of grid independence for the horizontal tube showing variation of the expansion length with the number of mesh element for operating condition case 6. 94

5.5 Assessment of grid independence showing liquid volume fraction contours for different element numbers in a horizontal pipe at 1600 mm from the inlet of the pipe for operating condition case 6. 95

5.6 Vertical flash tank mesh with inflation near the walls for the 220000 element mesh case. 96

5.7 Assessment of grid independence for the vertical flash tank showing variation of liquid separation efficiency with number of mesh element for operating condition case 5. 97

5.8 Configuration of the HPC of the University of Southern Queensland. . 98

6.1 Development of two-phase flow after expansion: (a) image from present experiments ($\dot{m}$ = 5.1 g/s and x = 5.7 %), (b) features impacting two-phase flow development after expansion device adapted from Hrnjak (2004). 103

6.2 Homogeneous flow (mixed flow) region of two-phase flow directly after the expansion device (flow direction from left to right). 103

6.3 Stratified flow at 1600 mm from the inlet, $\dot{m}$ = 10.2 g/s and x = 5.4% (flow direction from left to right). 104

6.4 Sequential frames to illustrate liquid droplet movement from top to bottom of the pipe between 150 mm and 300 mm from the inlet ($\dot{m}$= 13.1 g/s and x = 5.4 %, flow direction from left to right). 105

6.5 Sketch for droplet trajectory during the movement from the top to the bottom of the pipe. 106

6.6 Sequential frames to illustrate the observed liquid droplets merging between 275 mm and 300 mm from the inlet, $\dot{m}$ = 10.2 g/s and x = 5.4 %, flow direction from left to right. 106

6.7 Images of the two-phase flow at different mass flow rates directly after the expansion device at the upstream end of the pipe. Images extend from 0 mm to 300 mm from the inlet, flow direction from left to right. 107

6.8 Images of the two-phase flow at different mass flow rates at the downstream end of the pipe. Images extend from 1500 mm to 1800 mm from the inlet, flow direction from left to right. 108

6.9 Observed liquid droplet movement from top to bottom of the pipe at locations from 150 mm to 300 mm from the inlet, $\dot{m} = 13.1 \pm 0.2$ g/s, $x = 5.4$ %. 109

6.10 Image showing liquid film formation at the bottom of the pipe at locations from 0 mm to 300 mm from the inlet, $\dot{m} = 8.1 \pm 0.2$ g/s, $x = 5.5$ %). 110

6.11 Length of the expansion region from the inlet of tube based on criteria 1: phase separation at the top of the pipe. 111

6.12 Length of the expansion region from the inlet of tube based on criteria 2: phase separation at the bottom of the pipe. 111

6.13 Illustration of the definition of liquid height and vapour in the developed region. 112

6.14 Variation of liquid height with mass velocity at 300 mm from the inlet. 113

6.15 Relationship between the void fraction and the mass velocity in the developed region at 1665 mm from the inlet. 114

6.16 Variation of liquid height in the developed region with slip ratio = u_v/u_l at 1665 mm from the inlet. 115

6.17 Variation of the void fraction with the slip ratio in the developed region at 1665 mm from the inlet. 116

6.18 Void fraction in the developed region as a function of liquid and gas dimensionless numbers. 117

6.19 Void fraction in the developed region as a function of two-phase dimensionless numbers. 118

6.20 Expansion length at the bottom divided by diameter of the horizontal tube according to criteria 2 (liquid formation at the bottom of the pipe) as a function of liquid and gas dimensionless numbers. 119

6.21 Expansion length at the bottom divided by diameter of the horizontal tube according to criteria 2 (liquid formation at the bottom of the pipe) as a function of two-phase dimensionless numbers. 120

6.22 Comparison between the predicted and observed values of the normalised expansion length Ex_b/d at the bottom of the pipe. 122

6.23 Comparison between the predicted and observed values of void fraction α in the developed region in the horizontal pipe. 122

6.24 Liquid volume fraction (LVF) for $\dot{m} = 23.4$ g/s (a) LVF along the axial vertical plane; (b) LVF at 5 cm from the inlet; (c) LVF at 10 cm from the inlet; and (d) LVF at 20 cm from the inlet. 124

6.25 Liquid volume fraction along the axial vertical plane at the different operating conditions. 124

6.26 Contours of liquid volume fraction showing liquid formation at the bottom of the pipe on the axial vertical plane for $\dot{m} = 5.1$ g/s. 125

6.27 Contour lines of liquid volume fraction showing liquid formation at the bottom of the pipe on the axial verical plane $\dot{m} = 5.1$ g/s. 126

6.28 Zoomed-in view of contour lines of liquid volume fraction showing liquid formation at the bottom of the pipe on the axial vertical plane $\dot{m} = 5.1$ g/s. 126

6.29 Comparison between the experimental data and numerical simulations for the expansion length at the bottom of the pipe. 127

6.30 Liquid height identification on the central vertical plane of the pipe at 1665 mm from the inlet, according to the liquid volume fraction definition for $\dot{m}$ = 13.1 g/s. 128

6.31 Liquid volume fraction on the vertical planes perpendicular to the flow direction at 1665 mm from the inlet for the different operation conditions. 129

6.32 Comparison between the experimental data and numerical simulations for the liquid height on the central vertical plane of the pipe at 1665 mm from the inlet. 130

6.33 Simulated value of film height along the horizontal pipe based on different LVF values showing the expansion region length (L_{FD}) for $\dot{m}$ = 5.1 g/s. 131

6.34 Simulated values of the distance to the fully-developed region in the horizontal pipe for different inlet mass velocities. 131

7.1 Photograph showing observed liquid film on the vertical wall of the separator and liquid droplets distributed mostly towards to the bottom of the separator (VFT-V2 at 23.4 ± 0.2 g/s). 136

7.2 Observed two-phase flow in vertical flash tank separator VFT-V1. Inlet flow direction from left to right. 136

7.3 Observed two-phase flow in vertical flash tank separator VFT-V2. Inlet flow direction from left to right. 137

7.4 Observed two-phase flow in vertical flash tank separator VFT-V3. Inlet flow direction from left to right. 138

7.5 Observed two-phase flow in vertical flash tank separator VFT-V4. Inlet flow direction from left to right. 139

7.6 Observed two-phase flow in vertical flash tank separator VFT-V5. Inlet flow direction from left to right. 140

7.7 Numerical and experimental results for liquid separation efficiency with VFT-V1. 142

7.8 Numerical and experimental results for liquid separation efficiency with VFT-V2. 143

7.9 Numerical and experimental results for liquid separation efficiency with VFT-V3. 143

7.10 Numerical and experimental results for liquid separation efficiency with VFT-V4. 144

7.11 Numerical and experimental results for liquid separation efficiency with VFT-V5. 144

7.12 Comparison of experimental results for liquid separation efficiency for the various separators as a function of inlet mass velocity. 145

7.13 Comparison of numerical results for liquid separation efficiency for the various separators as a function of inlet mass velocity. 146

7.14 Vapour quality at the vapour outlet of the vertical flash tank separator. Results derived from experimental data. 147

7.15 Configuration of model geometries with d/D= 0.25, 0.5 and 1. 149

7.16 Comparison of numerical results showing the effect of d/D ratio. 150

7.17 Liquid separation efficiency as a function of dimensionless numbers. . . . 152

7.18 Liquid separation efficiency as a function of two-phase dimensionless numbers. 153

7.19 Comparison between the predicted value and the observed results of the liquid separation efficiency. 155

8.1 Typical inlet diverter and mist extractor in a vertical separator, adapted from Campbell (2014). 158

8.2 Inlet pipe supporter with O-ring grooves. 160

8.3 Dimensions and illustration of the extractor. 162

8.4 Configuration of VFT-V5-EXR: (a) section view from 3d model, (b) photograph of the assembly. 162

8.5 Comparison between CFD and experimental results for VFT-V5-EXR. 163

8.6 Impingement of droplets coalescence, and detachment. (a) sequence of frames showing a liquid drop falling; (b) sketch illustrating the key processes in the extractor. 164

8.7 Images of the modified vertical flash tank separator VFT-V5-EXR during operation. Inlet flow direction from left to right. 165

8.8 Configuration of VFT-V5-INT: (a) section view from 3d model; (b) photograph of the assembly. 166

8.9 Comparison between CFD and experimental results for VFT-V5-INT. . 167

8.10 Images of the modified vertical flash tank separator VFT-V5-INT during operation. Inlet flow direction from left to right. 168

8.11 Configuration of VFT-V5-OD: (a) section view from 3d model; (b) photograph of the assembly. 169

8.12 Comparison between CFD and experimental results for VFT-V5-OD. . 170

8.13 Images of the modified vertical flash tank separator VFT-V5-OD during operation. Inlet flow direction from left to right. 171

8.14 Configuration of VFT-V5-ODEXR: (a) section view from 3d model; (b) photograph of the assembly. 172

8.15 Comparison between CFD and experimental results for VFT-V5-ODEXR. 173

8.16 Images of the modified vertical flash tank separator VFT-V5-ODEXR during operation. Inlet flow direction from left to right. 174

8.17 Experimental results comparing the VFT-V5 and the enhanced design configurations. 176

8.18 CFD results comparing the VFT-V5 and the enhanced design configurations. 176

8.19 Experimental results for the vapour quality at the gas outlet of the separator for the different configurations. 177

8.20 Images presenting a comparison of the flow behaviour inside the vertical separator for the different enhancement configurations at $\dot{m}$= 10.2 ± 0.2 g/s. 179

A.1 Configuration of the vacuum condenser and its connections. 199

A.2 Schematic diagram of the O-ring flange. 200

A.3 Condenser vacuum side showing the location of the O-ring and flange combination. 201

A.4 Schematic diagram of the end plate flange and its dimensions. 202

A.5 Schematic diagram of the retaining flange and its dimensions. 202

A.6 Combination of the flange connection around the brass pipe. 203

A.7 Dimensions of the aluminium sealing flanges to connect to the PVC pipe. 204

A.8 Aluminium sealing flanges to connect the PVC pipe and the brass pipe. 204

A.9 Details of the flange combination connection to hold and seal the PVC and brass pipes on the test section connection side. 205

A.10 Section view of the condenser on the upstream test section connection side. 206

A.11 Expansion device (a) section view of the expansion device, (b) photo of 3D printed device. 207

A.12 Assembly of the horizontal test section tube, expansion device and needle valve with PVC end cup. 208

A.13 Special supporter clamp (a) views of the supporter clamp, (b) 3D view, (c) photo of 3D printed clamp. 210

A.14 Vertical flash tank separator (a) Aluminium flange for top and bottom of the tank, (b) illustration of the VFT-V3 separator. 212

A.15 Arrangement of the main parts of the experiment on the vertical separator. 213

B.1 Photograph of the hydraulic dead-weight tester Budenberg model 580. 215

B.2 Comparison of temperature reading between the mercury thermometer and RTD temperature sensor. 216

C.1 Experimental arrangement for the horizontal pipe experiment. 219

C.2 Experimental arrangement for the vertical flash tank experiment. . . . 220

List of Tables

2.1 Correlation of drag coefficient for spherical droplet for Yan et al. (2017), adopted from Zhou (2013). 26

4.1 Dimensions of the experimental geometries. 72

4.2 Power consumption and outlet temperature from the heat exchanger for the range of mass flow rates. 74

4.3 Specifications of mass flow rate meters. 80

4.4 Specifications of pressure transducers (Wika, 2011). 80

4.5 Manufactures' designated uncertainty of the measurement instruments. . 82

4.6 Experimental boundary conditions in horizontal tube. 84

4.7 Experimental boundary conditions in vertical flash tank separator. . . . 85

5.1 The turbulence model compatibility with the multiphase model from FLUENT (2012). 88

5.2 Boundary conditions in horizontal tube simulations. 92

5.3 Boundary conditions in vertical flash tank VFT-V1 simulations. 92

7.1 Dimensions of the model geometries for investigation of the d/D ratio. 148

A.1 Data on the VisiJet crystal plastic material. 208

B.1 Calibration of Wika pressure transducers. V_{meas}= measured voltage, L.P. lower pressure, and H.P. high pressure. 215

F.1 Measurements of liquid height in the fully developed region for the range of mass flow rates. 226

F.2 Measurements of mass flow rates of vertical flash tank VFT-V1 at operating condition 2.1 g/s. 227

F.3 Measurements of mass flow rates of vertical flash tank VFT-V3 at operating condition 8.1 g/s. 227

F.4 Sample of experimental uncertainty calculation of measured quantity in the horizontal pipe experiments for case 1. 229

F.5 Sample of void fraction uncertainty calculation for 2.1 g/s. 230

F.6 Sample of results for vapour quality uncertainty calculation for the gas outlet of the vertical flash tank separator. 231

F.7 Sample of separation efficiency uncertainty calculation for the vertical flash tank separator. 231

F.8 Sample of experimental uncertainty of measured quantities in the vertical flash tank separator experiments for case 1. 232

I.1 Experimental result from the horizontal pipe experiments for the range of mass flow rates. 243

I.2 Dimensionless parameters from the horizontal pipe experiments for the range of mass flow rates. 244

I.3 Experimental liquid separation efficiency from the vertical flash tank separator experiments for the range of mass flow rates. 244

I.4 Experimental vapour quality at the gas outlet from the vertical flash tank separator experiments for the range of mass flow rates. 245

I.5 Experimental liquid separation efficiency from the vertical flash tank separator (enhancement design options) experiments for the range of mass flow rates. 245

I.6 Experimental vapour quality at the gas outlet from the vertical flash tank separator (enhancement design options) experiments for the range of mass flow rates. 246

Notation

Roman symbols

A	Total cross sectional area, m^2
A_g	Area occupied by gas, m^2
A_L	Area occupied by liquid, m^2
As_{FT}	Aspect ratio of the flash tank (H/D)
cp	Specific heat, J/kg.K
D	Inside diameter of separator, m
d	Inside diameter of tube, m
d_d	Diameter of the secondary phase (bubble or droplet), m
dm	Droplet diameter, m
Ex	Expansion region length, m
f	Drag coefficient
F_q	External body force, N
$F_{lift,q}$	Lift force, N
$F_{vm.q}$	Virtual mass force, N
Fr	Froude number
H	Height of the flash tank, m
H_V	Height of the vapour phase in the horizontal tube, m
$h_{1,2,3,4,..}$	Enthalpy, kJ/kg
$\bar{h}_c$	Heat transfer coefficient inside tube, W/m^2K
h_{Ld}	dimensionless vertical height of liquid
ID	inside tube diameter, m
G	Total mass flux, $kg/m^2{\cdot}s$

Gg	Vapour mass flux, kg/m^2·s
Gl	Liquid mass flux, kg/m^2·s
g	Acceleration of gravity, taken as 9.81 m/s^2
Gr	Grashof number
K	Separation factor, m/s
k	Thermal conductivity, W/m.K
k_{pq}	Inter-phase momentum coefficient
k_{qp}	Inter-phase momentum coefficient
L	Length, m
m_{pq}	Mass transfer from phase p to phase q, kg/s
m_{qp}	Mass transfer from phase q to phase p, kg/s
$\dot{m}_g$	Vapour mass flow rate, kg/s
$\dot{m}_l$	Liquid mass flow rate, kg/s
$\dot{m}_{Loutlet}$	Liquid mass flow rate at the liquid outlet of the separator, kg/s
$\dot{m}_{Linlet}$	Liquid mass flow rate at the inlet of the separator, kg/s
$\dot{m}_t$	Total mass flow rate of mixture, kg/s
Nu	Nusselt number
P	Pressure, kPa
P_{id}	Dimensionless perimeter of interface
P_r	Prandtl number
q_c	Heat transfer from tube surface to working fluid, W
Q_l	Liquid volume flow rate, m^3/s
Q_t	Total volume flow rate, m^3/s
Q_v	Vapour volume flow rate, m^3/s
Q_q	Volume flow rate of phase q, m^3/s
Re	Reynolds number
R_{pq}	Interaction force between phases, N
S	Slip velocity
S_q	Mass source for each phase
T	Temperature, ℃
u	Velocity, m/s
u_l	Liquid local velocity, m/s
u_{sg}	Vapour superficial velocity, m/s

u_{sl}	Liquid superficial velocity, m/s
u_{st}	Total superficial velocity, m/s
u_v	Vapour local velocity, m/s
$\vec{U}_p$	Phase weighted velocity of phase p, m/s
$\vec{U}_q$	Phase weighted velocity of phase q, m/s
U_T	Terminal velocity, m/s
U_v	Vertical velocity, m/s
v	Kinematic viscosity, m^2/s
V_q	Volume of phase q, m^3
$\vec{v}_q$	Velocity of phase q, m/s
We	Weber number
x	Vapour quality

Greek symbols

α	Void fraction
β	Chord angle
B	Coefficient of thermal expansion
μ_g	Vapour dynamic viscosity, m^2/s
μ_l	Liquid dynamic viscosity, m^2/s
μ_{water}	Liquid dynamic viscosity, m^2/s
ρ_{air}	Air density, kg/m^3
ρ_g	Vapour density, kg/m^3
ρ_l	Liquid density, kg/m^3
ρ_{water}	Water density, kg/m^3
ψ	Liquid phase parameter (dimensionless)
η_L	Liquid separation efficiency
τ_p	Particulate relaxation time, s
τ_q	Stress-strain tensor of q phase
$\tau_{t,pq}$	Lagrangian integral time scale
θ	Angle
λ	Gas phase parameter (dimensionless)

λ_q	Shear of phase q, N/m
σ	Surface tension, kg/s^2
ξ	Factor for lagrangian integral calculation

Subscripts

b	Bottom
g	Vapour phase
H	Homogeneous
i	inside
in	inlet
l	Liquid phase
$LM\epsilon$	Mean logarithmic
NH	Non-homogeneous
o	outside
out	outlet
s	surface
t	Top
TP	Two-phase
FT	Flash tank

Superscripts

$*$	Critical

Acronyms & Abbreviations

A	Annular flow
As_{FT}	Aspect ratio of the flash tank
ASHRAE	American Society of Heating, Refrigerating and Air-Conditioning Engineers, Inc.
CFD	Computational Fluid Dynamics
COP	Coefficient of performance of cycle
CV	Control volume
DAQ	Data acquisition
EEV	Electronic expansion valve
FGB	Flash Gas Bypass
FT	Flash tank
HPC	High performance computer
I	Intermittent flow
IHX	Internal heat exchanger
LMTD	Log mean temperature difference
M	Mist flow
MPEG	Format of video recording
NI	National Instrument
PI	Pi theorem
RSM	Reynolds stress model
S	Stratified flow
SW	Stratified-wavy flow
SST	Shear stress transport
TEV	Thermostatic expansion valve

Chapter 1

Introduction

1.1 Value of flash tank separators

Air-conditioning, refrigeration and heat pump systems are used widely in domestic and commercial sectors and these systems use similar components (Mohanraj et al., 2009; Rasmussen, 2011). Much research is devoted to enhancing the main components of mechanical refrigeration systems such as compressors, fans and heat exchangers, and other work investigates cycle performance and attempts to reduce energy consumption. The vapour injection technique using a flash tank is an effective way to enhance the system's coefficient of performance (COP) (Elbel and Hrnjak, 2004). In refrigeration systems which use a vapour injection technique, a flash tank feeds the evaporator with the separated liquid, and the vapour is injected into the compressor (Ma and Zhao, 2008).

In mechanical vapour injection systems, the addition of a flash tank separator can play a role in enhancing the cooling capacity and system performance (Hanfei and Hrnjak, 2012). This modification reduces the high fraction of vapour (flash gas) at the inlet of the evaporator which is advantageous because (1) the vapour's heat transfer coefficient is lower than the liquid phase; and (2) an increased pressure drop is also experienced with the high void fraction which exists with the presence of vapour (Sirwan et al., 2013). Jang et al. (2010) reported that using a flash tank separator in a mechanical refrigeration (vapour injection) system enhances the coefficient of performance by

17 % relative to a non-injected system in their working conditions. The flash tank feeds the evaporator with just refrigerant liquid and passes the vapour portion of the flow to the suction line of the compressor (Hanfei and Hrnjak, 2012).

Figure 1.1 (A) shows a single stage vapour compression refrigeration system and associated P-h diagram to show the thermodynamic processes when using a flash tank separator, and Figure 1.1 (B) shows the same system and its thermodynamic processes without the flash tank. The evaporator in Figure 1.1 (A) receives only saturated liquid from the flash tank so, the enthalpy at the inlet of the evaporator is much lower than that in Figure 1.1 (B) in which a mixture is delivered to the evaporator. This does not directly lead to enhanced performance because the mass flow rate through the evaporator is reduced if a flash tank system is used. Instead, the system performance will be increased through more subtle effects: increased heat transfer coefficient and reduced pressure drop in the evaporator (Elbel and Hrnjak, 2004).

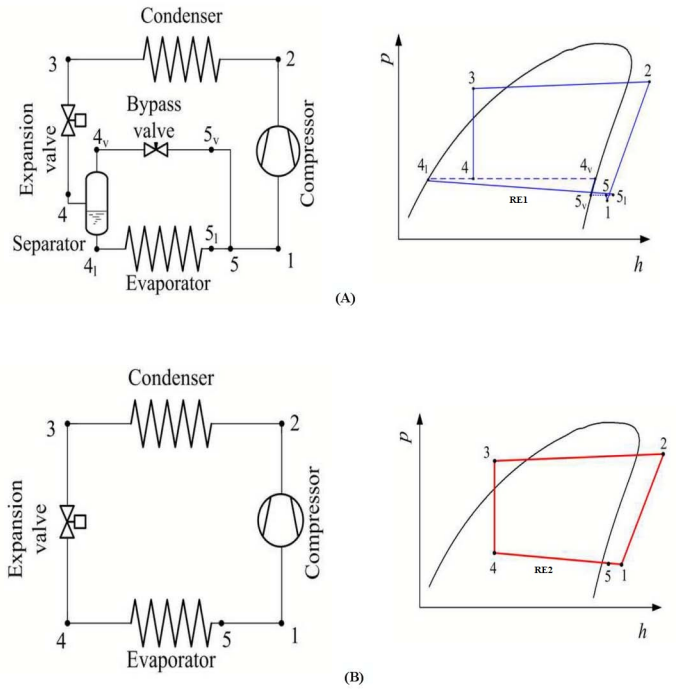

Figure 1.1: Schematic and P-h diagram of single stage compression refrigeration vapour injection system. (A) With a flash tank separator; (B) without a flash tank separator (Hanfei and Hrnjak 2012).

In two-stage compression refrigeration systems, flash tanks can also be used to work as intercoolers or economizers as shown in Figure 1.2 (Jang et al., 2010). This technique is used to increase the cooling capacity and system performance of two stage systems by injecting vapour at an intermediate point in the compression processes and using a second expansion device to provide low enthalpies at the evaporator inlet as shown in process (7-8) in Figure 1.2. Under certain conditions these additions can increase the coefficient of performance to 10 % more than a system without a flash tank (Jang et al., 2010). Ma and Zhao (2010) indicate that the refrigeration system's coefficient of performance can be increased up to 17 % by using a flash tank.

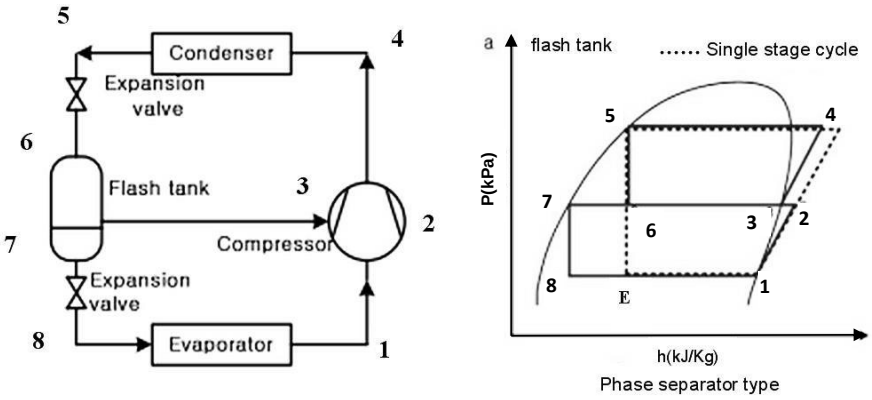

Figure 1.2: Schematic and P-h diagram of two stage vapour injection by using flash tank (Jang et al., 2010).

Sirwan et al. (2013) reported that when a flash tank is used to feed the evaporator with liquid only, the coefficient of performance and system capacity will be increased due to an increase in the liquid fraction, a decrease in vapour quality at the inlet of the evaporator, and an increase in heat transfer coefficient at the inlet of the evaporator. Shuxue and Guoyuan (2014) conducted an experimental study to confirm that the flash tank is an effective addition that can increase the coefficient of performance by 10-12 % and system capacity by 5-15 %.

1.2 Features of gravity separation

In a vertical gravity separator, which in the context of refrigeration systems would normally be referred to as a flash tank separator, three main features which have significant effects on the operation and separation performance should be considered (Mokhatab et al., 2012). The first feature is the flow pattern generated by the inlet hardware arrangement. Because a flash tank separator is located after the expansion device as shown in Figure 1.3, the flow pattern at the entrance to the separator is affected by the mass flow rate and quality (dryness fraction of the vapour) resulting from the expansion process occurring in the expansion device (Hrnjak, 2011). Depending on the mass flow rate, the flow after the expansion device may be droplet, stratified, annular, or a stratified-wavy flow pattern. Indeed, the mass flow rate has a direct effect on the two-phase flow behaviour in a vertical separator as shown in Figure 1.4. Shoukri (2002) confirmed the importance of flow rate on the two-phase flow patterns at the inlet of a flash tank.

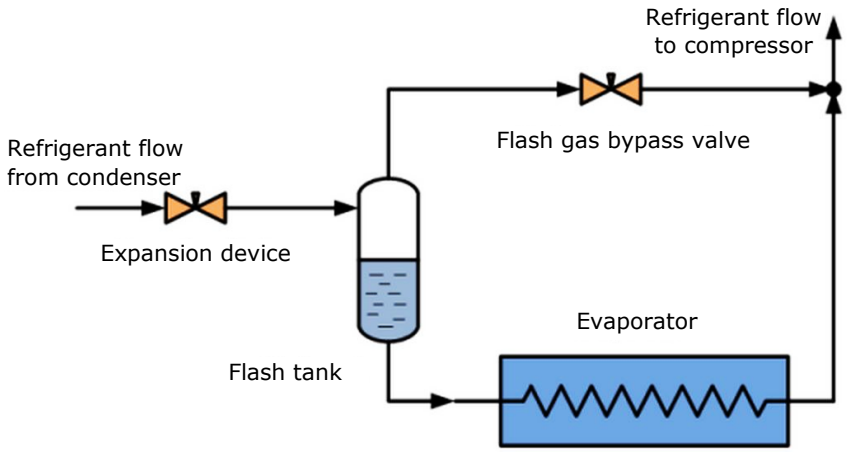

Figure 1.3: Schematic of the flash tank connection details in a refrigeration system (Hrnjak 2011).

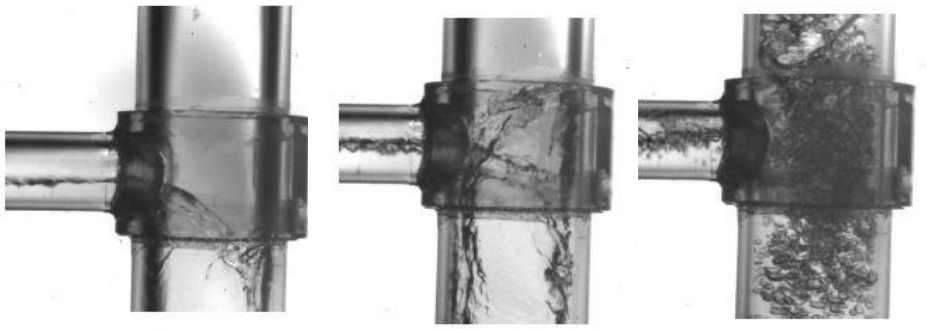

Figure 1.4: Effect of inlet mass flow rate on the two-phase flow behaviour inside a vertical separator (Hrnjak 2011).

The second feature of the vertical gravity separator is the gravity settling section. In this section, the large liquid droplets separate from the gas-liquid two-phase and move to the bottom of the flash tank due to gravity, while vapour and small droplets flow through the separated area to the top of the tank as shown in Figure 1.5 (GPSA, 2004). During this process, there are three main forces acting on the liquid droplets: gravity, buoyancy, and drag forces (Souders and Brown, 1934; Arnold and Stewart, 1998; GPSA, 2004; Wiencke, 2011). The effect of these forces will create an acceleration in the direction of the net force. The gravity force causes a separation when it is greater than the drag and buoyancy forces.

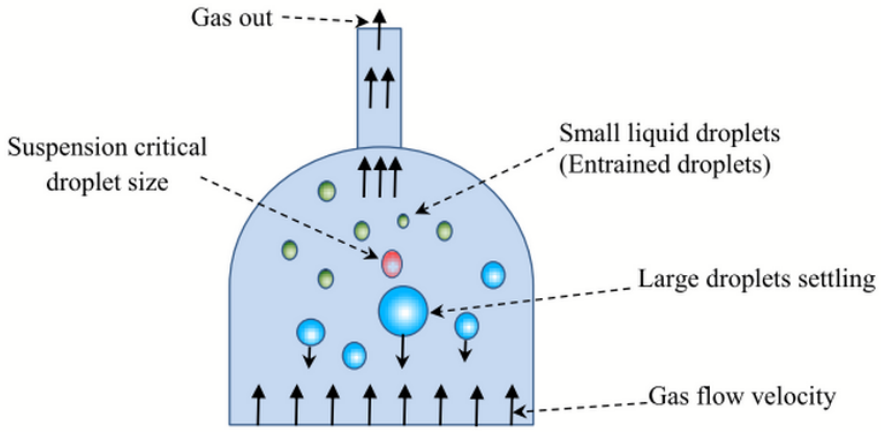

Figure 1.5: Different droplets size behaviour in a gravity separator (GPSA 2004).

Finally, the third feature of the vertical gravity separator is the mist elimination or mist extraction. It is a significant part of the separator, affecting droplets which are typically less than 10 μm (GPSA, 2004). It separates these droplets from the gas phase before the vapour leaves the separator as shown in Figure 1.6 (Arnold and Stewart, 1998). Khorshidi and Naderipour (2012) suggested that the height of a gas-liquid vertical separator can be increased if an eliminator needs to be used but sometimes this may result in unreasonably high separators which are not economic. The small droplets are better coalesced in the mist extractor which operates via an impingement effect.

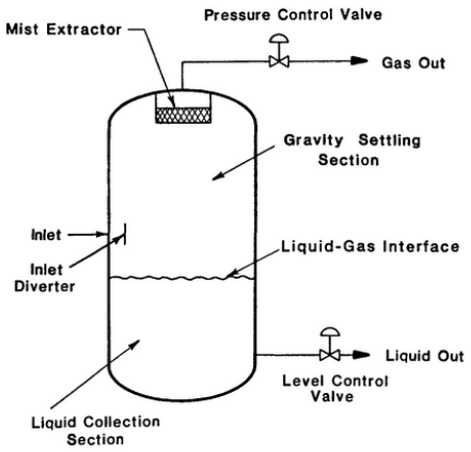

Figure 1.6: Vertical gravity separator showing a mist extractor (Arnold and Stewart 1998).

1.3 Design and optimisation challenge

In addition to the aspects introduced in section 1.2, to design an effective gravity flash tank separator for a mechanical refrigeration system, the aspect ratio of the flash tank should be considered (Mo et al., 2014). Refrigeration system performance can be impaired as a result of decreasing the separation efficiency when the size of the flash tank is not suitable to feed liquid to the evaporator and bypass the vapour to the compressor. Xu and Pham (2012), Hwang et al. (2010) and Heo et al. (2010) used a flash tank volume of 240 cm^3 in a 3.6 kW air conditioning system, but the separation performance and size optimization were not discussed. The sizing of a flash tank needs to be appropriate for the system capacity in order to obtain optimum system operation.

Several studies have investigated the design of the vertical separator such as Delgado and Pichardo (1999), Elbel and Hrnjak (2004), and Wiencke (2011), and these studies used settling theory, but uncertainty remains in determining likely range of droplet size, the droplet drag coefficient and the associated separation coefficient. Some studies report recommendations for the design the vertical separator; for example, Seader et al. (1998) suggested a range for the separation coefficient, Stanly and Walas (1990) suggested a range for the droplet size, and Zhou (2013) listed some correlations for estimating the drag coefficient.

An alternative to flash tank design via the application of settling theory using engineering approximations and empirical results is to use computational fluid dynamic (CFD) simulations. Different studies have used computational fluid dynamic simulation to quantify two-phase flow separation phenomena. Some of these studies investigated the two-phase flow in horizontal pipe such as Terzuoli et al. (2008), Walvekar et al. (2009) and Messa et al. (2014). Other studies investigated two-phase separation in vertical separators such as Pointon et al. (2009), Zhou (2013) and Zarrouk and Purnanto (2015). Although, such computational fluid dynamic simulation studies have confirmed that CFD can be successfully used to examine two-phase separation processes, including those operating in separator geometries, data required to design a vertical flash tank separator using water as the working fluid is not available in these studies. Furthermore, comprehansive information on the accuracy of the CFD simulations of the vertical flash tank separation efficiency has not been presented in these

studies.

1.4 Water as a refrigerant

Water is a natural refrigerant that can be used in refrigeration and air conditioning systems. Water represents the ultimate environmentally friendly refrigerant because it has a zero ozone depletion potential (ODP), zero global warming potential (GWP), and it is non-toxic and non-flammable (Wang et al., 2009). Therefore, water is classified as a safe refrigerant, falling into the A1 group with a refrigerant code of R718 (Kilicarslan and Müller, 2005). Water also has excellent chemical and thermodynamic properties such that it can be used below its normal freezing point, and above its normal boiling point, if it is mixed with appropriate solutions such as propylene glycol or ethylene glycol (Kilicarslan and Müller, 2005).
Water (R718) has been used in a wide variety of air conditioning and refrigeration applications and has received renewed attention as a natural refrigerant after the signing of the Montreal Protocol to reduce the environmental concerns (Wang et al., 2009). Water has a long history of having been used in adsorption, absorption, desiccant, and ejector-based refrigeration and air conditioning systems. New and improved water-based refrigeration systems are currently under development. Therefore, having design tools that can be applied with confidence to the associated two-phase fluid-flow problems is important.

1.5 Objectives of the thesis

The present work aims to generate experimental data that is then used to quantify the viability of using CFD as a tool for vertical flash tank separator design. It also seeks to provide knowledge that will make design of future flash tank separators easier, resulting in low cost and high performance separators. Water is used as a working fluid because some cooling systems operate with water as the working fluid and because it offers ease of handling in the laboratory environment. In order to achieve the objectives of the present work, the following tasks were completed.

1. Design and operate an appropriate water vapour vacuum system with a heat exchanger adequate for the two-phase flow investigations in a vertical flash tank.

2. Conduct an experimental investigation of two-phase flow development after an expansion device in a horizontal pipe.

3. Conduct an experimental investigation of the aspect ratio effect on the vertical flash tank performance.

4. Perform an experimental investigation of the proposed design enhancement options to improve the separation efficiency of a vertical flash tank.

5. Perform computational simulations of two-phase flow using computational fluid dynamics CFD in the horizontal tube and vertical flash tank experiments.

6. Establish correlations from the experimental results using non dimensional parameters to aid future vertical flash tank design .

1.6 Overview of the thesis

This section describes the structure of the work which is presented in this thesis. The thesis is arranged as following.

- Chapter 2 Literature review

  Various theoretical and experimental studies using gravitational vertical flash tank separators with application in air conditioning, refrigeration and heating are reviewed.

- Chapter 3 Basic definitions and terminology of two-phase flow

  The fundamentals of two-phase flow and definitions of the main variables are presented in this chapter.

- Chapter 4 Experimental apparatus

  This chapter introduces the design of the experimental apparatus and its components. A unique design of the experimental apparatus was used to achieve the two-phase flow experiments using water as the working fluid. Operating conditions of the experimental apparatus are presented, and the measurement methods and their arrangement are presented.

- Chapter 5 CFD Simulation

  The computational fluid dynamics (CFD) methods used to simulate the two-phase flow development in a horizontal tube and the performance of the vertical flash tank separator are presented in this section. Eulerian-Eulerian multiphase model and standard k-ϵ turbulence model was used in the numerical simulation.

- Chapter 6 Two-phase flow development after expansion in a horizontal pipe

  In this chapter, the inlet mass flow rate effect on the development of the two-phase flow after an expansion device in a horizontal pipe is presented. The results of this chapter were used to assess the development of the two-phase flow and the CFD simulation. In addition, empirical correlations were developed based on the experimental data to predict the expansion length at the bottom of the horizontal pipe.

- Chapter 7 Two-phase flow in a vertical flash tank

  This chapter presents the investigation of the liquid separation efficiency of vertical flash tank separators having different aspect ratios and operated at different inlet mass flow rates. CFD simulations were also performed on these configurations and results were assessed against the experiments. An empirical correlation for the liquid separation efficiency was developed from the experimental results.

- Chapter 8 Enhancement of a vertical flash tank separator

  In this chapter, design options that improve the liquid separation efficiency of one particular separator are presented. A CFD simulation was performed to predict the performance of the enhancement design options before proceeding to the experiments and the numerical and experimental results were compared.

- Chapter 9 Conclusions

  In this chapter, a brief summary of the overall outcomes of this study are presented. In addition, recommendations for future work are described.

Chapter 2

Literature review

2.1 Introduction

The function and use of vertical flash tank separators in chilling systems need to be considered to provide a suitable design. In order to design and optimize a vertical flash tank separator, a clear understanding of the two-phase flow development and associated phenomena in the inlet tube and vertical flash tank separator need to be obtained. Therefore, in this chapter, various theoretical, experimental and computational studies relating to vertical separation and vertical flash tank design, the performance of vertical flash tank separators, and application of vertical flash tank separators in chilling systems will be reviewed.

2.2 Configuration of vertical separators

A multiphase flow can consist of various phase combinations: liquid-liquid, gas-liquid, solid-liquid, and gas-solid or gas-liquid-solid. A separator can be used to separate one or two components from the multiphase flow. Khorshidi and Naderipour (2012) categorise two different types of vertical devices, based on the dominant separation mechanism: (1) momentum separation; and (2) gravity separation.

Momentum separation relies on changes to the flow direction such that the denser

material (having a higher momentum) is separated from the less-dense material (have a lower momentum). In the case of gas-liquid flows, momentum separation is most frequently achieved using a gas-liquid cylindrical cyclone (GLCC) separator to generate a swirling flow. In the case of gas-liquid gravity separation, the drag force on the liquid due to gas flowing in the vertical direction should be less than the gravitational force on the liquid in order to achieve separation. In the gravity separation of gas-liquids, the separator is sometimes referred to as a gravity flash tank separator.

Wang et al. (2000) presented some recommendations for the design of a gas-liquid cylindrical cyclone (GLCC) separator. The aspect ratio, which is the length to diameter of the separator, affects the performance and cost of the separator, so it is the most important parameter that should be considered. Furthermore, because the performance of GLCC depends on the tangential velocity of the swirling fluid, the inlet position of the GLCC should be considered in the separator design.

Some studies report configurations that can be used to improve the separation performance. For example, Grodal and Realff (1999) suggested using a wire mesh and mist extractor to separate the liquid drops that move with the gas through the gas outlet as it is not economic to separate these drops by gravity alone by making the separator larger. GPSA (2004) presented some other configurations for the vertical separator including inlet devices, wire meshes and mist extractors. Inlet devices reduce the momentum of the inlet stream and enhance the flow distribution of the gas and liquid phases inside the separator. The inlet device can be a diverter plate, half-pipe or vane.

2.3 Flash tanks in vapour compression refrigeration systems

Mechanical vapour compression systems can be enhanced by using a vapour injection technique. The vapour injection technique was first commercially used in 1979 for a room air conditioning system (Xu et al., 2011*b*). A flash tank separator was used in a refrigeration system as a liquid vapour separator by Sirwan et al. (2013) and Shuxue and Guoyuan (2014). Using a flash tank allows vapour to be injected into a rotary compressor with an injection control valve used to control the injection process. Refrigeration and air conditioning systems have received much attention from researchers in order to provide effective systems that meet performance and environment require-

ments (Heo et al., 2012). A vertical flash tank can be used when a layout area is small. The vertical flash tank also has low running cost, low weight, and it is not complex.

Elbel and Hrnjak (2004) conducted experimental work to improve the performance of a refrigeration system by using Flash Gas Bypass (FGB). The experimental refrigeration system used carbon dioxide refrigerant (R744) with two compressor stages as shown in Figure 2.1. The low stage compressor and high stage compressor displacements were 21.8 cm^3 and 13.2 cm^3, respectively. The results concluded that FGB increases the coefficient of performance and the cooling capacity of the refrigeration system by 7 % and 9 %, respectively.

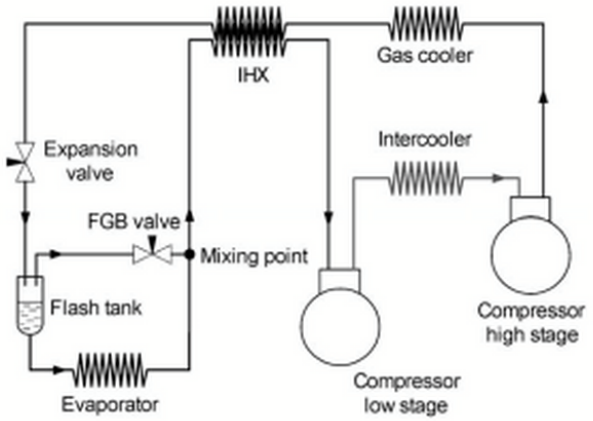

Figure 2.1: Flash tank in a two stage vapour compression system (Elbel and Hrnjak 2004).

Heo et al. (2010) studied the effect of flash tank vapour injection on the heating capacity and the performance of a two stage heat pump system at a low ambient temperature by using an inverter-driven twin rotary compressor. The study considered the compressor frequency range from 50 Hz to 100 Hz and the low ambient temperature conditions of -15, -5 and 5 ℃. The experimental work of this study involved two twin rotary compressors, indoor and outdoor units, a flash tank separator with a volume of 240 cm^3, and an electronic expansion valve (EEV). The results of this study showed that the coefficient of performance COP and heating capacity of the injection cycle were increased by 10 % and 25 % respectively at low ambient temperature. However, the power consumption in the injection cycle was higher than the power consumption

in the non-injection cycle; Figure 2.2 shows the results.

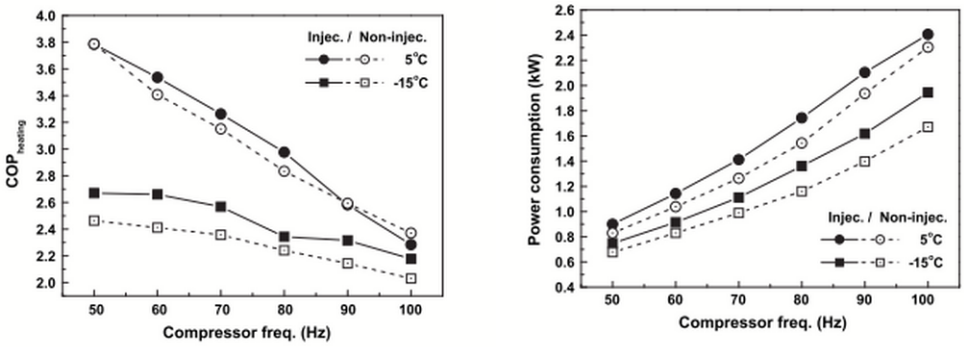

(A) (B)

Figure 2.2: Vapour injection effect: (A) COP variation with compressor frequency, (B) power consumption variation with frequency (Heo et al. 2010).

Mathison et al. (2011) developed a model of the refrigerant injection port that is used to inject the refrigerant during the compression process in a scroll compressor instead of injecting the refrigerant between compression stages as shown in Figure 2.3. The scroll compressor which involves more than one port to inject the economized refrigerant during the compression process was considered in order to study the effect of the number of the injection points on the cycle performance. The results showed that the system coefficient of performance and the system capacity can be increased by increasing the number of injection ports in the scroll compressor.

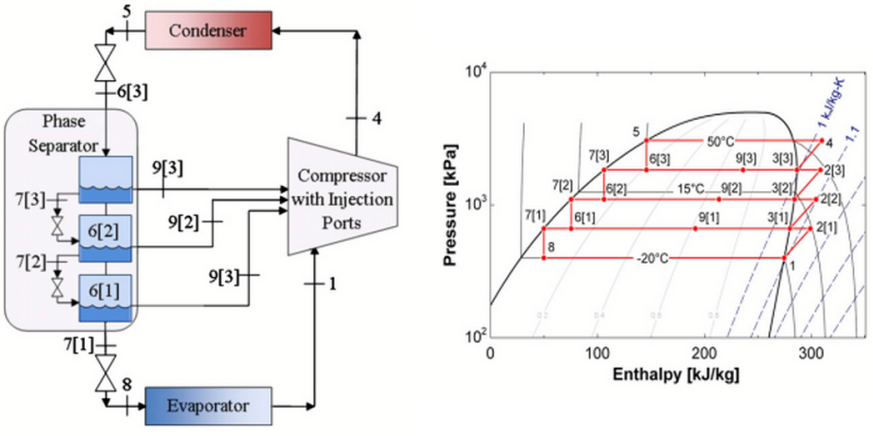

(A) (B)

Figure 2.3: Vapour compression cycle with multi injection ports: (A) Schematic of multi injection system, (B) P-h diagram of system (Mathison et al. 2011).

Jain et al. (2004) theoretically compared a three ton vapour compression refrigeration and air conditioning system with and without flash tank vapour injection into a scroll compressor. A perfect separation in the flash tank, and a 5 ℃ sub-cooling and superheating in the condenser and evaporator were considered. The result showed that coefficient of performance is increased by between 6 and 8 % as compared with a basic system without vapour injection. Moreover, in the vapour injection system, the compressor displacement is reduced as much as 16 % for the same load conditions.

Ma and Zhao (2008) conducted experimental work to compare the heating performance of a flash tank coupled with a scroll compressor system with a sub-cooler system. The experimental apparatus used R22 as a refrigerant, and included a scroll compressor, flash tank, sub-cooler heat exchanger and an electric heater, which was used to increase the glycol-water tank temperature. The experiment considered the working conditions of 45 ℃ condenser and -25 ℃ evaporator temperatures. The results showed that the heating capacity of the system with the flash tank is 10.5 % higher than that of the system with the sub-cooler. In addition, the coefficient of performance COP of the flash tank system is 4.3 % higher than that of the sub cooler system.

Jang et al. (2010) measured and analysed the effects of phase separator injection and internal heat exchanger injection on the heating performance of a two stage heat pump system driven by a twin rotary compressor. Figure 2.4 shows the schematic of the two stage vapour injection systems. The experimental system used R410A as refrigerant and the compressor frequency range from 50 to 95 Hz at ambient temperatures of -20,-15, -10, -5, and 7 ℃. The results showed that coefficient of performance COP and the heating capacity of the phase separator injection cycle were improved by 17 % and 25 % respectively compared to a non-injection cycle, while the COP and heating capacity of internal heat exchanger cycle were enhanced by 10 % and 25 % compared to a non-injection cycle respectively.

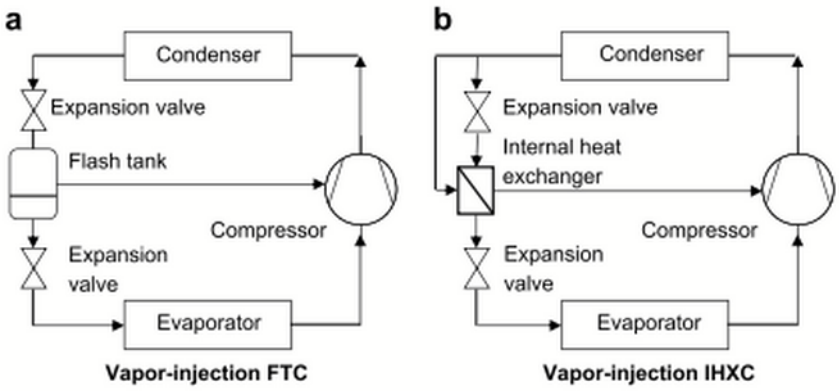

Figure 2.4: Schematic of two stage vapour injection, a) Flash tank separator system, b) Internal heat exchanger system (Jang et al. 2010).

Feng et al. (2009) presented an experimental study of a heat pump water heater performance using a refrigerant mixture of R22-R600a in an economizer vapour injection system. The experiment included the heat pump water heater system that consists of finned evaporator coil, dry filter, expansion valve, tube in tube condenser coil, liquid reservoir, and scroll compressor with port injection. The experiment also included a solenoid valve and an expansion valve. The experimental system was tested at three different ambient temperatures -15, -5 and 2 ℃. The results demonstrated that the advantages of the using refrigerant mixture (R22-R600a) are: increased the heating capacity, increased energy efficiency, and increased system performance. Further, at 15 % mass ratio of R600a, the outlet water temperature achieves the highest value.
Ma and Zhao (2010) presented the characteristics of a heat pump system with a flash tank coupled with a scroll compressor. Figure 2.5 illustrates the system and a pressure-enthalpy diagram of the cycle. The heat pump system was operated at low temperature and used R22 as the refrigerant. The results showed that the heat pump is improved by using a flash tank, and the coefficient of performance is 1.73 at the operation condition of -25 ℃ evaporator temperature, 45 ℃ condenser temperature, and 10 bar intermediate pressure.

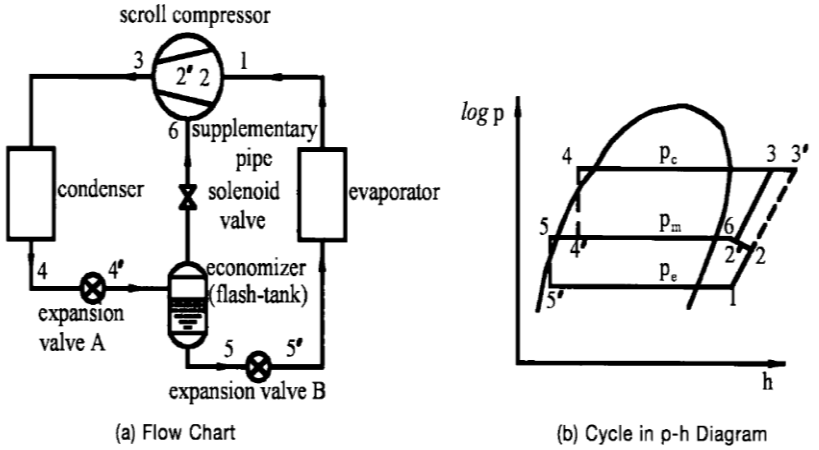

Figure 2.5: Heat pump system with flash tank: a) Schematic diagram of system, b) p-h diagram of heat pump system (Ma and Zhao 2010).

Heo et al. (2011) presented experimental work on vapour injection techniques for a double expansion sub-cooler and flash tank to enhance the heating performance of an air source heat pump system. In the experiment, the vapour compression heat pump with a refrigerant R410A and a twin rotary compressor was used as shown in Figure 2.6. In addition, the system involved three electronic expansion valves, which were used to control the pressures. The first and second valves were used to control the intermediate and low pressure, respectively. Whereas the third electronic expansion valve was used to control the amount of refrigerant injection into the twin rotary compressor. At working conditions which involved outdoor temperatures ranging from -5 ℃ to -15 ℃, a compressor frequency range from 50 Hz to 80 Hz, and an indoor temperature which was fixed at 20 ℃, the results showed that the average heating capacities of the flash tank, flash tank sub-cooler, and double expansion sub-cooler cycles are higher by 14.4 %, 6 %, and 3.8 %, respectively, compared with the sub-cooler cycle. In addition, the maximum coefficient of performance and heating capacity are improved at full opening of the third electronic expansion valve in the flash tank cycle.

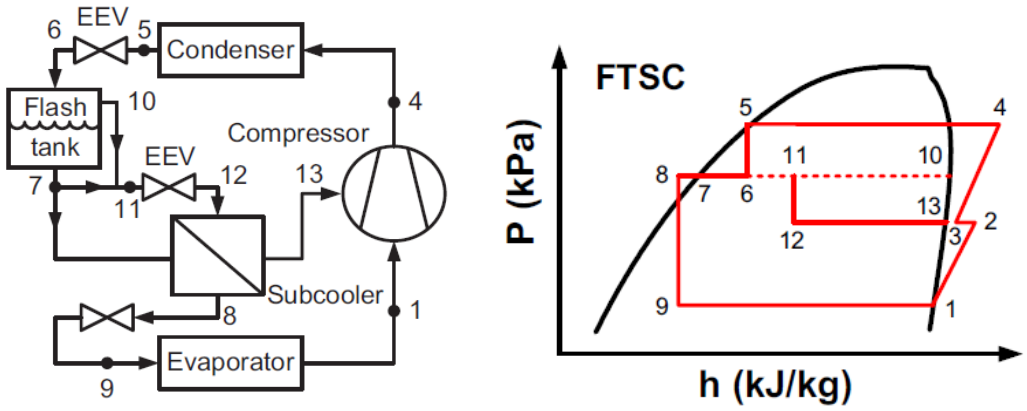

Figure 2.6: Flash tank and sub-cooler vapour injection air source heat pump (Heo et al. 2011).

2.4 Performance of vertical gas-liquid separators

Of the available mechanical separation techniques, gravitational vertical gas-liquid separation is an effective and simple method to separate liquid from gas-liquid two-phase flow (Khorshidi and Naderipour, 2012). The flash tank (FT) is a type of gravity separator which depends on the gravity force to achieve a successful separation (Svrcek and Monnery, 1993). The flow behaviour inside the vertical flash tank separator is effected by drag, buoyancy, and gravity forces, and the terminal velocity (liquid droplet settling) can be estimated based on the vapour and liquid velocities (Souders and Brown, 1934).

Hanfei and Hrnjak (2012) presented experimental work investigating the phase separation in a vertical gas-liquid separator. R134A was used as a working fluid in the experiment with inlet flow rates ranging from 10 g/s to 35 g/s and quality from 5 % to almost 30 %. The diameter of the separator and the orientation of the inlet pipe relative to the separator were varied in the experiment. The results show that the separation efficiency is increased by decreasing the mass flow rate and/or quality, as shown in Figure 2.7. Separation phenomena were also investigated using a visualization technique, which demonstrated that when the mass flow rate increased, the flow pattern change and liquid impingement on the wall occurred, as shown in Figure 2.8. Experiments also showed the separation efficiency at constant mass flow rate was improved by increasing the angle of inclination of the inlet pipe as shown in Figure

2.9. Figure 2.10 presents a photo of the flow behaviour inside the separator at different inlet pipe inclination angles.

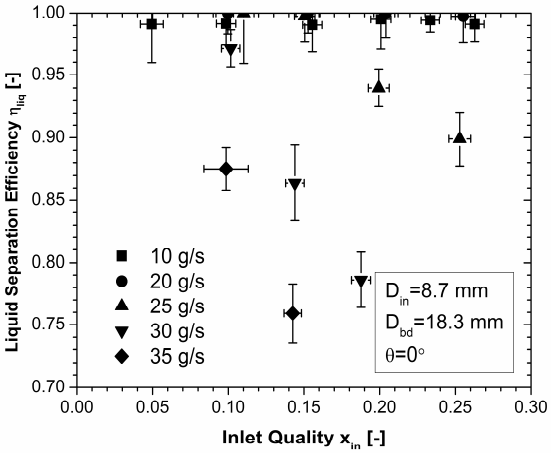

Figure 2.7: Variation of liquid separation efficiency with inlet quality and mass flow rate for inlet diameter of 8.7 mm and body diameter 18.3 mm of T-junction gravity separator (Hanfei and Hrnjak 2012).

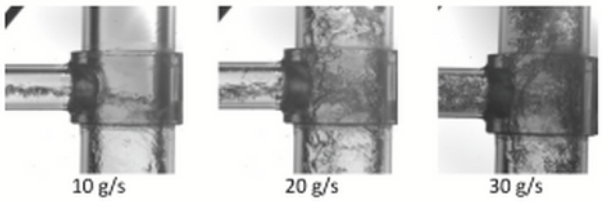

Figure 2.8: Photographs of flow at inlet quality 15 % and varied mass flow rates (Hanfei and Hrnjak 2012).

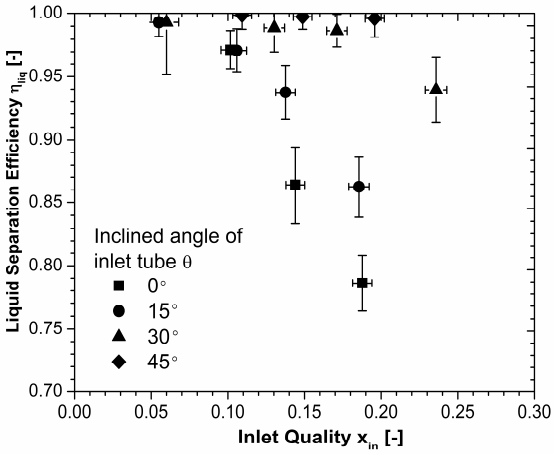

Figure 2.9: Variation of liquid separation efficiency with inlet quality and inlet inclination angles at 30 g/s (Hanfei and Hrnjak 2012).

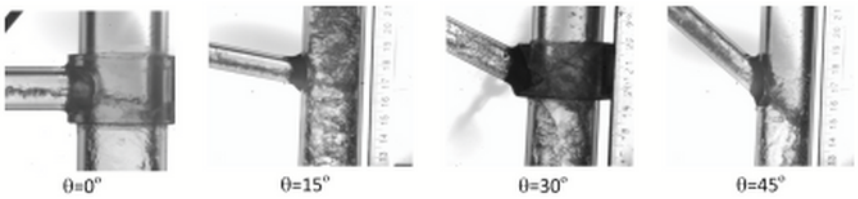

Figure 2.10: Photographs of flow showing effect of inlet inclination angle on the flow behaviour inside the vertical separator at 30 g/s mass flow rate and 15 % vapour quality (Hanfei and Hrnjak 2012).

Mo et al. (2014) conducted an experiment to investigate the separation in a condenser header. Air-water two-phase flow was used as a working fluid. The influence of the inlet flow pattern on the liquid separation efficiency of two-phase flow in the header was investigated. The results showed that the liquid separation efficiency was higher than 45 % when the flow pattern at the inlet was annular, while the liquid separation efficiency was higher than 80 % for slug flow at low liquid superficial velocity, but the liquid separation efficiency was essentially 100 % for stratified flow.

Xu et al. (2011*b*) investigated the control of vapour injection in a heat pump system using flash tank injection in both transient and steady state cases. An electronic expansion valve (EEV), upper stage expansion valve, a thermostatic expansion valve (TEV), and a lower stage expansion valve were used as shown in Figure 2.11. The experiment involved a vapour compression system which used a scroll compressor working with R410A. A flash tank with 0.07 m diameter and 0.32 m length was used in this system.

The results showed that to control the liquid level in the flash tank, the degree of superheat in the injected vapour can be used to set the mass flow rate as a result of setting the upper expansion valve.

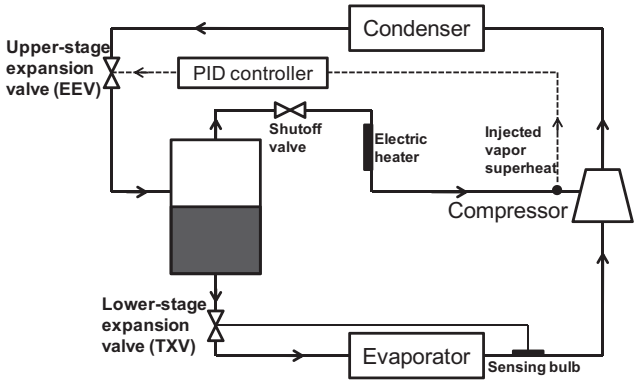

Figure 2.11: Schematic of the heat pump system with flash tank investigated by Xu et al. (2011).

Zheng et al. (2016) conducted an experimental study to investigate the effect of the mass flow rate on the liquid separation efficiency and the flow pattern at the inlet of a T-junction. The T-junction had an inlet horizontal tube (8 mm ID) and two vertical outlets of equal diameters (17.5 mm ID). The refrigerant R134a was used in all the experiments over a range of mass flux and vapour quality conditions spanning from 100 to 600 kg/m^2·s and 0.1 to 0.6, respectively. A high speed camera was used to record the flow patterns and flow behaviour inside the separator. Figure 2.12 shows images of the flow patterns at the horizontal inlet tube of the T-junction. The results revealed that the liquid separation efficiency deteriorated dramatically when the Froude number in the upward (gas outlet side) tube increased. The results also revealed that the highest liquid separation efficiency was achieved when the flow pattern was stratified at the inlet of the separator.

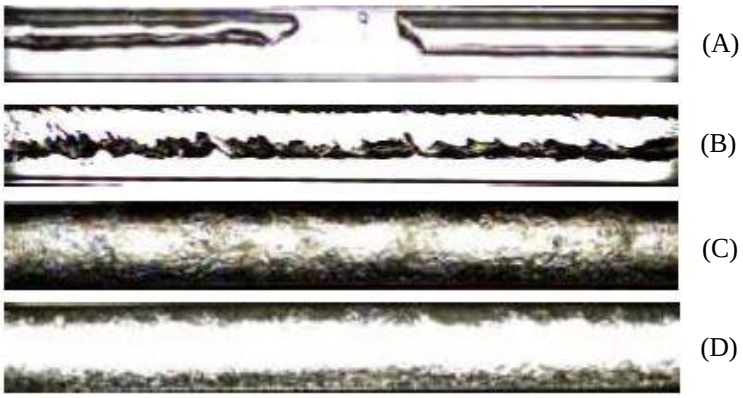

Figure 2.12: Typical flow patters in the horizontal tube inlet of a T-junction for different flow regimes: (A) Slug flow G = 100 kg/m^2·s, x_{in} = 0.073, (B) Stratified-wavy flow G = 100 kg/m^2·s, x_{in} =0.463, (C) Intermittent flow G = 400 kg/m^2·s, x_{in} = 0.372, (D) Annular flow G = 600 kg/m^2·s, x_{in} = 0.372 (Zheng 2016).

2.5 Vertical flash tank design using settling theory

In a vertical separator, the gravity force plays an important role in separating liquid droplets from gas-liquid two-phase flow (Delgado and Pichardo, 1999). Settling theory provides insight into the significance of certain physical processes that influence the separation of the liquid drops from the vapour phase (Elbel and Hrnjak, 2004). In order to apply setting theory in the design of a vertical separator, it is assumed that the liquid droplets act as uniform spherical particles that are separable from the vapour phase (GPSA, 2004). This assumption is justified for Weber numbers lower than 6. The Weber number is a dimensionless number expressing the ratio between the inertial force and the surface tension force (Villermaux and Bossa, 2009),

$$We = \frac{\rho_l . d_d . u^2}{\sigma} \tag{2.1}$$

where

ρ_l = Liquid density (kg/m^3).

u = Liquid velocity.

d_d = Droplet diameter (m).

σ = Surface tension (N/m).

Settling theory characterises the actual process that are taking place in the vertical separator. Whenever relative motion exists between a surrounding vapour and a liquid droplet, three main forces act on the liquid droplets: drag, gravity and buoyancy (Khorshidi and Naderipour, 2012). The resultant of these forces will cause acceleration in the direction of the net force. A force balance is established from Newton's law to determine the droplet acceleration in the upwards direction.

$$m.a = -F_g + F_b + F_d \tag{2.2}$$

where the gravity force F_g is always directed downward and is given by

$$F_g = \frac{\pi d_d^3}{6}.\rho_l.g \tag{2.3}$$

where the d_d is the droplet diameter, ρ_l is the liquid density, g is the gravitational acceleration constant. The bouncy force F_b is in the opposite direction to the gravity and is given as,

$$F_b = \frac{\pi d_d^3}{6}.\rho_g.g \tag{2.4}$$

where ρ_g is the vapour density.

The drag force F_d acts in the opposite direction of the droplet relative velocity, and its magnitude can be determined as follows,

$$F_d = \frac{1}{2}.\pi.C_D.\rho_g.(U_g + U_d)^2.\left(\frac{d_d}{2}\right)^2 \tag{2.5}$$

where U_g is the upward speed of the vapour (m/s), U_d is the downward speed of the droplet (m/s), C_D is the drag coefficient. By balancing the above three forces, the relative velocity difference for zero acceleration of the droplet (the terminal velocity difference) can be calculated as,

$$U_T = \sqrt{\frac{4.g.d_d^*.(\rho_l - \rho_g)}{3.\rho_g.C_D}} \tag{2.6}$$

where d_d^* is the droplet diameter for the terminal velocity difference. Souders and Brown (1934) presented the design theory for the vertical separators by arranging the Equation 2.6 as follows,

$$U_T = K\sqrt{\frac{\rho_l - \rho_g}{\rho_g}} \tag{2.7}$$

where K is the settling velocity coefficient or Sauders and Brown coefficient which is therefore given by

$$K = \sqrt{\frac{4gd_d^*}{3C_D}} \tag{2.8}$$

A critical situation arises if the vapour flow speed is sufficiently high that the droplet remains stationary within the vertical separator. In this situation, $U_d = 0$ and therefore $U_g = U_T$. Based on this condition, diameter D of the vertical separator can be determine as,

$$D = \sqrt{\frac{4\dot{V}}{\pi U_T}} \tag{2.9}$$

where $\dot{V}$ is the volumetric flow rate of gas (m^3/s).

Consequently, the required separator height H can be estimated as follows (Hrnjak, 2011),

$$H = \frac{4\dot{V}}{\pi D U_T} \tag{2.10}$$

Some studies have suggested that the range of droplet sizes of about 200 to 500 μm needs to be considered for the design of a separator (Stanly and Walas, 1990; Arnold and Stewart, 1998). When a mesh pad is used in a vertical separator, it can eliminate remaining droplets between 10 and 140 μm (GPSA, 2004).

The settling velocity coefficient (K) can be taken as a factor that indicates the compactness of a vertical separator, it can have a range of values based on the fluid properties and separator geometry (Svrcek and Monnery, 1993). Seader et al. (1998) suggested a range of K values between 0.03 and 0.107 m/s. In low pressure applications, the suggested K value is no more than 0.1 m/s and normally a 50 % safety margin is applied for separators without internal hardware such as an inlet diverter, vanes and mesh pads (Zhou, 2013).

Many correlations have been provided to estimate the droplet drag coefficient on the assumption that the droplet has a spherical shape. Yan et al. (2017) presented a list of drag coefficient correlations adopted from the Zhou (2013) as shown in Table 2.1.

Table 2.1: Correlation of drag coefficient for spherical droplet for Yan et al. (2017), adopted from Zhou (2013).

Literature	Correlation
White, F.M, 1991	$C_D = \frac{24}{Re_d} + \frac{6}{1+\sqrt{Re_d}} + 0.4$ $0 < Re_d < 2 \times 10^5$
Stoke's law	$C_D = \frac{24}{Re_d}$ $Re_d < 2$
Newton's Law	C_D=0.44 $500 < Re_d < 2 \times 10^5$
Intermediate Law	$C_D = \frac{18.5}{Re_d^{3/5}}$ $2 < Re_d < 500$
Schiller, 1935	$C_D = \frac{24}{Re_d}(1 + 0.15Re_d^{0.687})$ $Re_d < 1000$
Fair and Geyer, 1954	$C_D = \frac{24}{Re_d} + \frac{3}{Re_d^{0.5}} + 0.34$ $Re_d < 1 \times 10^4$

The droplet Reynolds number in Table 2.1 is defined as $Re_d = \frac{\rho_g d_d U_T}{\mu_g}$, where μ_g is the gas viscosity. The terminal velocity difference is solved U_T by an iterative process. GPSA (2004) presented a correlation to estimate the drag coefficient without an iterative process as shown in Equation 2.11, and then from Figure 2.13, the drag coefficient can be obtained.

$$C_D.Re^2 = \frac{0.95 \times 10^8.\rho_g.d_d^3.(\rho_l - \rho_g)}{\mu_g^2} \tag{2.11}$$

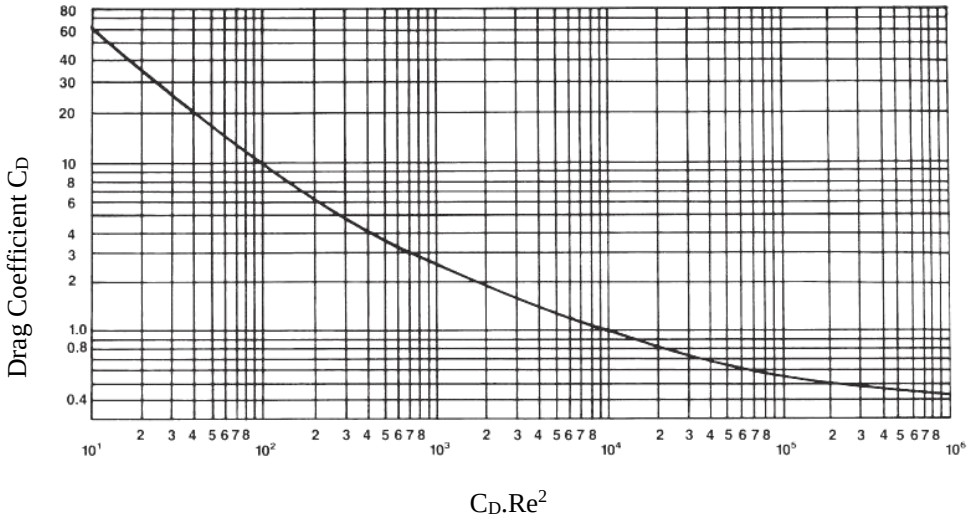

Figure 2.13: Drag coefficient values for the rigid spheres (GPSA 2004).

York (1954) introduced an improvement for the separator design using a wire mesh pad that updated the design methodology for the treatment of liquid separation problems. This design data led to the adoption of the Souders and Brown (1934) equations given in Equations 2.7 and 2.8.

Many studies based on the settling theory design have investigated the effect of the terminal velocity, droplet size and K value on the separator performance. To obtain a functional gravitational vertical separator, the fluid phases should be immiscible and have significantly difference densities (Hrnjak, 2011). Wu (1984) presented an approach that summarized the mechanisms of particle movement for gravity separators, applicable to vertical and horizontal separators. The effect of particle trajectory through two dimensions was considered to predict the particle motion and to develop the minimum separator length. However, the design droplet size was not specified.

Jekel and Reindl (2001) reviewed the literature on the principles governing gravity driven separation of liquid-vapour two-phase flow and design methods for separators, focusing on ammonia as the working fluid. Techniques for assessing separation performance in terms of the critical droplet size were presented for both vertical and horizontal separators. Equations of motion containing the three major forces that define the droplet trajectories in both vertical and horizontal separators were presented and implemented. Their recommendations were that the vapour velocity for a vertical separator should be 75 % to 90 % of the terminal velocity and the appropriate K value depends on the working fluid properties and droplet size.

Wiencke (2011) presented theoretical work to size a horizontal and vertical gravity liquid separator for industrial applications using ammonia as a refrigerant. The theoretical model was compared with observations which were taken from 85 industrial gravity separators. The study showed that the good design of a gravity separator not only depends on the separation velocities that are based on the critical droplet diameter but also needs to consider the fluid entering the separator and the methods of aiding the vapour to flow through the vapour outlet as these factors influence the three forces that effect the upward and downward velocities.

Khorshidi and Naderipour (2012) conducted an experimental study to design a gas-liquid vertical separator which was used in the Sarkhoun and Qeshm gas refinery with 2845 m^3/hr of gas phase and 24.54 m^3/hr of liquid. The experimental vertical vessel was 3 m in length and 2.45 m in diameter. The results showed that the length of

separator should be increased when an eliminator is not used due to the influence of K value on the terminal velocity U_T. The results also showed that the liquid droplets start to settle out when the vertical velocity is less than the terminal velocity $U_g < U_T$, .

2.6 CFD studies of separators

Many studies about the two-phase separation have been done numerically using computational fluid dynamic (CFD) simulations. Some of these studies investigated the two-phase separation in horizontal pipes such as Terzuoli et al. (2008), Walvekar et al. (2009) and Messa et al. (2014), while other studies investigated the vertical separation which includes the swirl separator such as Xiong et al. (2014) and cyclone separator such as Pointon et al. (2009), Zarrouk and Purnanto (2015) and Misiulia et al. (2017). Terzuoli et al. (2008) presented simulations of a stratified air-water two-phase flow in a horizontal rectangular channel using CFD codes (FLUENT and CFX). Experimental work was also performed to compare with the CFD simulations. A rectangular channel 0.1 m high, 0.2 m width and 13 m long was established and uniform air and water velocities of 3.66 m/s and 0.395 m/s were used to establish a stratified flow condition. In the CFD simulations, an inhomogeneous model was used to solve the velocities for each phase, while the homogeneous setting was adopted for turbulent flow simulated with the $k-\omega$ shear stress transport (SST) model. The results showed that water height in the channel is affected by different equilibrium conditions between drag force, gravitational force and frictional force which are acting on the fluid. The difference between the experimental and CFD simulation results was not specified.
Walvekar et al. (2009) conducted a numerical study using CFD Fluent version 6.2 to simulate three dimensional two-phase flow in a horizontal tube. Two immiscible liquids: oil and water were used as the working fluids. The horizontal pipe had a 0.024 m inside diameter and 9.7 m length and this geometry was used as the domain to simulate the two-phase flow. The Eulerian-Eulerian two-phase model with 0.001 s time steps were used to achieve transient simulation of the two-phase flow inside the horizontal pipe. Velocity inlet and pressure outlet were specified as a boundary conditions. The results were compared with the experimental results from other literature. The results revealed that the CFD was successful in simulating the two-phase dispersed

liquid-liquid flows, and an average relative deviation between the simulations and the experiment of 3.41% was obtained for the oil hold up parameter.

Messa et al. (2014) performed numerical simulations to predict the main features of fully suspended slurry flows, namely pressure gradient, solid-volume fraction and velocity profile in a horizontal pipe. The Eulerian-Eulerian two-phase model with the $k - \epsilon$ turbulence model was used. Velocity inlet and pressure outlet were set as the boundary conditions. The results showed that the simulations provided the pressure gradient within about $\pm$ 20 % of the measured values.

Xiong et al. (2014) used CFD simulation to investigate the two-phase flow inside a swirl-vane separator and to analyse the separation performance. A mixture of air and water was used as the working fluid. The results revealed that the separation efficiency of the swirl-vane separator depends on the flow patten and the water velocity, while the pressure drop is mainly affected by the air flow rate and water droplet diameter. The CFD simulation results apparently agreed with the experimental results, but the difference between the CFD simulation and experimental results was not quantified.

Pointon et al. (2009) presented a study using a commercial CFD package to simulate the separation process in a geothermal cyclone separator. The simulation was focused on the separation process and the sizing for very large cyclone separators using a wide range of fluid conditions. The results revealed that the CFD can be used to examine particular aspects of the cyclone separator design, including upstream piping arrangement and performance of the cyclone separator, but the validity of the simulation was not quantified.

Zarrouk and Purnanto (2015) reviewed recent research that utilises CFD for steam-water cyclone separator design. The study demonstrated that the CFD simulations provide insight to the two-phase behaviour and features that cannot be analysed from any empirical approach.

Misiulia et al. (2017) presented a CFD study to simulate the two-phase flow inside a cyclone separator and to optimize the geometry of the cyclone separator. Four main geometrical parameters were considered in the numerical optimization: core diameter, number of vanes, height of vanes and leading edge angle. The results indicated that the most significant geometrical parameters of the cyclone separator are the number of vanes, the vane angle and the vane height. A new optimised geometry was obtained from the CFD simulation but it was not validated with experimental results.

Obviously CFD simulation can be used to examine the two-phase flow separation process including separator geometry. However, from the existing studies it is different to obtain a clear understanding of the precision that can be expected from CFD when using it as a design tool for vertical flash tank separator. Although there are several studies that have applied CFD to phase separation applications with swirling flow conditions, few have applied CFD to the apparently simpler case of gravity separation in a vertical flash tank. There is a further need to establish fundamental design recommendations for optimising the liquid separation efficiency of vertical flash tank separators and it is conceivable that this can be achieved through CFD simulations, but only by careful comparison and assessment against experimental results.

2.7 Conclusion

This chapter presented theoretical, experimental and numerical studies that have been performed on separation applications. It also presented the important role of the vertical flash tank separator in air conditioning and refrigeration systems. The literature confirmed that using the vertical flash tank separator in air condition and refrigeration systems increases the system performance and its capacity by around 10 to 20 %. Therefore, the flash tank is an important component that is worth considering for air conditioning and refrigeration systems.

The liquid separation efficiency is an important parameter that characterise the performance of vertical flash tank separators. Using the flash tank allows vapour to be injected into compressor and provides separated liquid to be fed into evaporator, so the separation efficiency indicates how much separated liquid can be obtained from the flash tank separators. The separation efficiency can be affected by the aspect ratio of the separator, flow pattern in the inlet of the separator, inclination angle of the inlet pipe, and mass flow rate of the working fluid.

Settling theory is a theoretical approach for the vertical flash tank separator design. The settling theory considers drag, gravity and buoyancy on liquid drops and the resultant of those forces will cause acceleration in the direction of the net force. The literature provides some design recommendations such as the vapour velocity for the vertical separator should be 75% to 90% of the terminal velocity and the K value

should be no more than about 0.1 m/s. While such recommendations offer some guidance for the design process they do not provide a tool for vertical flash tank design optimisation.

In contrast to settling theory, CFD does potentially provide a method for vertical flash tank design optimisation. Studies of two-phase flow simulations using CFD were reviewed. However a clear understanding of the precision that can be obtained from CFD when using it as design tool for vertical flash tank separators can not be derived from the existing studies. Some CFD studies reported agreement with experimental measurement of key parameters to within a few percent, in others the agreement was much worse, and in still others, the CFD results were not even assessed relative to experiments. Therefore, this work aims to provide experimental data that contributes additional knowledge for flash tank design both through the direct application of empirical results and through the use of the data in the assessment of CFD as a flash tank design tool. A clear understanding of the precision of the CFD will be obtained by comparing the CFD with the experiments result.

Chapter 3

Basic definitions and terminology of two-phase flow

3.1 Introduction

This chapter introduces two-phase flow fundamentals. Primary variables and their relationship with each other are presented, and key non-dimensional two-phase flow parameters are introduced.

3.2 Definition of two-phase flow

Two-phase flow is the simplest case of multiphase flow and is restricted to two phases in close proximity travelling together at the same time. Each phase is homogeneous in physical structure and chemical composition. Two-phase flow is often associated with phase change phenomena such as boiling and condensation processes. This results in a complicated transport process in engineering applications compared with single phase flow. The two-phase flow of vapour and liquid which occurs in pipes, heat exchanger, and other equipment has been investigated intensively by many researchers for many years as the two-phase flow of liquid-vapour plays a significant role in many applications.

In order to understand the principles of two-phase flow, the basic definitions and dimensionless numbers associated with two-phase flow are introduced.

3.3 Vapour quality

One important factor in two-phase flow is vapour quality x, which is defined as the ratio of vapour mass to the total mass of the mixture (Bergman et al., 2011). The vapour quality can be used to identify the dryness or wetness of the mixture in the two-phase flow regime.

$$x = \frac{\dot{m}_g}{\dot{m}_t} \tag{3.1}$$

$$\dot{m}_t = \dot{m}_g + \dot{m}_l \tag{3.2}$$

$$\dot{m}_g = GAx \tag{3.3}$$

$$\dot{m}_l = GA(1 - x) \tag{3.4}$$

where

x = Vapour quality

$\dot{m}_g$ = Vapour mass flow rate (kg/s)

$\dot{m}_l$ = Liquid mass flow rate (kg/s)

$\dot{m}_t$ = Total mass flow rate of the mixture (kg/s)

G = Total mass flux (kg/m^2·s)

A = Total cross section area (m^2)

Vapour quality defines the proportions of the liquid and vapour phases in the mixture, and it can be calculated from thermodynamic properties such as enthalpy. For example,

$$x = \frac{h - h_f}{h_{fg}} \tag{3.5}$$

where h_f is the saturated liquid enthalpy, $h_{fg} = h_g - h_f$ is the difference between the specific enthalpy of the saturated vapour and saturated liquid, and h is the mixture specific enthalpy which can be defined as

$$h = \frac{\dot{m}_l h_f + \dot{m}_g h_g}{\dot{m}_l + \dot{m}_g} \tag{3.6}$$

3.4 Volume flow rate

In two-phase flow, the volume flow rate can be used to calculate the mass flow rate of a particular fluid. The volume flow rate of each phase is given by

$$Q_g = \frac{\dot{m}_g}{\rho_g} \tag{3.7}$$

$$Q_l = \frac{\dot{m}_l}{\rho_l} \tag{3.8}$$

So, from Equations 3.7 and 3.8, the total volume flow rate can be calculated by

$$Q_t = Q_g + Q_l \tag{3.9}$$

where

Q_g = Vapour volume flow rate (m^3/s)

Q_l = Liquid volume flow rate (m^3/s)

Q_t = Total volume flow rate (m^3/s)

ρ_g = Density of vapour (kg/m^3)

ρ_l = Density of liquid (kg/m^3)

3.5 Mass flux

Mass flux (mass velocity) is the mass of flow rate of a particular fluid per unit cross sectional area. It is an essential variable in two-phase flow analysis. The mass flux is defined in terms of the total mass flow rate and the total cross section area (Ishii and Hibiki, 2011).

$$G = \frac{\dot{m}_t}{A} \tag{3.10}$$

3.6 Velocities

For two fluids moving through a given cross sectional area, a number of definitions of the associated velocities are required because generally, in two-phase flow, the phases do not have the same velocity. Under these conditions, a relative velocity will exist between the two phases (Dinaryanto et al., 2016). Consequently, the velocity can be described as either an average local velocity or a superficial velocity.

3.6.1 Average Local Velocity

The average local velocity is the ratio between the volume flow rate of a particular phase and the cross sectional area that is occupied by that phase. It is a cross sectional average velocity.

$$u_g = \frac{Q_g}{A_g} \tag{3.11}$$

$$u_l = \frac{Q_l}{A_l} \tag{3.12}$$

where

u_g = Vapour local velocity (m/s)

A_g = Area occupied by vapour (m^2)

u_l = Liquid local velocity (kg/m^2)

A_l = Area occupied by liquid (m^2)

3.6.2 Superficial Velocity

Because of the difficulty of measuring A_l and A_g, the area occupied by the liquid phase and gas phase respectively, the superficial velocity is used. Superficial velocity is calculated by dividing the volume flow rate of each phase by the total cross section area (Setyawan et al., 2016).

$$u_{sg} = \frac{Q_g}{A} = \frac{Gx}{\rho_g} \tag{3.13}$$

$$u_{sl} = \frac{Q_l}{A} = \frac{G(1-x)}{\rho_l} \tag{3.14}$$

where

A = Total cross section area (m^2)

u_{sg} = Vapour superficial velocity (m/s)

u_{sl} = Liquid superficial velocity (m/s)

The total superficial velocity can be defined as the summation of the liquid and vapour superficial velocities.

$$u_{st} = u_{sl} + u_{sg} \tag{3.15}$$

In separated flows, where the phases travel at different velocities, the velocity ratio (also called the slip velocity) is also used to determine the local velocities of phases. The velocity ratio can be given by,

$$S = \frac{u_g}{u_l} = \frac{\dot{m}_g \rho_l A_l}{\dot{m}_l \rho_g A_g} \tag{3.16}$$

The velocity ratio also has a relationship with the vapour quality and void fraction (Fei, 2004).

$$S = \left(\frac{x}{1-x}\right)\left(\frac{\rho_l}{\rho_g}\right)\left(\frac{1-\alpha}{\alpha}\right) \tag{3.17}$$

where

α = Void fraction = A_g/A_t.

S = Velocity ratio.

Density is one of the thermodynamic properties for each phase that needs to be identified in two-phase flow. The effective total or mixture density is given by

$$\rho_{TP} = \rho_g x + (1 - x)\rho_l \tag{3.18}$$

where ρ_{TP} is the two-phase effective density.

3.7 Void fraction in two-phase flow

The void fraction is essential to understand two-phase flow pattern maps. It is defined as the ratio between the cross sectional area that is occupied by the vapour and the total cross sectional area of the channel (Wojtan et al., 2005; Xue et al., 2016). The void fraction represents a fundamental parameter needed to determine mean velocities of phases. Figure 3.1 illustrates the cross sectional void fraction in a circular pipe.

$$\alpha = \frac{A_g}{A_t} \tag{3.19}$$

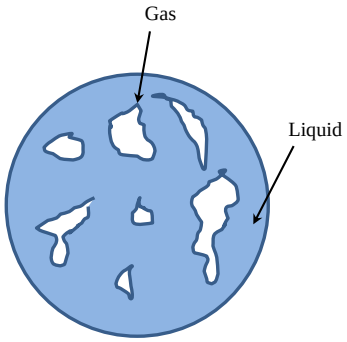

Figure 3.1: Cross sectional void fraction

In two-phase flow, a tool called the flow pattern map provides a picture of two-phase flow behaviour. However, to understand these flow pattern maps, the void fraction should be estimated (El Hajal et al., 2003). The void fraction can be easily calculated for two-phase flow when the liquid and vapour move at the same flow velocity, which is defined as homogeneous flow using (El Hajal et al., 2003)

$$\alpha_H = \left[1 + \left(\frac{1-x}{x}\right)\left(\frac{\rho_g}{\rho_l}\right)\right]^{-1} \tag{3.20}$$

However, in the two-phase flow regions where the phases travel at different velocities, which is defined as non-homogeneous flow, the void fraction can be estimated using (Rouhani and Axelsson, 1970)

$$\alpha_{NH} = \frac{x}{\rho_g}\left([1 + 0.12(1-x)]\left[\frac{x}{\rho_g} + \frac{1-x}{\rho_l}\right] + \frac{1.18(1-x)[g\sigma(\rho_l - \rho_g)]^{0.25}}{G{\rho_l}^{0.5}}\right)^{-1} \tag{3.21}$$

Equations 3.21 is a frequently used correlation that is based on experimental data. However, the Rouhani and Axelsson equation is found to underestimate the void fraction in non-homogeneous flow. In practice, for non-homogeneous flow, the void fraction falls between the homologous limit and the Rouhani and Axelsson equation.
The mean logarithmic void fraction ($\alpha_{LM\epsilon}$) which typically provides a better estimation of the non-homogeneous void fraction than the Rouhani and Axelsson equation is given by (El Hajal et al., 2003)

$$\alpha_{LM\epsilon} = \frac{\alpha_H - \alpha_{NH}}{\ln(\frac{\alpha_H}{\alpha_{NH}})} \tag{3.22}$$

where

$\alpha_{LM\epsilon}$ = Mean logarithmic void fraction.

α_H = Homogeneous void fraction.

α_{NH} = Non-homogeneous void fraction (Rouhani and Axelsson model).

Figure 3.2 presents a comparison of the different values of $\alpha_{LM\epsilon}$, α_H and α_{NH} for R410A at saturation temperature of 4 ℃ and mass flux of 400 kg/m^2·s in a circular tube with inside diameter of 8 mm.

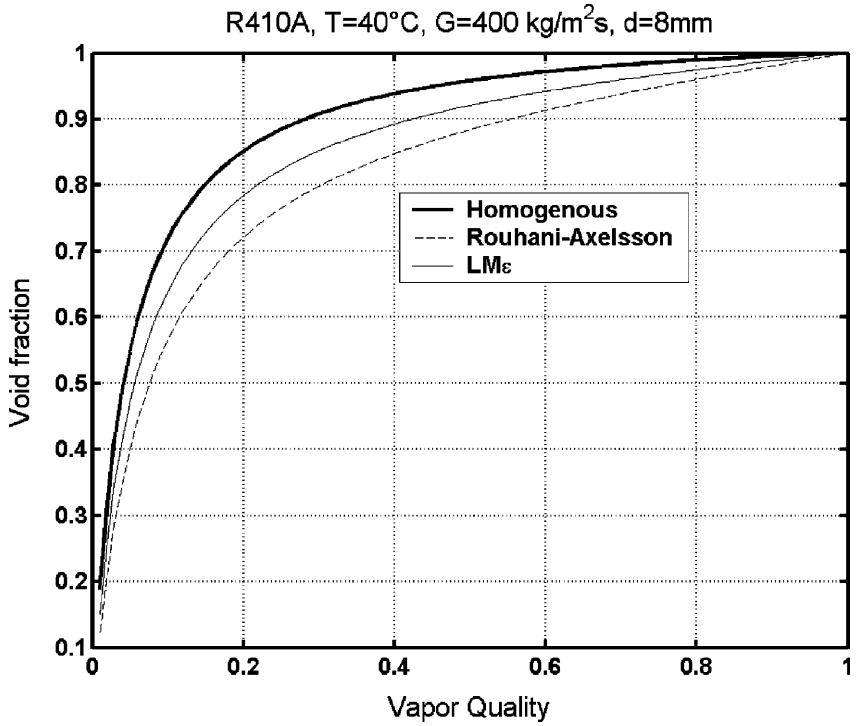

Figure 3.2: Comparison of the logarithmic mean void fraction $\alpha_{LM\epsilon}$ with the Rouhani and Alxelsson void fraction α_{NH} and homogeneous void correlation α_H for R410A in circular tube with inside diameter d= 8 mm at mass flux G=400 kg/m^2·s, saturation temperature T=40 ℃ (El Hajal et., 2003)

3.8 Two-phase flow regimes in a horizontal tube

The two-phase flow regime at the inlet of a flash tank separator can significantly influence the separation performance of the flash tank separator (Hanfei and Hrnjak, 2012). Xiong et al. (2014) reported that the separation efficiency of a two-phase flow separator is affected by the inlet flow regime.

Many flow pattern maps of adiabatic two-phase flow have been developed for a horizontal pipe, while other researchers considered the heat flux in their studies to investigate the two-phase flow regimes, such as Collier and Thome (1994) who defined the two-phase flow regimes during an evaporation process in a horizontal tube, as shown in Figure 3.3.

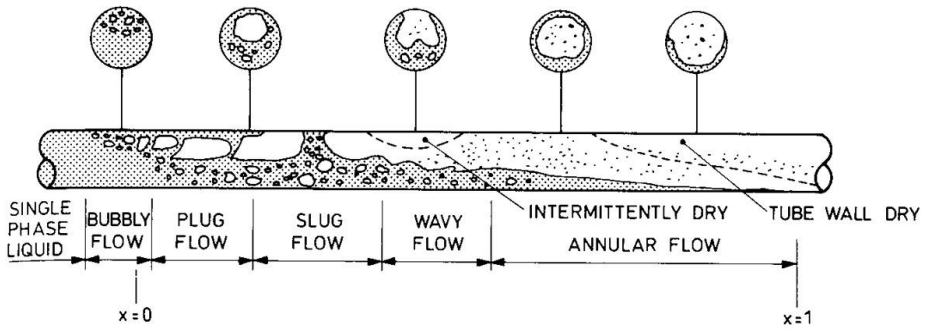

Figure 3.3: Two-phase flow regimes during the evaporation process in a horizontal tube (Collier and Thome, 1994).

The flow regime is a characteristic of two-phase flow which needs to be defined to determine other parameters such as heat transfer. According to flow rates, physical properties of the two phases and the geometry of the tube, a variety of flow patterns can occur (Dobson, 1994). In a horizontal tube, the two-phase flow patterns are different from a vertical tube as gravity acts normal to the flow direction in the horizontal tube (Saisorn and Wongwises, 2015).

The two-phase flow patterns in a horizontal tube can be classified into two main groups. Figure 3.4 illustrates the first group of the two-phase flow patterns that occur at a high value of void fraction, and Figure 3.5 illustrates the second group of the two-phase flow patterns that occur at a low value of void fraction (Dobson, 1994).

The first group includes five flow patterns: stratified flow, wavy flow, wavy-annular flow, annular flow and annular-mist flow. While the second group includes three flow patterns: slug, plug and bubbly flow. In the first group, the flow patterns are organized according to increasing vapour velocity. In contrast, the flow patterns in the second group are organised according to increasing liquid velocity or decreasing void fraction. The stratified flow pattern is generated when the vapour velocity is very low. As gravity plays an important role in this horizontal orientation, the liquid velocity in the top portion of the tube is mostly downward while the velocity in the bottom portion is in the mean flow direction (Milkie et al., 2016). The interface between liquid and vapour remains smooth as the velocity of vapour is low. When the vapour velocity is increased, the pattern become wavy flow. In the wavy flow regime the interface between the liquid and vapour becomes unstable as a result of shear forces acting on the surface of the liquid (Roman et al., 2016).

By further increasing in vapour velocity, waves start to wash up and around the tube wall causing a transition to annular flow. However, before reaching the annular flow pattern, a flow pattern called wavy-annular is generated (Zhuang et al., 2016). When the liquid film thickness become uniform at the top and bottom of the tube, the flow pattern is completely annular. In the annular flow pattern, the liquid film moves on the wall of the tube and high velocity gas is in the centre (Zhuang et al., 2016).

The last pattern of the first flow pattern group in Figure 3.4 is annular-mist flow. In this regime, liquid droplets move in the centre of the tube with the vapour as a result of shearing off the peak of the liquid waves due to high vapour velocity (Milkie et al., 2016). The appearance of the annular-mist pattern is an annular film with a mixture of mist and vapour in the centre of the tube.

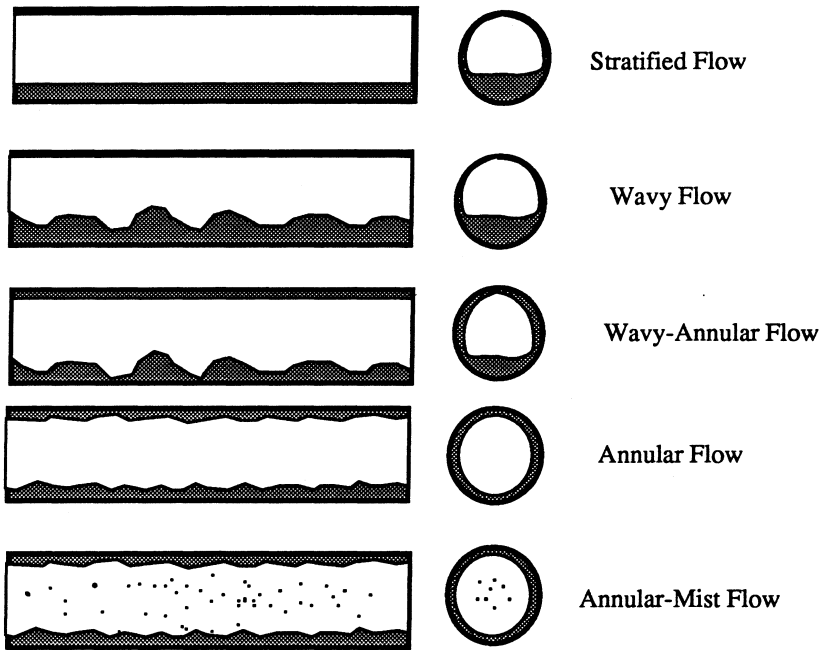

Figure 3.4: Flow regime classifications in a horizontal pipe at high void fraction (Dobson, 1994)

In the flow regimes of Figure 3.5, the slug flow occurs at low void fraction, it has bullet shaped bubbles with rounded noses and tails separated by liquid phase (Roman et al., 2016). In the slug flow, as the bubbles are typically large and the slug length depends on the tube diameter, bubbles can almost fill the tube (Abdulkadir et al., 2016). By further decreasing the void fraction, the plug flow pattern appears, in which the bubbles are smaller than that in the slug flow pattern and the liquid phase is continuous along the bottom of the tube (Ramezani et al., 2016). The last flow pattern in the second group is the bubbly flow pattern. The gas bubbles in this pattern are dispersed in the liquid phase. Due to buoyancy, there tends to be a higher concentration of bubbles in the upper half of the tube (Bottin et al., 2014).

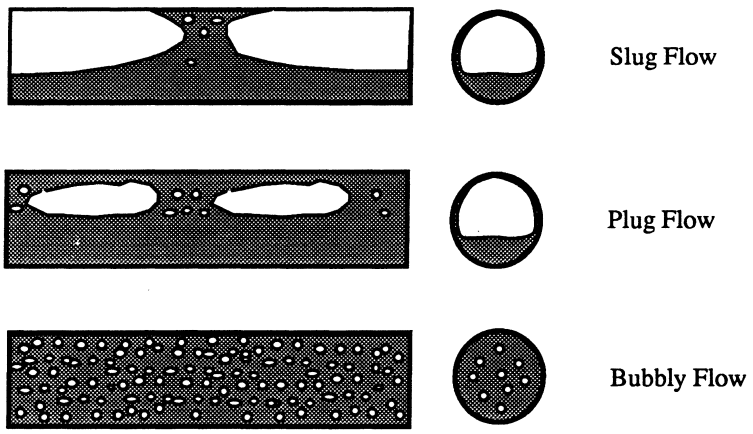

Figure 3.5: Flow regime classifications in a horizontal pipe at low void fraction (Dobson, 1994)

3.9 Two-phase flow regimes maps

This section explains the two-phase flow regime maps that identify the transition boundaries between the flow patterns; it is a diagram that typically uses the non-dimensional parameters to present the velocities of the liquid and gas (GPSA, 2004). Baker et al. (1954) presented the earliest two-phase flow pattern map for horizontal flow in a tube. In order to use this map, the mass velocities of liquid (G_l) and vapour (G_g) must be defined as shown in Figure 3.6. The gas-phase and liquid-phase parameters are essential to identify the gas and liquid mass velocities. To calculate the gas-phase and liquid-phase parameters, the properties of the fluid are combined as.

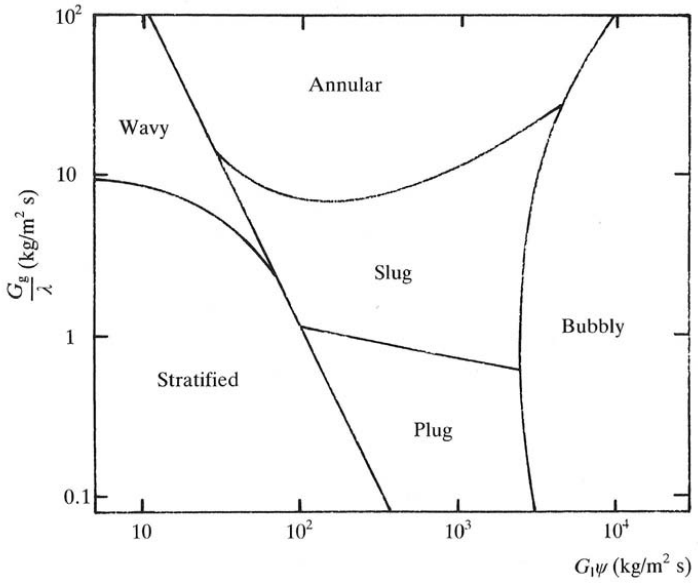

Figure 3.6: Air-water two-phase flow pattern map for horizontal flow in tube by Baker (1954).

$$\lambda = \left[\frac{\rho_g \rho_l}{\rho_{air}\rho_{water}}\right]^{0.5} \tag{3.23}$$

$$\Psi = \left(\frac{\sigma_{water}}{\sigma}\right)\left[\left(\frac{\mu_l}{\mu_{water}}\right)\left(\frac{\rho_{water}}{\rho_l}\right)^2\right]^{0.333} \tag{3.24}$$

Air and water properties are used as the reference properties at standard atmospheric pressure and room temperature. Air-water data were used to develop this map. In Figure 3.6, the parameters $\frac{G_g}{\lambda}$ and $G_l\Psi$ are the gas and liquid mass velocity.

Mandhane et al. (1974) also proposed a two-phase flow pattern map for a horizontal flow in pipe based on water-air two-phase flow data. Because of the transition between flow patterns do not occur suddenly, the transitions between flow patterns are shown by broad bands instead of lines as shown in Figure 3.7. To identify the flow pattern using this map, the superficial velocities for both liquid and gas phases should be defined.

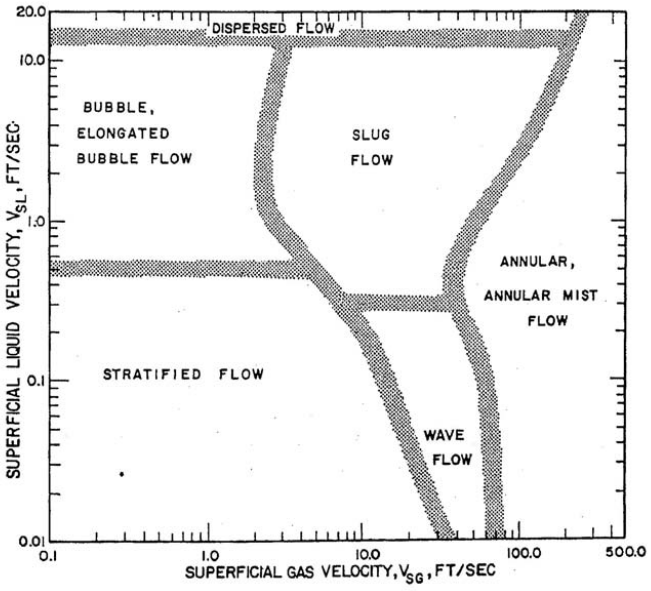

Figure 3.7: Air-water two-phase flow pattern map for horizontal flow in a tube by Mandhane et al. (1974).

Kattan et al. (1998) presented a modification of a two-phase flow pattern map which was proposed by Steiner (1993). The modification includes the influence of heat flux and dryout on the flow pattern transition boundaries. This map provides a linear-liner graph of vapour quality (vapour portion) with mass flux (mass velocity) for R410A, as shown in Figure 3.8. This map presents the transition curves of stratified-wavy flow (SW), fully stratified flow (S), intermittent flow (I), annular flow (A), bubbly flow (B), and mist flow (M).

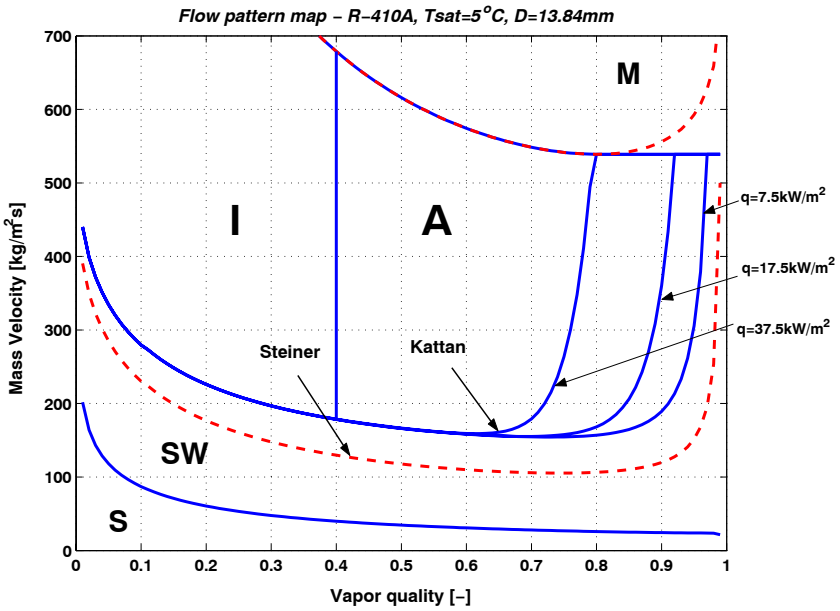

Figure 3.8: Two-phase flow pattern map for R410A at T_{sat}=5 ℃ in a 13.84 mm diameter horizontal tube by Kattan et al. (1998).

Wojtan et al. (2005) conducted a study to revise a two-phase flow pattern map that was introduced by Kattan et al. (1998) using refrigerant R22 and considered the heat flux effect on transition curves. The experimental work provided the void fraction inside the horizontal tube. The results shown in Figure 3.9 provide a new map of two-phase flow for R22 at T_{sat} = 5 ℃ in a 13.84 mm diameter of a horizontal tube, evaluated at 100 kg/m^2·s and 2.1kW/m^2, where the symbols have the following meanings (S) stratified flow, (SW) stratified-wavy flow, (I) intermittent flow, (A) annular flow, (M) mist flow and (D) transition zone between mist and annular flow.

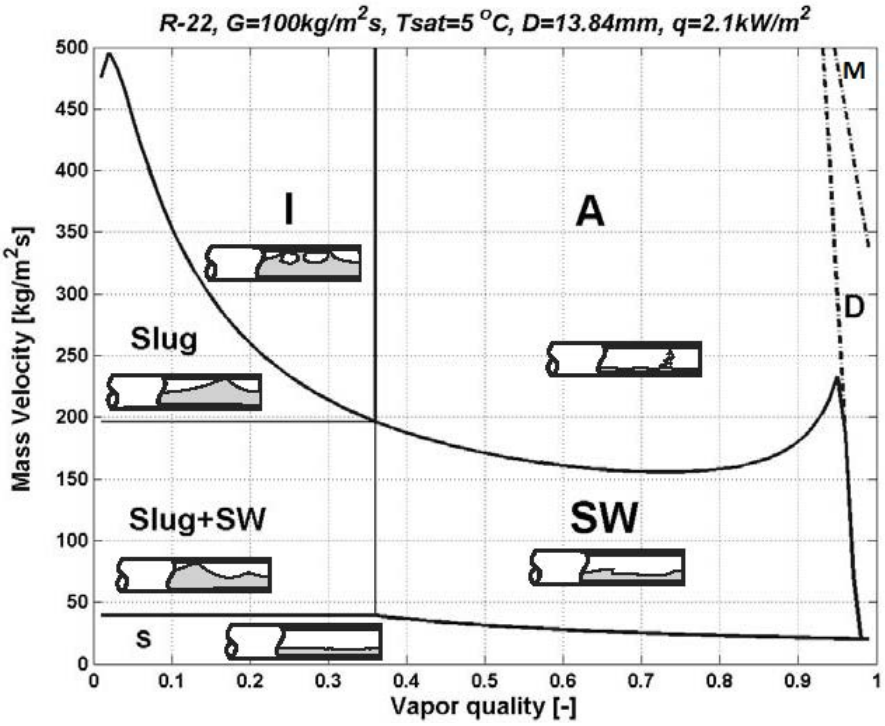

Figure 3.9: Flow pattern map for R22 at $T_{sat} = 5^oC$ in the 13.84 mm test section diameter, evaluated at 100 kg/m^2.s and 2.1 kW/m^2 by Wojtan et al. (2005).

3.10 Equations for regime transitions

In order to estimate the transition boundaries between the flow patterns, non-dimensional parameters have been defined in literature (Wojtan et al., 2005; Kanizawa and Ribatski, 2012; Acunha and Schneider, 2013; Ghajar and Bhagwat, 2013). Calculating the void fraction (see section 3.7) is the first step in defining the boundaries between the flow regimes. The void fraction is then used to calculate indicative non-dimensional values for the area occupied by liquid and/or gas as illustrated in Figure 3.10.

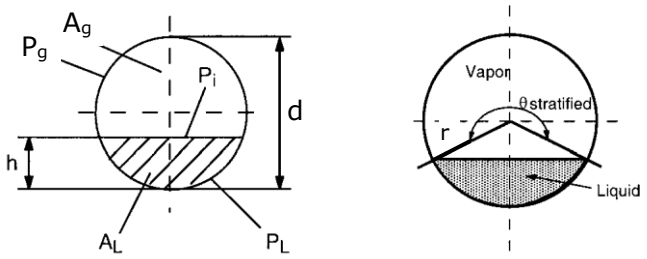

Figure 3.10: Stratified angle in two-phase flow (Thome 2003).

The non-dimensional area occupied by the liquid is

$$A_L = \frac{A(1-\alpha)}{d^2} \tag{3.25}$$

and the non-dimensional area occupied by the gas is

$$A_g = \frac{A\alpha}{d^2} \tag{3.26}$$

The non-dimensional height of the liquid is defined by

$$h_{Ld} = 0.5\Big(1 - \cos\Big(\frac{2\pi - \theta_{strat}}{2}\Big)\Big) \tag{3.27}$$

and the non-dimensional perimeter of the interface is

$$P_{id} = \sin\Big(\frac{2\pi - \theta_{strat}}{2}\Big) \tag{3.28}$$

In order to calculate the stratified angle θ_{strat} that is presented in Figure 3.10, the following geometrically defined equation is solved (El Hajal et al., 2003);

$$A_{Ld} = \frac{A_L}{d^2} \tag{3.29}$$

$$A_{Ld} = \frac{1}{8}[(2\pi - \theta_{strat}) - \sin(2\pi - \theta_{strat})] \tag{3.30}$$

Thome and Hajal (2003) presented the wavy transition curve which extends from stratified-wavy flow to intermittent and annular flow.

$$G_{wavy} = \left[\frac{16{A_g}^3 g d \rho_l \rho_g}{x^2\pi^2(1-(2h_{Ld}-1)^2)^{0.5}}\left[\frac{\pi^2}{25{h_{Ld}}^2}(1-x)^{-F_1(q)}\left(\frac{We}{Fr}\right)_L^{-F_2(q)} + 1\right]\right]^{0.5} + 50 - 75e^{-\left(\frac{(x^2-0.97)^2}{x(1-x)}\right)} \tag{3.31}$$

The non-dimensional empirical exponents accounting for the effect of heat flux on dryout during evaporation are $F_1(q)$ and $F_2(q)$:

$$F_1(q) = 646.0\left(\frac{q}{q_{crit}}\right)^2 + 64.8\left(\frac{q}{q_{crit}}\right) \tag{3.32}$$

$$F_2(q) = 18.8\left(\frac{q}{q_{crit}}\right) + 1.023 \tag{3.33}$$

where the critical heat flux q_{crit} was used to normalize the heat flux. The heat flux effect on dryout is not required for condensation and adiabatic conditions and hence in these cases, $q = 0$. and hence, the values of F_1 and F_2 become 0 and 1.023, respectively, (El Hajal et al., 2003). Based on many studies (Thome and Hajal, 2003; El Hajal et al., 2003; Cheng et al., 2008), q_{crit} can be calculated using

$$q_{crit} = 0.131{\rho_g}^{0.5} h_{Ld}[g\sigma(\rho_l - \rho_g)]^{0.25} \tag{3.34}$$

where h_{lg} is the latent heat of vaporization (J/kg).

Acunha and Schneider (2013) presented the transition curve from fully stratified to stratified wavy flow that can be calculated as,

$$G_{strat} = \left[\frac{(226.3)^2 A_L {A_g}^2 \rho_g(\rho_l - \rho_g)\mu_l g}{x^2(1-x)\pi^3}\right]^{0.333} + 20x \tag{3.35}$$

From Figure 3.9, there is a vertical line between annular and intermittent flow (El Hajal et al., 2003). This line can be calculated as,

$$x_{IA} = \left\{\left[0.2914\left(\frac{\rho_g}{\rho_l}\right)^{-1/1.75}\left(\frac{\mu_l}{\mu_g}\right)^{-1/7}\right] + 1\right\}^{-1} \tag{3.36}$$

This line intersects the stratified wavy curve flow and the mist curve. Thome and Hajal (2003) reported that the mist curve can be determined as,

$$G_{mist} = \left[\frac{7680 {A_g}^2 g d \rho_l \rho_g}{x^2 \pi^2 \xi}\left(\frac{Fr}{We}\right)_l\right]^{0.5} \tag{3.37}$$

The ratio between the Weber number and Froude number that occurs in Equation 3.37 can be calculated using

$$\left(\frac{Fr}{We}\right)_l = \frac{g d^2 \rho_l}{\sigma} \tag{3.38}$$

and the factor ξ is

$$\xi = \left[1.138 + 2log(\frac{\pi}{1.5 A_{Ld}})\right]^{-2} \tag{3.39}$$

where A_{Ld} is defined by Equation 3.30. Finally, the last transition curve, the bubbly curve is given by.

$$G_{bubbly} = \left[\frac{256 {A_{Ld}}^2 g d^{1.25} \rho_l(\rho_l - \rho_g)}{0.3164(1-x)^{1.75}\pi^2 {\mu_l}^{0.25} P_{id}}\right]^{1/1.75} \tag{3.40}$$

The bubbly flow occurs at very high mass velocities that are above the range shown in Figure 3.9.

3.11 Two-phase pattern map for water

As water was used in the present work, a two-phase flow pattern map was created for water two-phase flow based on the equations presented in the previous section and this map is presented in Figure 3.11. Matlab was used to create the pattern map using water properties and for a horizontal tube of diameter 25 mm, corresponding to that used in the present work. The Matlab code is presented in the Appendix D.

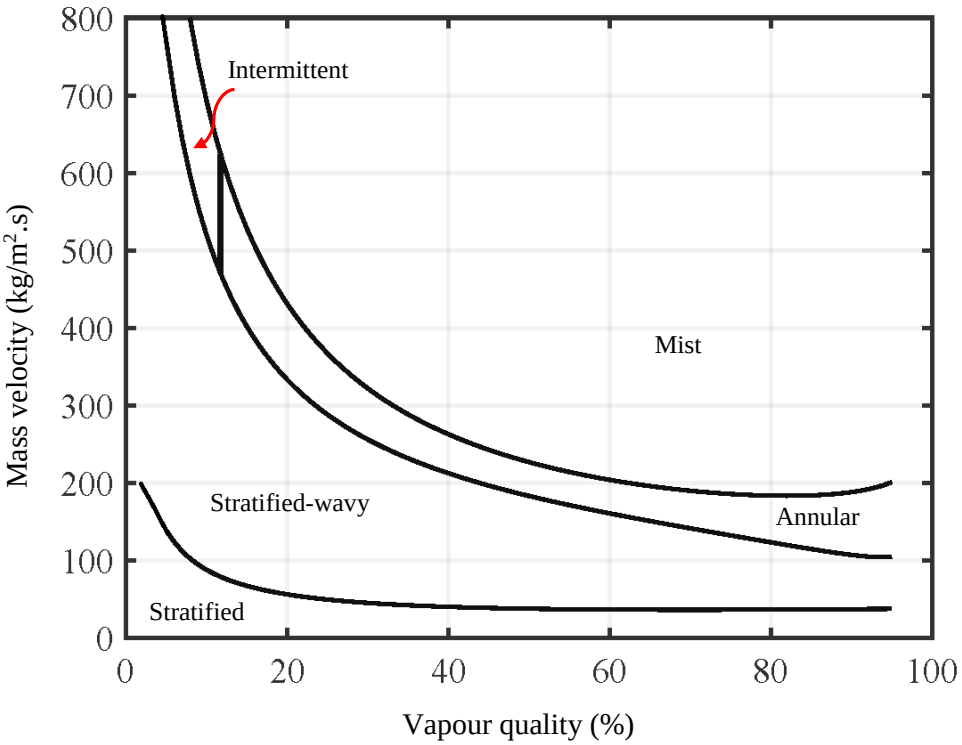

Figure 3.11: Two-phase regimes map for water according to the equations presented in section 3.10 for d= 25 mm and saturated conditions at 23 ℃.

3.12 Non-dimensional two-phase flow numbers

In the present study on the vertical flash tank separator, there are independent parameters which are required for the dimensional analysis. These parameters are,

$\dot{m}$: Mass flow rate (kg/s)

x : Vapour quality, dryness fraction (dimensionless)

d : Inlet tube diameter (m)

D : Flash tank diameter (m)

l : Inlet tube length (m)

H : Tank height (m)

μ_g, μ_l : Viscosity of gas and liquid fluid (N.s/m^2)

ρ_g, ρ_l : Density of gas and liquid (kg/m^3)

σ : Surface tension (N/m)

α : Void fraction

Because the flow is adiabatic, the temperature and specific heat are not used. In addition, μ_g can be neglected because its influence on the flow pattern is not significant (Hanfei and Hrnjak, 2012).
Reynolds number (Re), Froude number (Fr) and Weber number (We) are the important non-dimensional numbers in two-phase flow and they can be defined individually as follows (Hrnjak, 2004).

$$Re = \frac{\rho u D}{\mu} \tag{3.41}$$

$$Fr = \frac{u^2}{gD} \tag{3.42}$$

$$We = \frac{\rho u^2 D}{\sigma} \tag{3.43}$$

The Equations 3.41, 3.42 and 3.43 are valid for single phase flow (Li et al., 2017), but they can also be applied to liquid and/or gas phases individually to characterise the flow behaviour inside a two-phase flow system. For the two-phase flow in a vertical flash tank separator, the dimensionless numbers can be written as follows (Triplett et al., 1999; Cioncolini and Thome, 2017).

$$Re_{TP} = \frac{GD}{\mu_{TP}} \tag{3.44}$$

$$Fr_{TP} = \frac{G^2}{gD\rho_{TP}^2} \tag{3.45}$$

$$We_{TP} = \frac{G^2 D}{\sigma \rho_{TP}} \tag{3.46}$$

where the ρ_{TP} is the effective two-phase density that has been defined in Equation 3.18, while the μ_{TP} is the effective two-phase dynamic viscosity which can be estimated as,

$$\mu_{TP} = \left(\frac{x}{\mu_g} + \frac{1-x}{\mu_l} \right)^{-1} \tag{3.47}$$

and D is the diameter of the vertical flash tank.

The aspect ratio is a geometric shape dimensionless parameter of a vertical separator which can be defined as the ratio between the height of a vertical separator to the diameter of the separator.

$$As_{FT} = \frac{H}{D} \tag{3.48}$$

In a horizontal tube, the two-phase non-dimensional numbers can be used as presented in Equations 3.44, 3.45 and 3.46, except the reference diameter is the tube diameter (d). For the single phase gas or liquid phase, the non-dimensional numbers can be defined as presented in Equations 3.41, 3.42 and 3.43, but again, the reference diameter would be the horizontal tube diameter. The velocity of the gas and/or liquid phase at the inlet where the flow is homogeneous (mixed well) can be calculated based on the Equations 3.11 and 3.12 (El Hajal et al., 2003) (Hrnjak, 2004).

3.13 Conclusion

The basic definitions and terminology of two-phase flow has been presented. The key points are as follows.

1. Superficial velocity is a parameter that can be used to characterise the vapour and liquid velocities as there is difficulty in measuring the area occupied by liquid and vapour in two-phase flow system.
2. Flow pattern maps are useful in defining the flow pattern type based on the operating condition.
3. Non-dimensional parameters play an important role in estimating the void fraction and the curves which define the boundaries of the different flow patterns.
4. Void fraction estimation can be enhanced by using the mean logarithmic formula.
5. The two-phase flow pattern is affected by variation of void fraction in the two-phase flow system.

Chapter 4

Experimental apparatus

4.1 Introduction

An experimental apparatus was designed and built at the University of Southern Queensland to investigate the two-phase flow behaviour directly after an expansion device in a horizontal pipe and gravitational separation phenomenon in a vertical flash tank separator. The experimental apparatus consisting of the test section (horizontal pipe and/or vertical flash tank separator), vacuum pump, condenser, heat exchanger and expansion device will be discussed in this chapter. Measurement techniques employed in the experiments are also reported.

4.2 Apparatus layout

Two different arrangements of the experimental apparatus were used. The first arrangement was for the investigation of the two-phase flow behaviour directly after an expansion device in a horizontal pipe. The second arrangement was for the investigation of the liquid separation efficiency of a vertical flash tank separator. Water was used as the working fluid and mass flow rates from about 2 to 23 g/s were obtained with this apparatus. The experimental apparatus of the first arrangement consisted of a water supply source, heat exchanger, expansion device, horizontal pipe (test section), vacuum condenser, vacuum pump, water pump and cooling water tank containing ice. The second arrangement consisted of a water supply source, heat exchanger, expansion device, vertical flash tank separator, vacuum condenser, vacuum pump, water pump, cooling water tank containing ice. The measurement instruments used in the first and second arrangements were pressure transducers, thermocouples and mass flow rate meters, and these were all connected to a data acquisition system. A digital camera was used to record video of the flow inside the horizontal tube and the vertical flash tank separator. Figure 4.1 and 4.2 show a schematic diagram of the first and the second arrangement of the experimental apparatus, including measurement instruments.

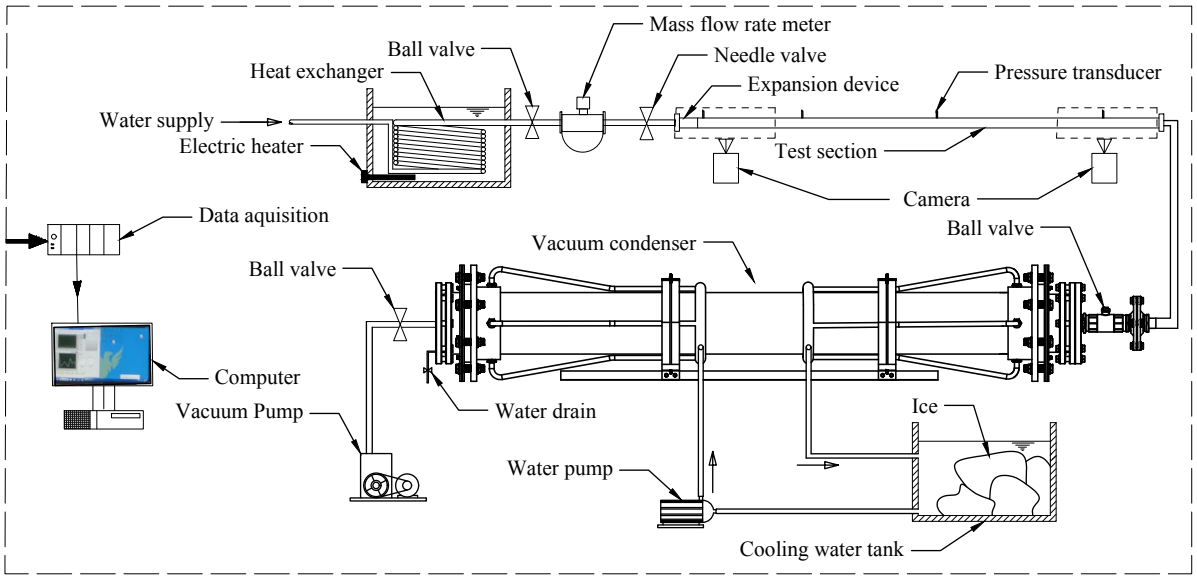

Figure 4.1: Schematic diagram of the expansion device and horizontal pipe experimental apparatus.

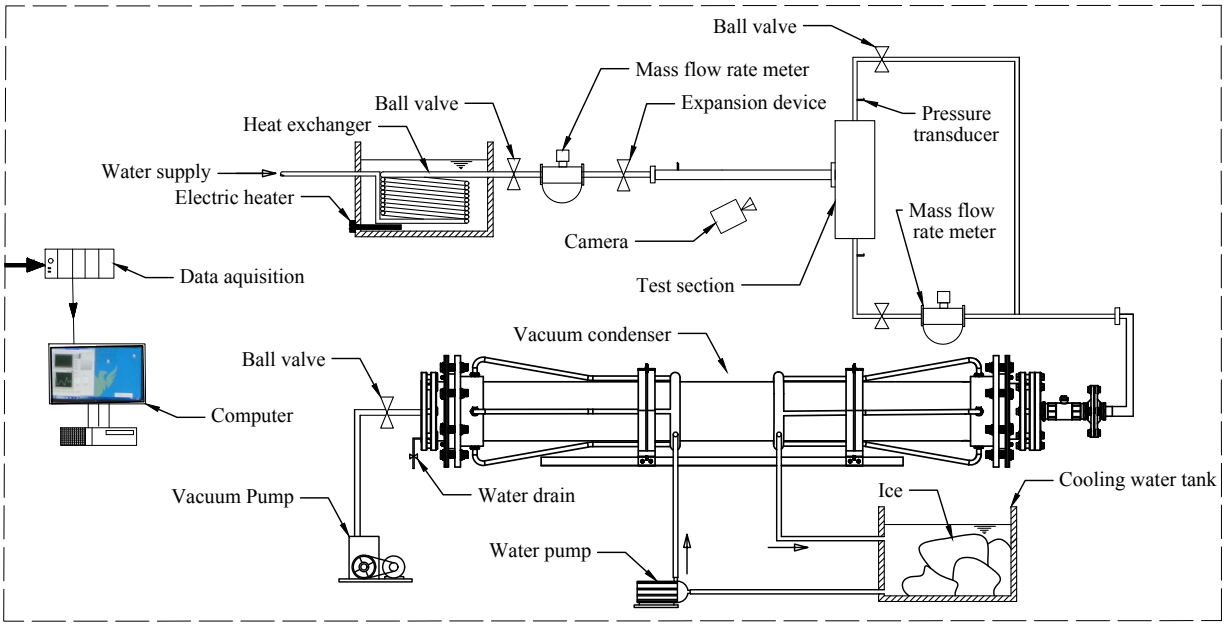

Figure 4.2: Schematic diagram of the vertical tank separator experimental apparatus.

All experiments in the present study were performed in the P10 laboratory of the University of Southern Queensland. Figures 4.3 and 4.4 present photographs of the experimental apparatus of the first and the second experiment arrangements.

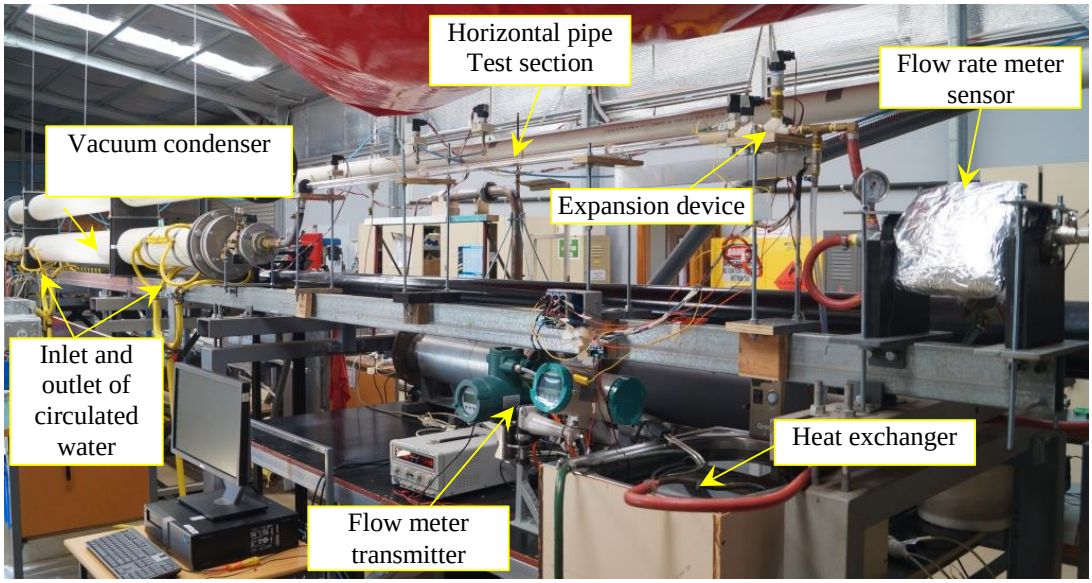

Figure 4.3: Photograph of the horizontal pipe experiment arrangement.

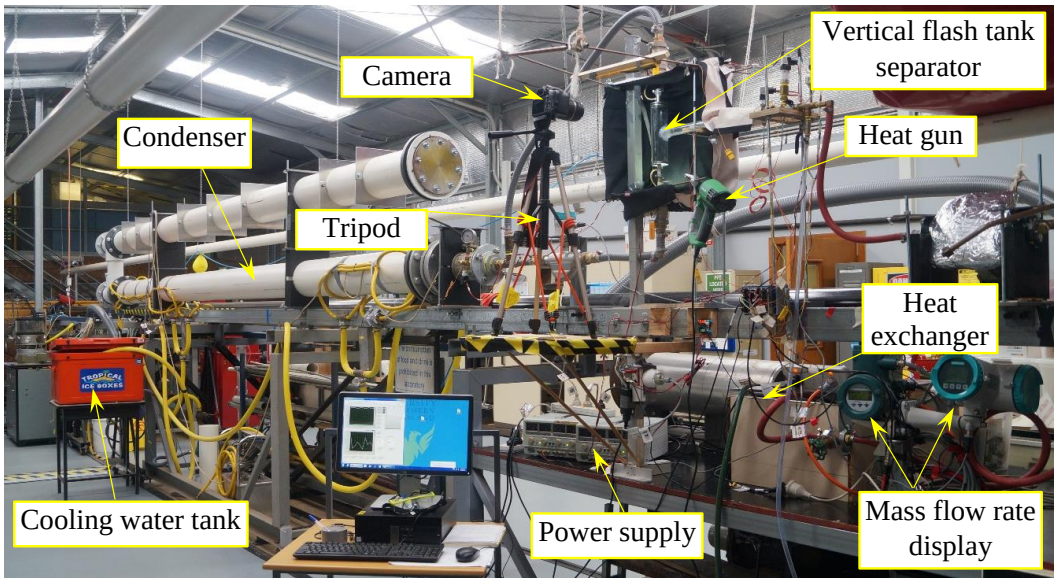

Figure 4.4: Photograph of the vertical separator experiment arrangement.

Two unique parts were established for the present work:

1. Vacuum condenser, connected between the vacuum pump and the test section to provide large receiving volume under low pressure.

2. Expansion device to provide a uniform velocity of vapour containing uniformly dispersed liquid droplets at the entrance to the horizontal pipe.

4.3 Vacuum Condenser

The vacuum condenser was employed in order to provide a stable and low pressure receiving volume for the water and vapour throughout the duration of the experiment. It was connected between the test section and the vacuum pump. It was configured using a brass pipe (inner pipe) and a PVC pipe (outer pipe), between which a 1.5 mm annulus was formed. Figure 4.5 illustrates the configuration and pipe connection details. The inner pipe, which has a 204.31 mm outside diameter, had a 5 mm thick wall and was 6.2 m long, and was connected with the vacuum pump through a combination of flanges. The PVC pipe has a 207 mm inside diameter and 5 mm thick wall and was 5.7 m long, and was connected with the water pump through flexible hoses which distributed the cooling water evenly to the annulus. Four of brass hose fittings (tailpieces) were used at each end of the condenser on the PVC flange to connect the flexible hoses which carry the cooling water. These fitting were distributed around the PVC pipe with 90 degree separation between each of them to ensure that the cooling water is distributed uniformly. Figure 4.6 shows the arrangement of the brass hose fittings around the PVC pipe.

The ends of the PVC pipe were sealed using a combination of flanges. Bolts and nuts were used to connect all flanges to seal the brass pipe and the PVC pipe of the condenser. Figure 4.7 presents the connection details of all combinations of the flanges.

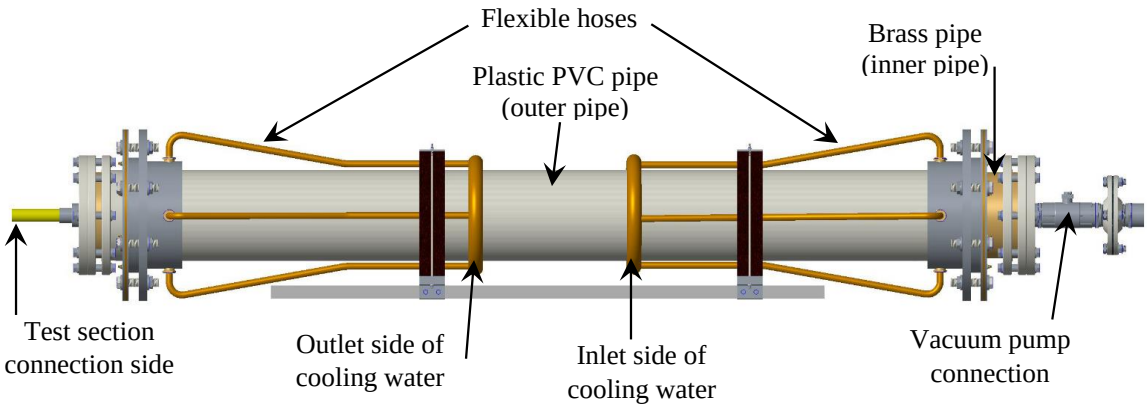

Figure 4.5: Schematic diagram of the condenser configuration and connection details of the condenser.

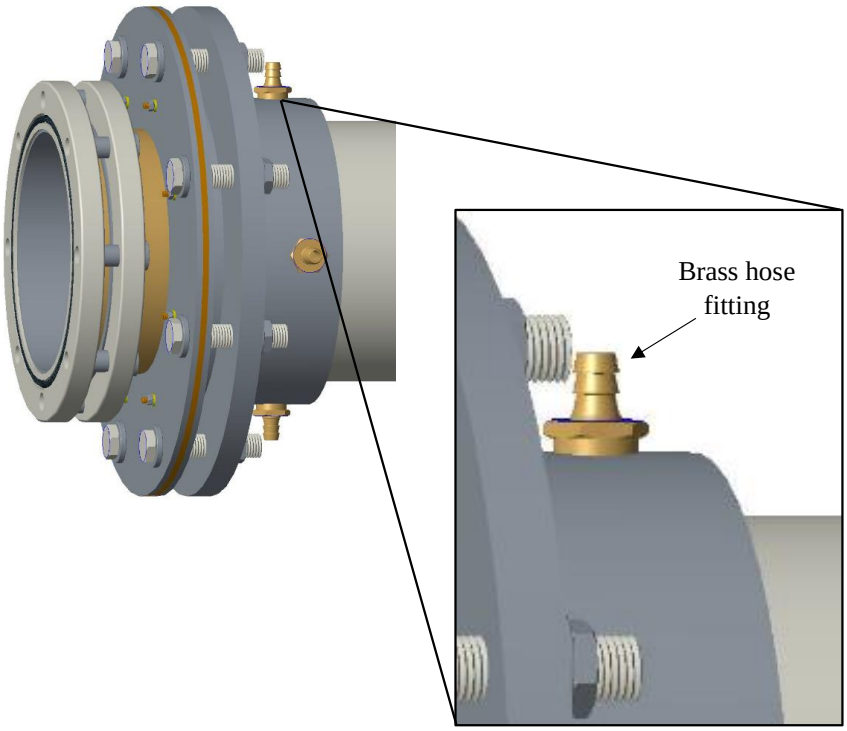

Figure 4.6: Arrangement of the brass hose fittings around the PVC pipe.

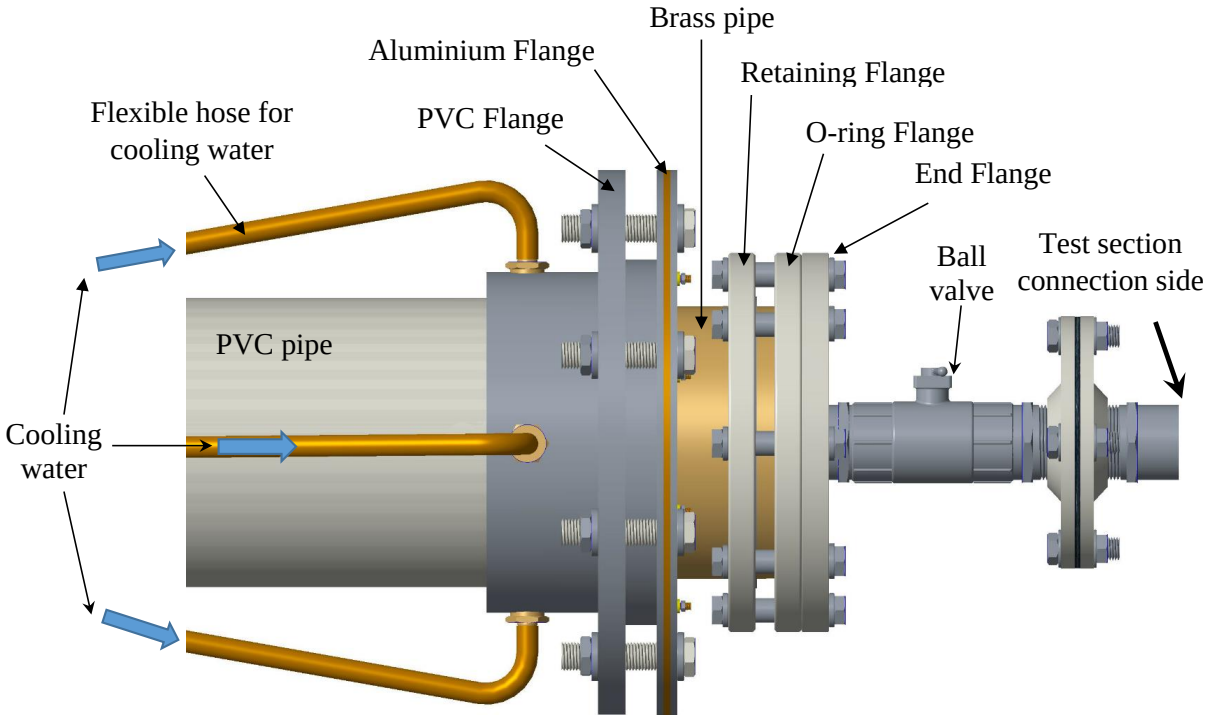

Figure 4.7: Details of the flange combination connection to hold and seal the PVC and brass pipes (test section connection side).

The combination of flanges of the PVC pipe was used to seal the cooling water in the annulus around the brass pipe (inner pipe), these flanges consisted of PVC flange and aluminium flange. The PVC flanges were commercial units while the aluminium flanges were manufactured in the Engineering workshop at University of Southern Queensland. The aluminium flanges have a groove for an O-ring to provide sealing for the cooling water path. Figure 4.8 shows a sectional view of the condenser at the test section end showing the inside configuration and cooling water path. Additional details on the condenser and flanges are presented in Appendix A.

In order to obtain a low pressure inside the condenser during the experiments operating time, a vacuum pump was operating during the experiment. However, the initial pressure inside the condenser was 3.7 kPa and this rose quickly when the two-phase test water flow entered the condenser. Therefore, a cooling water tank with ice was used to cool the condenser during the experiments, creating a sufficiently low and constant pressure for the duration of each experiment.

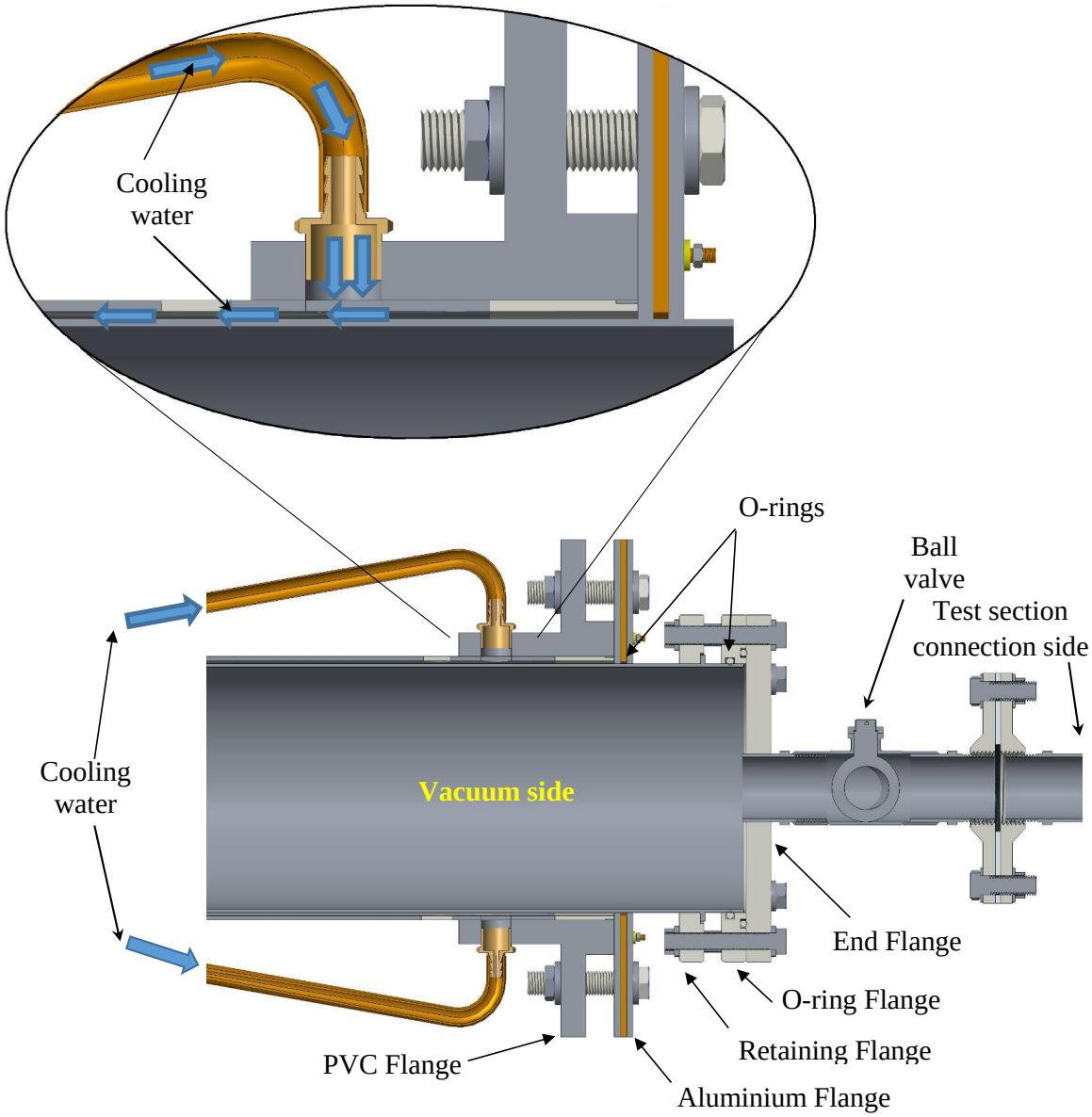

Figure 4.8: Section view of the condenser (upstream test section connection side).

The condenser outlet cooling water temperature ($T_{cool,out}$), pressure inside the condenser and the operating mass flow rate were measured by an RTD, pressure transducer and mass flow meter, respectively.

The volume of the cooling water tank was 60 liter and this tank was filled with 18 liter of chilled water which was pumped to the condenser. The chilled water was circulated in the annulus between the PVC pipe and the brass pipe of the condenser using a water pump (Micton, 240 V single phase) as illustrated in Figure 4.9. The time period during which the condenser can operate under low, constant pressure is reduced when

the operating mass flow rate was increased. To compensate, the amount of ice was increased for the higher mass flow rate experiment conditions. The temperature of the cooling water at the outlet of the condenser was about 7 ℃ which was achieved by adding about 28 kg of ice to the cooling water tank. At this condenser outlet temperature, the pressure inside the condenser inner pipe was recorded to be 1 kPa. As the cooling water was running inside the condenser annulus, the pressure inside the condenser was stable for the duration of each experiments which lasted about 330 seconds.

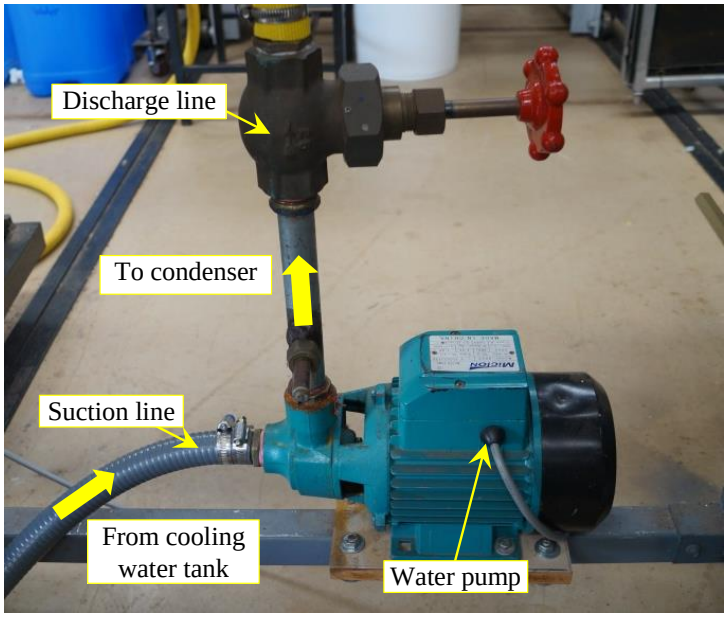

Figure 4.9: Photograph of the condenser water pump.

The final configuration of the vacuum side and test section side on the condenser, including all the flange combinations and fittings are presented in Figures 4.10 and 4.11.

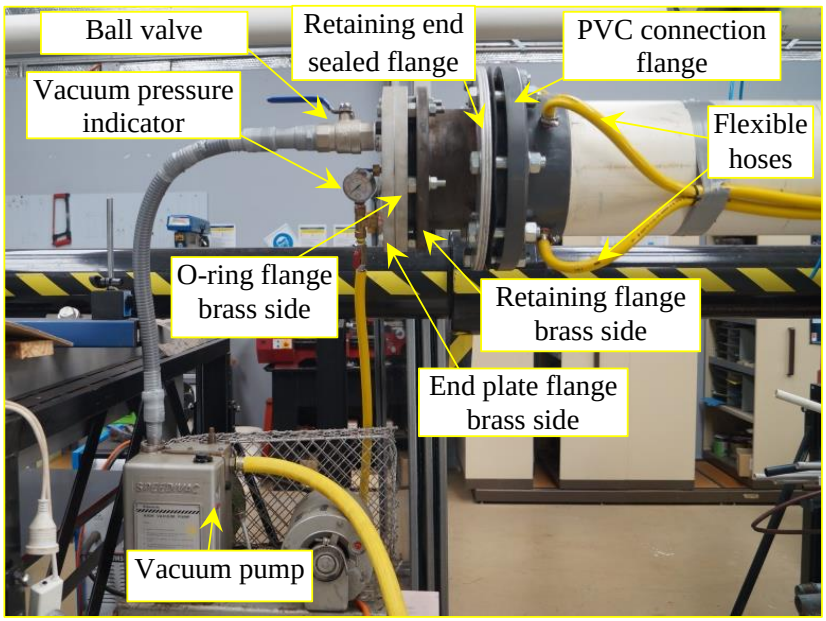

Figure 4.10: Photograph of the condenser flanges and connections on the vacuum pump side.

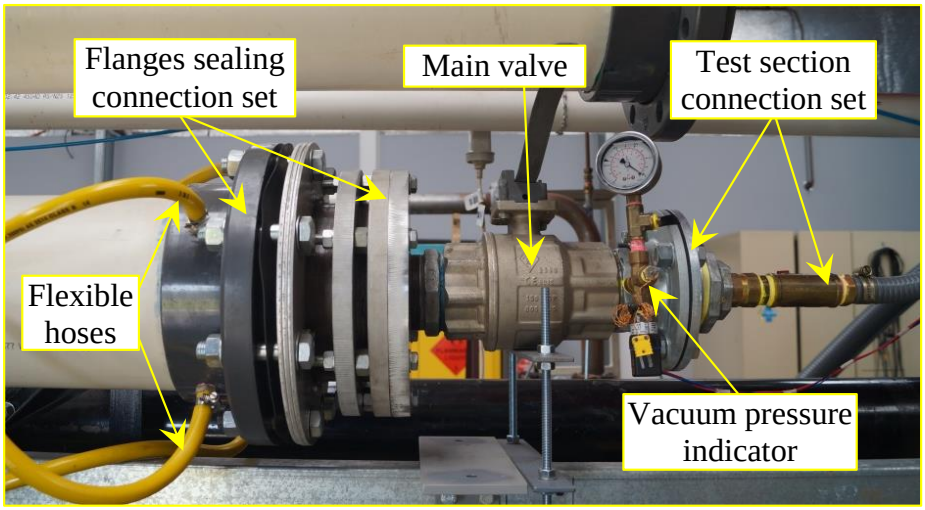

Figure 4.11: Photograph of the condenser flanges and connections on the test section side.

4.4 Expansion device

VisiJet crystal (EX 200 material) was used to fabricate the expansion device using a 3D printer model ProJet^{TM} SD & HD 3500. The VisiJet material has a limited maximum working temperature of around 65 ℃. The expansion device was designed to provide a uniform two-phase flow distribution across the horizontal pipe inlet. Figure 4.12 shows the configuration of the expansion device.

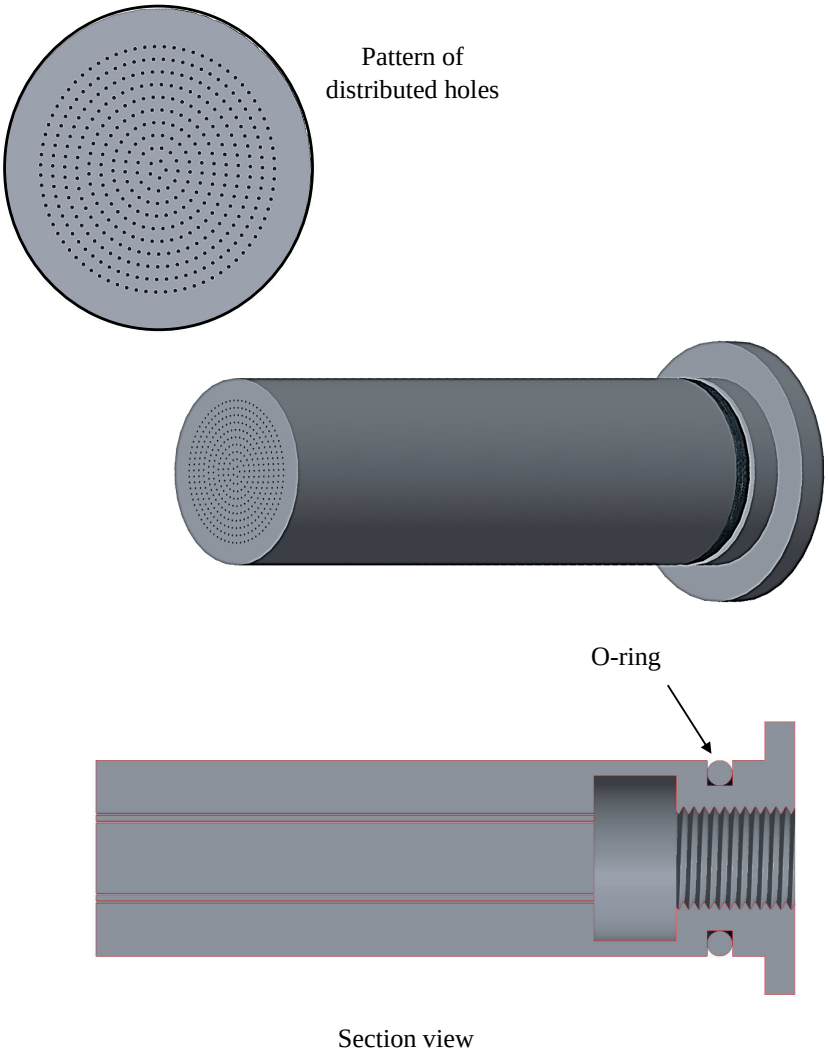

Figure 4.12: Geometry of the expansion device and its section view.

A needle valve was used to control the mass flow rate at the inlet of the horizontal pipe before the water entered the expansion device. The expansion device was designed to provide a pressure drop and discharge the required operating mass flow rate. In order

to design the expansion device, each hole represented a capillary tube and the following assumptions were made: the flow in the expansion device is one-dimensional and adiabatic; the gravity effect is not considered; the working fluid inside the expansion device is at its thermodynamic equilibrium state in all the sections along the expansion device and the flow in the two-phase region is homogeneous (Abed and Abdulkadhim, 2016). A constant area control volume was selected to analyse the expansion device as shown in Figure 4.13.

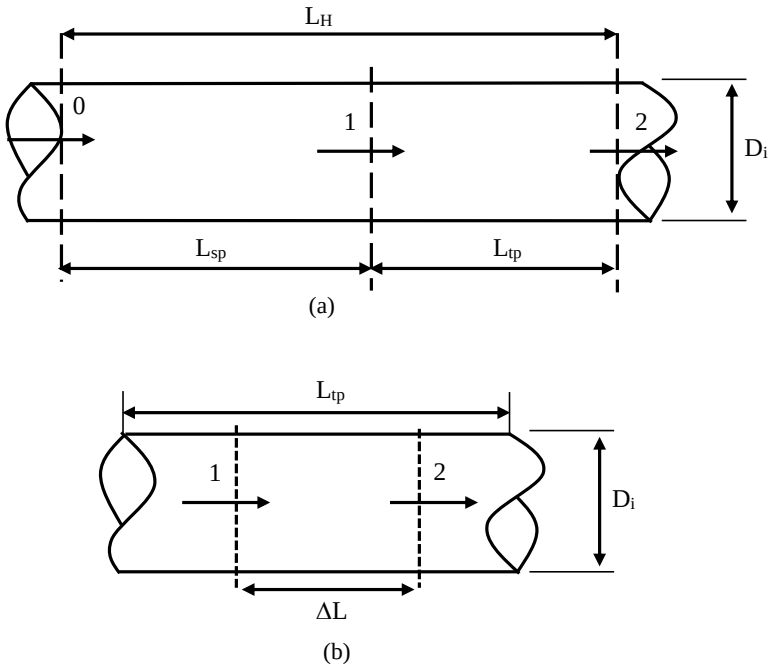

Figure 4.13: Short control volume for analysis of the expansion device (a) Total length of the hole (b) Segment in two-phase region.

The total length of the hole is

$$L_H = L_{sp} + L_{tp} \tag{4.1}$$

where L_H is the total length of the hole, L_{sp} sub-cooled region length and L_{tp} two-phase region length. The mass, momentum, and energy conservation equations which can be presented as follow

$$\rho_1 u_1 = \rho_2 u_2 \tag{4.2}$$

$$[(p_1 - p_2) - f\Delta L u^2/(2D_i v)]A = \dot{m}(u_1 - u_2) \tag{4.3}$$

$$(h_1 - h_2) + (u_2^2 - u_1^2)/2 = 0 \tag{4.4}$$

where ρ is the density, u is the velocity, p is the pressure, v is the specific volume, A is the cross section area of the hole, $\dot{m}$ is the mass flow rate, D_i is the diameter of the single hole in the expansion device, h is the enthalpy and u is the velocity.

In the sub-cooled flow region, the density of the working fluid varies little and nearly maintains a constant value, so in this case, the working fluid can be considered as an incompressible fluid. The flow rate will not change and the velocity maintains a constant value when flowing in the sub-cooled region. The enthalpy of the entire region is considered a constant value on the basis of the energy conservation equation. Therefore, the flow in the sub-cooled region can be considered as isothermal and isoenthalpic. The corresponding vapour pressure of the inlet of the two-phase region temperature is actually the outlet temperature of the sub-cooled flow regions. The sub-cooled length L_{sp} can be determined by (Gu et al., 2003)

$$L_{sp} = \frac{(p_0 - p_1)2D_i}{f_1 \rho_1 u_1^2} \tag{4.5}$$

In the two-phase flow region, the region is divided into many small segments depending on a small pressure drop as shown in Figure 4.13 (b). When the working fluid flows from position 1 to position 2, u and v are both variables. However, u/v is a constant determined by energy conservation equation and continuity equation. The ΔL can be calculated by (Gu et al., 2003)

$$\Delta L = \frac{A(p_1 - p_2) - \dot{m} u_m}{f_m \dot{m} u_m / D_i / 4} \tag{4.6}$$

where f_m is the mean friction factor that can be calculated from $f_m = (f_1 + f_2)/2$, u_m is the mean velocity that can be calculated from $u_m = (u_1 + u_2)/2$, $u_1 = \dfrac{\dot{m} v_1}{A}$ where the v_1 is the specific volume at point 1 and $u_2 = \dfrac{\dot{m} v_2}{A}$ where the v_2 is the specific volume at point 2. Therefore, the whole length of the hole L_H will be obtained by adding up all the segment lengths plus the value of L_{sp}.

The friction factor f_1 for the single-phase region, can be calculated (Gu et al., 2003) using

$$f_1 = \begin{cases} 64/Re & Re < 2320 \\ 0.316Re^{-0.25} & 2320 < Re < 8 \times 10^4 \end{cases} \tag{4.7}$$

and for the friction factor f_2 for the two-phase region, the friction factor is calculating using

$$f_2 = \frac{3.1}{\sqrt{Re}} exp\left(\frac{1-x}{2.4}\right) \tag{4.8}$$

In order to ensure that the required mass flow rate is uniformly discharged from the water source to the horizontal tube on the vertical plane at the inlet of the horizontal tube, 400 holes were distributed uniformly on the expansion device as shown in Figure 4.12. The 400 hole device provided uniformity of the velocity distribution at the inlet of the horizontal tube. The diameter of holes was selected to generate the required pressure drop cross the expansion device. The 400 holes with 0.3 mm diameter provided 92.2 kPa pressure drop cross the expansion device at the maximum mass flow rate ($\dot{m}$ = 23.4 g/s) of the operating conditions.

4.5 Test sections

In the present study, two different test sections have been used. The first test section was a horizontal pipe which was used to investigate the two-phase flow behaviour after the expansion device. The second test section was a vertical flash tank separator which was used for the investigation of the liquid separation efficiency. In the case of the flash tank separator, five different volumes were actually tested.

4.5.1 Horizontal tube

Based on the use of water as the working fluid, the expansion device was designed and fabricated to fit within the horizontal tube with a 25 mm internal diameter (ID) and a 32 mm outside diameter. The horizontal pipe is a transparent acrylic pipe which was used in the present study to allow visual inspection of the details of the two-phase flow after the sudden expansion. In order to track the development of the two-phase flow and cover all the possible flow patterns in a horizontal tube that could appear between the expansion device and the inlet of a vertical separator, a 2 m transparent horizontal tube was used.

The horizontal tube was connected with the expansion device and sealed using an O-ring. The combination of the horizontal tube and expansion device was connected with a needle valve using some fittings as show in Figure 4.14.

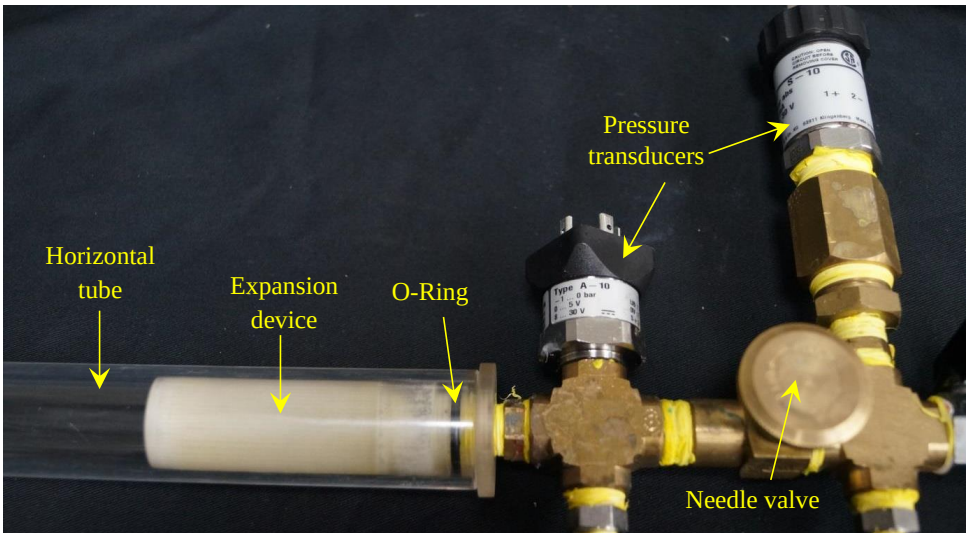

Figure 4.14: Configuration of the expansion device connection with the horizontal pipe test section.

Pressure transducers and a thermocouple were placed on the horizontal tube to record and continuously monitor the pressure and temperature inside the tube. Figure 4.15 shows a photograph of the connection details of the expansion device, the needle valve at the inlet of the horizontal pipe, and the pressure and temperature sensors.

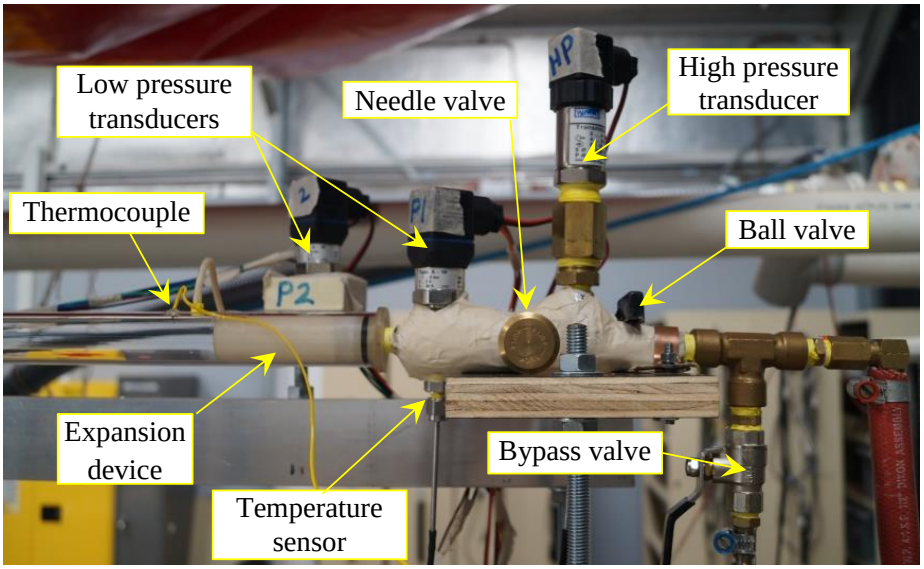

Figure 4.15: Connection details at the inlet of the horizontal pipe.

The tube was secured in a horizontal orientation using a frame and special clamps to ensure that the tube was stationary and horizontal during the operating of the experiments. The mass flow rate and vapour quality are the main parameters that affect the flow development in the horizontal tube (Hrnjak, 2011). In this study, the flow rate was varied from about 2 to 23 g/s and the vapour quality was maintained in the vicinity 5%. Figure 4.16 shows the horizontal pipe and its arrangement in the laboratory.

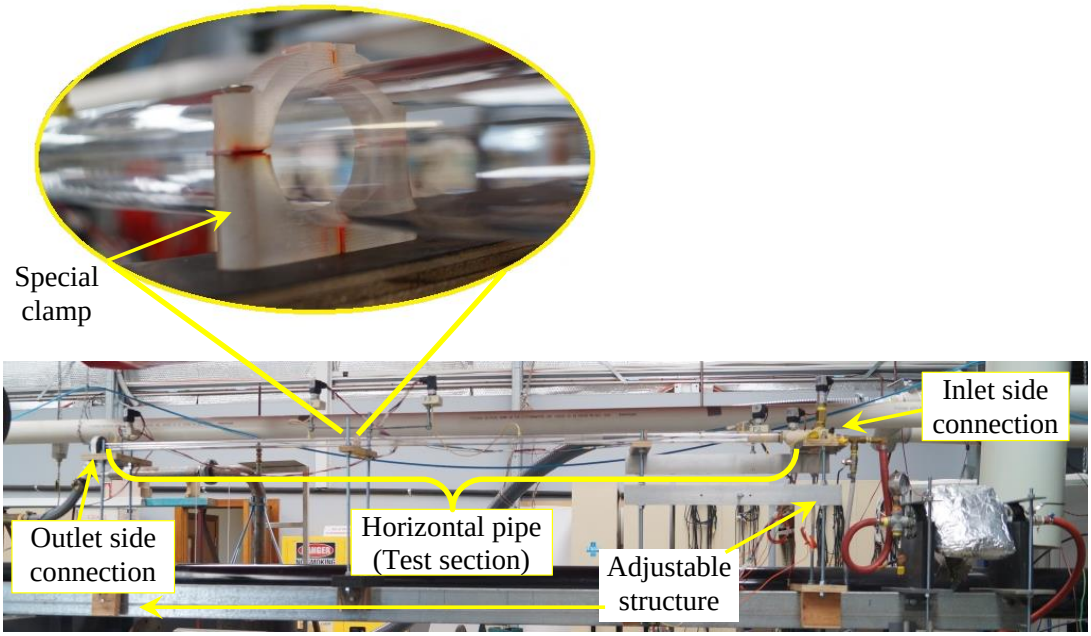

Figure 4.16: Horizontal transparent acrylic pipe and special clamp.

4.5.2 Vertical flash tank separator

The body of the vertical flash tank separator has a 50 mm internal diameter and 5 mm wall thickness. There was no separation enhancer installed inside the vertical separator tank for the initial work. The separator has two outlets: the liquid outlet, which is at the bottom of the tank and has a 10 mm inside diameter ($d_{L,out}$), and the gas outlet, which is at the top of the tank and also has a 10 mm inside diameter ($d_{G,out}$). The appropriate length of the inlet tube of the vertical flash tank separator has been identified as 300 mm which was determined from the horizontal tube experiments where the expansion length and flow pattern in the horizontal tube were determined. The vertical flash tank separator was constructed using a transparent acrylic pipe to allow visual inspection. In order to connect the liquid and gas outlets with the body of the flash tank separator, aluminium flanges with O-rings were fabricated. The aluminium flanges enable convenient swapping of separators when required. Figure 4.17 illustrates a photograph of the vertical flash tank separator.

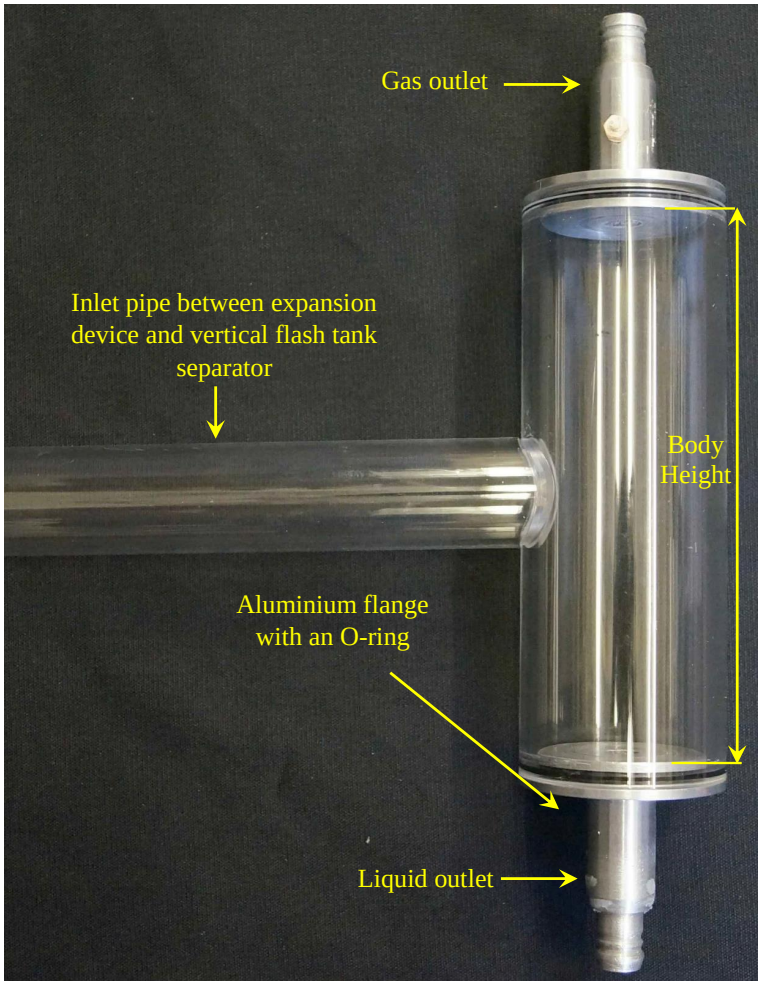

Figure 4.17: Photograph of the vertical flash tank separator.

The inlet tube with an internal diameter $d = 25$ mm was connected with the separator at the centre of the separator's body height. The vertical flash tank separators were built with five different heights to investigate the liquid separation efficiency of the different configurations. Only the height was changed from 50 mm to 250 mm but the inside diameter of the separator remained constant at 50 mm, so five different aspect ratios (AS_{FT}) were obtained as a geometric dimensionless parameter. Transparent acrylic was used to build the separator to enable visualisation of the flow. Figure 4.18 shows the general geometry of the vertical flash tank separator and Table 4.1 presents the dimensions of the five volumes of the vertical flash tank separator.

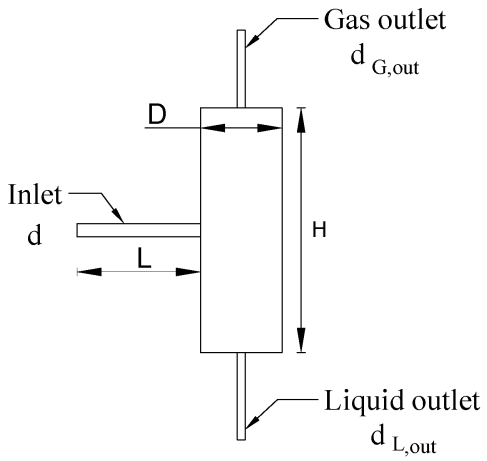

Figure 4.18: Arrangement of the vertical flash tank separator.

Table 4.1: Dimensions of the experimental geometries.

Name of design	AS_{FT} (H/D)	H (cm)	D (cm)	d (cm)	L (cm)	Volume (cm^3)
VFT-V1	1	5	5	2.5	30	98.15
VFT-V2	2	10	5	2.5	30	196.31
VFT-V3	3	15	5	2.5	30	294.46
VFT-V4	4	20	5	2.5	30	392.62
VFT-V5	5	25	5	2.5	30	490.78

4.6 Vacuum pump

A Speedivac Edwards high vacuum pump model ES 200A was used to provide a vacuum in the condenser. A flexible hose 25.5 mm inner diameter was used to connect the vacuum pump with the condenser. Figure 4.19 shows the connection of the vacuum pump with the condenser.

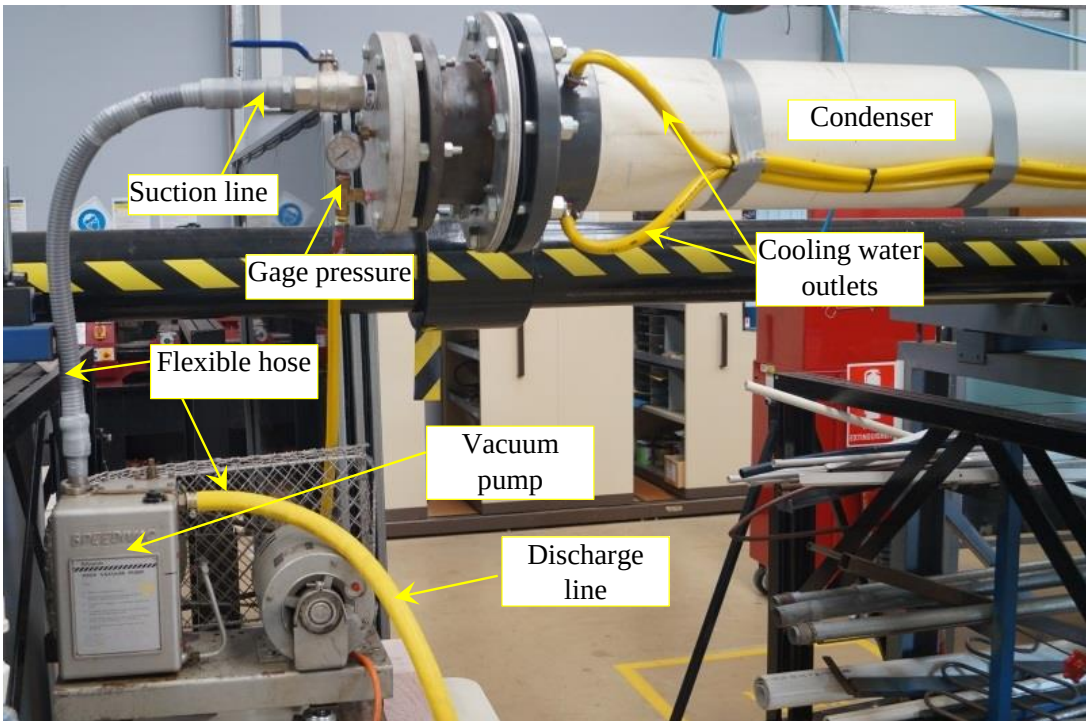

Figure 4.19: Connection of the vacuum pump with the condenser.

4.7 Coil heat exchanger

A coil heat exchanger with an electrical element heater were used in the experimental apparatus to heat up and control the temperature of the water before entry to the expansion device. The town water enters the heat exchanger which raised its temperature to 58 ℃. The water in the tank receives heating energy from a 2.5 kW immersion element electrical heater. An additional resistance heater of 1.5 kW power with temperature controller was used to control the temperature of the water in the tank when required. The hot water flows through a flow meter and ball valve before entering the expansion device. The heat exchanger consists of a copper coil, water tank and electrical heating elements. The heat exchanger coil was located between the water source and the main flow meter upstream of the test section. Figure 4.20 shows a photo of the heat exchanger. Table 4.2 shows the calculation of the power consumption according to the inlet and outlet temperatures of the coil heat exchanger across the range of mass flow rates in the experiments.

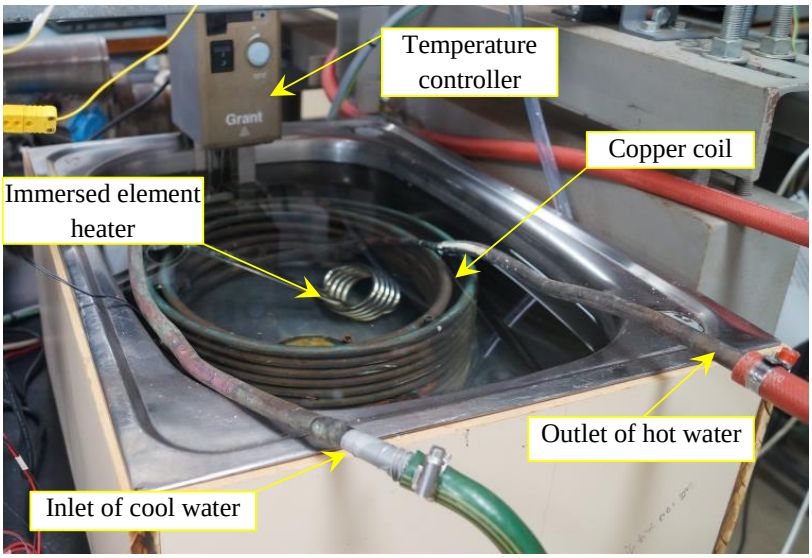

Figure 4.20: Photograph of the coil heat exchanger arrangement.

Table 4.2: Power consumption and outlet temperature from the heat exchanger for the range of mass flow rates.

Flow rate (g/s)	Nominal inlet temperature (℃)	Target outlet temperature (℃)	Power consumption (kW)
2.1	21	58	0.324
5.1	21	58	0.788
8.18	21	58	1.26
10.21	21	58	1.58
13.1	21	58	2.02
23.4	21	58	3.62

4.8 Adiabatic enclosure

In order to obtain adiabatic operating conditions in the experiments, a cloth enclosure and heat gun were used to maintain the temperature of the walls of the test section at the water saturation temperature for the required operating pressure. The heat gun was a Hitachi model RH650V with LCD displaying the temperature and flow speed. By using the enclosure and the heat gun, the surfaces of the test sections were maintained relatively clear by preventing the condensation. In the horizontal tube experiments, the adiabatic enclosure was used at the upstream station while in the vertical flash tank separator experiments, the enclosure was used around the entire separator. Figure 4.21 presents the adiabatic enclosure arrangement in the experiments.

The RTD sensors were used to measure the temperature around the walls of the test sections in both the horizontal pipe and vertical separator experiments. Because the laboratory temperature was lower than the saturation temperature by about 6 ℃ and it varied from day to day, the adiabatic enclosure was used. The temperature of the environment inside the enclosure was assumed to be same as the temperature of the surfaces of the test sections. The RTD sensors were located at different positions around the test sections and very close to the surfaces. As the saturation temperature depended on the required operating pressure, the saturation temperature range was varied with the operating condition but was between 20 and 23 ℃, and the adiabatic enclosure temperature was varied accordingly.

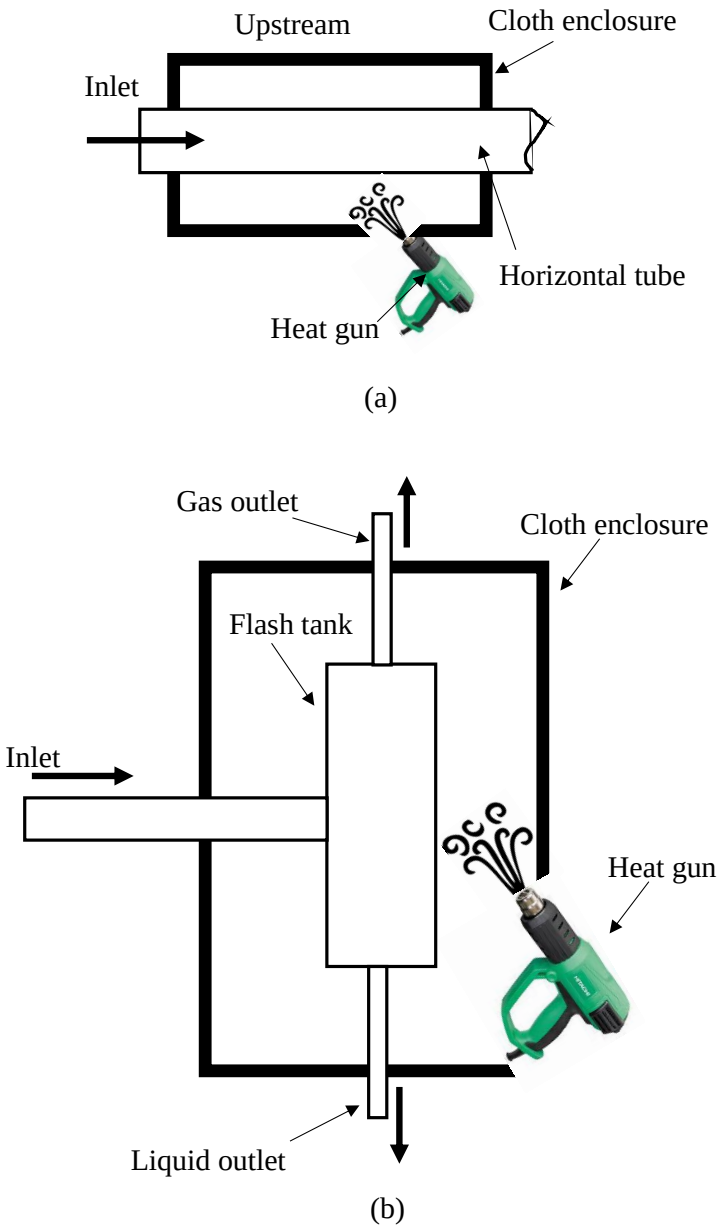

Figure 4.21: Adiabatic enclosure arrangement in the experiments: (a) Horizontal tube, (b) Vertical flash tank.

4.9 Flow visualisation technique

Flow visualisation was performed using a digital video camera, Sony Alpha model A57. A full resolution was used in all experiments while recording the two-phase flow in the horizontal tube and vertical flash tank separator. MPEG format for video recording at 1440 x 1080 (25 fps) and 12 Mega bit per second was used. A steady shot mode was used to activate the image stabilization system. A white light led JR-50W was used to provide illumination.

In the horizontal tube experiments, the camera was used in two positions: directly after the expansion device and at 1500 mm downstream from the inlet. Both positions have same length of visualised portion which is 600 mm long. Figure 4.22 presents a photograph of the adiabatic enclosure at the upstream location in the horizontal tube experiments.

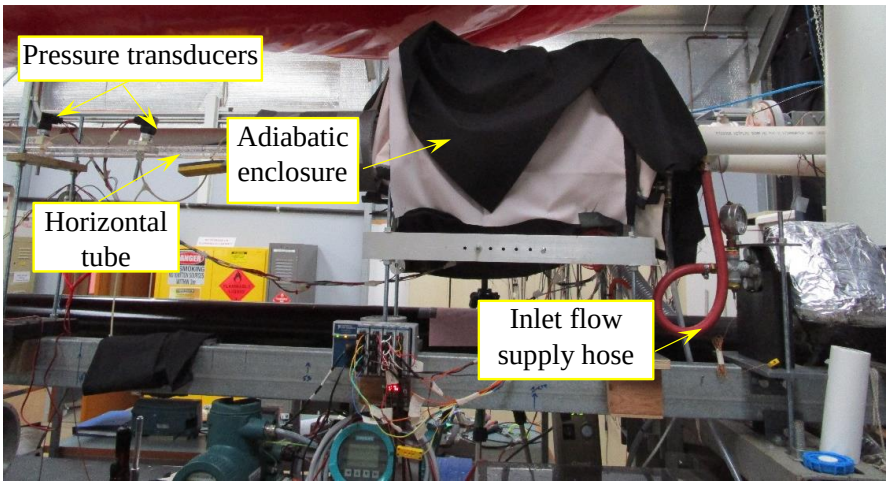

Figure 4.22: Photograph of the adiabatic enclosure around the horizontal tube.

In the vertical flash tank separator experiments, the camera was set in a position to focus on the separator body. Using the adiabatic enclosure, as discussed previously and illustrated in Figure 4.21, improved the clarity of the images by preventing the condensation on the wall of the separator. The adiabatic enclosure technique provided an effective way to control the wall temperature of the test section as the temperature inside the laboratory varied from day to day. Figure 4.23 depicts the adiabatic enclosure to control the wall temperature of the vertical flash tank separator.

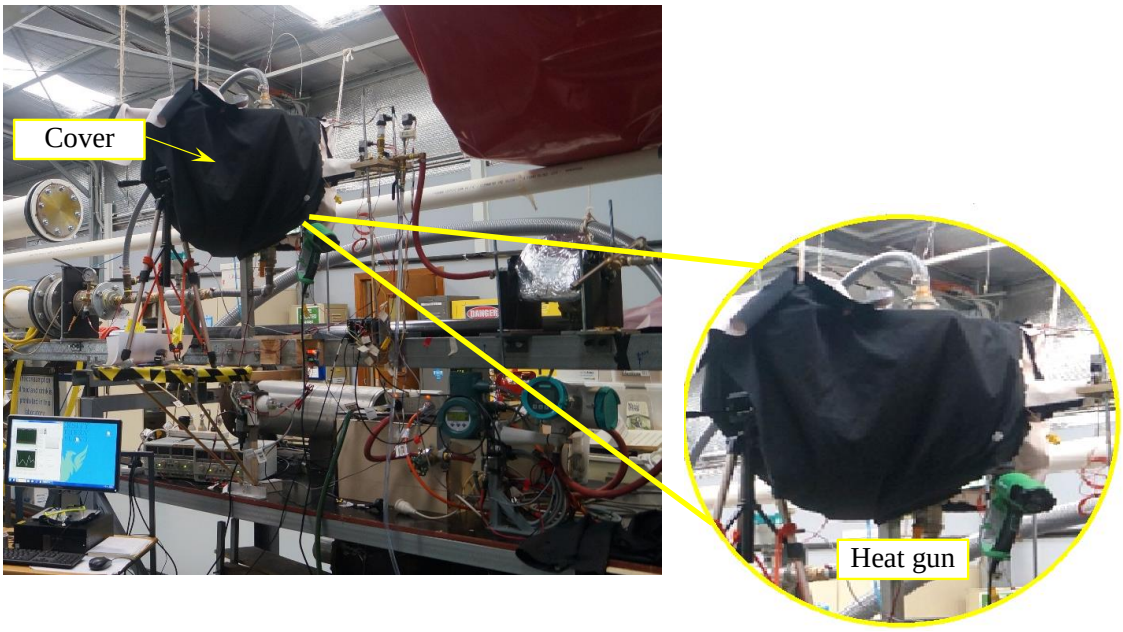

Figure 4.23: Photograph of cover and heat gun technique to control separator wall temperature.

4.10 Instruments

4.10.1 Overview

In the horizontal tube experiment, the temperature measurements at the inlet and outlet of the horizontal pipe were obtained using thermocouples. Five pressure transducers of type Wika 10-A were distributed along the horizontal pipe. A mass flow meter was located after the heat exchanger but before the needle valve on the inlet line of the horizontal pipe. In the vertical flash tank experiment, equipment was arranged to measure the flow rate at the liquid outlet and at the inlet of the separator using two different mass flow rate meters, from manufactures Siemens and Yokogawa. Thermocouple and pressure transducers were still in use to record the temperatures and the pressure at the inlet and outlets of the vertical separator. All of the measurement equipment was connected to a data acquisition system and the data was saved to a computer using LabView software. Figure 4.24 illustrates the measurement instrument arrangement and equipment of the experimental apparatus.

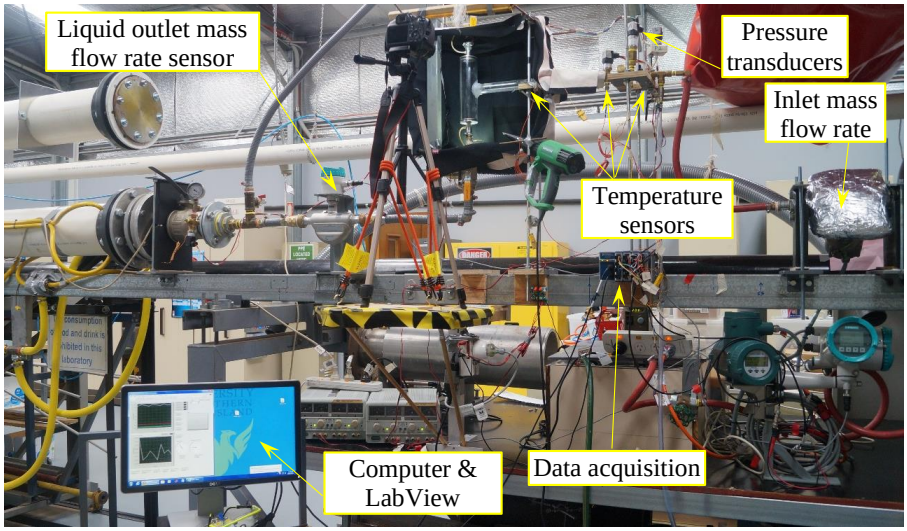

Figure 4.24: Arrangement of the measurement instruments and experimental apparatus in the vertical separator case.

4.10.2 Mass flow rate meters

In the horizontal tube experiment, the Yokogwas mass flow meter was used to measure the inlet mass flow at the entry to the expansion device. The Yokogwa mass flow rate consists of transmitter model RCCF31 and sensor model RCCS32, which according to the test report that was provided by the manufacturer, has an accuracy of 0.1 %. These two parts were mounted and connected by a 4 wires cable. The transmitter was connected to data acquisition using LabView.

In the vertical flash tank experiment, the Yokogwa and Siemens meters were used to measure the total mass flow rate at the inlet of the separator and separated liquid at the liquid outlet respectively. The Siemens flow meter consists of a transmitter model FCT030 and sensor model FCS400, which according to the test report that was provided by the manufacturer, has an accuracy of 0.2 %. The meter is a multi-parameter device offering accurate measurement of mass flow, volume flow, density, temperature and fraction. The manufacturers specifications of the mass flow rate meters is presented in Table 4.3.

Table 4.3: Specifications of mass flow rate meters.

Type	Mass flow range (kg/h)	Operating voltage (V)	Operating temperature range (℃)	Accuracy (%)
Siemens	0-3700	30	-20 $\cdots$ +60	0.2
Yokogawa	0-3000	30	-20 $\cdots$ +55	0.1

4.10.3 Pressure transducers

Wika model 10-A pressure transducers in two ranges were used. One transducer suitable for the pressure before the expansion device was used, and five of the transducers suitable for pressure after the expansion device were also used. Selected details of these transducers are presented in Table 4.4. Calibrations for all pressure transducers are presented in Appendix B.

Table 4.4: Specifications of pressure transducers (Wika, 2011).

Type	Pressure range (bar)	Non-Linearity (%)	Operating temperature range (℃)	Accuracy (%)
Wika 10-A	-1 - 0	0.5	0 $\cdots$ +80	0.5
Wika 10-A	0 - 4	0.5	0 $\cdots$ +80	0.5

4.10.4 Temperature sensors

Type K thermocouples were used to measure the temperature at the inlet and outlet of the horizontal pipe in the horizontal pipe experiments and at the inlet pipe, gas outlet and liquid outlet of the separator in the vertical separator experiments. RTD platinum resistors, PT100 were used to measure the temperature around the test section in the adiabatic enclosure. RTDs were also used to measure the temperature of the water before and after the needle valve. The RTDs were contained within stainless steel welded closed end sheaths. The sheath of the sensor was 316 stainless steel, 3 mm

diameter. All the thermocouples and RTDs were connected to the data acquisition systems.

4.10.5 Data Acquisition

National Instruments (NI) compact DAQ-9178 8-slot USB chassis was used. All pressure transducers, thermocouples and RTD sensors were connected to the DAQ-9178 and a programme was written using National Instrument LabView to monitor and record the data. The first group of three NI 9219 (4 universal channels at 100 S/s with 24-bit resolution, sending data to a host PC over USB) were connected to the pressure transducers, thermocouples and RTD. The second groups of modules included one of NI 9223 (4-Channel Voltage Input 16-Bit Simultaneous Analogue Input) which was used for the mass flow rate meters.

4.11 Analysis of Experimental uncertainty

In the experiments, the systematic uncertainty of the measured parameters was considered according to the manufacture data of the instruments. Three parameters were directly measured in the experiments: mass flow rate, pressure and temperature. All the measurement instruments were calibrated before running the experiments, the calibration test report of the instruments was provided by the manufacturers. Table 4.5 shows the designated uncertainty of the instruments based on manufacturers data.

Table 4.5: Manufactures' designated uncertainty of the measurement instruments.

Measured parameters	Instrument type	Operating range	Uncertainty (±)
P	Wika 10-A	0 - 100 kPa	0.5 kPa
T	RTD (PT100)	-50 - +200 ℃	0.1 ℃
	Thermocouple (Type K)	0 - +200 ℃	0.75 ℃
$\dot{m}_{total}$	Siemens	Max 3700 kg/h	0.2 g/s
$\dot{m}_{Loutlet}$	Yokogawa	Max 1500 kg/h	0.1 g/s

The random errors arising in the experiments were identified by repeating the measurements several times to estimate the mean and the standard deviation (σ) of the measured quantities. Uncertainties arising from the random errors are defined as $\pm 2\sigma$ values and combined with the systematic uncertainties on the basis that the errors are statistically independent. More details illustrating the quantification of random errors and the uncertainty analysis can be found in Appendix F.

4.12 Operating conditions

Based on the working fluid (water), the design of the expansion device and limitations of the apparatus, a range of mass flow rates was used in the horizontal tube and the vertical flash tank experiments: 2.1 to 23.4 $\pm$ 0.2 g/s. This range of the mass flow rates arise because of the design limitations of the expansion device. According to the mass flow rate range and pressure drop across the expansion device, the vapour quality after the expansion device was calculated to be in the vicinity 5%. Water was used as the working fluid in the experiments. Tables 4.6 and 4.7 present the experimental operating conditions for the horizontal tube and vertical flash tank experiments, respectively. The vapour quality at the inlet of the horizontal tube directly after the expansion device was calculated based on the pressure and enthalpy values as presented in Appendix D. The enthalpy across the expansion device was assumed constant because the process in the expansion device is a throttling process which was assumed to be adiabatic. The local atmospheric pressure in the laboratory was approximately 93.8 kPa. The procedure for operating the experiments is presented in the Appendix C.

Table 4.6: Experimental boundary conditions in horizontal tube.

Parameter	Case 1	Case 2	Case 3	Case 4	Case 5	Case 6
Inlet mass flow rate (± 0.21 g/s)	2.1	5.1	8.1	10.2	13.1	23.4
Inlet temperature (± 1.6 ℃)	20.2	20.4	21.5	21.8	22	23.1
Pressure drop across the expansion device (± 0.15 kPa)	11.1	22.2	25.4	37.7	47.4	94.8
Inlet pressure (± 0.55 kPa)	2.36	2.39	2.56	2.61	2.64	2.82
Vapour quality (± 0.6%)	5.8	5.8	5.8	5.4	5.4	5.2
Outlet pressure (± 0.53 kPa)	2.06	2.09	2.26	2.31	2.34	2.52

Table 4.7: Experimental boundary conditions in vertical flash tank separator.

Parameter	Case 1	Case 2	Case 3	Case 4	Case 5	Case 6
Inlet mass flow rate (± 0.21 g/s)	2.1	5.1	8.1	10.2	13.1	23.4
Inlet temperature (± 1.6 ℃)	21.4	21.8	22	22.4	22.7	23.5
Pressure drop across the expansion device (± 0.15 kPa)	8.4	18.3	24.7	36.5	45.9	94.1
Inlet pressure (± 0.55 kPa)	2.54	2.61	2.64	2.71	2.76	2.82
Vapour quality (± 0.6%)	5.6	5.5	5.5	5.4	5.3	5.3
Pressure at liquid outlet (± 0.52 kPa)	2.05	2.12	2.15	2.22	2.27	2.33
Pressure at gas outlet (± 0.52 kPa)	2.05	2.12	2.15	2.22	2.27	2.33

4.13 Conclusion

The experimental apparatus described herein has been designed and built specifically for the experimental investigation of the present work. Water was used as the working fluid to determine the two-phase flow behaviour after an expansion device in a horizontal tube and to investigate the performance of a vertical flash tank.

A special expansion device was developed to provide a pressure drop and uniform inlet velocity at the inlet of the horizontal tube. The expansion device, which consisted of 400 holes with 0.3 mm diameter was fabricated using a 3D printer. Pressure transducers, thermocouples and mass flow meters were used to measure the pressure, temperature and mass flow rate respectively during the experiments.

Operating boundary conditions of the experiments have been presented for the horizontal tube and vertical flash tank.

Chapter 5

CFD Simulation

5.1 Introduction

In the two-phase flow experiments, parameters such as pressure, temperature and mass flow rate have an important effect on the experiment and can be measured relatively easily. However, when more details are required such as volume fraction distribution for liquid and gas phases respectively, experimental work is more difficult and expensive.

In order to obtain a more complete assessment of the flow condition without complex experimental work, Computational Fluid Dynamic (CFD) simulation offers an alternative approach. In CFD simulations, descretised version of the differential equations which model the two-phase flow behaviour are solved. In the present work, CFD simulations using FLUENT 17.1 were used to predict the two-phase flow behaviour after an expansion device in a horizontal pipe and to assess liquid separation efficiency of a vertical separator.

Water was used as the working fluid in the CFD simulations. Gas and liquid two-phase flow were presented as vapour and liquid droplets respectively at the inlet of the horizontal pipe and in the vertical separator although the separator inlet flow was almost fully developed. This chapter presents the numerical methodology used to simulate the two-phase flow behaviour and separator performance.

5.2 CFD Two-phase flow modelling approaches

Within the CFD two-phase modelling options in ANSYS 17.1 FLUENT, there are three different models: Volume of fluid (VOF), Mixture model and Eulerian model. The most appropriate choice of these model is influenced by the flow regime to be simulated, and four categories can be easily identified: gas-liquid or liquid-liquid flows, gas-solid flows, liquid-solid flows and three-phase flows (Hu and Cheng, 2016). In the gas-liquid flow regime, there are different flow patterns such as bubbly flow, droplet flow, slug flow, stratified wavy flow and stratified flow (Roman et al., 2016). Consequently, the first step towards CFD simulation of a multiphase problem is to determine which of the flow regimes describe the flow of the particular problem that needs to be simulated.
Many numerical simulations of gas-liquid two-phase flow have used the Eulerian model in different geometries including sudden expansion (Roul and Sahoo, 2012) and flow in a horizontal tube (Walvekar et al., 2009) because it is more accurate than the VOF and Mixture models (Roul and Sahoo, 2012). In the Eulerian approach, the liquid phase and vapour phase are both treated as a continuous phase by using the volume fraction for each phase (FLUENT, 2012). The Eulerian two-phase model solves a set of two-phase differential equations for each phase, so it is the most complex of the two-phase models (Roul and Sahoo, 2012). Consequently, the computational effort required for the solution of the Eulerian model is higher than that in the VOF and Mixture models because the number of transport equations that need to be solved in Eulerian model is higher than that in VOF and Mixture models.
In the present work, as the flow regime is gas-liquid two-phase flow and the phases are mixed well directly after the expansion device then these phases are being separated, the Eulerian model was used. The $k-\epsilon$ turbulence model was used for each phase to represent the turbulence in the present work. The governing equations of the Eulerian model and $k-\epsilon$ turbulence model are presented in Appendix D.

The $k-\epsilon$ turbulent model was selected according to the turbulent model compatibility with the multiphase model chart that is provided by FLUENT (2012) as shown in Table 5.1.

Table 5.1: The turbulence model compatibility with the multiphase model from FLUENT (2012).

Multiphase Models	$k-\epsilon$	$k-\omega$	Reynolds stress	LES
Eulerian model	Yes	No	Yes	No
VOF model	Yes	Yes	Yes	Yes
Mixture model	Yes	Yes	Yes	No

The LES is the large eddy simulation turbulence model. In the present simulations, because there is no swirl flow, the Reynolds stress turbulence model was not used because the the Reynolds stress turbulence model is typically used for the swirl flow to account the effect of the streamline curvature and rapid change in strain rate in the rotational flow (Rafiee et al., 2016).

5.3 Computational domains

In the present work, domains were created for the horizontal pipe and vertical flash tank separators. The design module in the ANSYS Workbench 17.1 was used to create the domains.

5.3.1 Horizontal tube

The domain of the horizontal tube under investigation is presented in Figure 5.1. The geometry was taken from the experimental configuration presented in Chapter 4. The inside diameter is 25 mm and the length of the circular tube is 2000 mm. In order to reduce the computational time, the domain represents half of the physical experiment with the symmetry along the vertical plane being exploited.

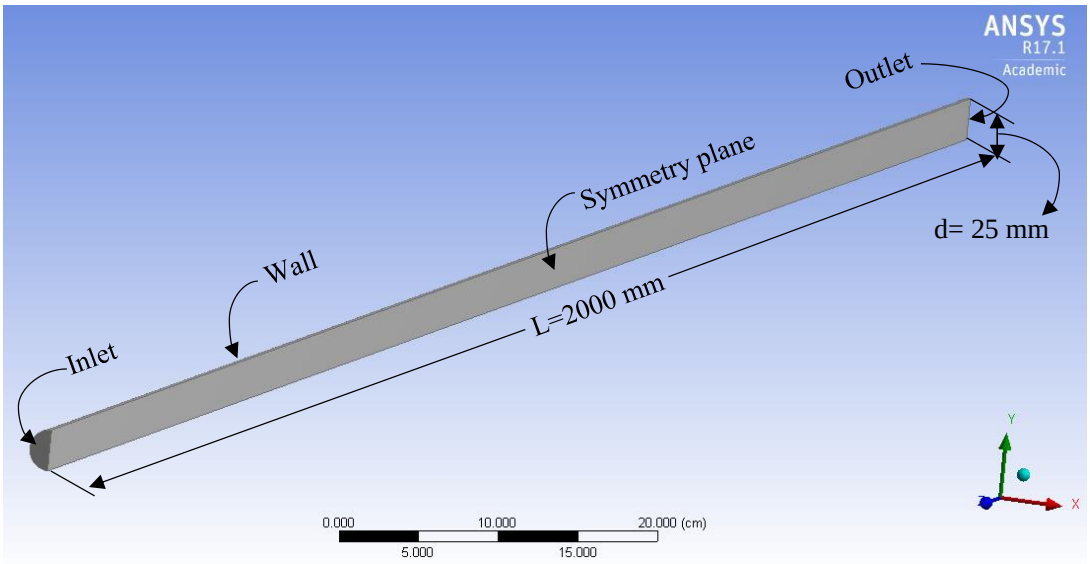

Figure 5.1: Computational domain of the horizontal tube geometry.

5.3.2 Vertical flash tank

The domain of the vertical flash tank geometry was also created in the 3D mode with exploitation of the symmetry plane as shown in Figure 5.2. The geometry was taken from the experimental configuration presented in Chapter 4. Table 4.1 in Chapter 4 presented the dimensions of the five different aspect ratios that were used in the experiments. Therefore, in the CFD simulation, five domains of the vertical flash tank separator were created in the design module of the ANSYS 17.1. The height H of the each domain was different.

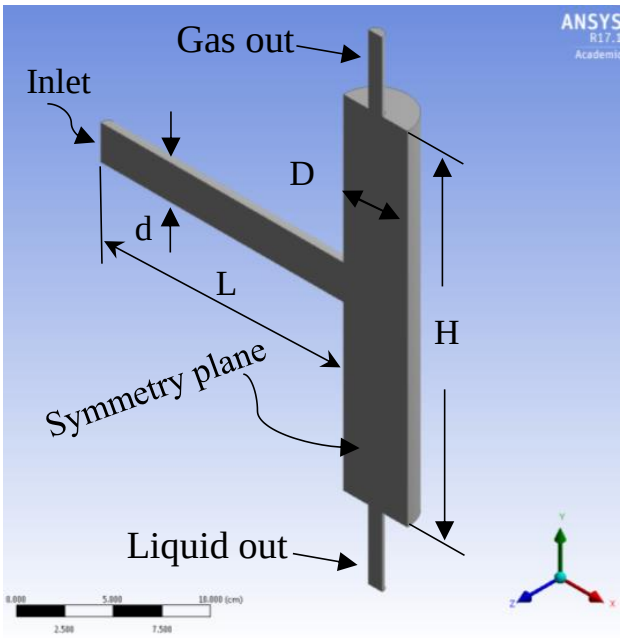

Figure 5.2: Computational domain of the vertical flash tank geometry.

5.4 Boundary conditions

5.4.1 Horizontal tube

In order to generate simulations consistent with the experiments data, the experimental operating conditions were used in the CFD simulation. Water was used as the working fluid. At the inlet, the liquid droplet size is selected according to the expansion device design which has 400 holes with 0.3 mm diameter, so the liquid droplet diameter is selected to be 300 μm.

On the assumption that homogeneous flow is formed directly after the expansion device, the velocity at the inlet of the horizontal tube can be calculated based on the homogeneous void fraction (El Hajal et al., 2003). The liquid velocity was calculated from

$$u_l = \frac{\dot{m}_l}{\rho_l A(1-\alpha_g)} \tag{5.1}$$

where the A is the total cross section area of the horizontal pipe, ρ_l is the liquid density, $\dot{m}_l$ is the liquid mas flow rate and α_g is the gas void fraction which can be calculated from Equation 3.20.

Similarly, the gas velocity at the inlet was calculated from

$$u_g = \frac{\dot{m}_g}{\rho_g A \alpha_g} \tag{5.2}$$

where the ρ_g is the gas density, $\dot{m}_g$ is the gas mass flow rate.

The inlet boundary condition was specified as uniform velocity distribution for each phase at the inlet of the horizontal tube. A pressure outlet was used for the outlet boundary condition. The no slip wall was applied for the wall boundary.

Six cases were simulated for the same domain of the horizontal tube, each case corresponding to a particular mass flow rate that was used in the experiments. Table 5.2 presents the boundary conditions which were used in the simulation in each case.

Table 5.2: Boundary conditions in horizontal tube simulations.

Boundary	Case 1	Case 2	Case 3	Case 4	Case 5	Case 6
Inlet (inlet velocity, m/s)	u_l=0.33 u_g=0.33	u_l=0.89 u_g=0.89	u_l=1.37 u_g=1.37	u_l=1.52 u_g=1.52	u_l=1.91 u_g=1.91	u_l=2.1 u_g=2.1
Outlet (pressure outlet, kPa)	2.06	2.09	2.26	2.31	2.34	2.52
Wall	No slip	No slip	No slip	No slip	No slip	No slip

5.4.2 Vertical flash tank

In the vertical flash tank separator, the boundary conditions were also specified from the experiments. The inlet velocity was used at the inlet of the vertical flash tank domain, and pressure outlet was applied at the liquid and gas outlet. As the same operating conditions were used in the horizontal tube and the vertical flash tank separator experiments, the liquid velocity and gas velocity at the inlet of the vertical flash tank domain were also specified using Equations 5.1 and 5.2, based on the homogeneous void fraction. Table 5.3 presents the boundary conditions which were used in the simulations of the vertical flash tank separators.

Table 5.3: Boundary conditions in vertical flash tank VFT-V1 simulations.

Boundary	Case 1	Case 2	Case 3	Case 4	Case 5	Case 6
Inlet (inlet velocity, m/s)	u_l=0.33 u_g=0.33	u_l=0.89 u_g=0.89	u_l=1.37 u_g=1.37	u_l=1.52 u_g=1.52	u_l=1.91 u_g=1.91	u_l=2.1 u_g=2.1
Liquid outlet (pressure outlet, kPa)	2.05	2.12	2.15	2.22	2.27	2.33
Gas outlet (pressure outlet, kPa)	2.05	2.12	2.15	2.22	2.27	2.33
Wall	No slip	No slip	No slip	No slip	No slip	No slip

5.5 Mesh independence study

5.5.1 Mesh quality

The meshes created for both the horizontol pipe and the vertical flash tank simulations were created from tetrahedral elements which has benefits such as reduced computational time and improved mesh quality for three dimensional domains of complex shapes (Vallée et al., 2008; Gruau and Coupez, 2005). The meshes were generated and optimized using Ansys Meshing. An unstructured grid was obtained using global and local sizing parameter after a series of tests. According to the Fluent user guide (FLUENT, 2012), obtaining good mesh quality will give accurate solutions and fast convergence.

The mesh quality can be represented by three factors namely, orthogonal quality, aspect ratio, and skewness value (Rudolf, 2009). The orthogonal quality ranges from 0 to 1 and 0 represents low mesh quality. The minimum orthogonal quality should always be greater than or equal to 0.01 (FLUENT, 2012). The aspect ratio is relevant to the wall function and should be small enough to allow the solution to capture the flow details near the wall (Lanzafame et al., 2013). The skewness value, which is inversely related to solution accuracy, should be small enough to minimize error in the solution (Ali et al., 2017). For the meshes used in the present simulations, the orthogonal quality was 0.9 with a minimum value of 0.07, the aspect ratio was 3.56, and skewness value was 0.26. These values indicate that according to the established criteria, good mesh qualities were obtained and used in the present simulations.

5.5.2 Horizontal pipe

Five computational grids of 7000, 16232, 45000, 199356 and 298566 elements distributed within the domain were used to investigate the necessary grid size for computational simulation of the horizontal pipe case. The inflation method was used to generate a fine mesh near the wall. Figure 5.3 illustrates the mesh with mesh inflation near the wall of the horizontal tube. The operating condition case 6 presented in Table 5.3 was used in the simulations for the different element number meshes.

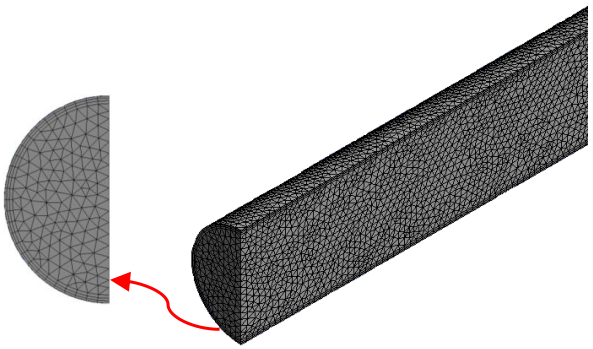

Figure 5.3: Horizontal tube mesh with inflation near the wall for the 199356 element mesh case.

Figure 5.4 shows an assessment of grid independence for the horizontal tube, showing the variation of the expansion length for different mesh elements. In this figure, the result for the 199356 and 298566 elements is close and the difference between them is 0.15. While the maximum difference of 6.9 was recorded between 7000 and 298566.

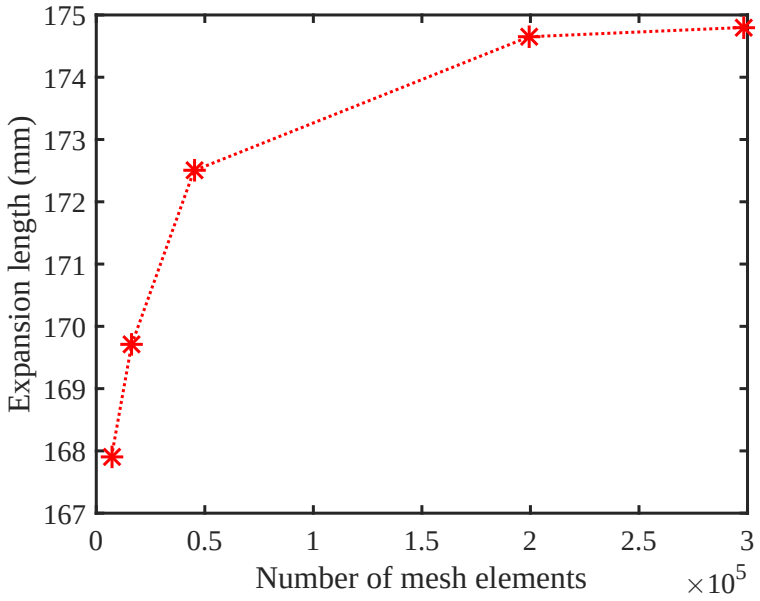

Figure 5.4: Assessment of grid independence for the horizontal tube showing variation of the expansion length with the number of mesh element for operating condition case 6.

As can be seen from the Figure 5.4, the simulations using the two highest number of mesh elements achieved convergence with very low variation. In addition, the 298566 mesh elements did not change the convergence significantly compared to the mesh with 199356 elements.

Figure 5.5 shows the liquid volume fraction distribution in the horizontal pipe at

1600 mm from inlet of the tube for different mesh densities. The red area represents the liquid film at the bottom of the pipe and the transitional colours between the red and blue represents the interface between the phases. The figure illustrates the significant effect of the different element numbers on the resolution of the interface of two-phase flow. It can be seen that there is no significant change in the liquid volume fraction and the smoothing of interface between the liquid and vapour when the mesh number increased beyond 199356. Therefore, based on the convergence results illustrated in Figure 5.4 and the interface behaviour between the liquid and gas illustrated in Figure 5.5, the number of mesh elements selected as the optimum number to be used in the primary simulations of the horizontal pipe flow of the present work was 199356.

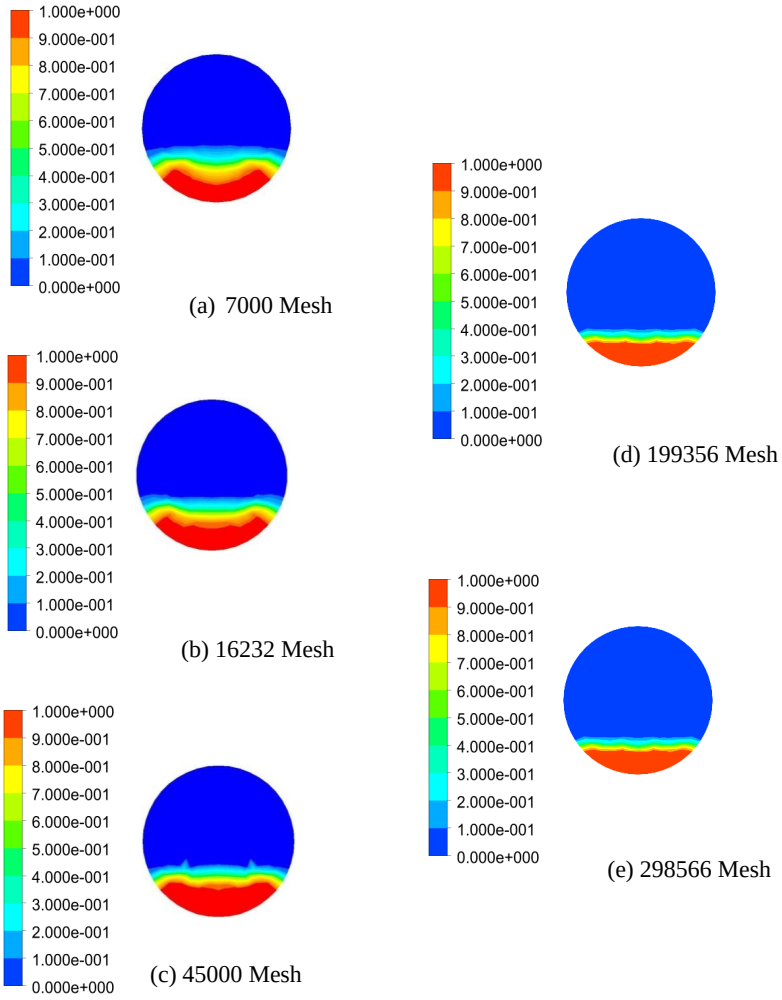

Figure 5.5: Assessment of grid independence showing liquid volume fraction contours for different element numbers in a horizontal pipe at 1600 mm from the inlet of the pipe for operating condition case 6.

5.5.3 Vertical flash tank

The geometry of the vertical flash tank was discretized into tetrahedral elements and in order to generate a fine mesh near the walls, the inflation method was used. Figure 5.6 illustrates the mesh of the vertical flash tank. Four computational grids of 8500, 180000, 220000 and 280000 were used to investigate the grid independence in the vertical flash tank case. The operating condition case 5 presented in Table 5.3 was used to simulate the liquid separation efficiency for the different element number meshes. The geometry of the VFT-V5 was used to investigate the mesh number effect on the liquid separation efficiency.

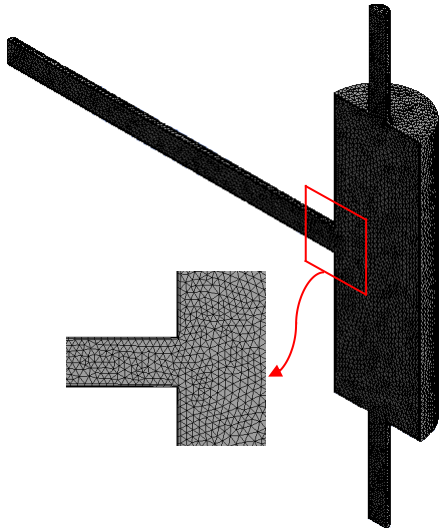

Figure 5.6: Vertical flash tank mesh with inflation near the walls for the 220000 element mesh case.

Figure 5.7 shows an assessment of grid independence for the vertical flash tank separator, showing the variation of the liquid separation efficiency of the VFT-V5 for different mesh elements. In this figure, the result for the 220000 and 280000 elements is close and the difference between them is 0.001. While the maximum difference of 0.401 was recorded between 8500 and 280000.

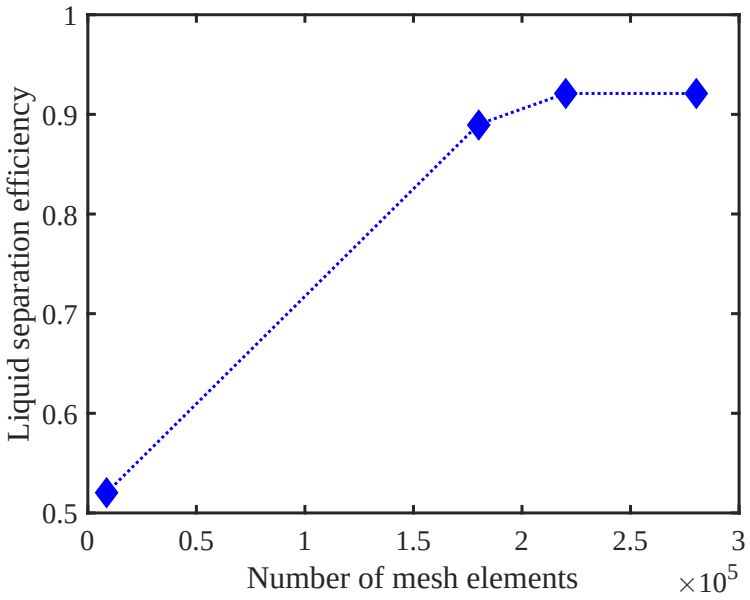

Figure 5.7: Assessment of grid independence for the vertical flash tank showing variation of liquid separation efficiency with number of mesh element for operating condition case 5.

As can be seen from the Figure 5.7, the simulations using the two highest number of mesh elements achieved convergence with very low variation. In addition, the 280000 mesh elements did not change the convergence significantly compared to the mesh with 220000 elements. Therefore, the number of mesh elements selected for the primary simulations of the vertical flash tank separator of the present work was 220000.

5.6 High performance computing facility

In order to run the two-phase flow simulations at the target resolution and obtain high simulation accuracy in a reasonable time frame, a high performance computer facility (HPC) at USQ was used to run Fluent 17.1. For every experiment of the present work, a case file was prepared and loaded on the HPC. The 'Fawkes' HPC has 29 computer nodes, along with 1 administration node, 1 login node and a file server node. There are 2 x Intel ES2650v3 processors with a tree memory configuration. Figure 5.8 illustrates the HPC configuration.

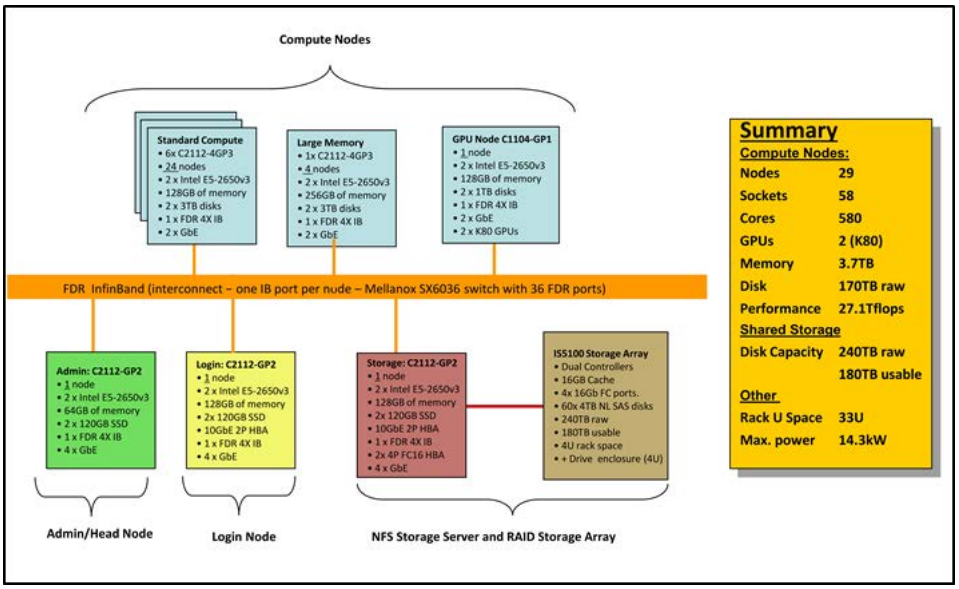

Figure 5.8: Configuration of the HPC of the University of Southern Queensland.

5.7 Convergence

In the CFD simulations, convergence must be considered to obtain a valid solution. In the simulations of the present work, the mesh was optimized to obtain a high quality according to the metrics discussed in Section 5.5. When the number of computational elements is optimized to obtain high quality of mesh, accurate numerical solutions should be obtained with good convergence (Volk et al., 2017).

Convergence for the steady state simulations is typically considered to have occurred when the residual error values are in the range of 10^{-4} to 10^{-5} and the net imbalance is less than 1% of the smallest flux through the domain boundary (FLUENT, 2012). In the present work, convergence was assessed by monitoring the residual of the momentum and continuity equations and values in the range of 10^{-5} were generally achieved. In addition, the net flux imbalance across the domain boundaries was less than 0.1 %.

5.8 CFD solver setting

In the present work, the CFD simulations used the $k - \epsilon$ turbulence model for each phase and the Eulerian-Eulerian two-phase model was applied. The Eulerian approach was used in these simulations because it is apparently more accurate than other two-phase approaches (Kalteh et al., 2011; Hrnjak, 2004). The solver settings used were as follows:

- Steady state pressure based solver.
- Standard $k - \epsilon$ for each phase, two-phase model with standard wall function treatment.
- Boundary condition setting on inlet and outlet.
- Second order upwind discretization method for momentum and turbulence equations.
- Reduction of the under-relaxation factors to have a less aggressive simulation process.
- Control monitor of the iterative process to check the convergence.
- Initialization and setting of post processing.

5.9 Conclusion

Computational Fluid Dynamic CFD simulations using Fluent version 17.1 have been described. The $k - \epsilon$ turbulence model was used for each phase and the Eulerian-Eulerian two-phase flow model was adopted. The simulations were performed in 3 dimensional domains using the pressure-based solver and implicit formulation for steady state solutions. According to the homogeneous flow assumption, the velocity inlet is applied with a uniform velocity distribution for each phase as an inlet boundary condition. Pressure outlet is used for the outlet boundary conditions. No slip wall boundary conditions were applied. A mesh independence study was completed to select an optimum number of mesh element for the horizontal pipe and vertical flash tank separator. Based on the convergence and difference between the mesh element numbers in CFD results, the optimum number of mesh element was selected. By comparing the lower resolution with the highest resolution of the mesh, the minimum differences were 0.15 and 0.001 which obtained by the optimum number of the mesh element 199356 and 220000 for the horizontal and vertical flash tank separator respectively. A high performance computer HPC was used to obtain high simulation accuracy in a reasonable time frame.

Chapter 6

Two-phase flow development after expansion in a horizontal pipe

6.1 Introduction

The inlet flow conditions for the vertical flash tank separator, which include velocities of each phase, void fraction and liquid drop size, are affected by inlet tube diameter, mass flow rate and vapor quality (Hrnjak, 2011). The inlet flow distribution can also be affected by the position of the expansion device. Several studies have been performed to investigate the influence of the inlet operating condition on the two-phase flow distribution and its flow pattern in headers and vertical separators (Zheng et al., 2016). However, there is no information in literature on two-phase flow of water after an expansion device but before the inlet of the vertical separator. The objective of this chapter is to provide suitable data for validation of CFD simulations that can be used in the design of vertical separators. CFD simulations and experimental results will therefore be presented to describe the two-phase flow behaviour of water after an expansion device in a horizontal pipe. Objectives include definition of (1) the flow characteristics that apply at the inlet of the vertical separator; and (2) the appropriate

length of horizontal pipe between the expansion device and the vertical separator.

6.2 Development of two-phase flow after the expansion device

In order to understand the flow development after an expansion device, flow regions and forces that influence the flow need to be considered. Figure 6.1 illustrates the forces which have an influence on the flow. As a result of these forces, liquid is accumulated at the bottom of the tube and a vapour region is established at the top (Bowers and Hrnjak, 2008). Many studies have been published on the two-phase flow patterns presenting observations of the two-phase flow for different refrigerants and fluids. In the present study the development of two-phase flow was observed directly after the expansion device up to the end of the horizontal pipe and water was used as the working fluid. There are three regions after the expansion device: (1) the homogeneous region in which the liquid and vapour are very well mixed together, (2) the developing region in which the flow is changing continuously, and (3) the developed region in which the flow pattern remains the same with stream wise distance (Fei, 2004; Bowers and Hrnjak, 2008).

In the present study, the video record reveals that the two-phase region, which is directly after the expansion device, is mixed well as shown in Figure 6.2 which was extracted from the video record of an experiment with $\dot{m} = 13.1 \pm 0.2$ g/s and quality of 5.4 %. Hrnjak (2004) reported that the liquid and vapour move together at a certain velocity directly after the expansion device where both phases are mixed together (slip ratio is equal to one). Then, as the flow continues downstream, due to the effect of viscous and gravity forces, the phases are separated from each other as a result of the liquid velocity reduction (Hrnjak, 2004). When a significant amount of separation occurs, a distinctive feature is the liquid layer development at the bottom of the tube. Figure 6.1 illustrates the liquid film formation at the bottom as a result of the viscous and gravity force effect. The separation region is regarded as starting at the point where the liquid first appears in a continuous layer at the bottom of the tube. Downstream of this region, the flow is described as a stratified flow as the liquid

has largely accumulated at the bottom while the vapour is moving on the top. Figure 6.3 illustrates a stratified flow pattern from the present experiments.

(a)

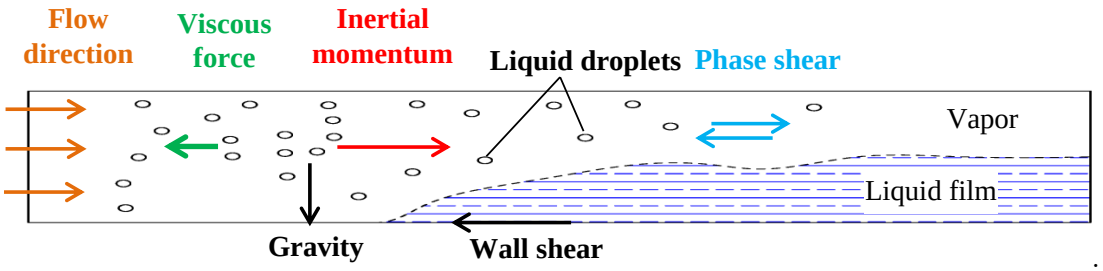

(b)

Figure 6.1: Development of two-phase flow after expansion: (a) image from present experiments ($\dot{m}$ = 5.1 g/s and x = 5.7 %), (b) features impacting two-phase flow development after expansion device adapted from Hrnjak (2004).

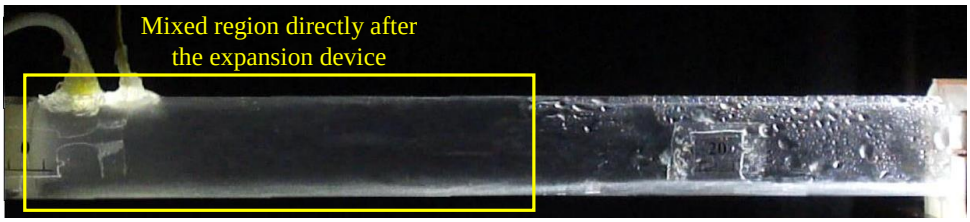

Figure 6.2: Homogeneous flow (mixed flow) region of two-phase flow directly after the expansion device (flow direction from left to right).

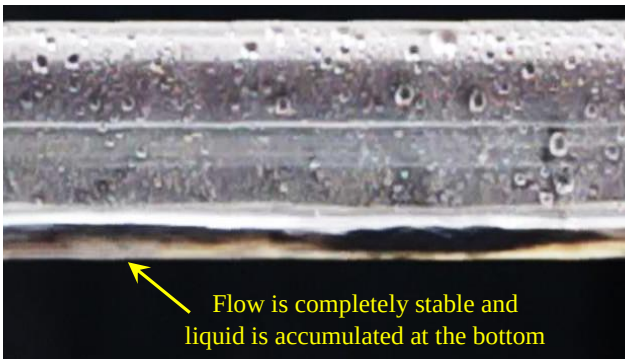

Figure 6.3: Stratified flow at 1600 mm from the inlet, $\dot{m} = 10.2$ g/s and $x = 5.4\%$ (flow direction from left to right).

As a result of the effect of shear forces from the interaction between phases and the tube wall and the no slip condition of the wall, the slip ratio grows and becomes larger until the liquid is separated from the gas phase (Hrnjak, 2004). In all operating conditions, liquid droplets are observed moving on the wall of the tube immediately after the expansion device, then they start to move towards the bottom of the tube as a result of liquid velocity reduction and the gravity effect. Figure 6.4 presents the observed liquid droplet movement from the top to bottom of the pipe. A circle with an arrow highlights the liquid drop and its direction. According to observation in Figure 6.4, a sketch for liquid droplet trajectory is produced as shown in Figure 6.5 to illustrate the path of the liquid droplet during the movement from the top to the bottom of the pipe. In addition, liquid droplets merging is observed in all the operating conditions. Figure 6.6 presents sequential frames illustrating liquid droplet merging at locations between 275 mm and 300 mm from the inlet for $\dot{m} = 10.2$ g/s and $x = 5.4$ %. Images in Figures 6.7 and 6.8 present the experimental observation of the two-phase flow directly after the expansion device and further downstream near the exit of the tube respectively.

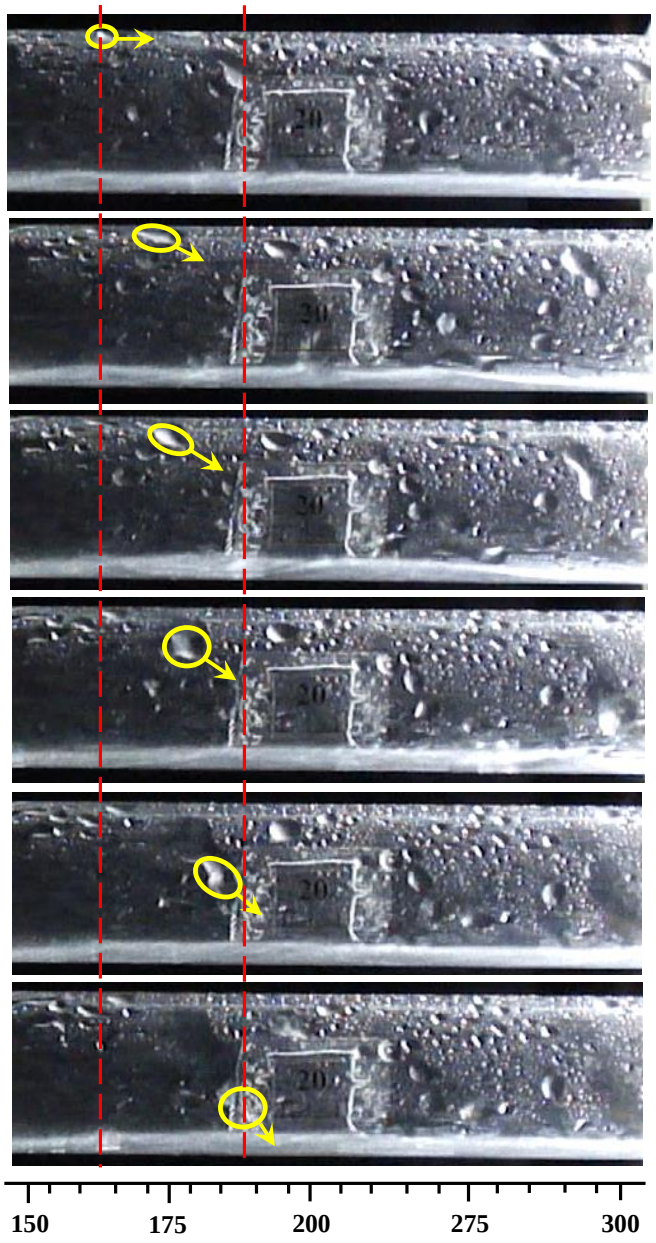

Figure 6.4: Sequential frames to illustrate liquid droplet movement from top to bottom of the pipe between 150 mm and 300 mm from the inlet ($\dot{m}$= 13.1 g/s and x = 5.4 %, flow direction from left to right).

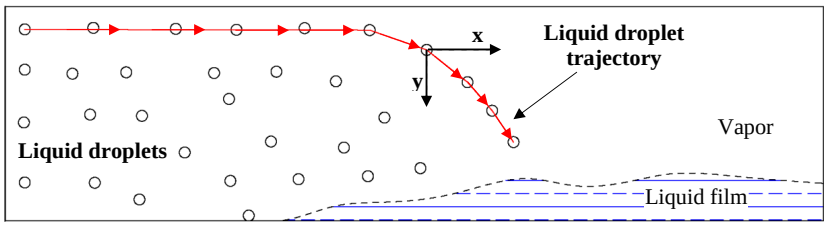

Figure 6.5: Sketch for droplet trajectory during the movement from the top to the bottom of the pipe.

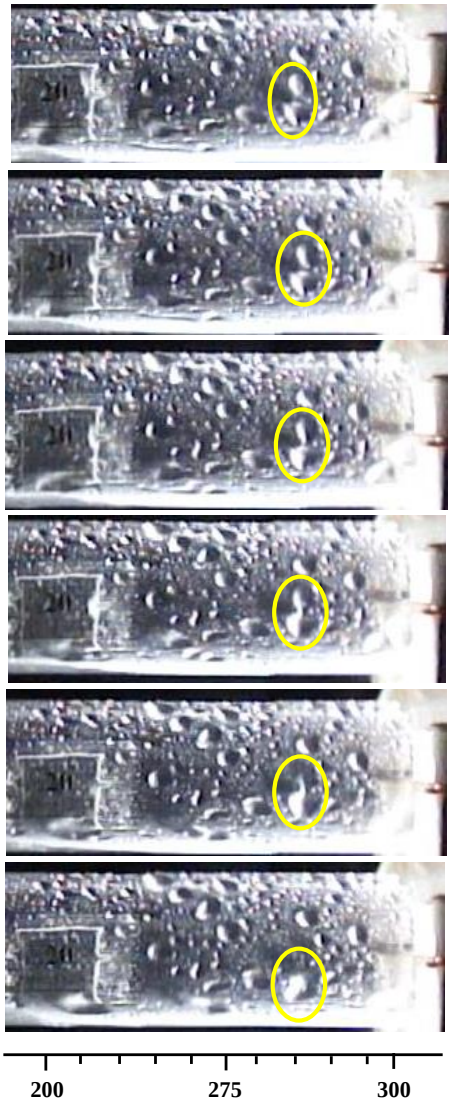

Figure 6.6: Sequential frames to illustrate the observed liquid droplets merging between 275 mm and 300 mm from the inlet, $\dot{m} = 10.2$ g/s and $x = 5.4$ %, flow direction from left to right.

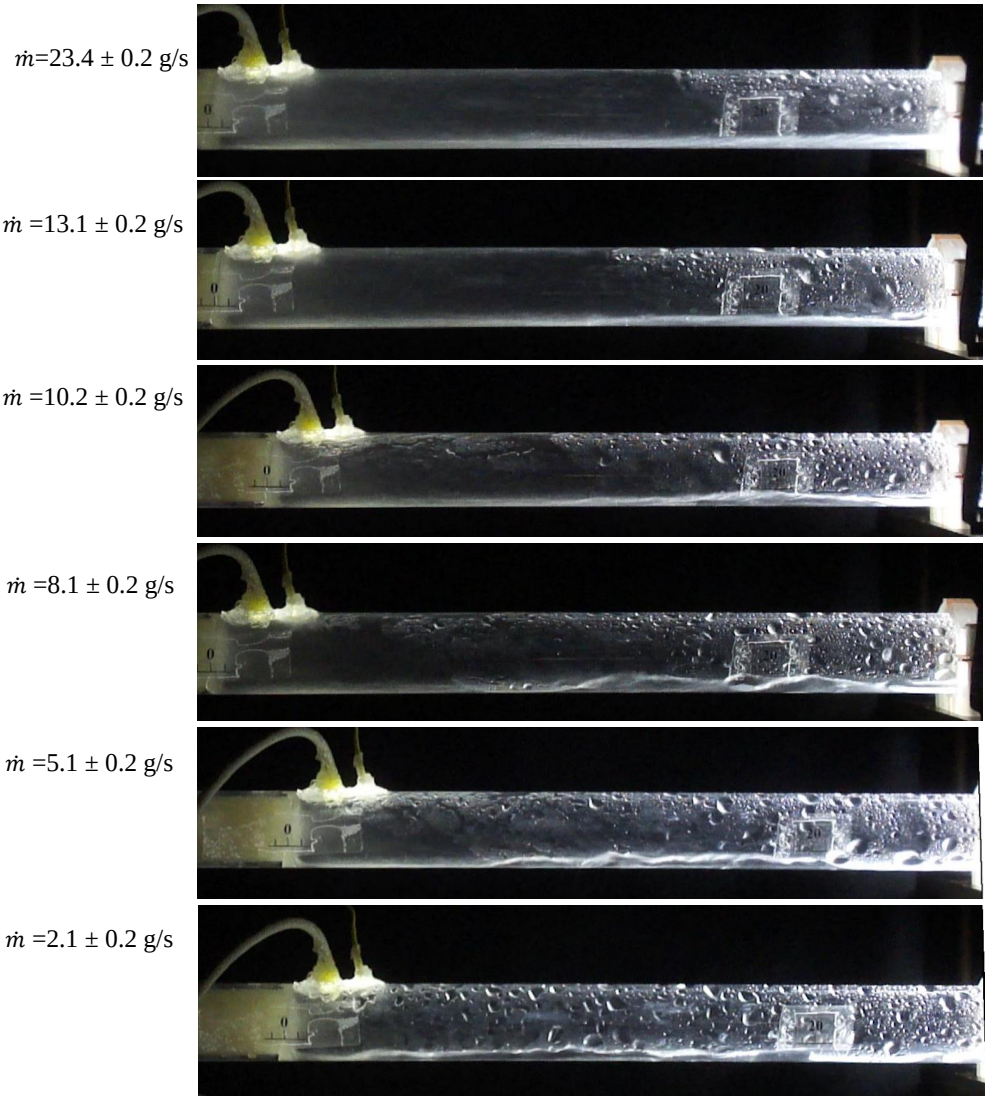

Figure 6.7: Images of the two-phase flow at different mass flow rates directly after the expansion device at the upstream end of the pipe. Images extend from 0 mm to 300 mm from the inlet, flow direction from left to right.

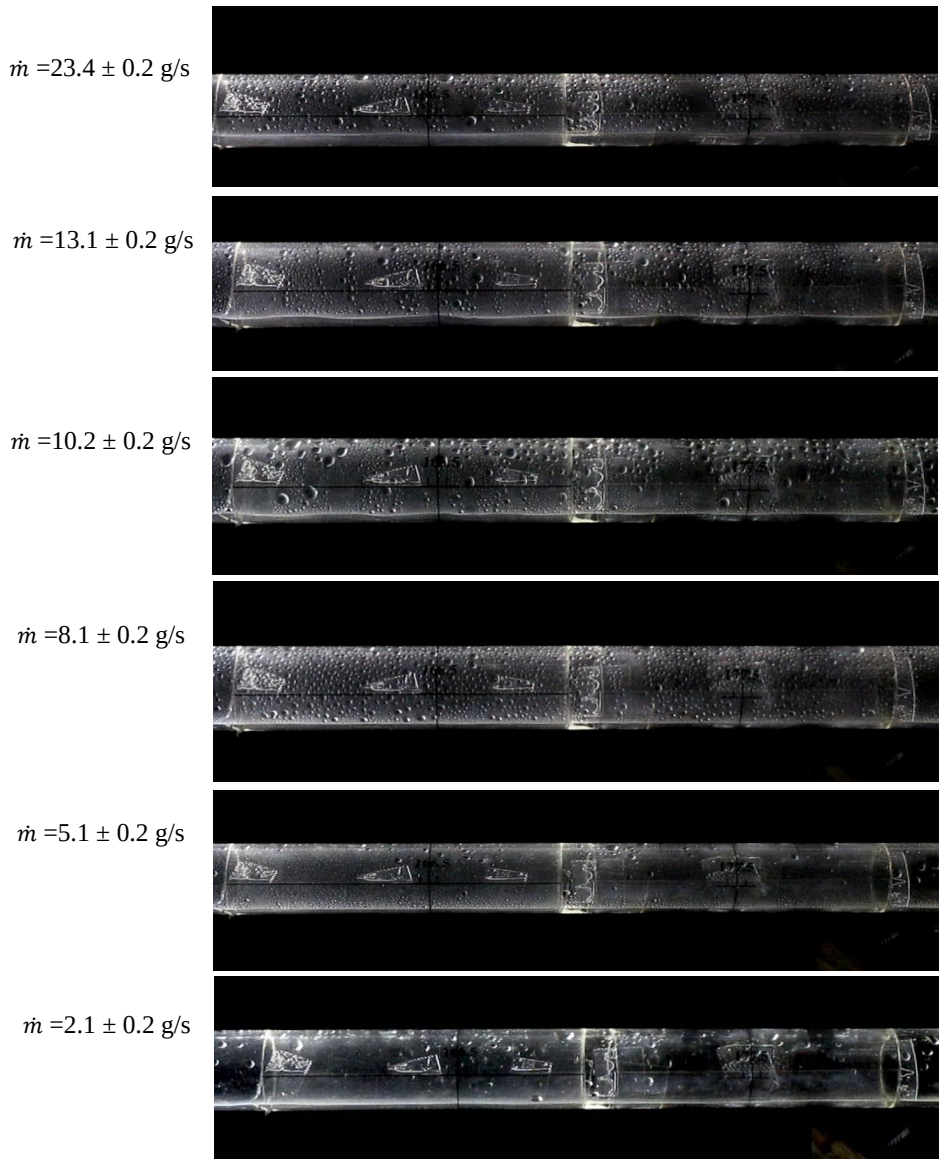

Figure 6.8: Images of the two-phase flow at different mass flow rates at the downstream end of the pipe. Images extend from 1500 mm to 1800 mm from the inlet, flow direction from left to right.

6.3 Expansion length

Two main criteria for definitions the expansion length have been used by Hrnjak (2004), Fei (2004) and Bowers (2009).

- The first criteria is when the liquid droplets at the top of the pipe start moving to the bottom of the pipe. The starting point of the downward movement of the liquid droplets is considered to define the expansion length at the top of the pipe.
- The second criteria is the clear formation of a liquid film at the bottom of the pipe. This criteria defines the expansion length at the bottom of the pipe.

Liquid droplets start to move to the bottom of the pipe after a streamwise movement directly after the expansion device as presented in Figure 6.4. The movement of these droplets typically has a significant trajectory angle in the vicinity 60° as shown in Figure 6.9.
Liquid film formation is observed at the bottom of the pipe for all the operating conditions. Figure 6.10 illustrates identification of the start of the liquid film from one of the operating conditions.

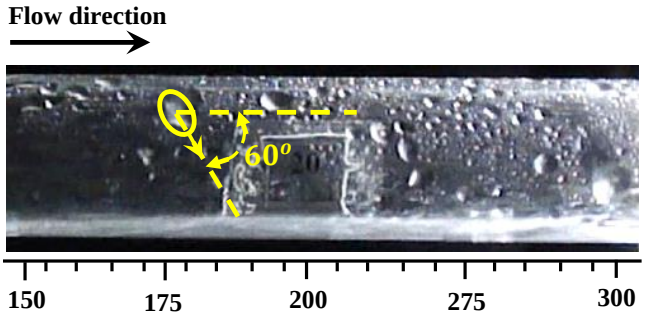

Figure 6.9: Observed liquid droplet movement from top to bottom of the pipe at locations from 150 mm to 300 mm from the inlet, $\dot{m} = 13.1 \pm 0.2$ g/s, $x = 5.4$ %.

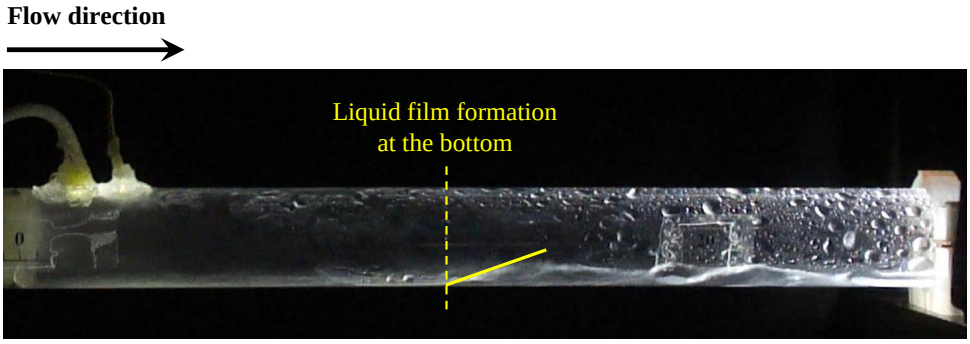

Figure 6.10: Image showing liquid film formation at the bottom of the pipe at locations from 0 mm to 300 mm from the inlet, $\dot{m} = 8.1 \pm 0.2$ g/s, $x = 5.5$ %).

Figure 6.11 presents the influence of mass velocity on the expansion length according to the first criteria: significant liquid droplet movement toward the bottom of the pipe. Figure 6.12 presents the expansion length according to the second criteria: liquid formation at the bottom of the pipe. The location of droplets near the top of the pipe that have detectable movement in the downwards direction changes with time. The location of the detectable start of the liquid film at the bottom of the pipe also changes with time. Hence there are uncertainties in the application of the expansion length criteria. In each figure, the error bars denote the estimated uncertainty in defining the distance from the experimental data. The mass velocity has a significant effect on the expansion length. The expansion length increases as a result of higher initial velocity, and the two criteria produce similar results for the expansion length over the range of mass velocities in the experiments.

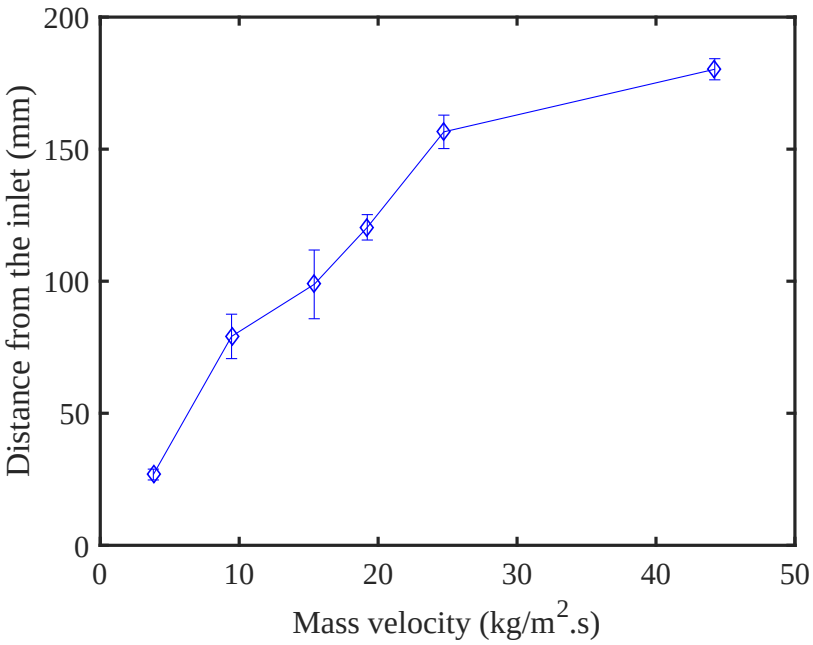

Figure 6.11: Length of the expansion region from the inlet of tube based on criteria 1: phase separation at the top of the pipe.

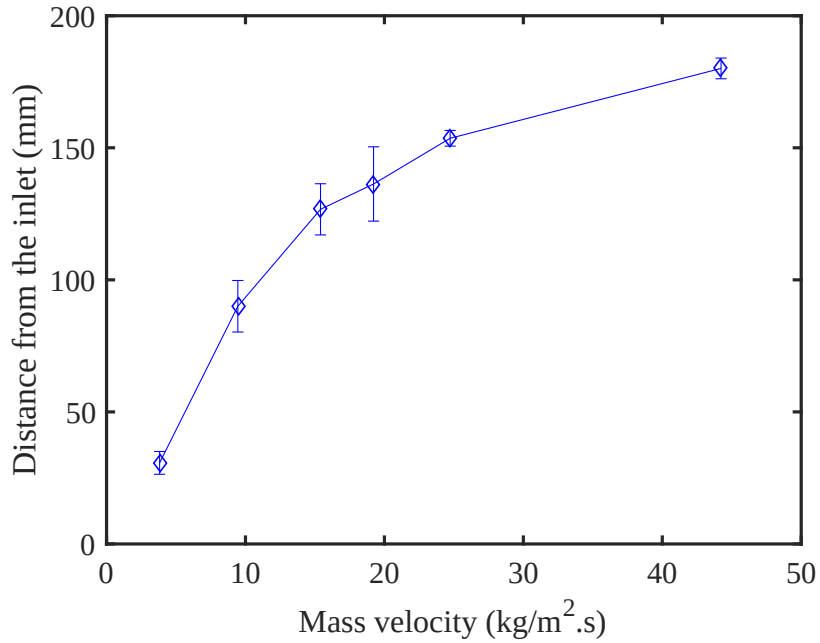

Figure 6.12: Length of the expansion region from the inlet of tube based on criteria 2: phase separation at the bottom of the pipe.

6.4 Liquid height in the developed region

Liquid height is used to calculate the void fraction in the developed region. At each condition, the average liquid height was measured using image analysis in the developed region. The experimental results revealed that the liquid height is constant, starting at around 200 mm from the inlet to the end of the pipe, as shown in Figure 6.8. So, from the 200 mm station, the flow was steady along the pipe and no further change in flow structure was observed. Figure 6.13 illustrates the definition of liquid height and vapour inside the horizontal pipe in the developed region, including the chord angle; these quantities are used to calculate the void fraction in the developed region.

Figure 6.14 presents the experimental data of the liquid height variation with the mass velocity. The experiment showed that the mass flow rate has a direct influence on the liquid height in the developed region. The highest liquid height was obtained at maximum flow rate of 23.4 ± 0.2 g/s, while the lowest liquid height was observed at lowest flow rate of 2.1 ± 0.2 g/s. The error bars presented in Figure 6.14 present the uncertainty in liquid height measurements which arises mainly from edge detection uncertainties due to liquid meniscus and lighting.

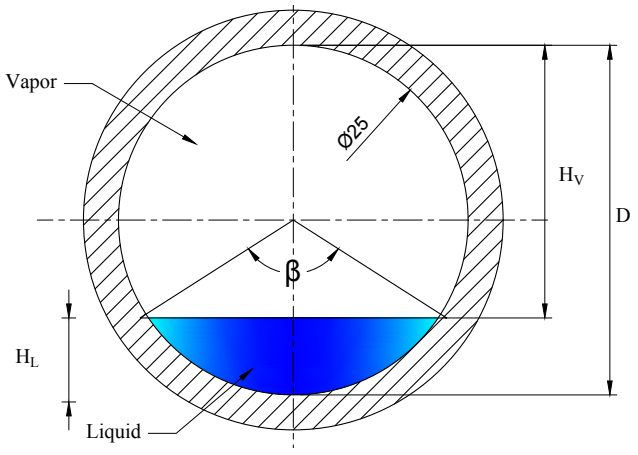

Figure 6.13: Illustration of the definition of liquid height and vapour in the developed region.

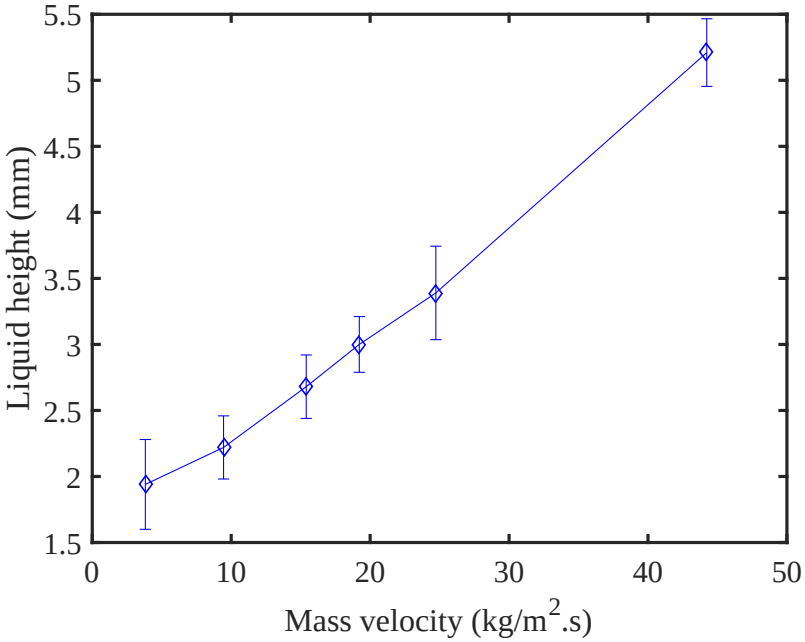

Figure 6.14: Variation of liquid height with mass velocity at 300 mm from the inlet.

6.5 Void fraction analysis

The void fraction has been estimated from the cross-section area occupied by vapour phase and the total cross-section area of the pipe (Srisomba et al., 2014). The void fraction can be calculated based on the chord angle and then the area occupied by liquid is easily estimated. Finally, the void fraction can be obtained from the ratio between the area occupied by vapour to the total area of the pipe.

$$\alpha = \frac{A_V}{A_V + A_L} \tag{6.1}$$

$$A_V = A_t - A_L \tag{6.2}$$

$$A_L = \frac{D^2}{8}(\beta - \sin(\beta)) \tag{6.3}$$

where the β is the chord angle that can be calculated from

$$\beta = 2\cos^{-1}(1 - \frac{D - H_V}{(D/2)}) \tag{6.4}$$

where H_V is the height of the vapour phase and D is the tube diameter as shown in Figure 6.13.

Figure 6.15 present the experimental relationship between the void fraction and mass velocity in the developed region at 1665 mm from the inlet. Because of the void fraction was calculated from the liquid heights, the void fraction uncertainty presented in this figure arises from the liquid height uncertainty. As can be seen, there is a significant influence of the mass velocity on the void fraction in the developed region. The increase in the mass velocity leads to decrease the void fraction due to the increase of the liquid height.

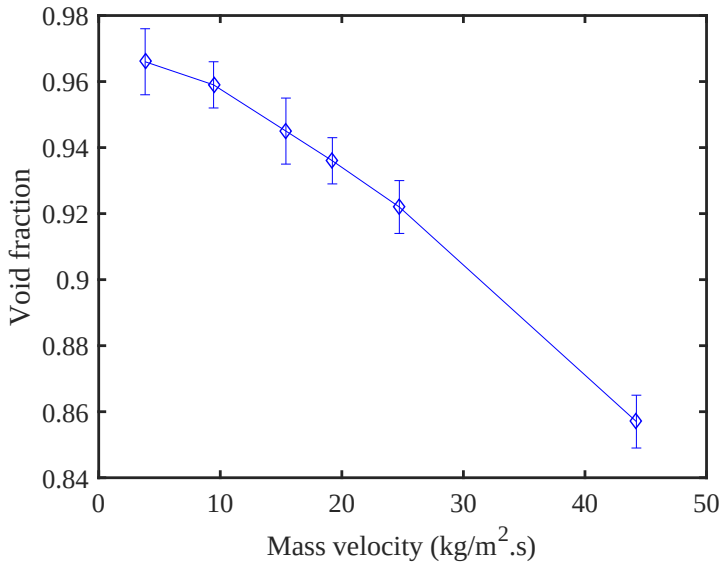

Figure 6.15: Relationship between the void fraction and the mass velocity in the developed region at 1665 mm from the inlet.

6.6 Local velocity and slip ratio

As the void fraction has been defined, the local velocity of the vapour and liquid phases can also be calculated.

$$u_l = \frac{(1-x)\dot{m}}{(1-\alpha)\rho_L A_t} \tag{6.5}$$

$$u_v = \frac{(x)\dot{m}}{(\alpha)\rho_g A_t} \tag{6.6}$$

Then, the liquid height can be presented as a function of slip ratio (u_v/u_l) in the developed region as shown in Figure 6.16. It can be seen that when the liquid height is increased as a result of increasing the mass flow rate, the slip ratio is increased. There is an inverse relationship between the void fraction and slip ratio when the liquid height is increased as presented in Figure 6.17.

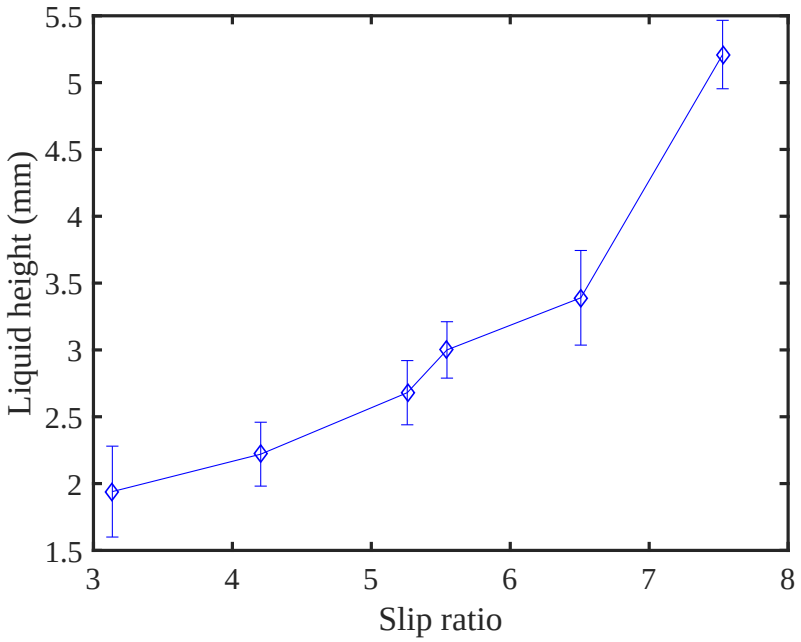

Figure 6.16: Variation of liquid height in the developed region with slip ratio = u_v/u_l at 1665 mm from the inlet.

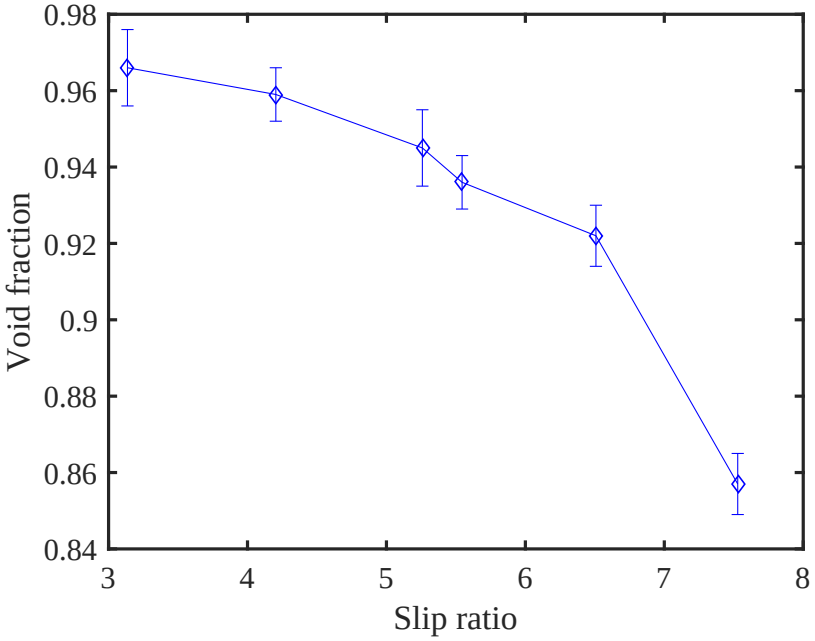

Figure 6.17: Variation of the void fraction with the slip ratio in the developed region at 1665 mm from the inlet.

6.7 Dimensionless Parameters

Chapter 3 defined several the dimensionless numbers, and based on the operating conditions for the present work, the dimensionless numbers have been calculated. Void fraction in the developed region is presented in Figures 6.18 as a function of liquid and gas dimensionless numbers, and the two-phase dimensionless numbers are used to present the void fraction in Figure 6.19. Figure 6.20 presents the expansion length according to criteria 2 (liquid film formation at the bottom of the pipe) using liquid and gas dimensionless numbers, and Figure 6.21 presents the expansion length using the two-phase dimensionless numbers.

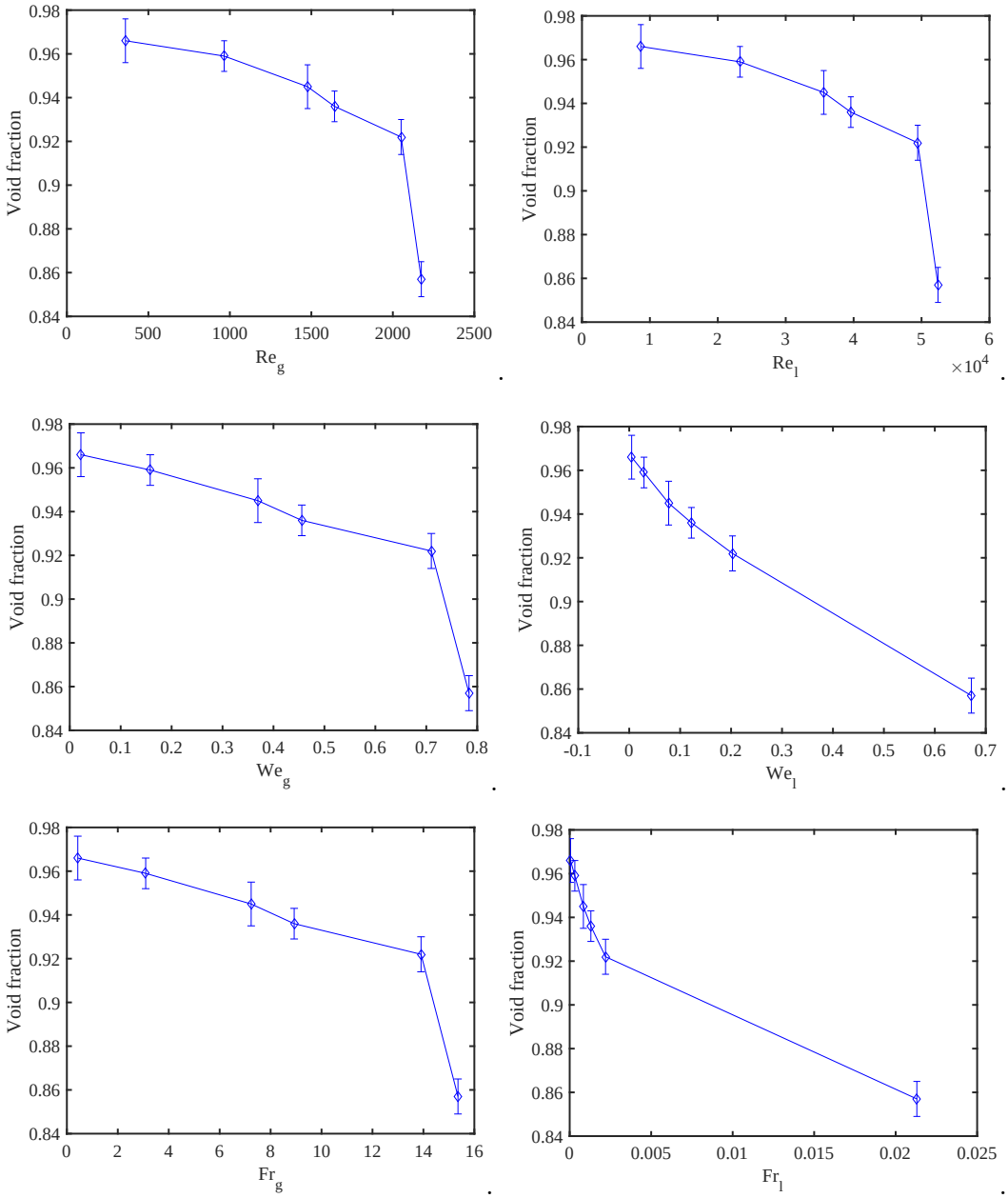

Figure 6.18: Void fraction in the developed region as a function of liquid and gas dimensionless numbers.

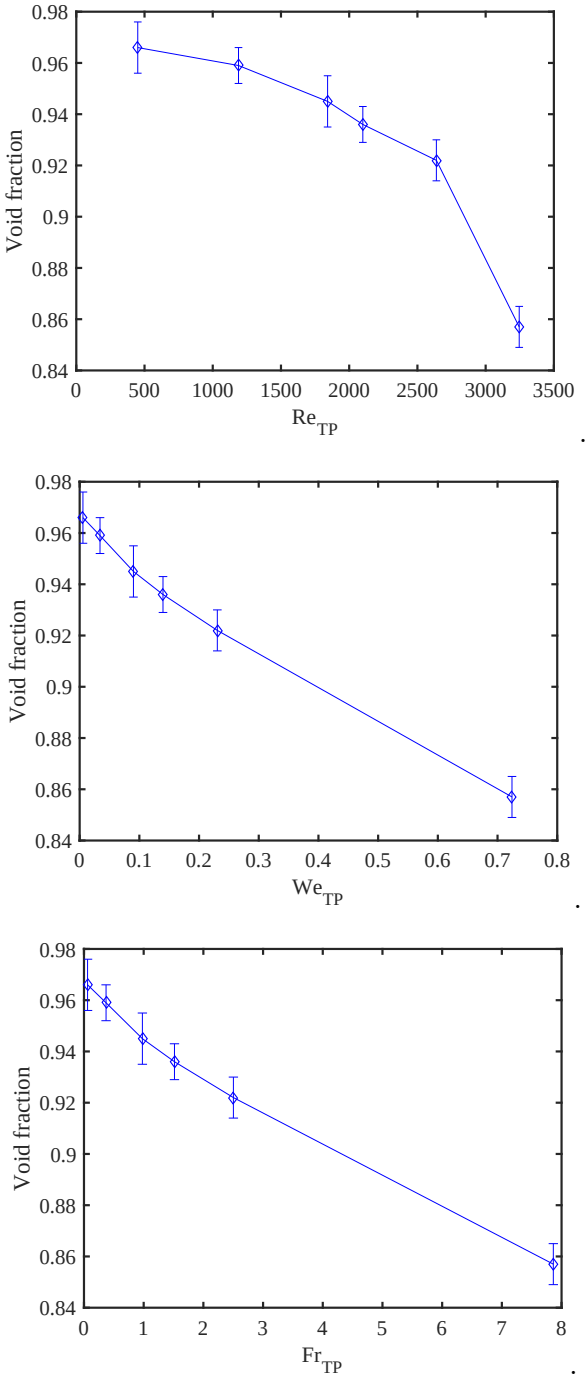

Figure 6.19: Void fraction in the developed region as a function of two-phase dimensionless numbers.

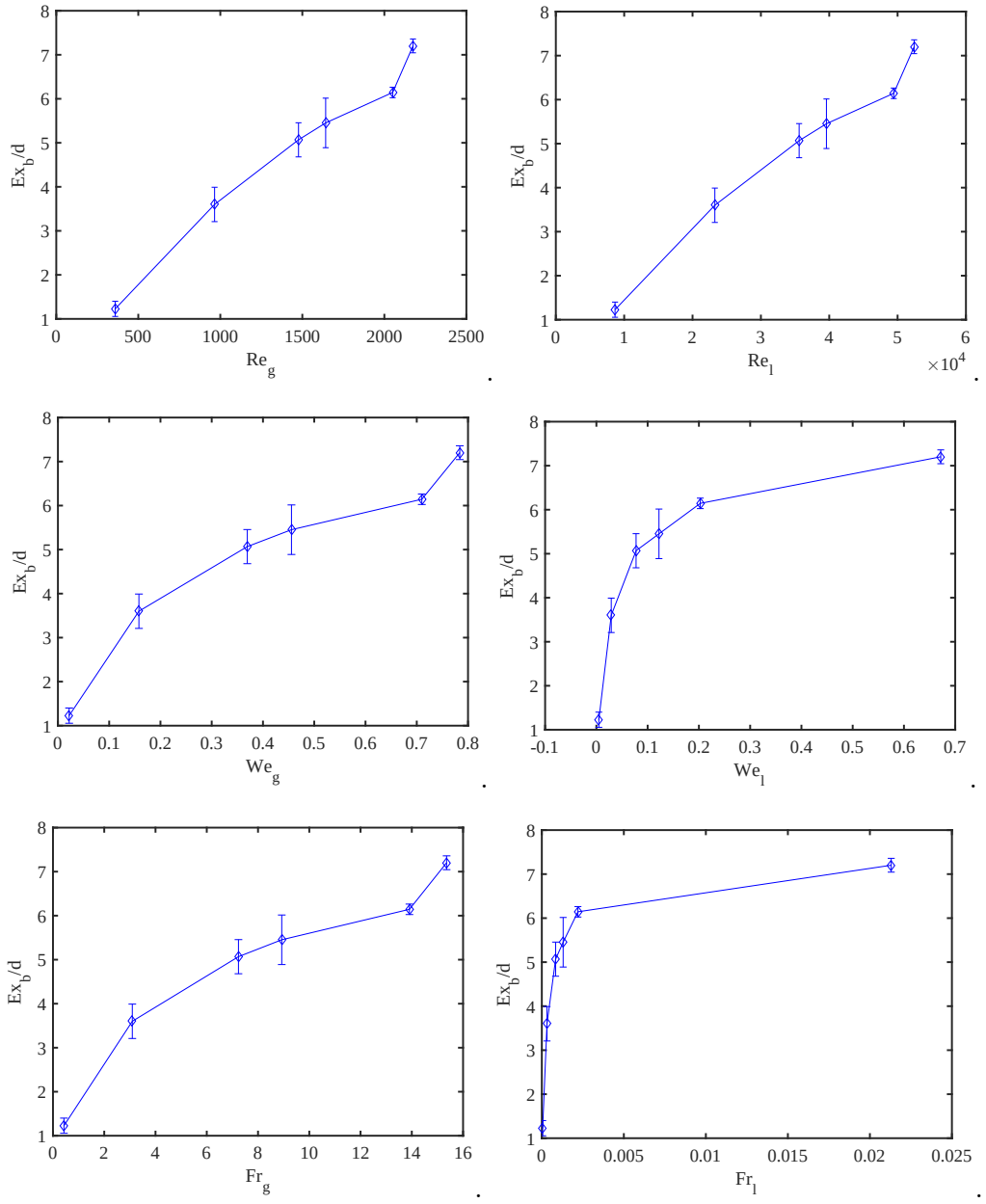

Figure 6.20: Expansion length at the bottom divided by diameter of the horizontal tube according to criteria 2 (liquid formation at the bottom of the pipe) as a function of liquid and gas dimensionless numbers.

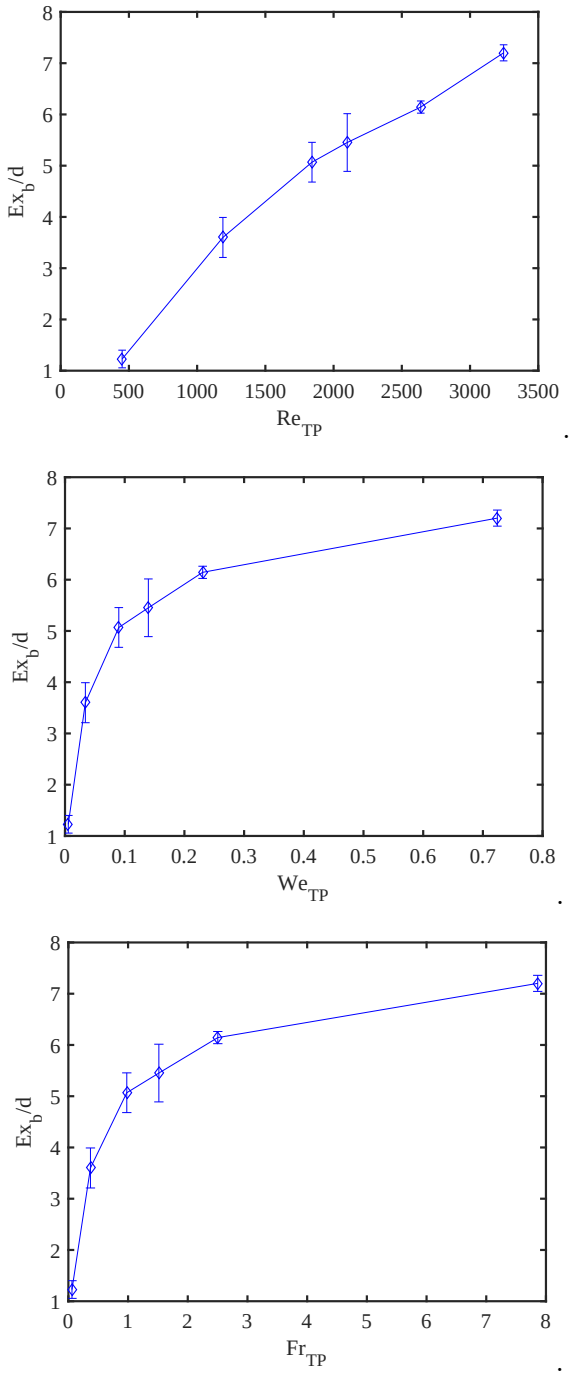

Figure 6.21: Expansion length at the bottom divided by diameter of the horizontal tube according to criteria 2 (liquid formation at the bottom of the pipe) as a function of two-phase dimensionless numbers.

6.8 Empirical correlation to identify the expansion region in a horizontal pipe.

Based on the experimental results, an empirical regression model for the flow development length in a horizontal pipe has been developed as a function of the two-phase dimensionless numbers of the horizontal pipe: Re_{TP} , Fr_{TP} and We_{TP}.

$$Ex_b/d = 5.906 Re_{TP_hp}^{0.953} We_{TP_hp}^{3.086} Fr_{TP_hp}^{-3.162} \tag{6.7}$$

For the expansion length at the bottom of the pipe, the model in Equation 6.7 has an R^2 value equal to 0.99. It can be used to predict the expansion length at the bottom for the present range of experimental data using the two-phase dimensionless numbers. For the void fraction in the developed region of the horizontal pipe a similar empirical model was developed.

$$\alpha = 0.295 Re_{TP_hp}^{0.166} We_{TP_hp}^{0.037} Fr_{TP_hp}^{-0.128} \tag{6.8}$$

For the void fraction, the model in Equation 6.8 has an R-squared value equal to 0.99. It can be used to predict the void fraction in the developed region for the present range of experimental data. Figures 6.22 and 6.23 compare the predicted values with the experimental observed values for the Ex_b/d and the void fraction respectively.

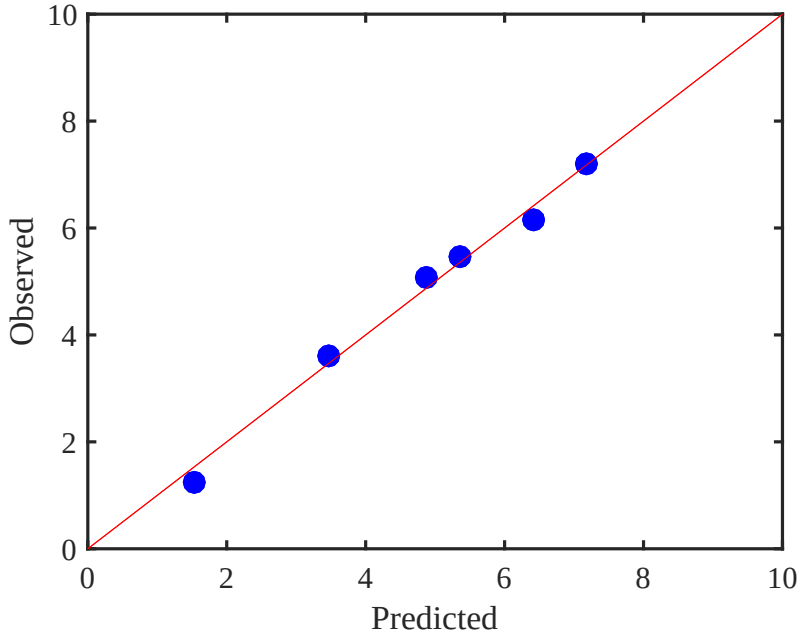

Figure 6.22: Comparison between the predicted and observed values of the normalised expansion length Ex_b/d at the bottom of the pipe.

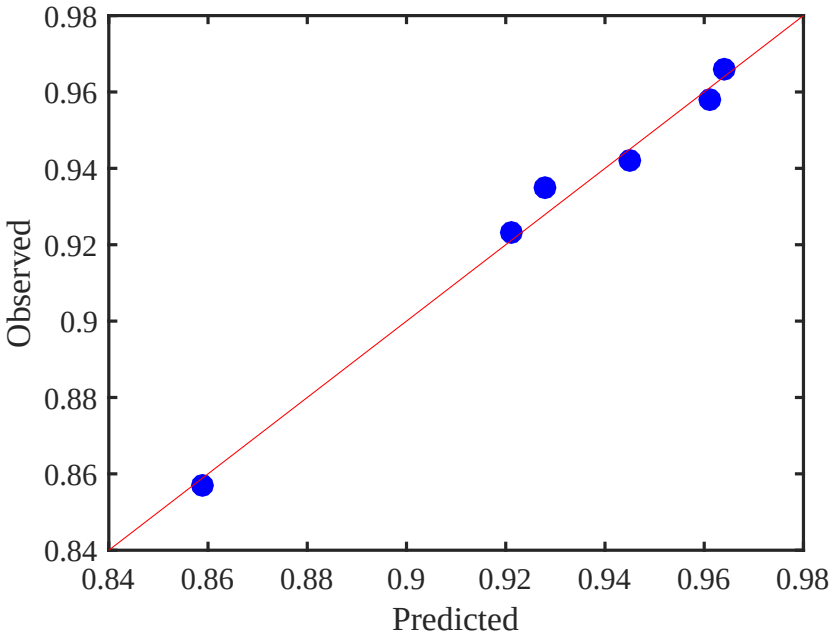

Figure 6.23: Comparison between the predicted and observed values of void fraction α in the developed region in the horizontal pipe.

6.9 CFD simulation results

6.9.1 Two-phase flow development on the bottom of the pipe

In order to show the simulated two-phase flow development after the expansion device, contours of the liquid volume fraction were plotted along the axial vertical plane from the inlet of the tube as illustrated in Figure 6.24 for the case of $\dot{m} = 23.4$ g/s. Liquid volume fraction distribution on three cross-section planes at distances of 5 cm, 10 cm and 20 cm from the inlet are also shown in Figure 6.24. When the volume fraction of the liquid is equal to 1, the two-phase flow is completely single phase in liquid state and when the two-phase flow becomes completely single phase vapour, the liquid volume fraction is equal to zero. The cross-section contours on the plane at 20 cm (Figure 6.24d) illustrate the flow in the fully developed region as the liquid height remains the same at stations further downstream and there is no significant change after this plane. In addition, the plane (d) indicates there is no further separation in this area. The differences in the liquid volume fraction distribution between the planes at 5 cm, 10 cm, and 20 cm (Figure 6.24b, c, and d) also demonstrates that the flow is developing within this region. Contours of the simulated liquid volume fraction at the different operating conditions are presented in Figure 6.25.

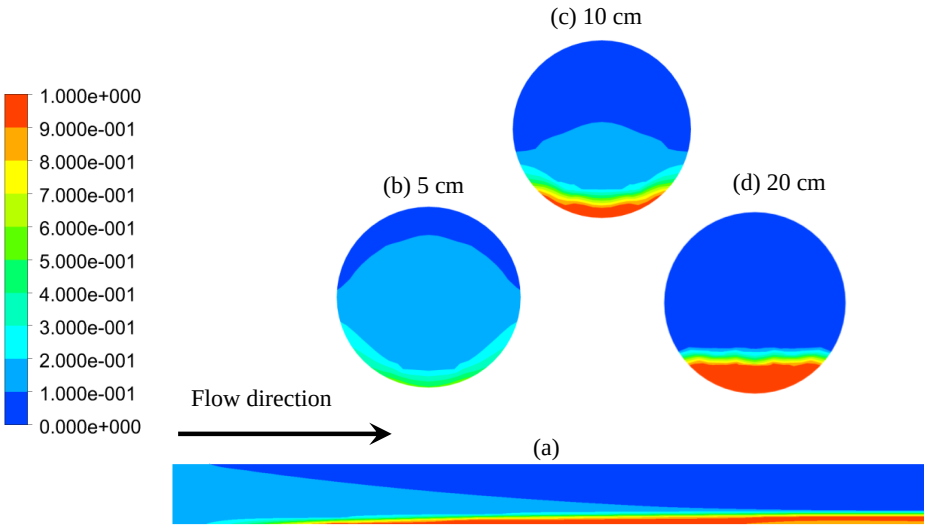

Figure 6.24: Liquid volume fraction (LVF) for $\dot{m}$ = 23.4 g/s (a) LVF along the axial vertical plane; (b) LVF at 5 cm from the inlet; (c) LVF at 10 cm from the inlet; and (d) LVF at 20 cm from the inlet.

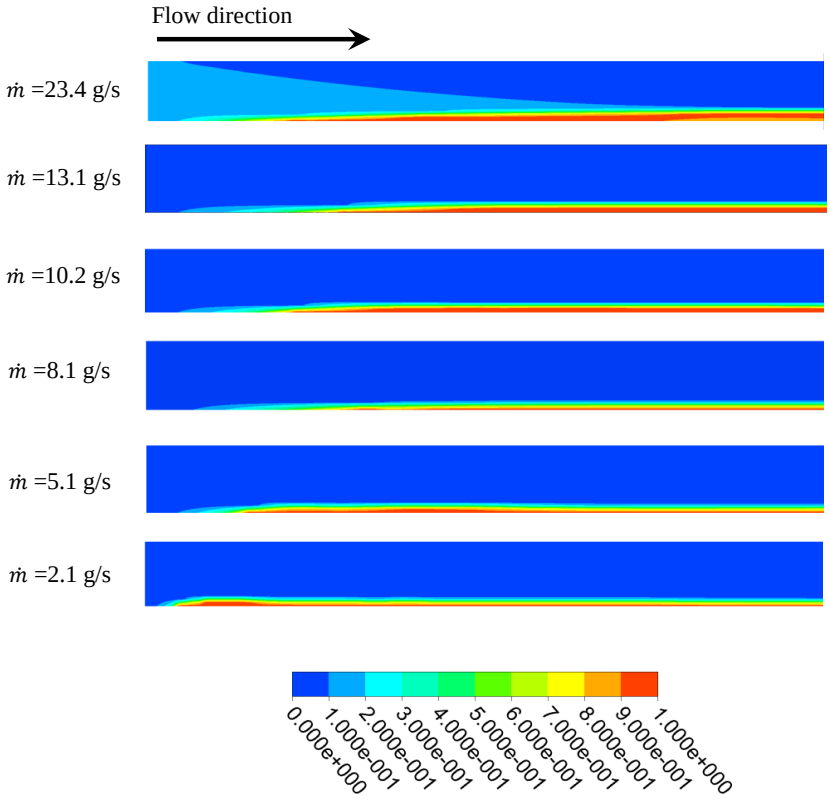

Figure 6.25: Liquid volume fraction along the axial vertical plane at the different operating conditions.

To compare the simulated results for the length of the developing region with the data from experiments, a method for quantifying the simulated position where the initiation of film development occurs is needed. Liquid volume fraction results are shown in Figure 6.26 for $\dot{m} = 5.1$ g/s. In order to specify the location of the start of the liquid film, Figure 6.27 presents contour lines, and a zoomed-in view showing the starting point of the liquid layer formation is presented in Figure 6.28

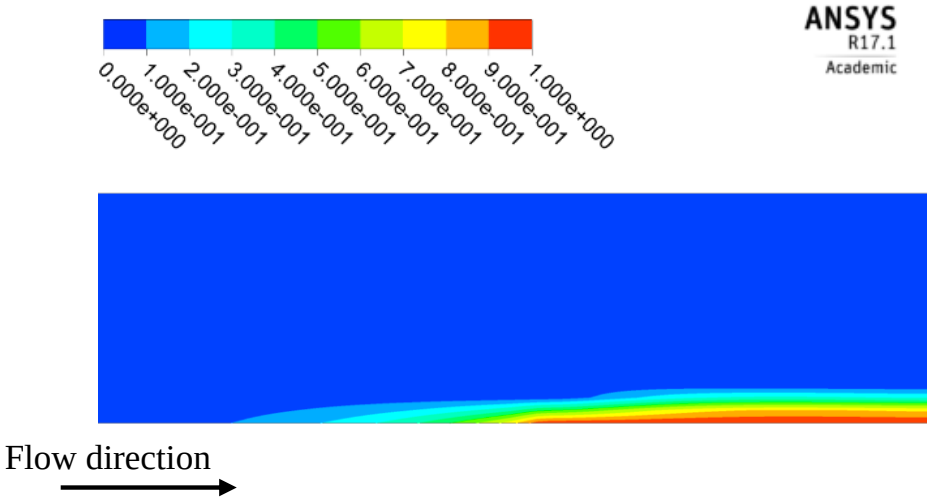

Figure 6.26: Contours of liquid volume fraction showing liquid formation at the bottom of the pipe on the axial vertical plane for $\dot{m} = 5.1$ g/s.

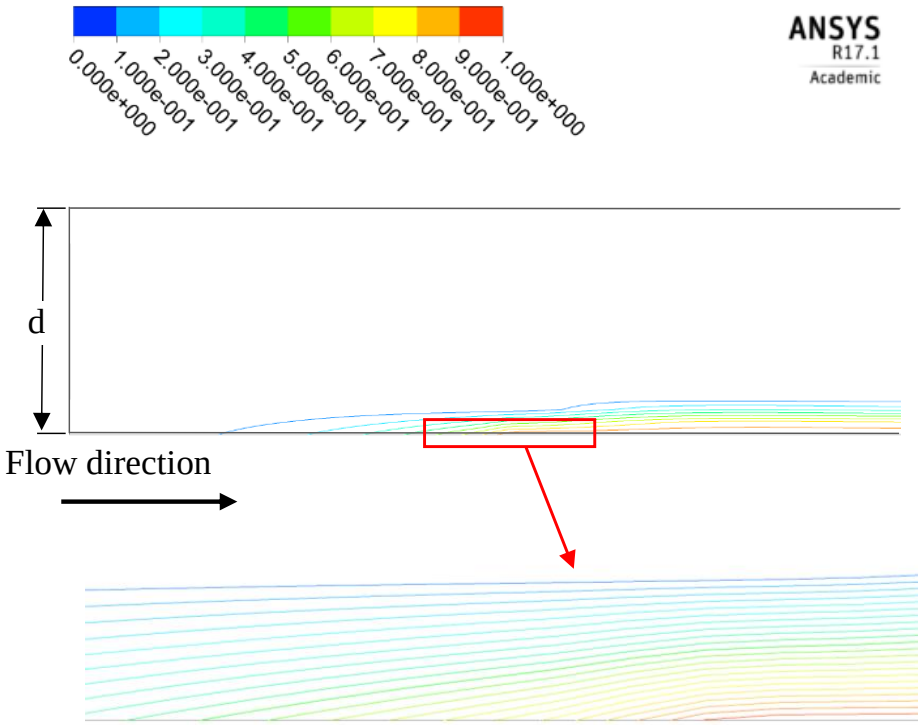

Figure 6.27: Contour lines of liquid volume fraction showing liquid formation at the bottom of the pipe on the axial verical plane $\dot{m} = 5.1$ g/s.

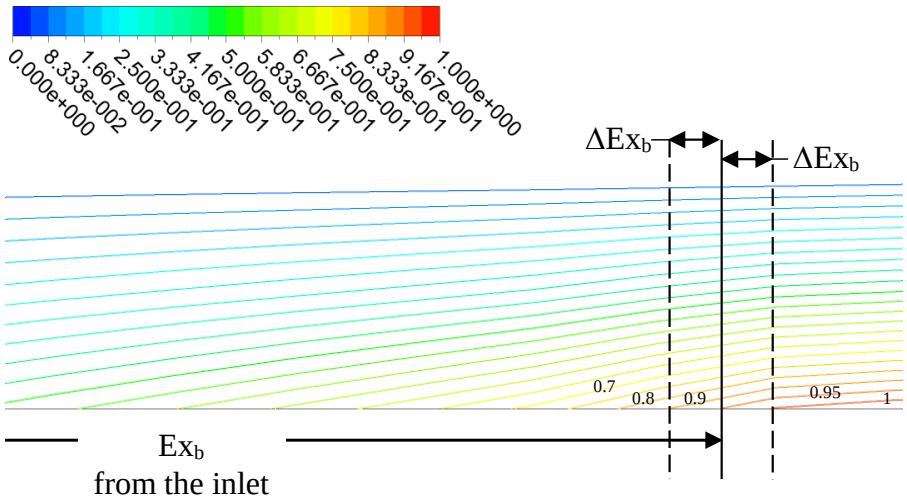

Figure 6.28: Zoomed-in view of contour lines of liquid volume fraction showing liquid formation at the bottom of the pipe on the axial vertical plane $\dot{m} = 5.1$ g/s.

In the present work, the simulated expansion length at the bottom of the pipe Ex_b is defined as the distance from the inlet to the location where the LVF = 0.95 on the lower-most wall of the pipe. For the case of $\dot{m}$ = 5.1 g/s illustrated in Figure 6.28, Ex_b = 82.7 mm. A value for the LVF of 0.95 was chosen in preference to the value of 1.00 because a value of unity might be approached asymptotically in some simulations, potentially leading to unrealistically long expansion length values. The quantity ΔEx_b shown on Figure 6.28 is defined as the distance between LVF contours of 0.90 and 0.95 and is presented as an indicator of the uncertainty associated with defining the expansion length in the simulations.

The experimental data and simulations are compared in Figure 6.29. The simulations underestimate the expansion length and the mean difference between the experimental data and the numerical results is 8 %. The uncertainty in defining the expansion length from the simulations vary from ΔEx_b = 0.9 mm in the lowest mass flow rate case up to ΔEx_b = 2.1 mm in the highest mass flow rate case. Therefore, these uncertainness are very small relative to those associated with the data from the experiments.

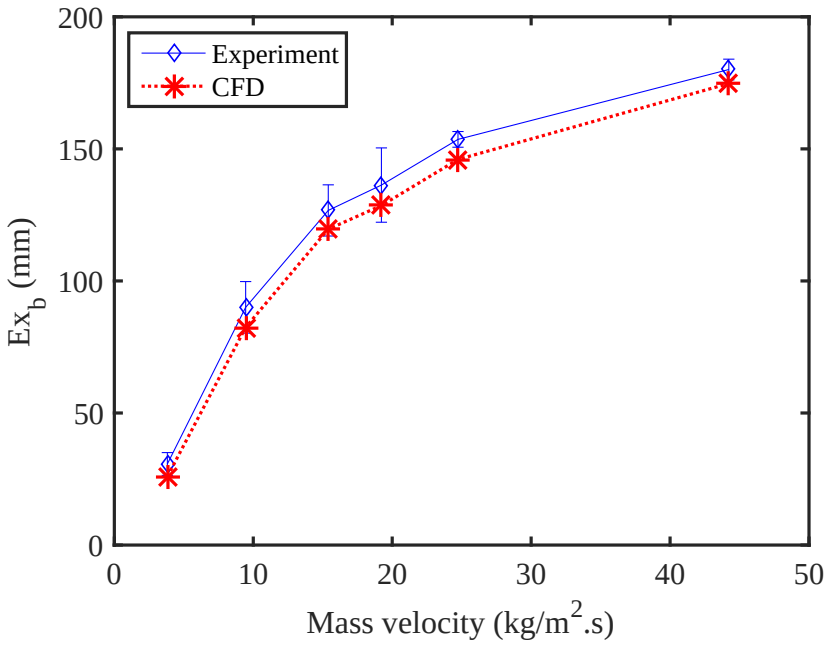

Figure 6.29: Comparison between the experimental data and numerical simulations for the expansion length at the bottom of the pipe.

6.9.2 Liquid height in developed region

In order to determine the liquid height according to the liquid volume fraction definition and compare it with the experimental data, a central vertical plane at 1665 mm from the inlet is defined in the CFD simulations. Figure 6.30 illustrates the liquid volume fraction distribution at this location and includes the liquid height definition which is illustrated by the distance between the two vertical lines. The liquid height is defined by the zone in which the liquid volume fraction is greater than 0.95, an approach consistent with that adopted for the expansion region. The simulated liquid volume fraction in the fully developed region for the different operating conditions is shown in Figure 6.31. It is seen that the mass flow rate has a significant effect on the liquid height. The experimental results are also included in Figure 6.32 and it is observed that the experiments and numerical simulations have same trend, although the difference between the experimental and numerical results is about 8 %.

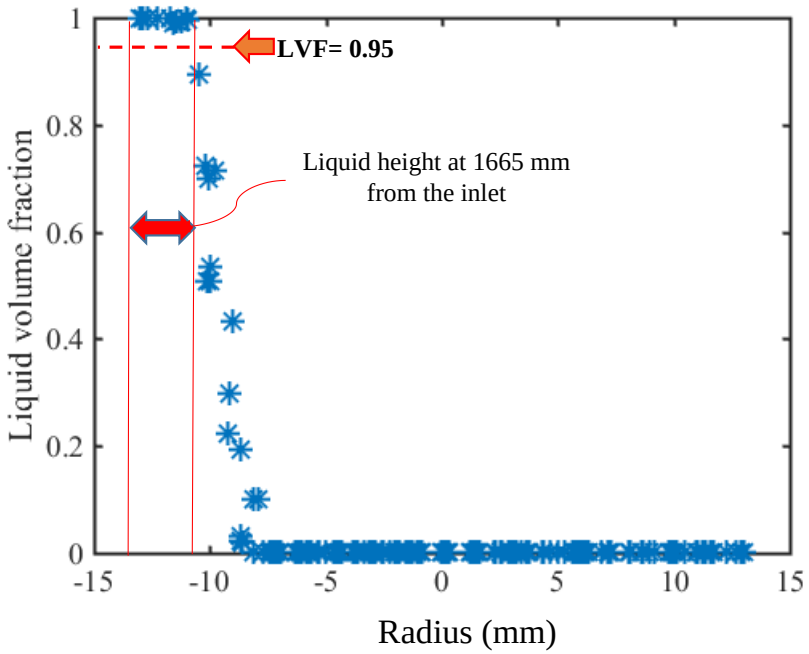

Figure 6.30: Liquid height identification on the central vertical plane of the pipe at 1665 mm from the inlet, according to the liquid volume fraction definition for $\dot{m}$ = 13.1 g/s.

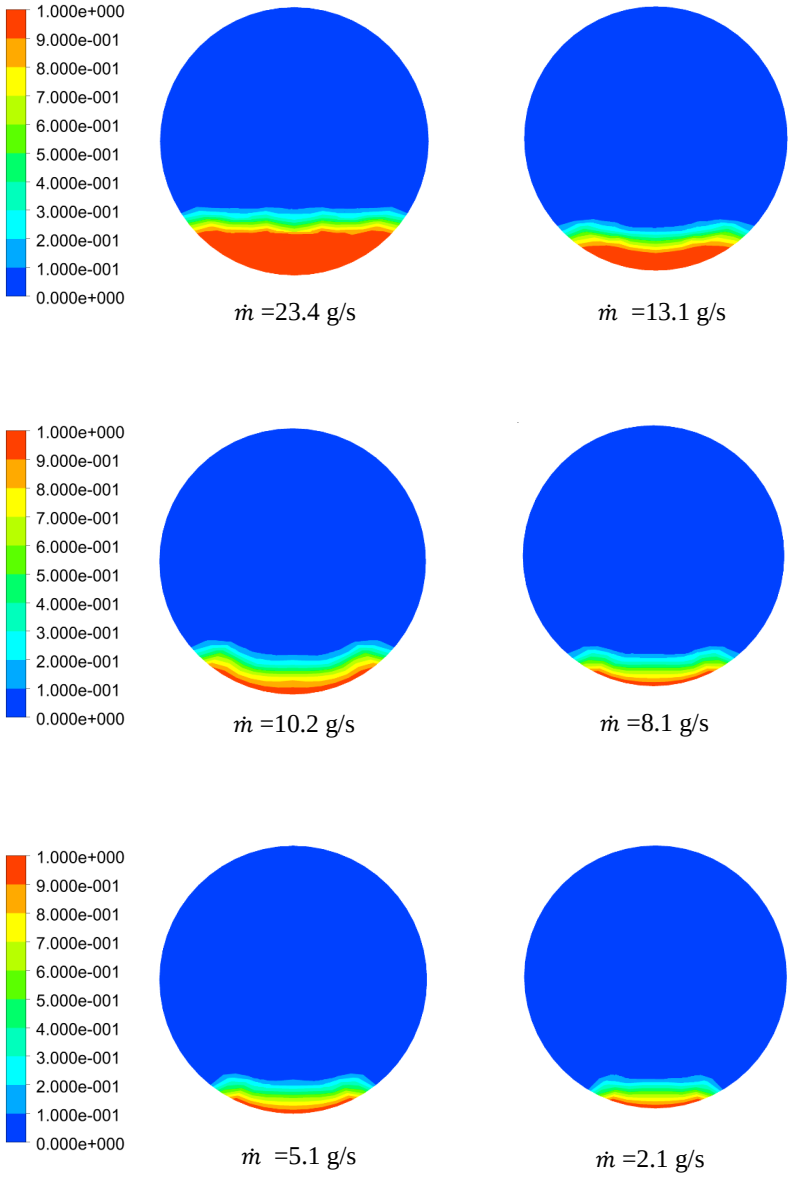

Figure 6.31: Liquid volume fraction on the vertical planes perpendicular to the flow direction at 1665 mm from the inlet for the different operation conditions.

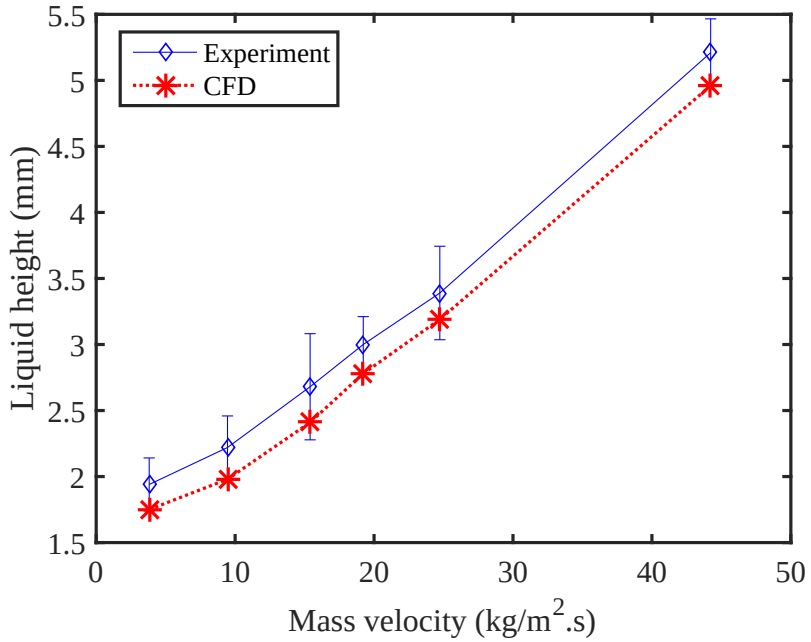

Figure 6.32: Comparison between the experimental data and numerical simulations for the liquid height on the central vertical plane of the pipe at 1665 mm from the inlet.

6.10 Length to fully-developed region

In order to identify the required length of the inlet pipe for the vertical flash tank separator, the CFD simulations for the horizontal pipe were completed to determine the location where the fully-developed region is first established. Figure 6.33 illustrates the expansion region length (L_{FD}) and film height (H_L) in the horizontal pipe for $\dot{m} =$ 5.1 g/s. The expansion region and film height were defined using LVF = 0.95 consistent with the previous approaches. Figure 6.33 also illustrates that a constant film height is maintained after the expansion region, so the two-phase flow is completely stable and this is a characteristic of the fully-developed region.

Figure 6.34 illustrates the expansion length in the horizontal pipe for different inlet mass velocities. The figure also indicates that the maximum expansion length across all operating conditions is less than 200 mm. Hence, the required length of the inlet pipe for the vertical flash apparatus described in Chapter 4 was specified conservatively as 300 mm.

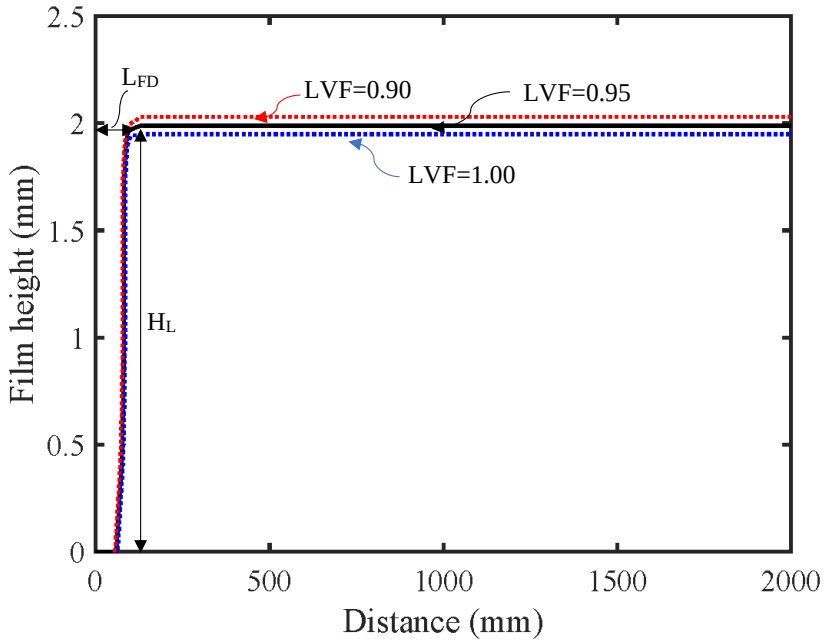

Figure 6.33: Simulated value of film height along the horizontal pipe based on different LVF values showing the expansion region length (L_{FD}) for $\dot{m}$ = 5.1 g/s.

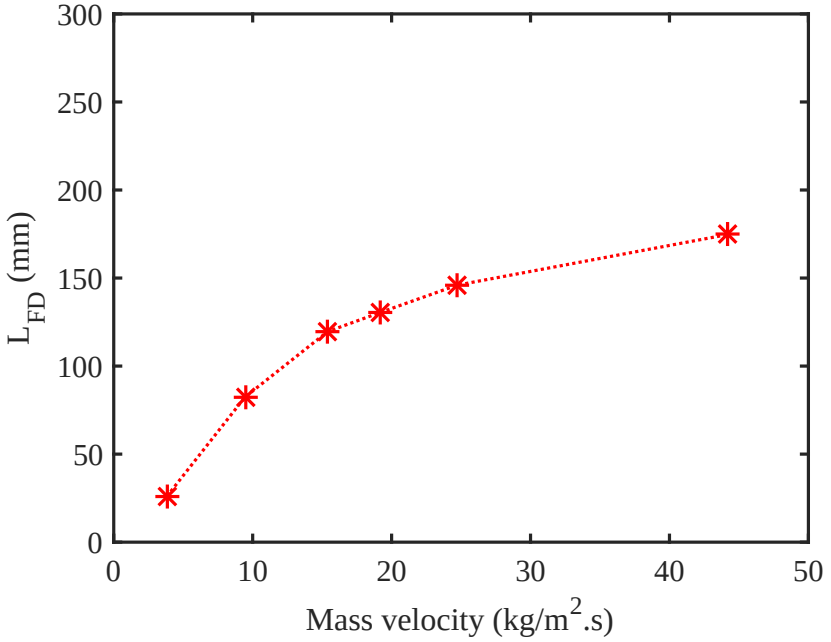

Figure 6.34: Simulated values of the distance to the fully-developed region in the horizontal pipe for different inlet mass velocities.

6.11 Conclusion

Experimental and CFD investigations of two-phase flow of water in a 25 mm inner diameter and 2 m long horizontal pipe have been carried out. The influence of the flow rate on the two-phase flow development after expansion device has been observed. The main results can be summarized as follows.

1. The two-phase flow develops gradually after the expansion device. The expansion length was less than 200 mm for all conditions tested.

2. Increase the mass flow rate has a direct, and significant effect on the expansion length.

3. An increase of the mass flow rate causes an increase in the void fraction and a reduction in the slip ratio in the developed region.

4. A fully-developed stratified flow pattern was observed in all the experiments within the pipe length.

5. Comparison of the experimental data and simulations indicate, the simulations underestimate the expansion length and fully-developed liquid film height by about 8 %.

6. Using the experimental data, empirical correlations have been developed to predict (a) the expansion length at the bottom of the horizontal pipe and (b) the void fraction in the developed region. Both correlations achieved R^2 values of 0.99.

7. The distance to the fully-developed region was identified from the CFD simulation result. Therefore, the required length of the inlet pipe of the vertical flash tank separator has been selected.

Chapter 7

Two-phase flow in a vertical flash tank

7.1 Introduction

This chapter presents experimental investigations and CFD simulations of the liquid separation efficiency of the vertical flash tank separator using water as the working fluid. Liquid separation efficiency is affected by the geometry of the vertical flash tank separator. The inlet flow condition has an effect on the flow distribution in a vertical flash tank separator and hence can also effect the separation efficiency. If the inlet flow for the flash tank is drawn from a horizontal tube, which is the case in the present work, then the flow conditions in that tube can also affect the performance of the vertical flash tank separator. The expansion length and flow pattern in the horizontal tube have been determined, and according to the outcomes of Chapter 6, an appropriate length of the inlet tube of the vertical flash tank separator has been identified as 300 mm. In this chapter, the height of the vertical flash tank separator will be changed to investigate its influence on the performance of the vertical separator using the same range of mass flow rates that was used for the horizontal pipe in the Chapter 6.

7.2 Performance of the vertical flash tank

The performance of the vertical flash tank separator is measured primarily by the liquid separation efficiency. In order to identify liquid separation efficiency for the vertical flash tank separators, the liquid mass flow rate at the inlet and liquid mass flow rate at the liquid outlet of the flash tank need to be measured. In addition, pressure and temperature at the inlet and outlets of the vertical flash tank separators were measured to estimate the vapour quality and enthalpy. The liquid separation efficiency can be calculated as a ratio between the liquid amount at the liquid outlet and the liquid amount at the inlet (Hanfei and Hrnjak, 2012).

$$\eta_L = \frac{\dot{m}_{L,outlet}}{\dot{m}_{L,inlet}} = \frac{\dot{m}_{L,outlet}}{\dot{m}_t(1-x)} \tag{7.1}$$

where

η_L = Liquid separation efficiency.

$\dot{m}_{L,outlet}$ = Liquid mass flow rate at the liquid outlet of separator (kg/s).

$\dot{m}_{L,inlet}$ = Liquid mass flow rate at inlet of separator (kg/s).

$\dot{m}_t$ = Total mass flow rate at the inlet of separator (kg/s).

x = Vapour quality at the inlet.

In the experiment, no vapour bubbles were visually detected within the column of liquid at the bottom of the flash tank at the liquid outlet. Thus, it is assumed that there was no vapour leaving the flash tank through the liquid outlet. Under these conditions, the liquid separation efficiency η_L is sufficient to specify the separation performance of the vertical flash tank separator.

7.3 Flow behaviour inside the vertical tank

7.3.1 Experiments

The experiments revealed that at low inlet mass flow rate, the liquid entered the separator at a sufficiently low velocity that the liquid stream fell towards the liquid outlet on entering the separator and there was no liquid stream impingement on the vertical side of the separator opposite the inlet. However, small liquid drops were still observed on the separator's wall and inlet pipe. When the inlet mass flow rate was increased, the liquid stream had a sufficiently high velocity that it impinged on the vertical wall of the flash tank separator as illustrated in Figure 7.1. Near the point where the liquid stream impinged the wall, some portion of the liquid stream was directed upward against gravity. The majority of the liquid that was initially directed upward due to the impact with the surface subsequently fell under gravity; the local upward velocity of the vapour is not sufficient to make a significant contribution to lifting the liquid phase against the downward gravity force as was the case in the work of Tuo and Hrnjak (2014*b*). Figures 7.2 to 7.6 present images of the observed two-phase flow inside the range of vertical flash tank separators at various inlet mass flow rates and with vapour quality of around 5 %. Precise definition of the flow conditions is found in Tables 4.6 and 4.7, Section 4.12, in Chapter 4.

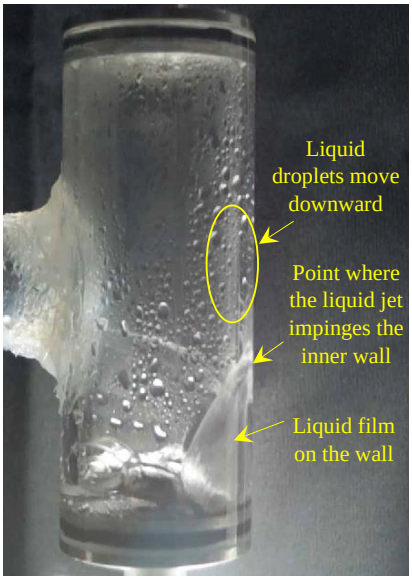

Figure 7.1: Photograph showing observed liquid film on the vertical wall of the separator and liquid droplets distributed mostly towards to the bottom of the separator (VFT-V2 at 23.4 ± 0.2 g/s).

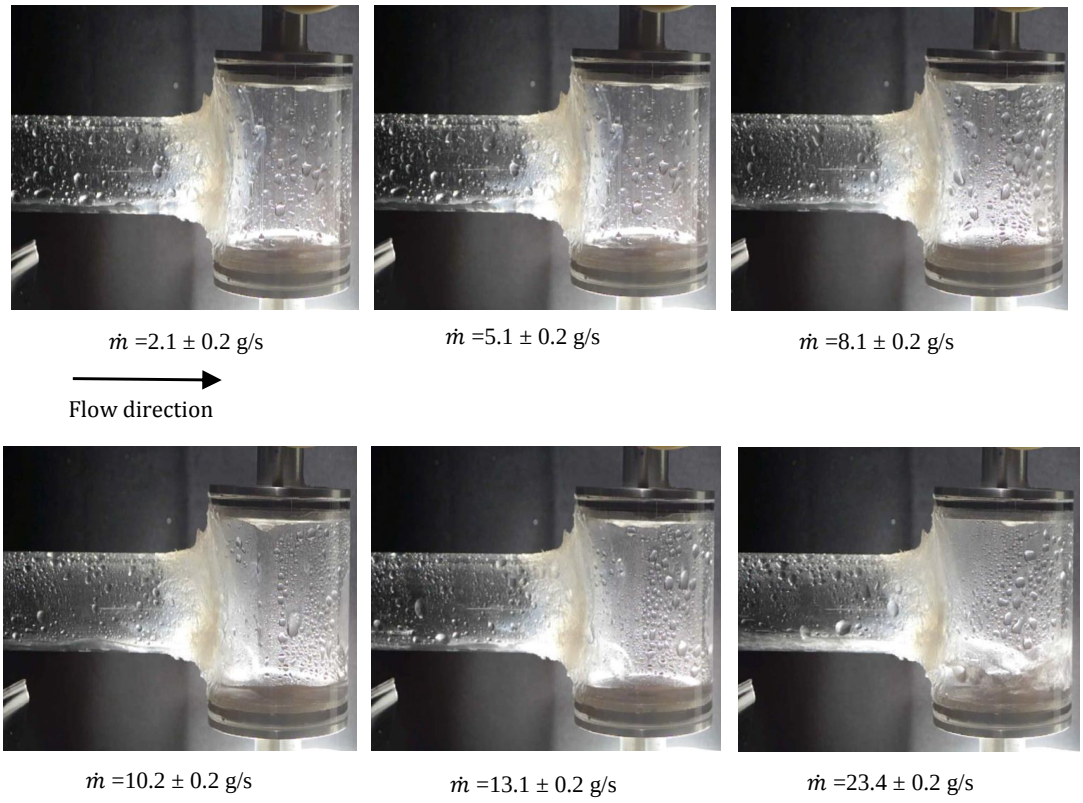

Figure 7.2: Observed two-phase flow in vertical flash tank separator VFT-V1. Inlet flow direction from left to right.

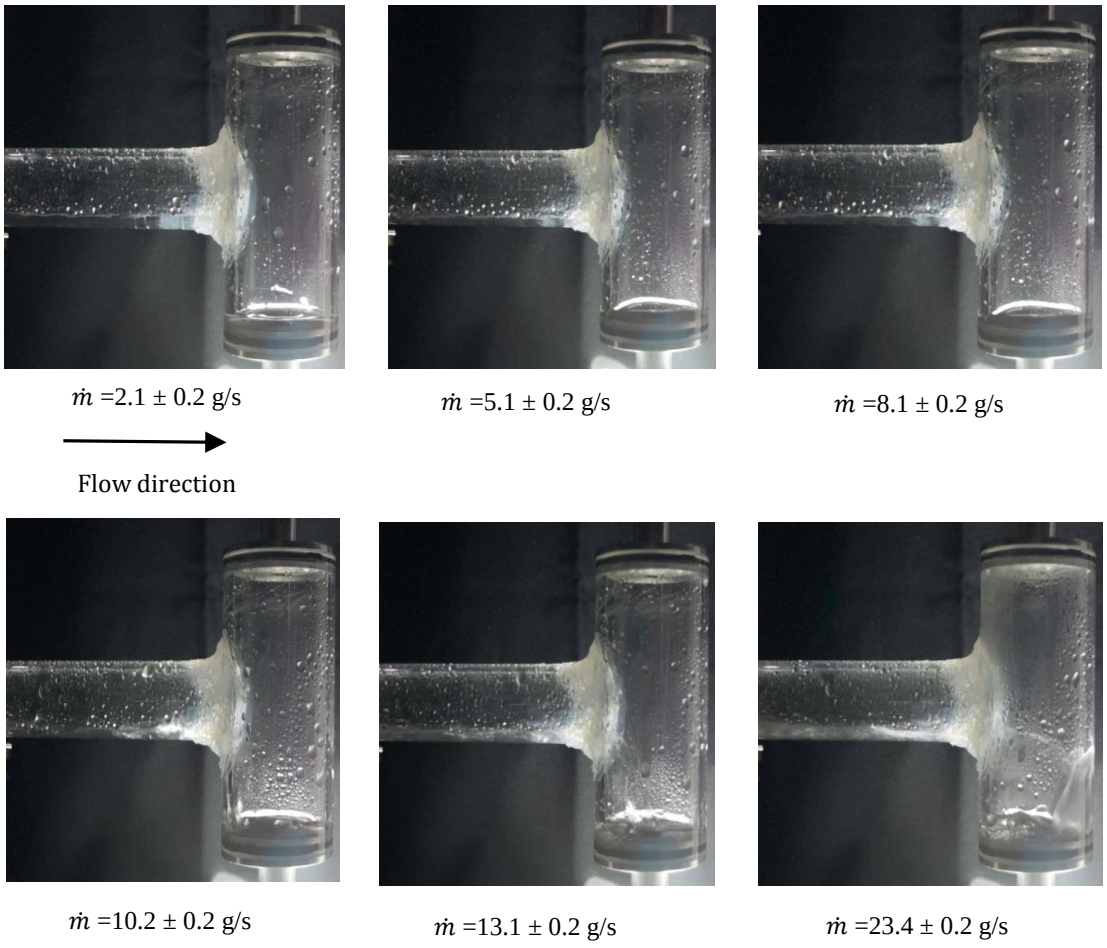

Figure 7.3: Observed two-phase flow in vertical flash tank separator VFT-V2. Inlet flow direction from left to right.

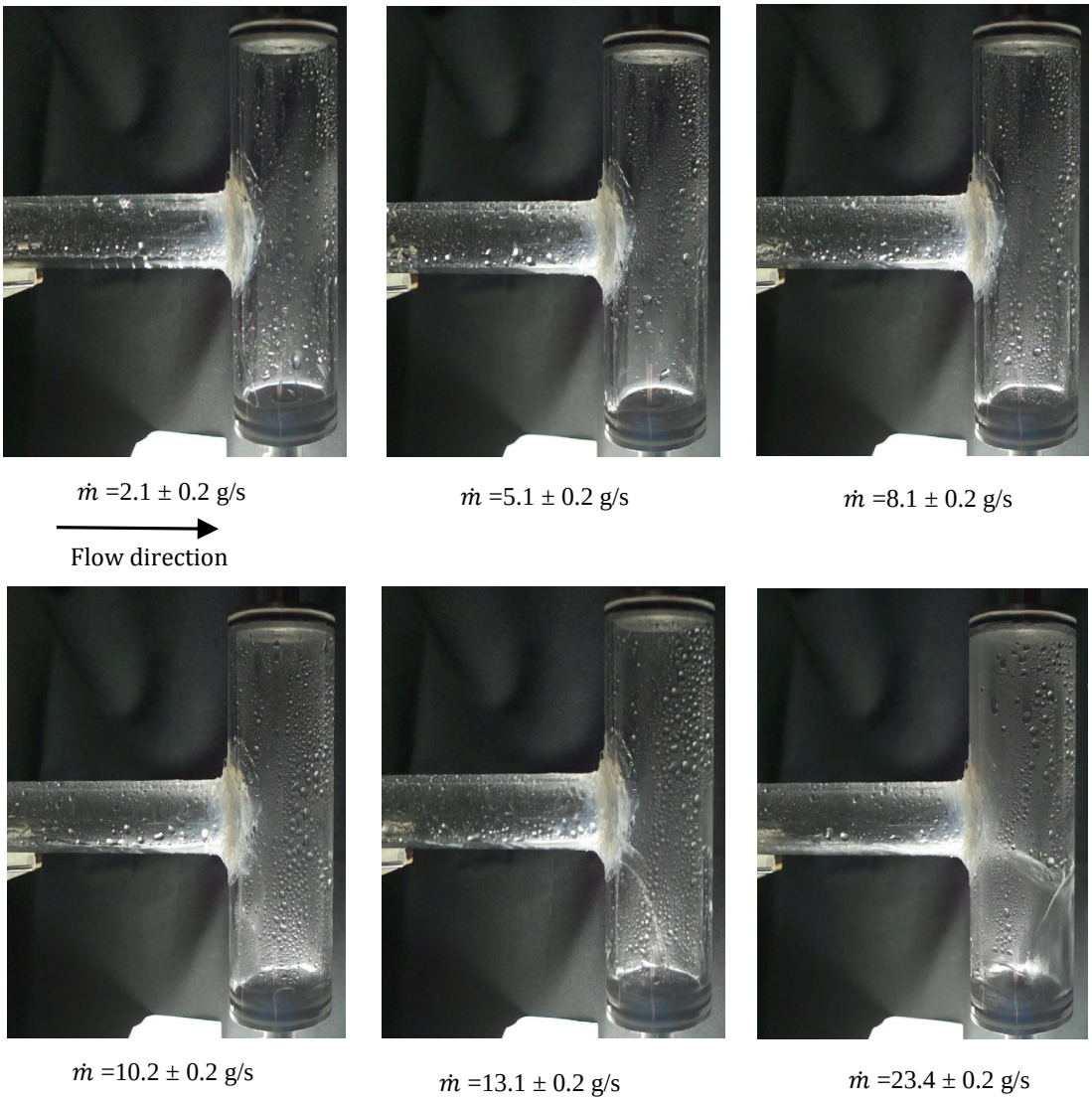

Figure 7.4: Observed two-phase flow in vertical flash tank separator VFT-V3. Inlet flow direction from left to right.

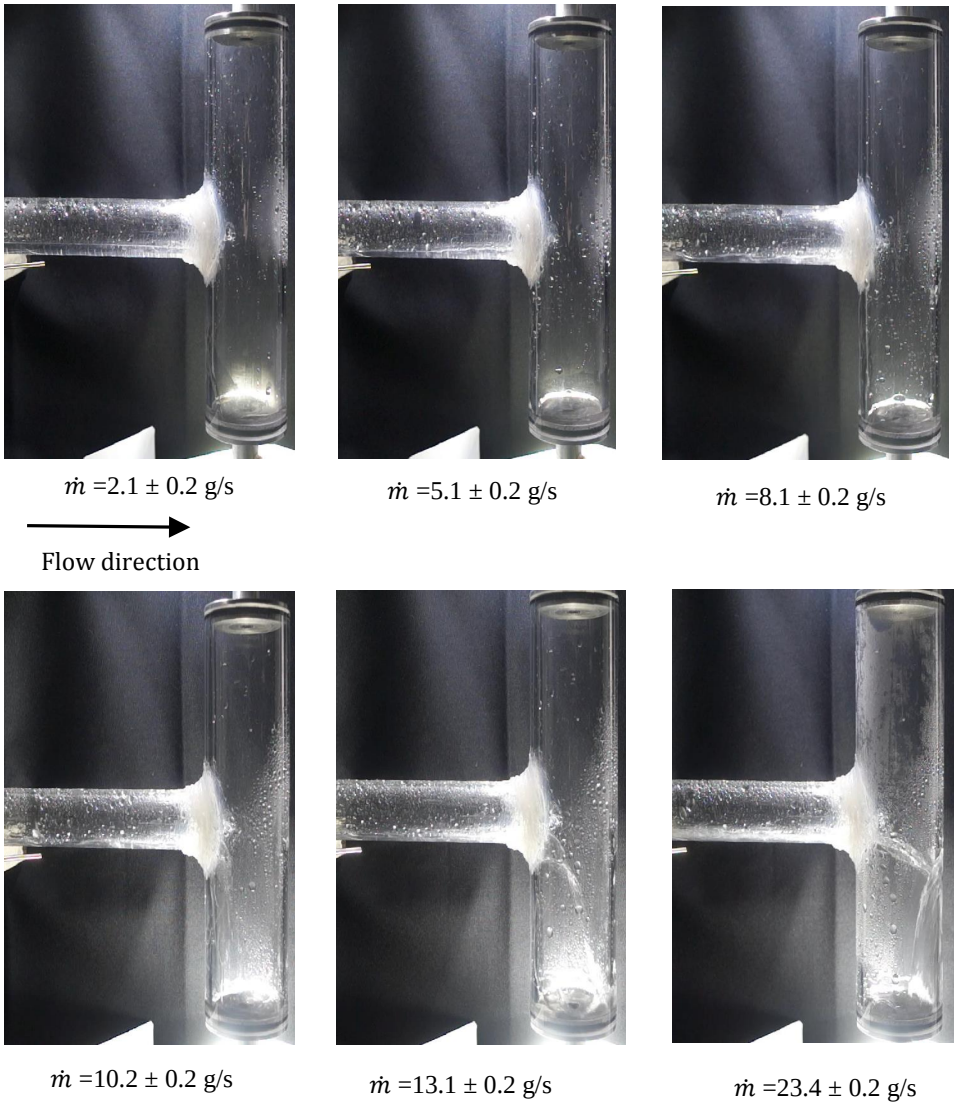

Figure 7.5: Observed two-phase flow in vertical flash tank separator VFT-V4. Inlet flow direction from left to right.

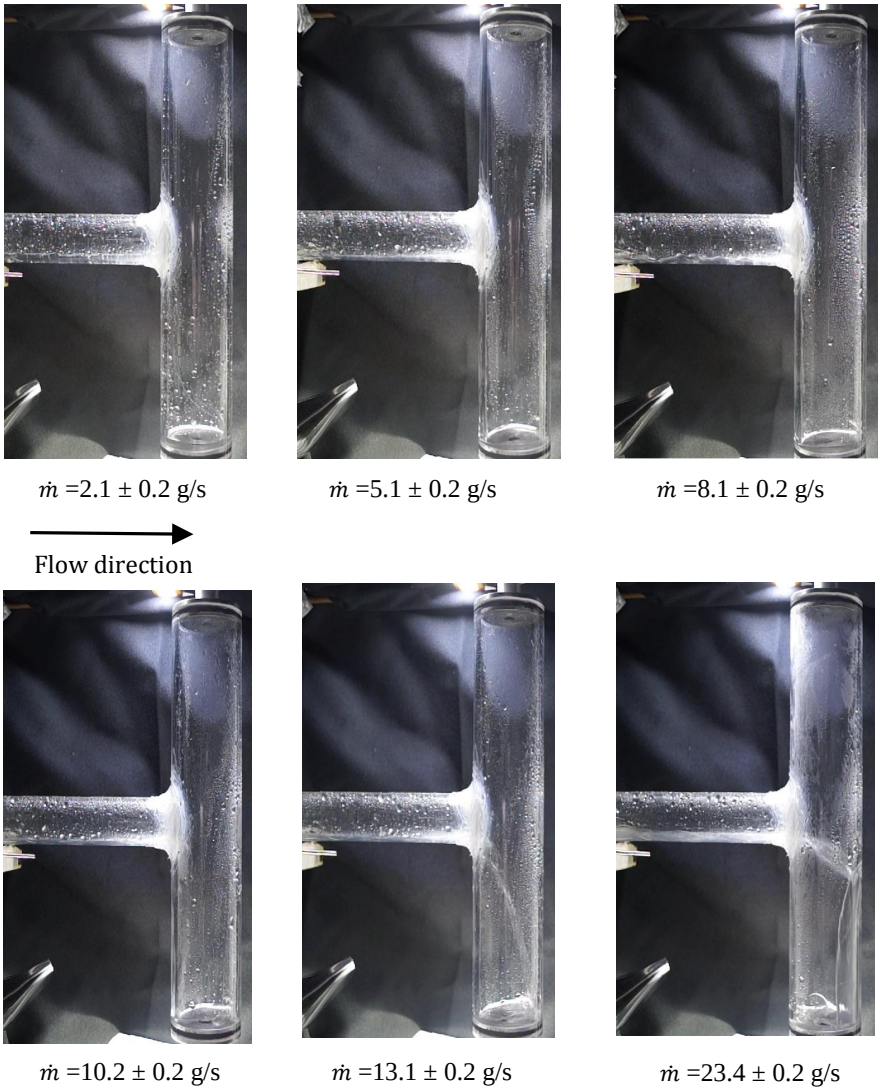

Figure 7.6: Observed two-phase flow in vertical flash tank separator VFT-V5. Inlet flow direction from left to right.

7.3.2 Numerical simulation

Numerical simulation (CFD) was performed using FLUENT version 17.1. Simulations were performed for all the models of the vertical flash tank separator by applying the boundary conditions defined from the experiments as presented in Chapter 4. As for the experiments, water was specified as the working fluid in the simulations. An Eulerian model with the Eulerian-Eularian approach was applied with the standard $k-\epsilon$ turbulent model for each phase. For further details on the methodology of the numerical simulations including convergence and mesh independence, see Chapter 5.

7.4 Comparison of numerical and experimental results

In this section, the numerical and experimental results are presented and compared for each model of the vertical flash tank separator. The results present the variation of the liquid separation efficiency of the vertical separator with the inlet mass velocity.

7.4.1 Effect of the mass flow rate

For each vertical tank, the mass flow rate was the only parameter that was changed in the experiment. Hence the variation of the liquid separation efficiency with the inlet mass velocity for different volumes of the vertical flash tank separator is presented in Figures 7.7 to 7.11. Generally, the results revealed that the liquid separation efficiency increased gradually as a result of increasing the inlet mass flow rate. The trend of the numerical results is similar to that in the experimental results and good agreement was observed between the numerical and experimental results. However, the simulations consistently underestimate the separation efficiency by an amount that varies between about 0.01 and 0.02. For example, in the highest separation efficiency, which was achieved by VFT-V5 at an inlet mass velocity of 44.23 kg/m^2·s, the experiment gave η_L=0.96 whereas the simulation indicated 0.94.

As the mass flow rate at the inlet and liquid outlet of the vertical tank were measured using mass flow meters, uncertainty of the mass flow rates measurement at the inlet and liquid outlet of the vertical tank directly affects uncertainty in the liquid separation efficiency. In the Figures 7.7 to 7.11, the error bars denote the estimated uncertainty of the efficiency due to the mass flow rate measurements from the experimental data. The highest value of the uncertainty in efficiency in the experiments for the vertical tank was about $\pm$ 0.058.

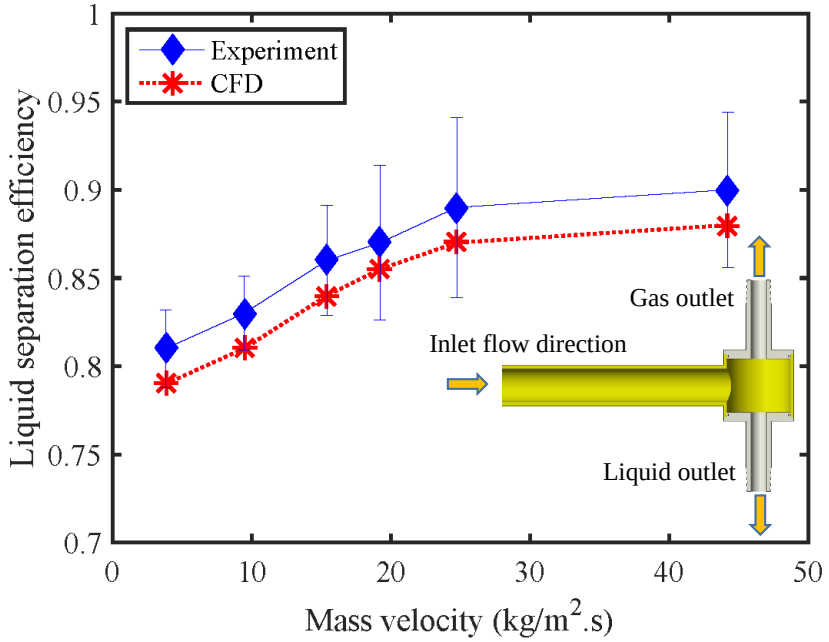

Figure 7.7: Numerical and experimental results for liquid separation efficiency with VFT-V1.

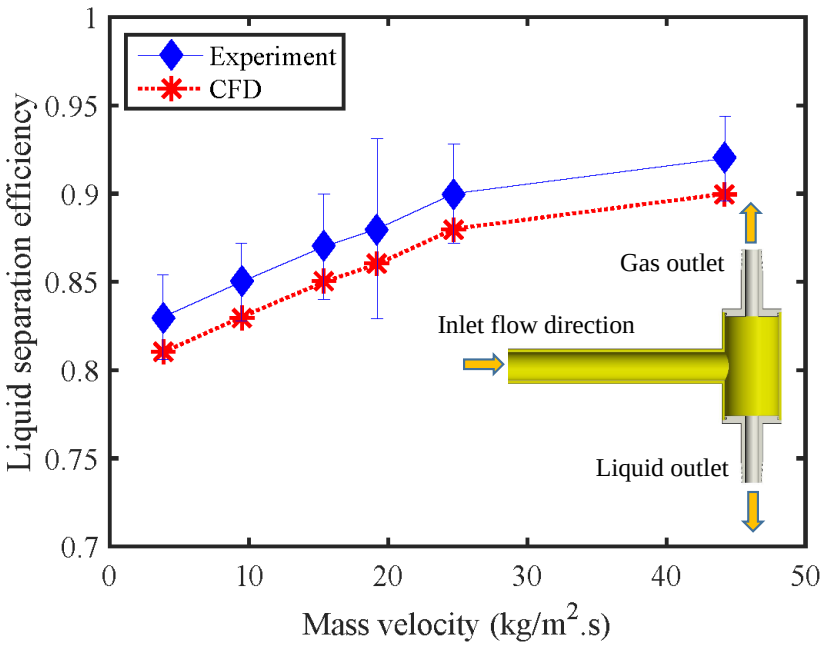

Figure 7.8: Numerical and experimental results for liquid separation efficiency with VFT-V2.

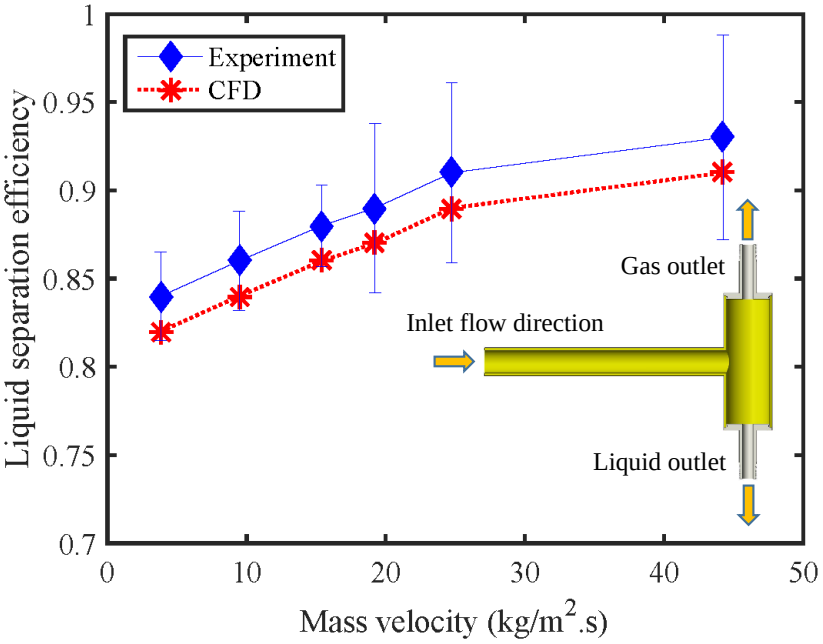

Figure 7.9: Numerical and experimental results for liquid separation efficiency with VFT-V3.

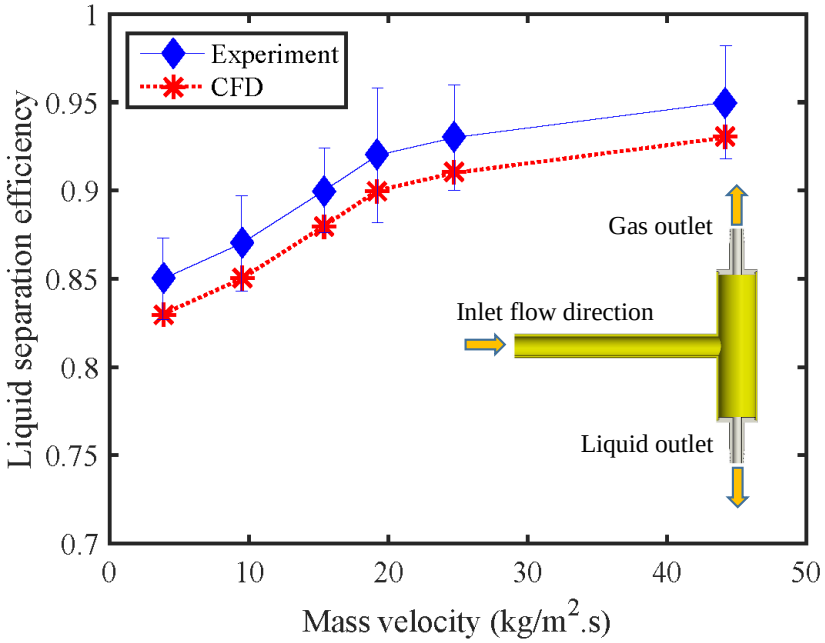

Figure 7.10: Numerical and experimental results for liquid separation efficiency with VFT-V4.

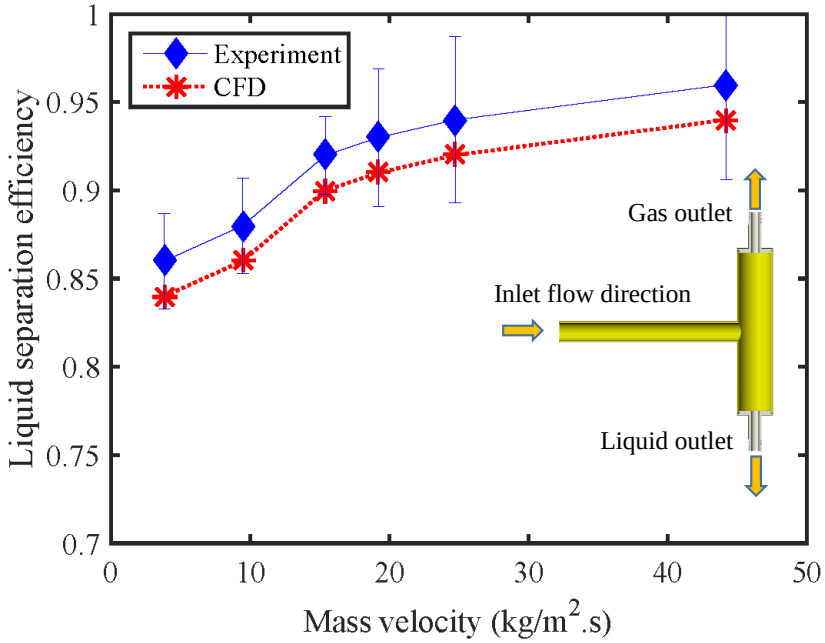

Figure 7.11: Numerical and experimental results for liquid separation efficiency with VFT-V5.

7.4.2 Effect of the height

Figure 7.12 compares the experimental results for liquid separation efficiency against the inlet mass flow rate for the different separators. The results revealed that the highest value of the liquid separation efficiency was achieved by VFT-V5. The lowest efficiency was recorded for the VFT-V1 over the same range of the inlet mass flow rate. Figure 7.13 presents a comparison of numerical results for liquid separation efficiency. The numerical results demonstrated the same trend and behaviour as the experimental results.

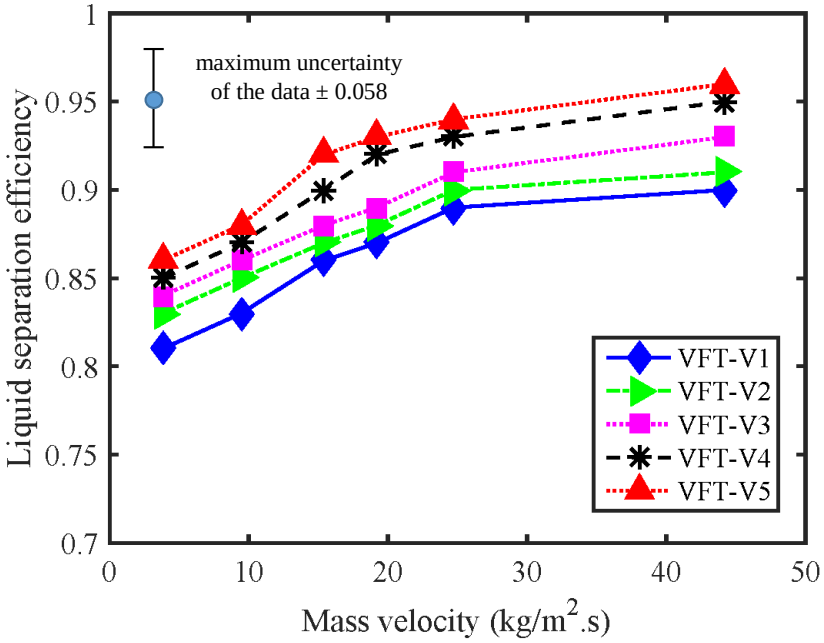

Figure 7.12: Comparison of experimental results for liquid separation efficiency for the various separators as a function of inlet mass velocity.

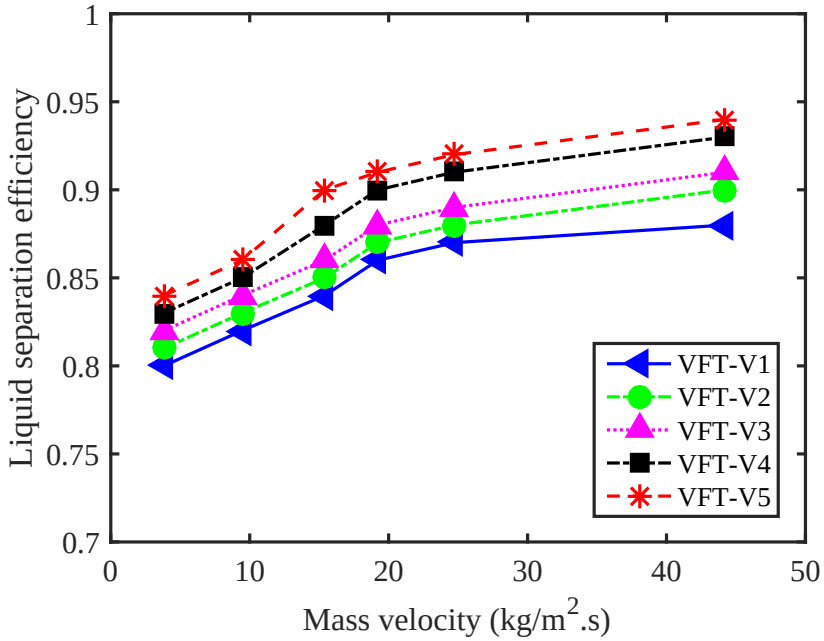

Figure 7.13: Comparison of numerical results for liquid separation efficiency for the various separators as a function of inlet mass velocity.

7.4.3 Vapour quality at the vapour outlet

The vapour state at the gas outlet of the vertical flash tank separator is described by its vapour quality. In the present work, the vapour quality was calculated based on the measured parameters from the experiments such as the mass flow rate and pressure. In order to calculate the total mass flow rate at the gas outlet of the vertical tank, the mass continuity equation was used

$$\dot{m}_{t,G,out} = \dot{m}_t - \dot{m}_{t,L,out} \tag{7.2}$$

where $\dot{m}_t$ is the total mass flow rate at the inlet of separator which was measured by the Yokogwa flow meter and $\dot{m}_{t,Lout}$ is the total mass flow rate at the liquid outlet of separator which was measured by the Siemens flow meter. The vapour quality at the gas outlet can be calculated as a ratio between the vapour mass flow rate to the total mass flow rate that flows through the gas outlet of the vertical flash tank (Elbel and Hrnjak, 2004).

$$x_3 = \frac{\dot{m}_g}{\dot{m}_{t,Gout}} \tag{7.3}$$

where the $\dot{m}_g$ is the vapour mass flow rate that can be calculated from the total inlet mass flow rate and vapour quality at the inlet of the vertical flash tank separator

$$\dot{m}_g = \dot{m}_t x_1 \tag{7.4}$$

where the x_1 is the vapour quality at the inlet of the vertical flash tank. Figure 7.14 presents a comparison of the outlet vapour quality for the different vertical separators as a function of the inlet mass velocity. As can be seen from Figure 7.14, the highest value of the vapour quality was recorded for VFT-V5 and the lowest value was recorded for VFT-V1, with the vapour quality increasing gradually as the inlet mass flow rate is increased. The mass flow rates at the inlet and liquid outlet of the vertical separator were measured by flow meters and uncertainties in these measurements have a direct impact on the uncertainty in the deduced vapour quality at the gas outlet. The highest value of uncertainty has been added to the figure. The results revealed that the outlet flow at the gas outlet was not 100 % vapour, so there are some liquid drops moving with the vapour through the gas outlet of the separator.

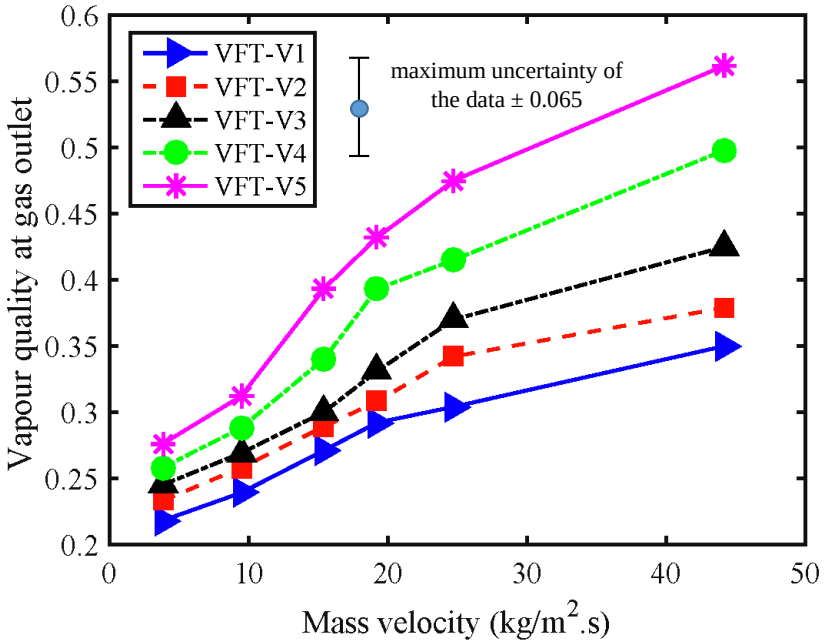

Figure 7.14: Vapour quality at the vapour outlet of the vertical flash tank separator. Results derived from experimental data.

7.5 Effect of d/D ratio

Experiments were only performed with inlet pipe diameters of $d = 25$ mm and separator diameters of $D = 50$ mm. However, because the CFD offered a good simulation of the experimental results, additional simulations were performed to examine the effect of changing the value of aspect ratio, d/D. The simulation strategy followed the methodology described previously in Chapter 5. As the highest value of the liquid separation efficiency in the experiments was achieved by VFT-V5, the VFT-V5 base-line configuration was used to investigate the effect of the d/D ratio. Table 7.1 shows the dimensions of the model geometries for investigation of the different values of d/D. Figure 7.15 shows the configurations of the model geometries that were created.

Table 7.1: Dimensions of the model geometries for investigation of the d/D ratio.

Design	d (mm)	D (mm)	$d_{L,out}$ (mm)	$d_{G,out}$ (mm)	d/D	Notes
VFT-V5-d/D-0.25	25	100	10	10	0.25	simulation only
VFT-V5-d/D-0.5	25	50	10	10	0.5	base-line used in experiments and simulations
VFT-V5-d/D-1	25	25	10	10	1	simulation only

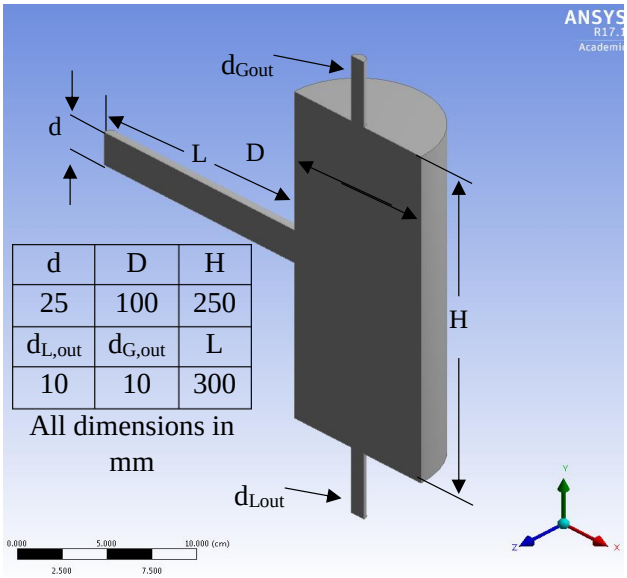

VFT-V5-d/D-0.25

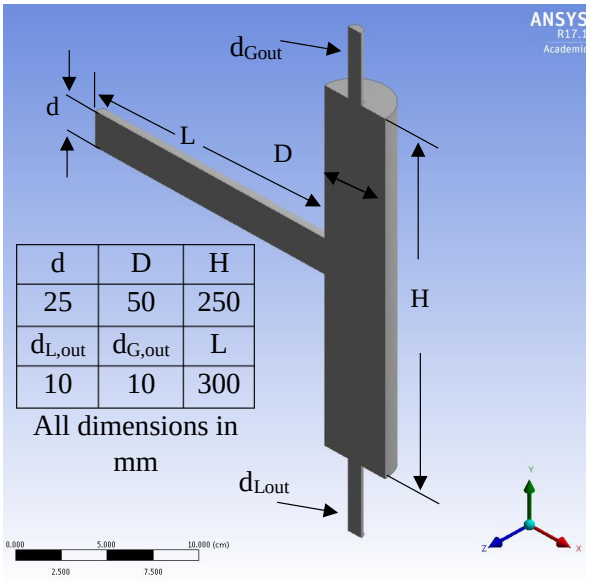

VFT-V5-d/D-0.5

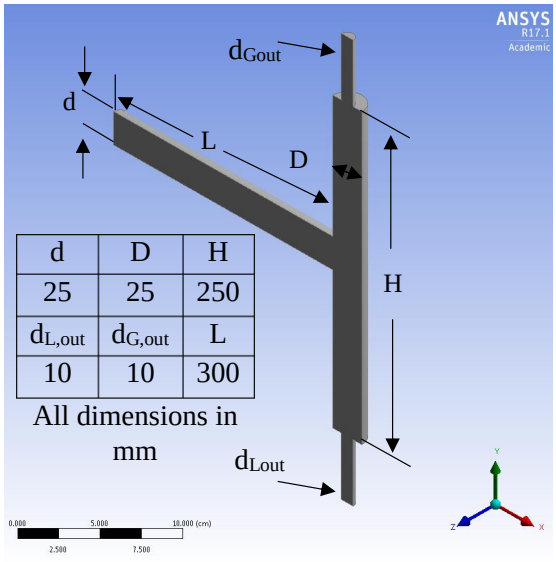

VFT-V5-d/D-1

Figure 7.15: Configuration of model geometries with d/D= 0.25, 0.5 and 1.

Figure 7.16 presents the results from the CFD simulations of the three ratios of d/D. The liquid separation efficiency for $d/D = 1$ decreases with increasing mass flow rate, a result which is the same as that obtained by Hanfei and Hrnjak (2012). The reason for this effect is that when the mass flow rate increased, the two-phase velocities increase and a point is reached where the liquid inertia force and vapour drag force gradually dominate the gravitational force (Hanfei and Hrnjak, 2012). When a portion of the incoming liquid stream diverts into the upward direction after impingement on the wall, a portion of separator's cross-section area is further reduced, and consequently the local velocity of the vapour increases and thus, the drag force also increases. Therefore, as more liquid moves with the gas through the gas outlet for $d/D = 1$, the liquid separation efficiency is decreased. For $d/D = 0.25$, the liquid separation efficiency is about 3.5 % higher than that for $d/D = 0.5$. In both cases, the efficiency increases with increasing mass flow rate.

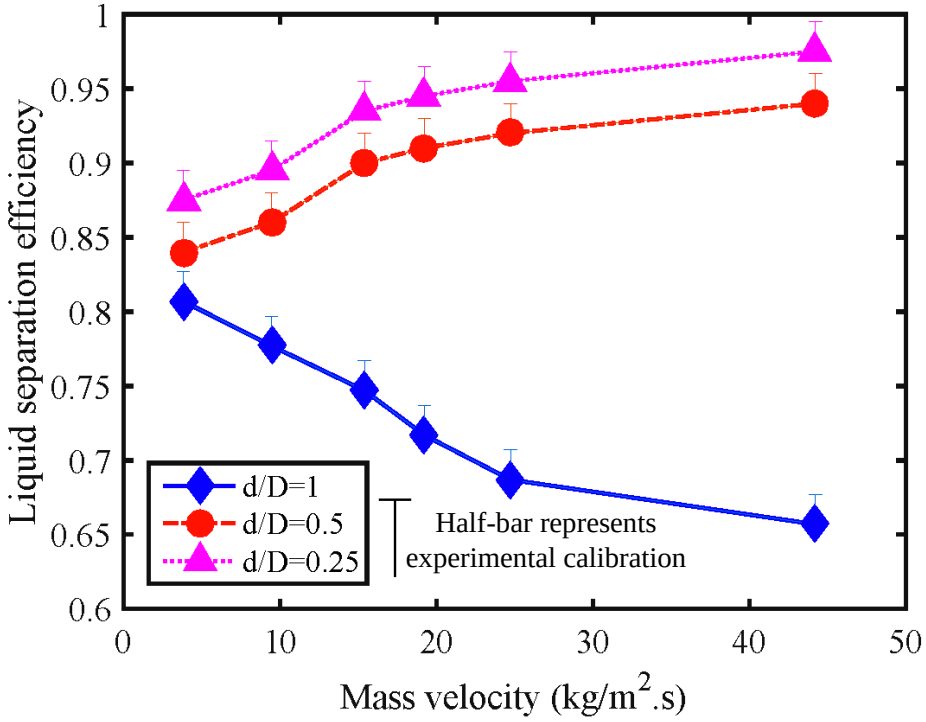

Figure 7.16: Comparison of numerical results showing the effect of d/D ratio.

According to the comparison between the experimental and numerical results of the VFT-V5 (Figure 7.11), the CFD underestimated the data by about 0.02. This value has been used as a calibration offset for the results of the virtual experiment and so the half-bars on the Figure 7.16 represents the expected increase in efficiency if physical experiments were actually performed.

Although VFT-V5 with $d/D = 0.25$ offers superior performance, the VFT-V5 configuration with $d/D = 0.5$ was used for testing the enhanced design options to improve the efficiency of the liquid separation for two reasons. Firstly, the behaviour of the separation efficiency for $d/D = 0.25$ is very similar to $d/D = 0.5$, only the $d/D = 0.25$ gives 3.5 % improvement in efficiency relative to $d/D = 0.5$. Secondly, as the VFT-V5 with $d/D = 0.5$ already exists with its components and accessories such as the aluminium flanges and its O-ring, the extra costs to perform the experiments on $d/D = 0.5$ were only marginal.

7.6 Empirical correlation

Reynolds, Weber and Froude numbers for both liquid and gas phases have been used to present the experimental result, and in addition the two-phase version of these numbers Re_{TP}, We_{TP} and Fr_{TP} have been used to correlate the experimental results. In order to interpret the experimental operating conditions and their effects on the two-phase flow behaviour in the vertical flash tank separator, all of the dimensionless numbers have been calculated according to the operating boundary conditions. Chapter 3 presented the definitions of the dimensionless numbers of the liquid and gas phase, including the two-phase numbers. Figure 7.17 presents the experimental results of the liquid separation efficiency against the dimensionless numbers of the gas and liquid phases. Figure 7.18 presents the variation of the liquid separation efficiency with the two-phase dimensionless numbers.

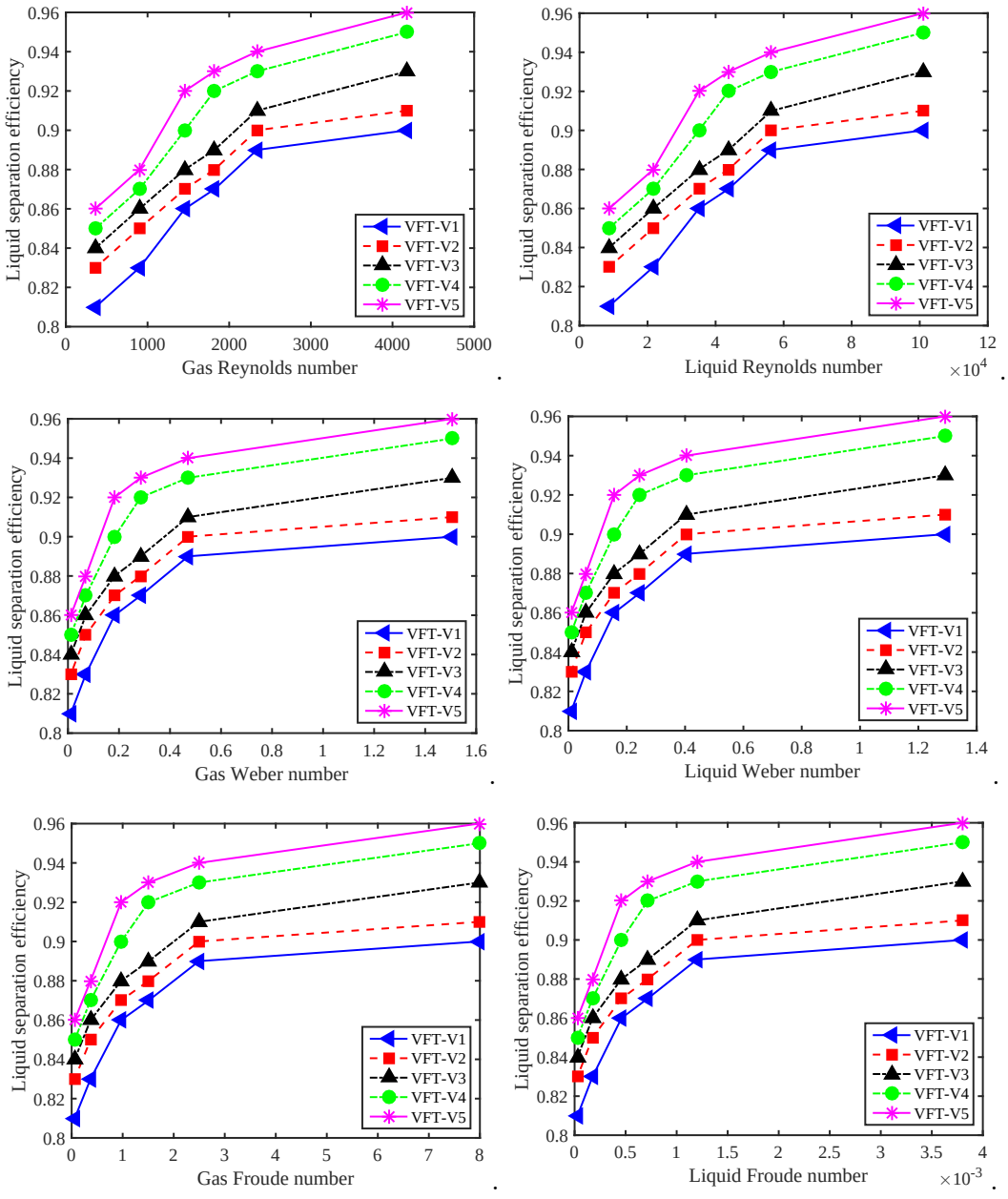

Figure 7.17: Liquid separation efficiency as a function of dimensionless numbers.

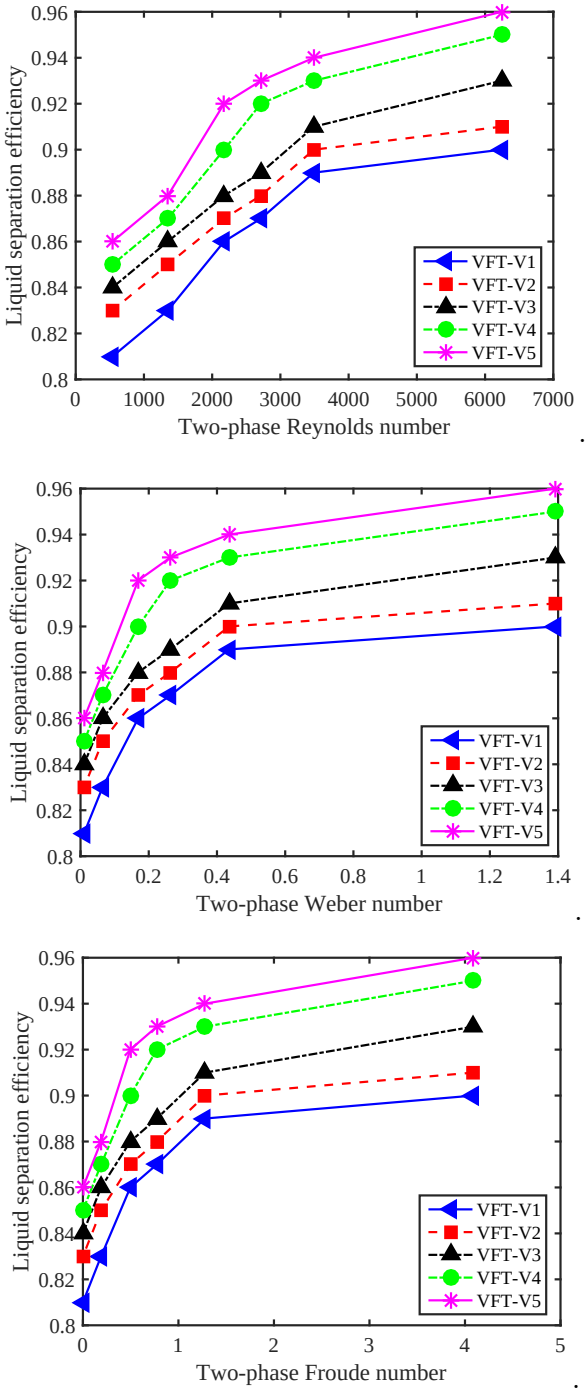

Figure 7.18: Liquid separation efficiency as a function of two-phase dimensionless numbers.

Based on the experimental data, an empirical correlation was developed for the liquid separation efficiency of the vertical flash tank separator as a function of the two-phase dimensionless numbers and aspect ratio of the separator: Re_{TP} , Fr_{TP}, We_{TP} and

As_{FT}. The correlation was assumed to be in the form

$$\eta_L = A1\ Re_{TP}^{A2}\ We_{TP}^{A3}\ Fr_{TP}^{A4}\ As_{FT}^{A5} \tag{7.5}$$

where, η_L is the liquid separation efficiency, Re_{TP} is the two-phase Rynolds number, We_{TP} is the two-phase Weber number, Fr_{TP} is the two-phase Froude number, As_{FT} is the aspect ratio of the separator and A1, A2, A3, A4, and A5 are the coefficients to be estimated. Using nonlinear estimation analysis in a software called STATISTICA version 10, the coefficients were estimated.

Based on the estimated coefficients, the correlation is

$$\eta_L = 0.01056\ Re_{TP}^{0.01016}\ We_{TP}^{-1.62583}\ Fr_{TP}^{1.6469}\ As_{FT}^{0.03833} \tag{7.6}$$

with $R^2 = 0.91$, which is a rather low value. Therefore, many attempts were made to obtain higher values of R^2, with additional coefficients added to the above model to improve its accuracy. The final form of the assumed model is

$$\eta_L = A1 + Re_{TP}^{A2}\ We_{TP}^{A3}\ Fr_{TP}^{A4}\ As_{FT}^{A5} \tag{7.7}$$

and repeating the estimation process in nonlinear estimation, the new values of the estimated coefficients were obtained.

$$\eta_L = -4.64 + Re_{TP}^{0.0069}\ We_{TP}^{-0.692}\ Fr_{TP}^{0.694} As_{FT}^{0.0061} \tag{7.8}$$

with $R^2 = 0.98$, the above model was tested to predict the liquid separation efficiency based on the experimental operating conditions as shown in Figure 7.19, which presents a comparison between the predicted values and the observed results of the liquid separation efficiency based on the experimental operating conditions of the present work.

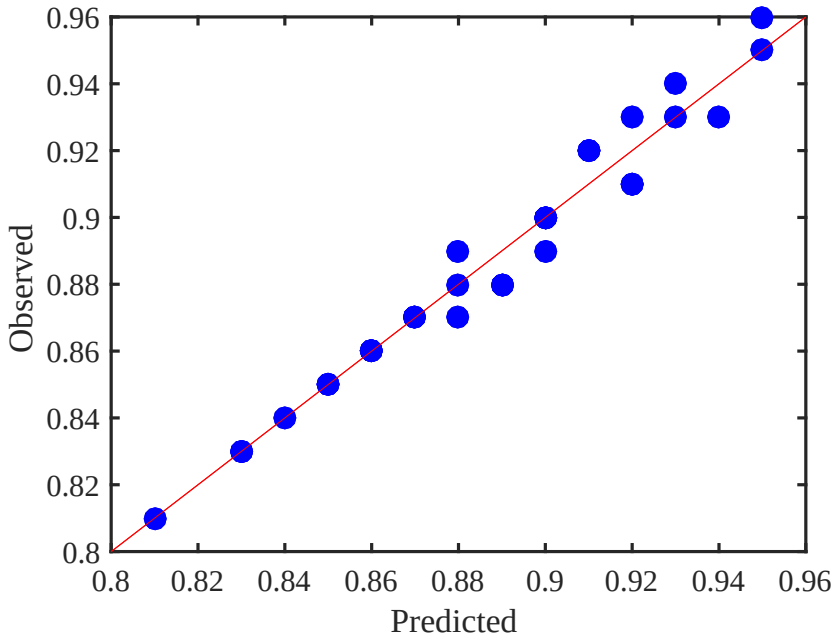

Figure 7.19: Comparison between the predicted value and the observed results of the liquid separation efficiency.

7.7 Conclusion

Numerical and experimental investigations of the liquid separation efficiency of a vertical flash tank separator have been performed for a range of different separator heights and mass flow rates. Outcomes can be summarized as below.

1. The highest value of the liquid separation efficiency was achieved by the VFT-V5 configuration, which has the largest height.

2. For any given tank, the inlet mass flow rate has a significant effect on the liquid separation efficiency and vapour quality which increase with increasing mass flow rate.

3. The highest values of the vapour quality were achieved by the VFT-V5 configuration and these values varied from 0.27 to 0.56.

4. Liquid stream impingement on the inner side of the separator increased when the inlet mass flow rate increased.

5. All the experimental results of the liquid separation efficiency using the different sizes of the vertical separator have been compared with the numerical results at the same operating condition. The simulations underestimated the liquid separation efficiency by approximately 0.02 over the range of conditions tested.

6. Through CFD virtual experiments, the d/D ratio is demonstrated to have a significant effect on the liquid separation efficiency. The liquid separation efficiency is decreased when the d/D ratio is increased.

7. An empirical correlation with $R^2 = 0.98$ was developed to predict the liquid separation efficiency based on the experimental data.

Chapter 8

Enhancement of a vertical flash tank separator

8.1 Introduction

Chapter 7 presented experimental results of liquid separation efficiency for different heights of a vertical flash tank separator using water as the working fluid. Experimental results revealed that the highest value of the liquid separation efficiency was 96 % and this was achieved by the VFT-V5 with a flow rate of 23.4 g/s. However, further improvement in the VFT-V5 performance is possible. CFD was used to evaluate design options for modifying the VFT-V5 and then the proposed design options have been experimentally investigated and their performance compared with the CFD results.

8.2 Performance enhancement techniques

There are many ways to enhance the performance of a separator including the introduction of inlet devices, wire meshes and mist extractors, GPSA (2004). Inlet devices reduce the momentum of the inlet stream and enhance the flow distribution of the gas and liquid phases inside the separator. The inlet device can be a diverter plate, half-pipe or vane, GPSA (2004). A wire mesh and mist extractor can be used to separate the liquid drops that move with the gas through the gas outlet as it is not economic to separate these drops by gravity alone by making the separator larger (Grodal and Realff, 1999). Figure 8.1 shows a mist extractor and an inlet diverter in a vertical separator.

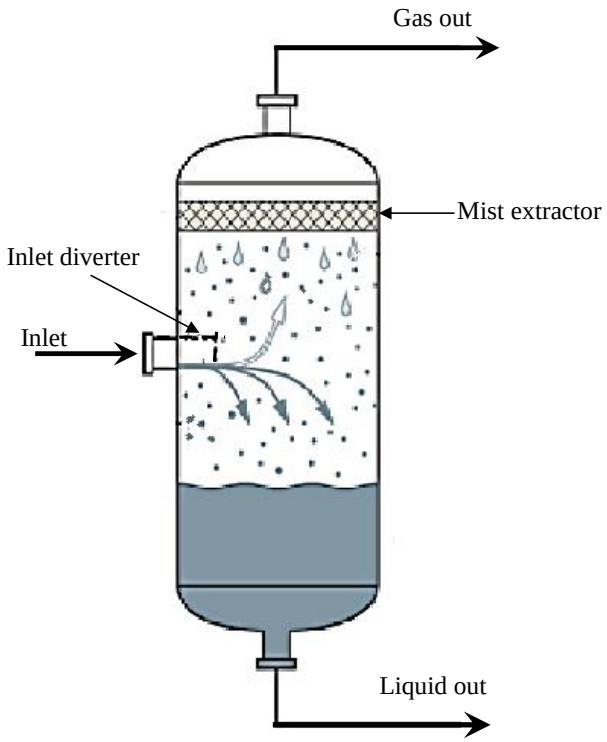

Figure 8.1: Typical inlet diverter and mist extractor in a vertical separator, adapted from Campbell (2014).

Correlations or design rules for extractors do not currently exist. Many studies discuss the function of extractors, but do not offer design advice. In the present work, CFD was used to obtain suitable dimensions for the extractor and the position of the inlet pipe based on the operating mass flow rate and the size of the separator.

8.3 Enhancement options

Four methods have been investigated to improve the performance of the VFT-V5: add an extractor to the gas outlet; re-locate the inlet tube to protrude into the separator's body; use an inlet flow diverter; and finally, add the gas extractor to the configuration with the inlet diverter. To assess the enhancement design options, CFD was used to simulate the flow before the experiments were performed.

8.4 Procedure of the CFD assessment

The CFD simulations were performed using the CFD methodology and assumptions that are described in Chapter 5. The numerical results of the enhancement options were compared with the numerical results of the unmodified VFT-V5. The results revealed that the proposed enhancement options all improved the performance. The results revealed that the modification in which the inlet flow direction is changed has the most dramatic effect on the liquid separation efficiency.
The proposed enhancement options were fabricated according to the geometry tested in the CFD simulations. After finishing the experiments, the numerical simulations were run again using the actual boundary conditions that were defined from the experimental measurements. Only CFD results from the post-experiment simulations are presented in this chapter.

8.5 Experimental arrangement

The proposed enhancement options were fabricated for integration into the existing hardware. The equipment and settings that were used in Chapter 7, have again been used for this work. Modifications to the vertical flash tank necessary for the present work are presented in this section.

8.5.1 Inlet pipe supporter

An inlet pipe supporter with an O-ring was designed and used in all geometries of the enhancement options to support the inlet pipe and provide good sealing. Figure 8.2 shows the inlet pipe supporter configuration and its dimensions. The inlet pipe supporter was 3D printed using PolyLactic Acid (PLA) material. The supporter was bonded to the vertical pipe using a room temperature vulcanization (RTV) silicone.

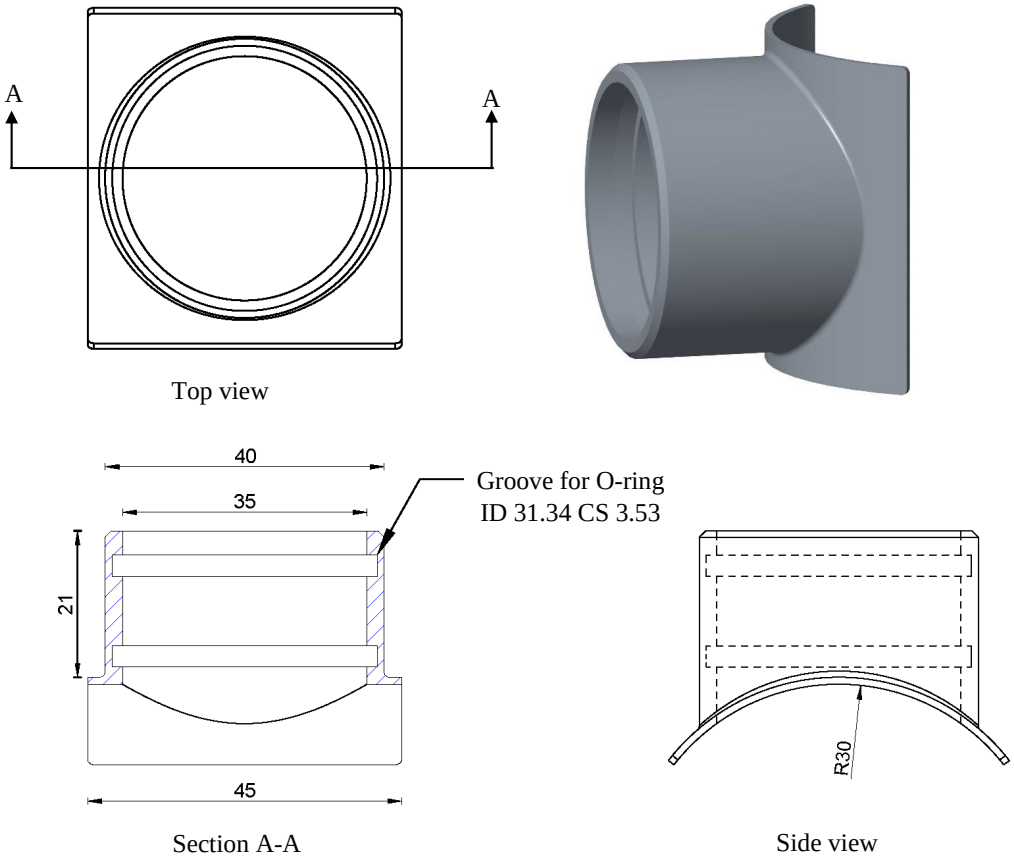

Figure 8.2: Inlet pipe supporter with O-ring grooves.

8.5.2 Operating conditions and measurements

The operating conditions of all the experiments covered the mass flow rate range from 2.1 to 23.4 ± 0.2 g/s and the corresponding vapour quality was in the vicinity of 5%. For the measurement and data recording, two mass flow rate meters have been used: one at the liquid outlet to measure the separated liquid mass flow rate and the second at the inlet of the separator to measure the total mass flow rate. A camera, type Sony Alpha model 57A was used to record video of flow. Details the measurement apparatus, experimental equipment, and operating conditions are presented in Chapter 5.

8.6 Design enhancements

Four new proposed additions to the geometry of the basic VFT-V5 arrangement were fabricated with guidance from the CFD simulations. The geometry of each enhancement option and the resulting performance increase are described in this section.

8.6.1 Extractor at the gas outlet of the VFT-V5

This proposed design option is designated VFT-V5-EXR and involves the addition of an extractor inside the VFT-V5 separator at the gas outlet. The extractor is a very simple design according to Campbell (2014), and it is used to extract or eliminate the liquid drops that move with the gas through the gas outlet. However, a special proposed design of an extractor was used in the present work. The dimensions of the proposed extractor were finalised using CFD simulation in order to obtain a high separation performance. A range of the extractor diameters was simulated in CFD, and according to the highest predicted liquid separation efficiency, a 18.53 mm radius was selected. Figure 8.3 presents the final dimensions of the proposed design. The extractor was printed using PolyLactic Acid (PLA) material. The extractor was connected to the top flange of the gas flow outlet after machining the inside diameter of the existing flange to fit the 12 mm diameter and the 20 mm long spigot of the printed extractor. Figure 8.4 shows the configuration of VFT-V5-EXR and the position of the extractor through

a section view from a 3D model. The VFT-V5EXR was installed in the experimental apparatus and tested under the experiment operating conditions described in Chapter 4.

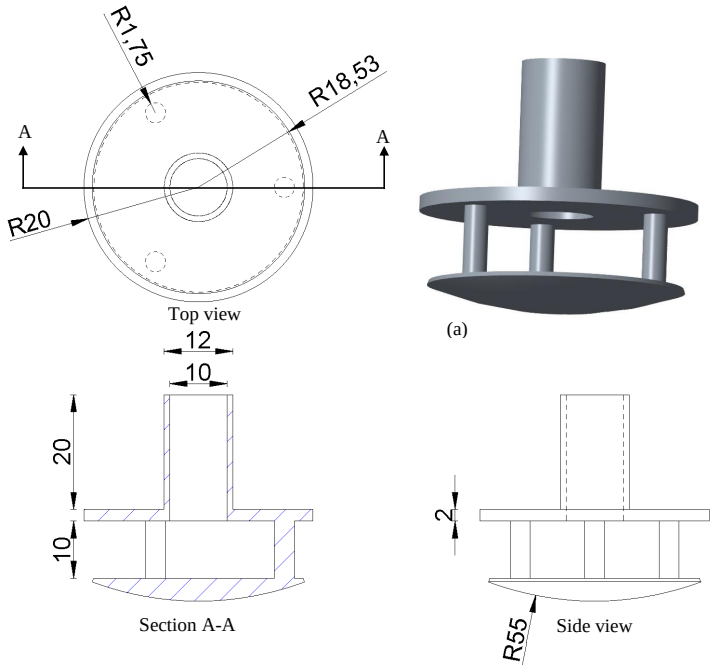

Figure 8.3: Dimensions and illustration of the extractor.

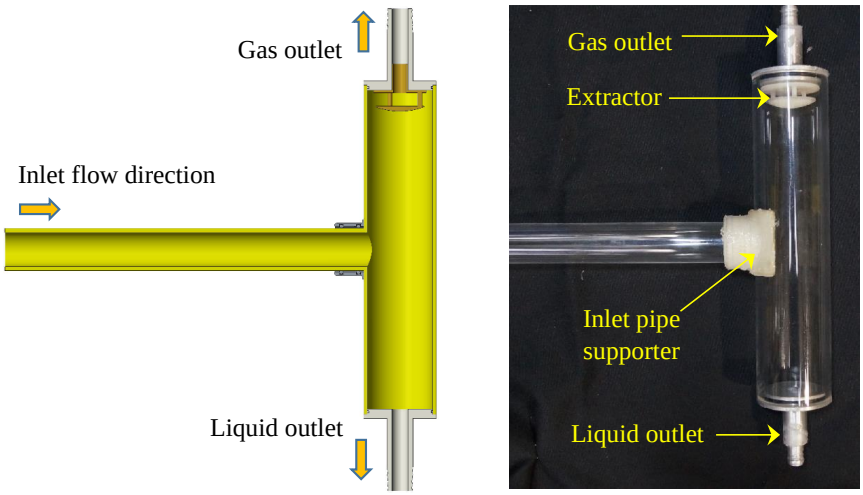

Figure 8.4: Configuration of VFT-V5-EXR: (a) section view from 3d model, (b) photograph of the assembly.

Figure 8.5 presents the numerical and experimental results for the liquid separation efficiency of the VFT-V5-EXR. The CFD gives the same trend as the experiment, but has a lower magnitude by about 0.02. The extractor affects liquid drops that move with the gas towards the gas outlet by causing impingement of liquid drops onto the extractor followed by coalescence into droplets large enough to disengage from the bottom of the extractor and drop through the rising gas flow into the liquid holding part of the separator as shown in Figure 8.6. Figure 8.7 presents the images of VFT-V5-EXR at the different operating conditions. As can be seen, in each case there are some liquid drops on the inner wall of the upper half of the separator due to the drag force effect and impingement of the incoming stream. The observed flow pattern at the inlet of the vertical separator was stratified flow at all of these operating conditions.

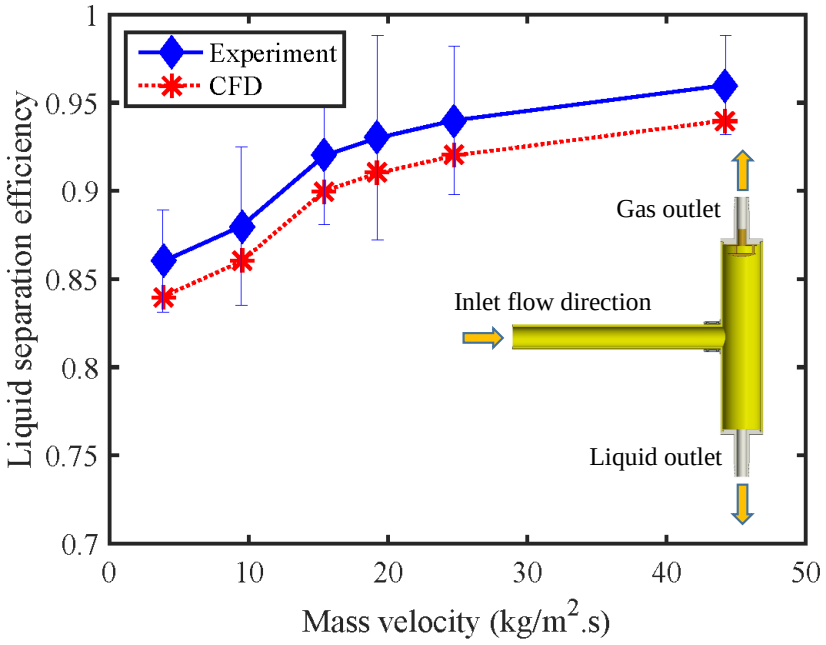

Figure 8.5: Comparison between CFD and experimental results for VFT-V5-EXR.

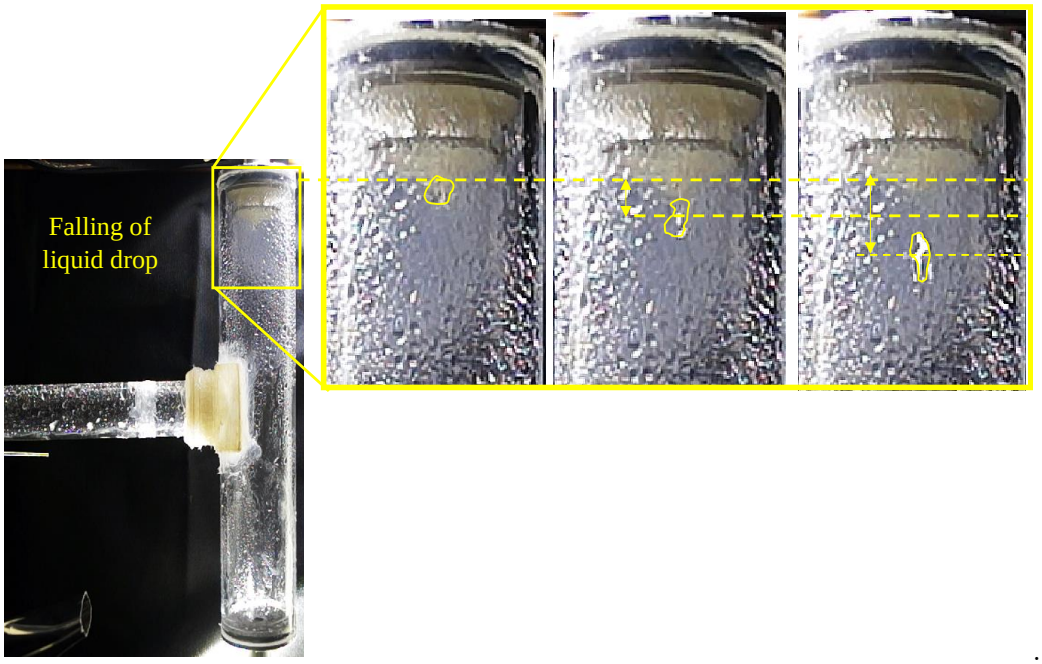

(a)

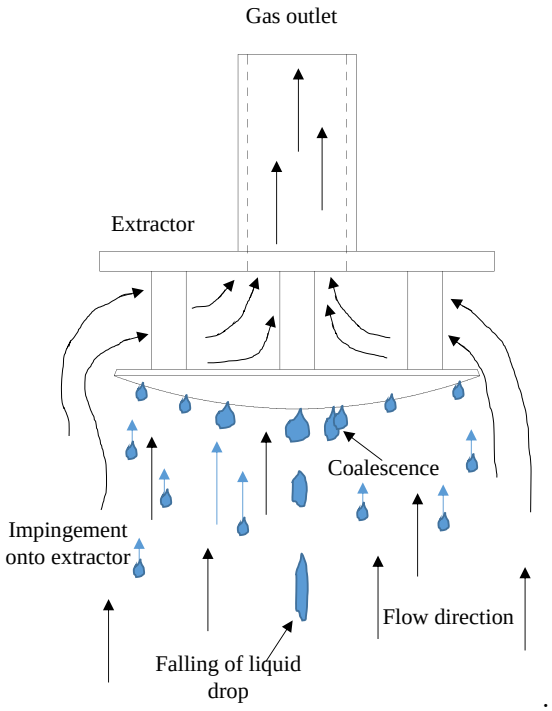

(b)

Figure 8.6: Impingement of droplets coalescence, and detachment. (a) sequence of frames showing a liquid drop falling; (b) sketch illustrating the key processes in the extractor.

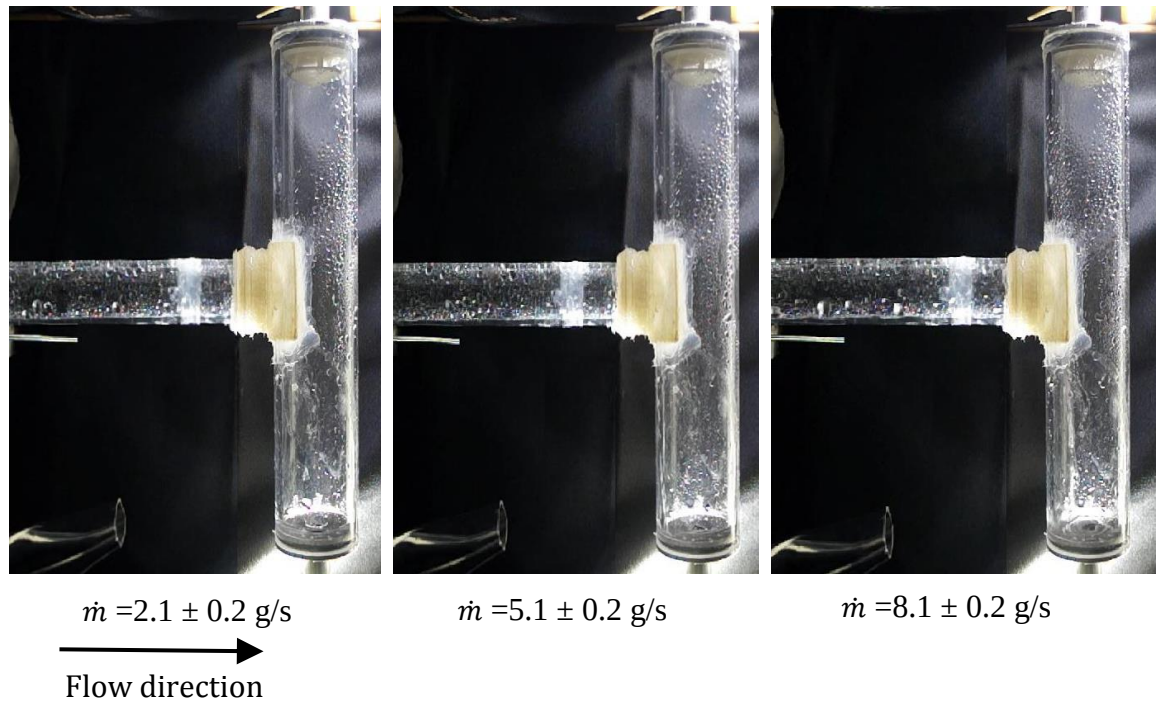

Figure 8.7: Images of the modified vertical flash tank separator VFT-V5-EXR during operation. Inlet flow direction from left to right.

8.6.2 Inlet moved inside separator

The second enhancement option was created by changing the position of the inlet pipe. The end of inlet pipe was moved inside and positioned 15 mm away from the opposite wall of the separator. In this arrangement there is no extractor at the top of the separator on the gas outlet, and this configuration is designated VFT-V5-INT. CFD was use to simulate a range of the inlet pipe positions using a mass flow rate of 13.1 g/s. According to the highest predicted liquid separation efficiency, a position which is 15 mm away from opposite wall was selected. Figure 8.8 presents the final configuration of the VFT-V5-INT which has the same volume of the VFT-V5 except the inlet pipe is moved the inside the separator.

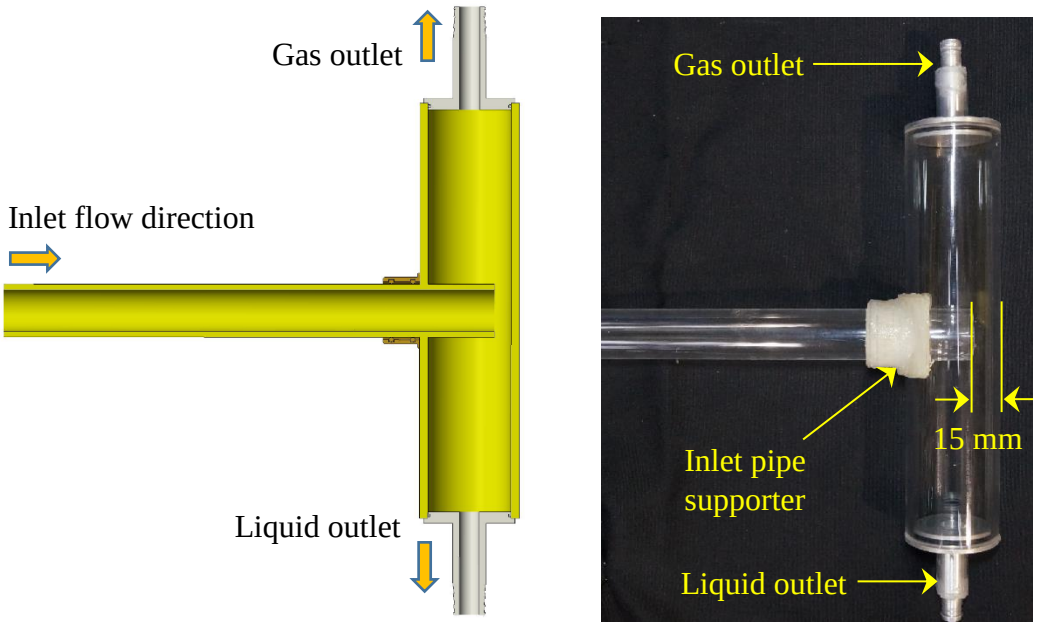

Figure 8.8: Configuration of VFT-V5-INT: (a) section view from 3d model; (b) photograph of the assembly.

Figure 8.9 presents the numerical and experimental results for the liquid separation efficiency of the VFT-V5-INT. Both numerical and experimental results give the same trend of liquid separation efficiency with the inlet mass velocity change, but the CFD underestimates the efficiency by about 0.02 in all cases. The new position of the inlet pipe increased the liquid separation efficiency and reduced the number of liquid drops on the upper side of the separator. Droplets on the wall of the separator arise from impingement of the incoming jet on the wall of the separator. Figure 8.10 presents images of the VFT-V5-INT during operation. In this configuration, there is no extractor at the top of the separator. The observed two-phase flow pattern at the inlet of the vertical separator was stratified flow.

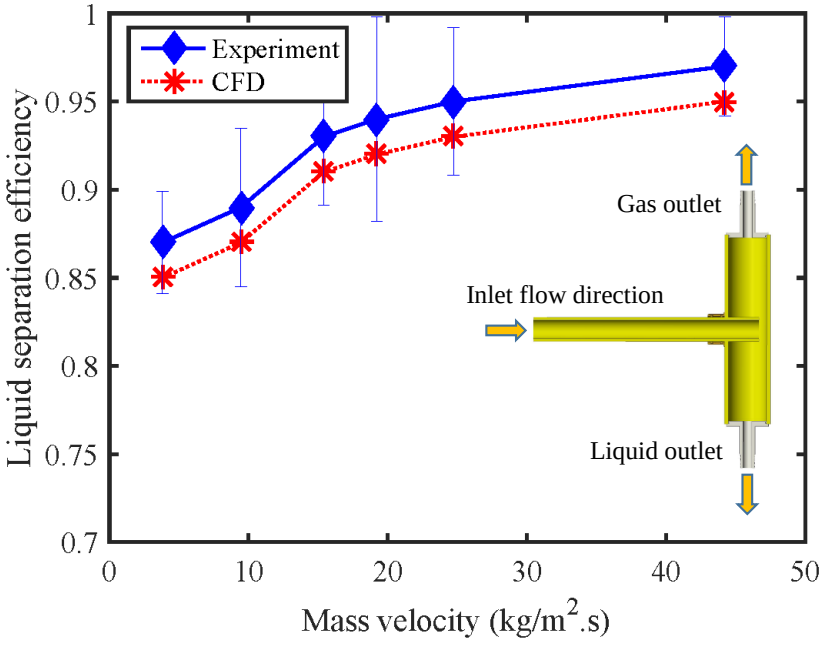

Figure 8.9: Comparison between CFD and experimental results for VFT-V5-INT.

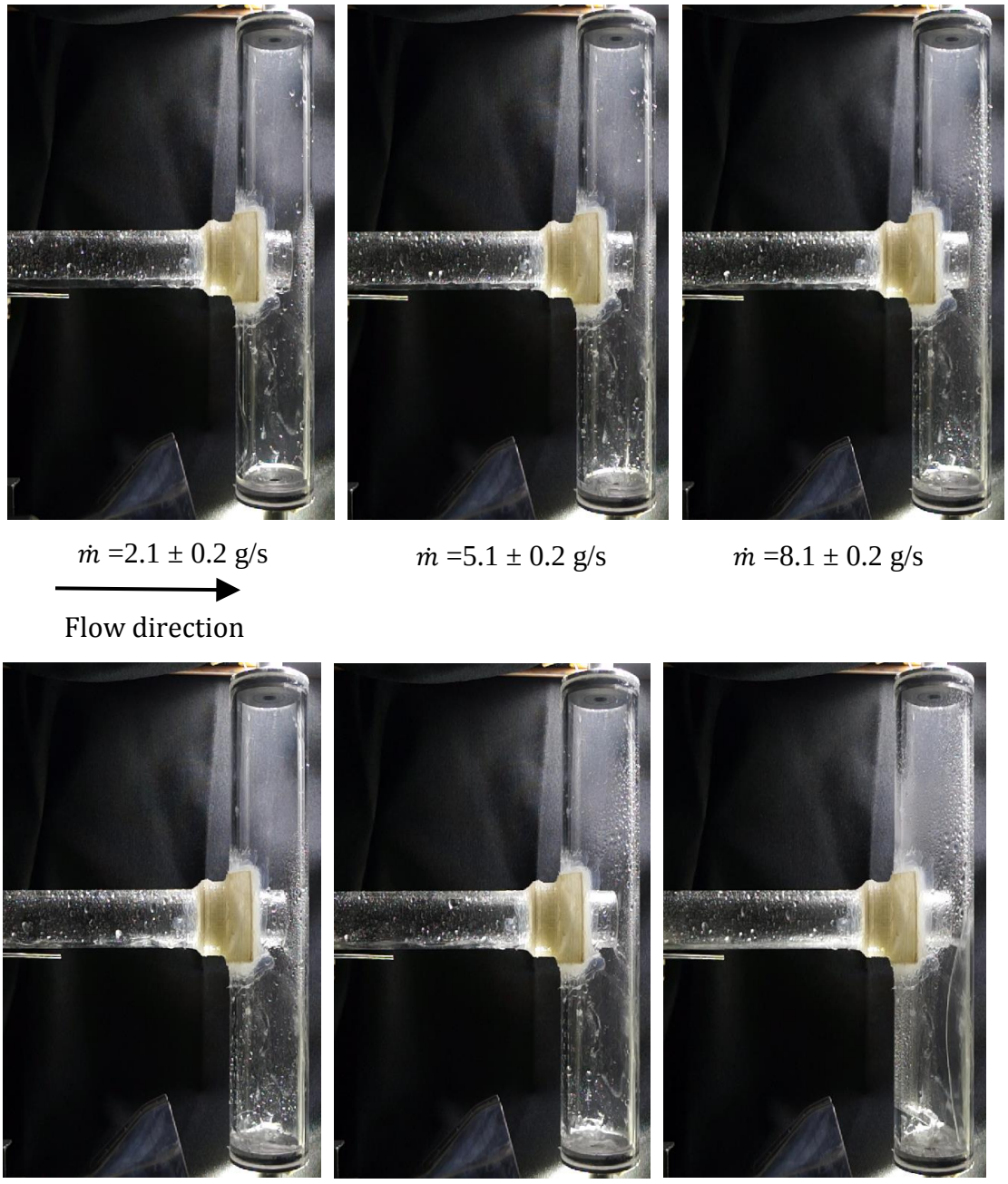

Figure 8.10: Images of the modified vertical flash tank separator VFT-V5-INT during operation. Inlet flow direction from left to right.

8.6.3 Change the direction of inlet flow

In order to change the direction of inlet flow to direct it downwards, a square hole with a 25 mm hydraulic diameter was created on the bottom side of the inlet pipe, and the circular end of the inlet pipe was closed. The centre of the hole of 25 mm hydraulic diameter is exactly on the centre of the separator's body. This technique gives a downwards vertical direction for the inlet flow instead of the normal horizontal direction. The inlet flow is oriented in same direction of the gravity force, so the liquid droplets are directed downward to where the liquid outlet side is located. It is also likely that the closed end of the inlet pipe acts in a similar way to the wall opposite the inlet in VFT-V5-INT. This arrangement is designated VFT-V5-OD.

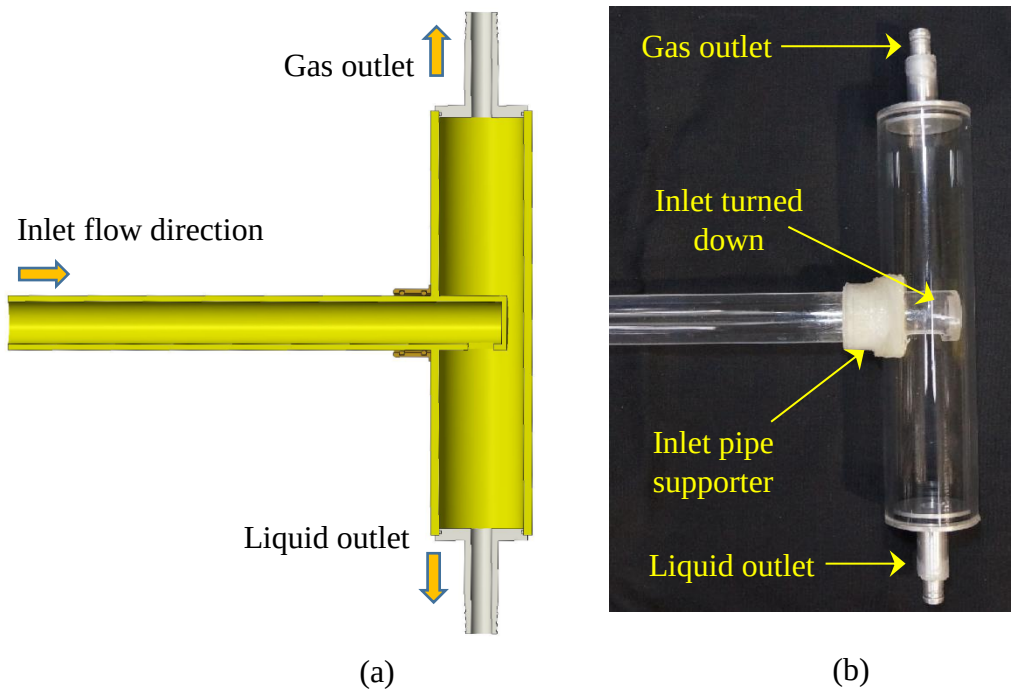

Figure 8.11: Configuration of VFT-V5-OD: (a) section view from 3d model; (b) photograph of the assembly.

Figure 8.12 presents the numerical and experimental results of the liquid separation efficiency of the VFT-V5-OD. The numerical and experimental results give the same trend of the liquid separation efficiency variation with the inlet mass velocity and in this case, the CFD underestimates the magnitude by about 0.01 across all the conditions. The orientation of the inlet flow has a significant effect on the liquid separation efficiency. There is no inlet jet impact on the wall of the separator, so no part of the liquid flow will be diverted toward the top of the separator. Figure 8.13 presents images of the VFT-V5-OD during operation and it is seen that there are very few droplets on the upper half of the separator in comparison to the VFT-V5-EXR and VFT-V5-INT cases shown in Figure 8.10 and 8.7 respectively. In this arrangement, there is no extractor at the top of the separator. The observed two-phase flow pattern at the inlet was stratified flow.

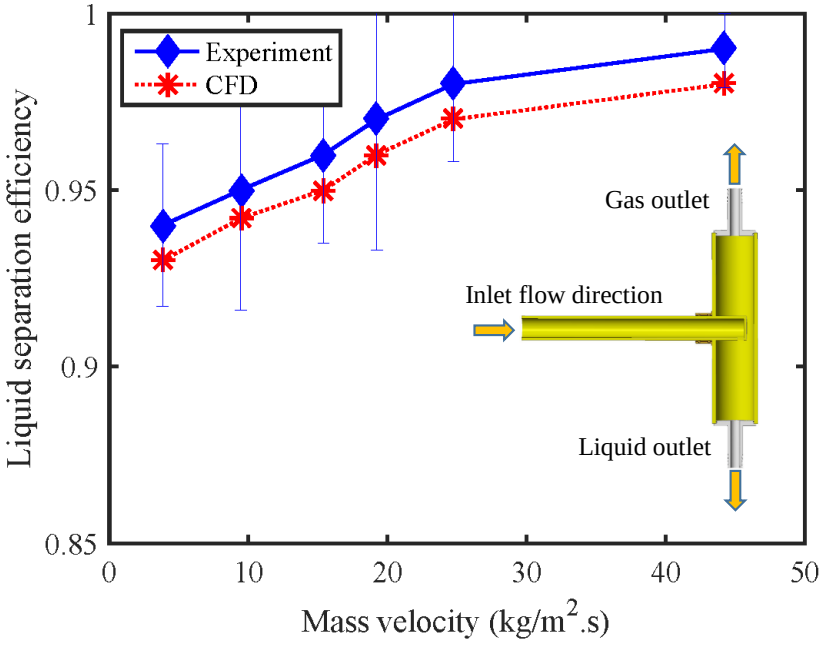

Figure 8.12: Comparison between CFD and experimental results for VFT-V5-OD.

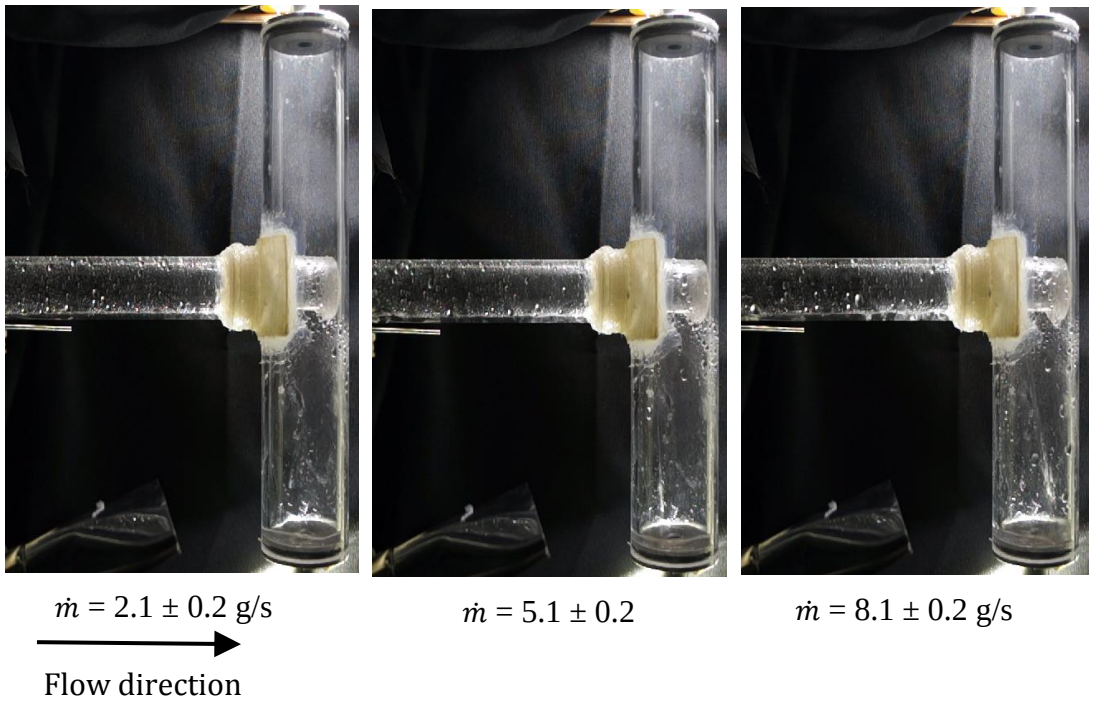

Figure 8.13: Images of the modified vertical flash tank separator VFT-V5-OD during operation. Inlet flow direction from left to right.

8.6.4 Extractor at the outlet of VFT-V5-OD

The last of the enhancement options was arranged by adding the extractor to the VFT-V5-OD configuration, which achieved the best results of the previously investigated options. This combined configuration is designated VFT-V5-ODEXR. Figure 8.14 illustrates the internal configuration of the VFT-V5-ODEXR.

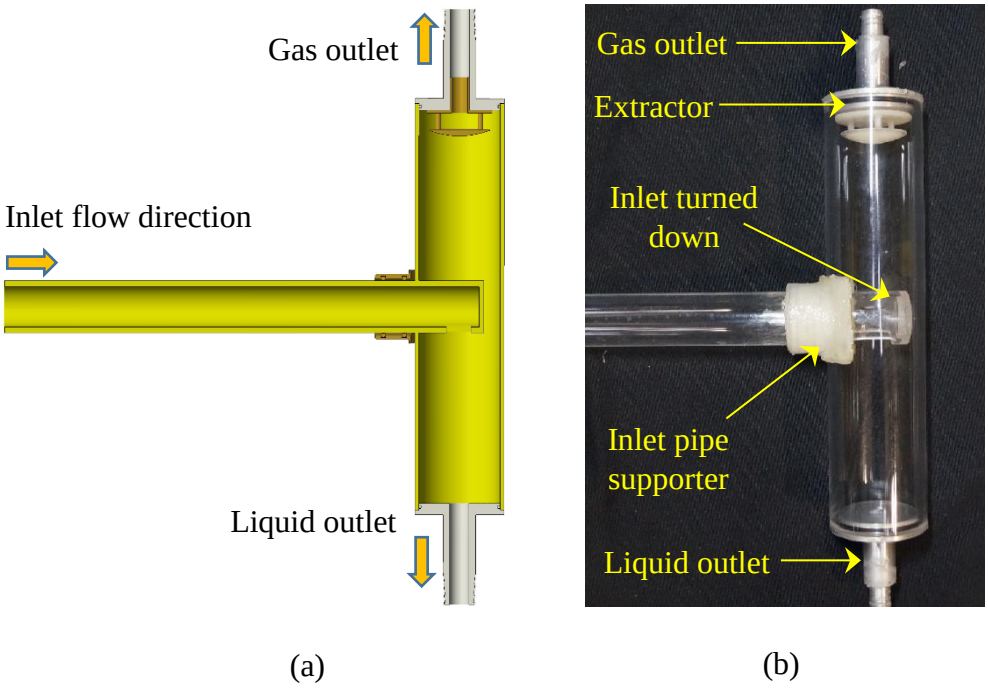

Figure 8.14: Configuration of VFT-V5-ODEXR: (a) section view from 3d model; (b) photograph of the assembly.

Figure 8.15 presents the numerical and experimental results for the liquid separation efficiency of the VFT-V5-ODEXR. The numerical and experimental results give the same trend of the liquid separation efficiency variation with the inlet mass velocity but the CFD underestimates the efficiency by between 0.01 and 0.02 across the range of conditions tested. The combined effect of using the extractor and making the inlet flow direction downward increases the liquid separation efficiency relative to either of these options operating alone. Figure 8.16 presents images of the VFT-V5-ODEXR during operation. The observed two-phase flow pattern at the inlet was stratified flow.

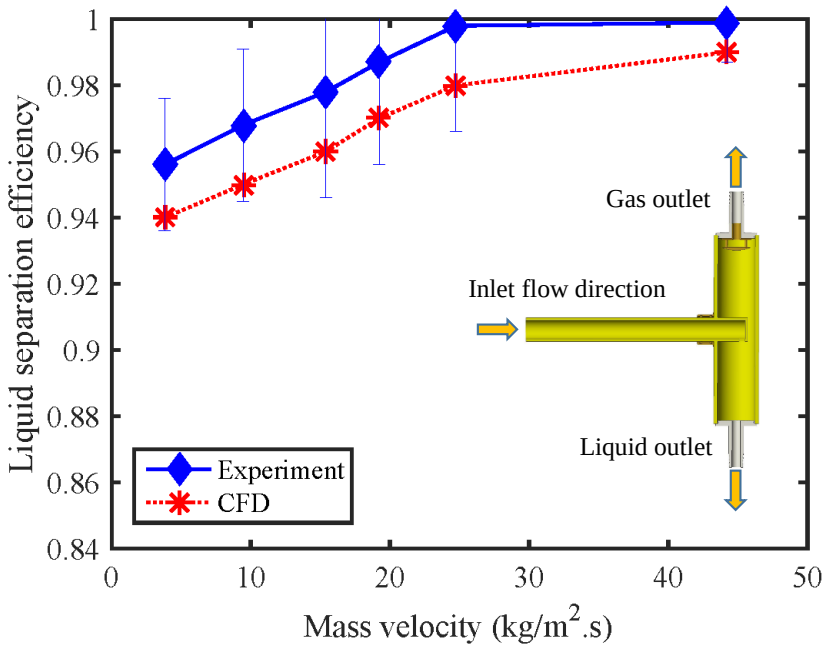

Figure 8.15: Comparison between CFD and experimental results for VFT-V5-ODEXR.

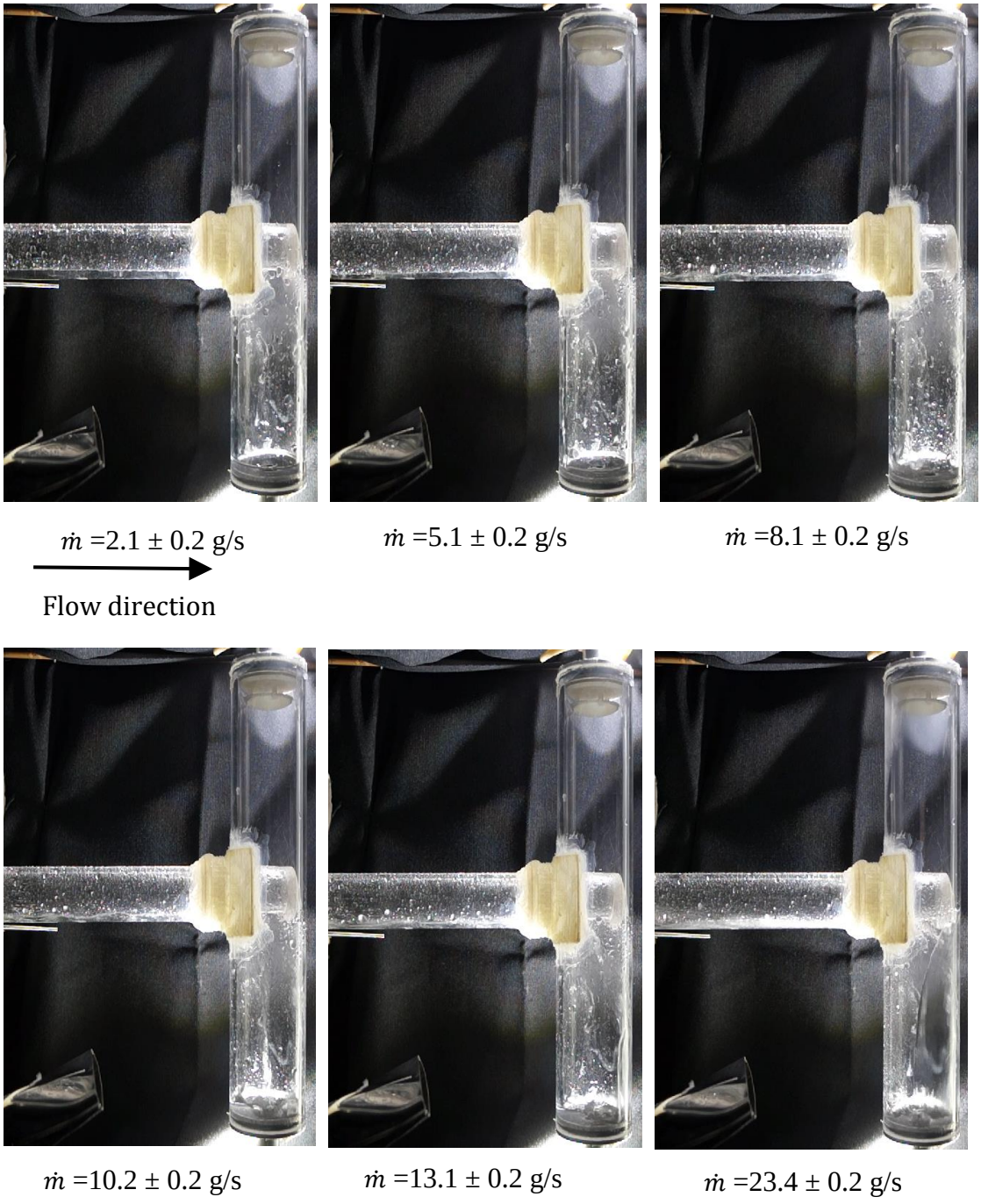

Figure 8.16: Images of the modified vertical flash tank separator VFT-V5-ODEXR during operation. Inlet flow direction from left to right.

8.7 Comparison with the VFT-V5 baseline

All the experimental and numerical results of the enhanced efficiency arrangements are compared with the numerical and experimental results from the baseline VFT-V5 configuration in this section.

8.7.1 Liquid separation efficiency

Figures 8.17 and 8.18 present the experimental and numerical simulation results respectively. Generally, the liquid separation efficiency is increased by increasing the inlet mass flow rate. The highest overall values of the liquid separation efficiency were achieved by the VFT-V5-ODEXR configuration.
In the VFT-V5-INT, the separation performance is higher than that in the VFT-V5 by about 1% due to the effect of the inlet pipe position. The VFT-V5-EXR configuration is more effective: the results revealed that the liquid separation efficiency is 2 % higher than that in the VFT-V5 configuration. The extractor is effective in extracting the liquid drops at the gas outlet at all operating conditions. Similarly, the extractor effect in model VFT-V5-ODEXR increased the performance by 2% relative to that in VFT-V5-OD configuration. In the VFT-V5-OD configuration, the orientation of the inlet flow has a significant effect on the separator performance, It causes an increase of about 8 % in efficiency. There is no impact of the incoming jet flow on the opposite wall, and consequently, the liquid is not diverted to the top side of the separator. Figures 8.17 and 8.18 show that the orientation of the inlet flow increased the performance of the separator dramatically. Therefore, using the extractor with downward flow orientation in the VFT-V5-ODEXR gives the highest value of the separation performance of the vertical flash tank separator. However, further improvement to enhance the separation efficiency of the VFT-V5-ODEXR at flow rates less than 20 g/s may be achieved by using a fine wire mesh with the extractor to trap the tiny liquid droplets that move with the vapour through the gas outlet.

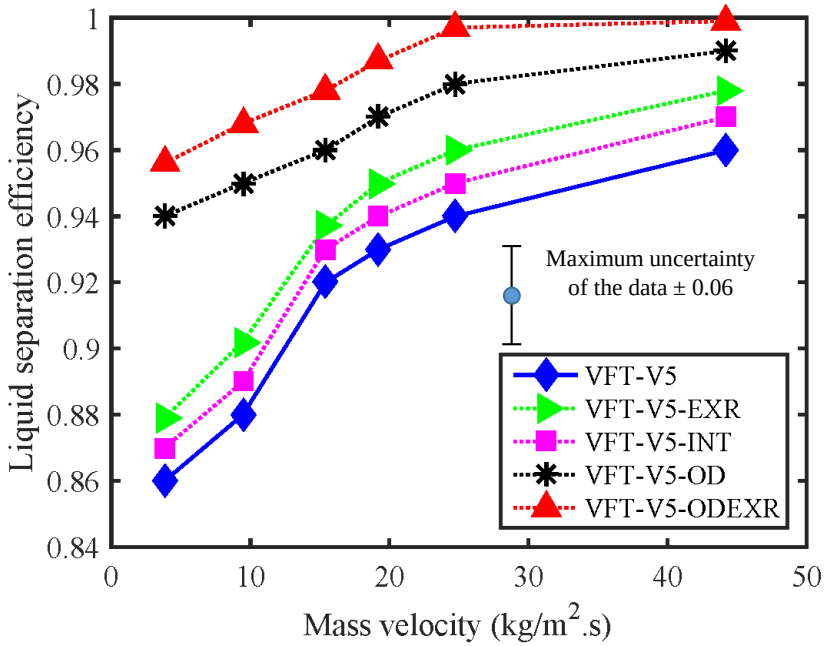

Figure 8.17: Experimental results comparing the VFT-V5 and the enhanced design configurations.

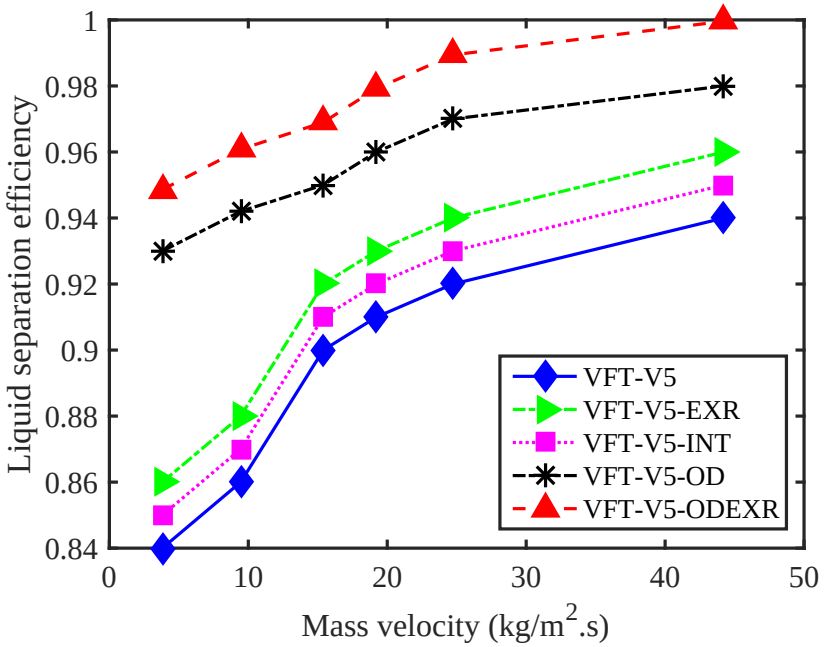

Figure 8.18: CFD results comparing the VFT-V5 and the enhanced design configurations.

8.7.2 Vapour quality at the gas outlet

Figure 8.19 presents the experimental results for the vapour quality at the gas outlet of the vertical separator cross all operating conditions of the enhanced efficiency configurations and the reference VFT-V5 configuration. The vapour quality has been increased as a result of applying the enhancement techniques to the vertical flash tank separator. The results revealed that the highest value of the vapour quality was achieved by the VFT-V5-ODEXR. Figure 8.19 also confirms that the extractor can reduce the number of the liquid drops that move with the gas through the gas outlet, so the vapour state in the VFT-V5-ODEXR is close to the saturated vapour state especially at the high mass flow rates.

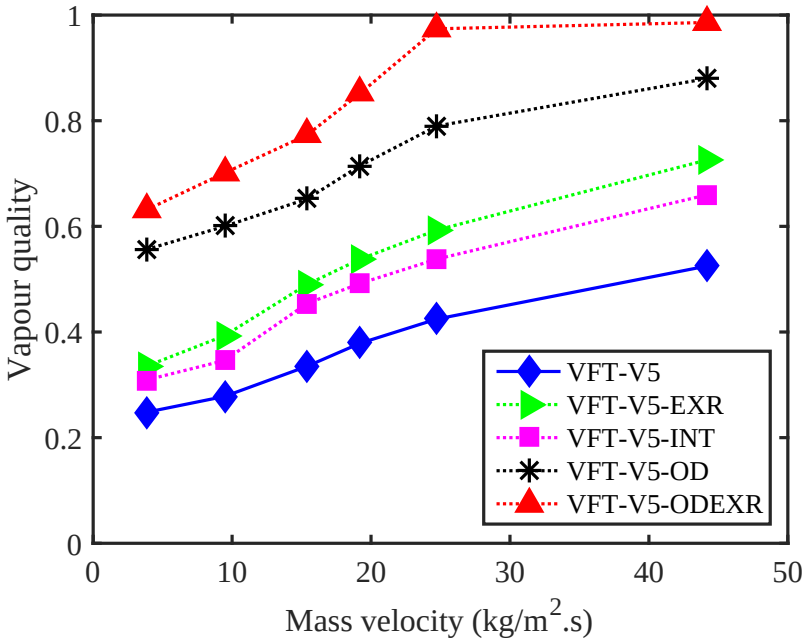

Figure 8.19: Experimental results for the vapour quality at the gas outlet of the separator for the different configurations.

8.7.3 Flow behaviour inside the separator

Comparing the images presented in Figure 8.20, it can be seen that at the same inlet flow condition (10.2 ± 0.2 g/s) there is a relatively high number of liquid drops appearing on the upper half of the separator in the of VFT-V5 and VFT-V5-EXR configuration. This is a result of the impinging and splashing of the incoming jet on the wall of the separator. The number of liquid drops is reduced in VFT-V5-INT due to the position of the inlet pipe and in the VFT-V5-OD and VFT-V5-ODEXR, the liquid drops do not appear on the upper half of the separator due to the downward direction of the inlet flow which prevents the liquid drops from impacting on the inside wall of the separator above the inlet.

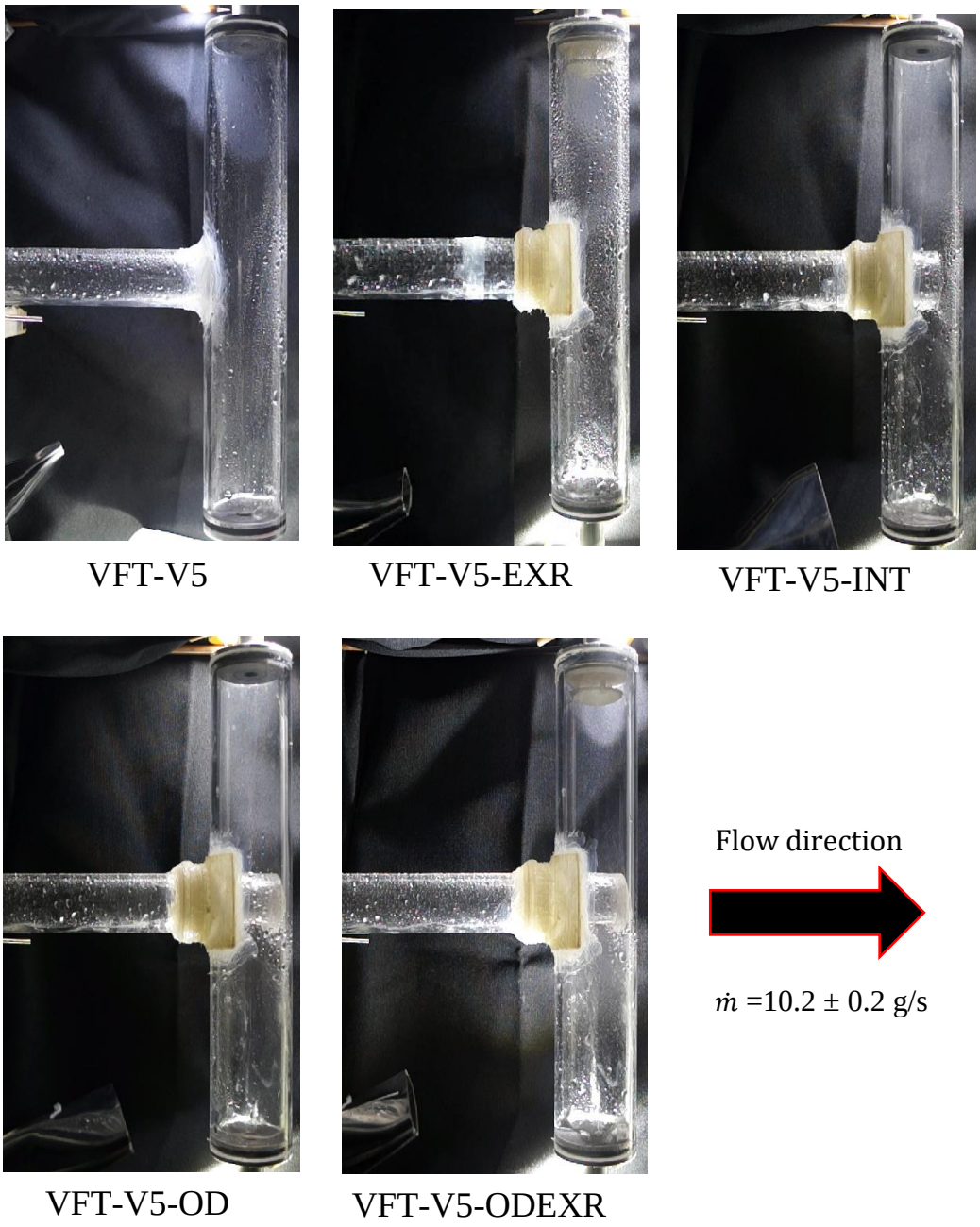

Figure 8.20: Images presenting a comparison of the flow behaviour inside the vertical separator for the different enhancement configurations at $\dot{m}$= 10.2 ± 0.2 g/s.

8.8 Conclusion

Separation enhancement configurations for the basic vertical flash tank separator (VFT-V5) were investigated numerically and experimentally. The enhancement options were shown to be effective in increasing the liquid separation efficiency. The numerical and experimental results can be summarized as follows:

1. The highest value of the liquid separation efficiency of approximately 99.9 % was achieved by the VFT-V5-ODEXR configuration with a flow rate of 23.4 $\pm$ 0.2 g/s. This configuration used an extractor at the gas outlet and a downward direction of the inlet flow.

2. The downward inlet flow orientation has a significant effect on the liquid separation efficiency as a result of preventing the impingement of the incoming stream on the inside wall. Without the downward restriction to flow direction, droplets impacting the wall can splash in the upwards direction, increasing the mass of liquid flowing with vapour through the gas outlet.

3. The extractor increases the liquid separation efficiency by improving the removal of the liquid drops that move with the gas towards the gas outlet.

4. The vapour quality at the gas outlet is also improved by the enhanced configuration and the highest value was achieved by the VFT-V5-ODEXR.

5. Reasonable agreement has been obtained between the experimental and numerical results, with the CFD typically under-predicting the liquid separation efficiency by between 1% and 2% over the range of conditions tested.

Chapter 9

Conclusions

9.1 Description of work

Vertical flash tank separators are used widely. Refrigeration and air conditioning are two of the most important applications. Using a vertical flash tank separator in a refrigeration or air conditioning system has many advantages such as improving the coefficient of performance, improving the heat transfer coefficient in the evaporator and reducing the thermal stress in the compressor.

Many studies have been completed and reported in literature about the performance of vertical flash tank separators, but these studies have primarily considered the effect of the flash tank separator on the performance and capacity of air conditioning and refrigeration systems. Few studies have considered the design problem of optimising separation efficiency in vertical separators. In the present work, a new apparatus was designed and built to investigate two-phase flow behaviour after an expansion device in a horizontal tube and to investigate the performance of a vertical flash tank separator using water as the working fluid. Separation enhancement options were proposed and analysed, then tested experimentally to assess performance improvement of a vertical flash tank separator. Numerical simulation was implemented in the design process.

A digital camera, mass flow meters, pressure and temperature sensors were used to record the two-phase flow behaviour in the horizontal tube and inside the vertical flash tank separator.

9.2 Outcomes

9.2.1 Two-phase flow in a horizontal pipe

The experimental apparatus was designed to operate over a mass flow rate range from 2.1 to 23.4 ± 0.2 g/s with vapour quality in the vicinity of 5 %.

- The two-phase flow developed gradually after the expansion device reaching the developed region where the flow maintains a steady condition at about 165 cm from the expansion device.
- Increase of the inlet mass flow rate decreased the void fraction and reduced the slip ratio in the developed region.
- The expansion length increased from 30.7 to 180.1 mm when the mass flow rate increased from 2.1 to 23.4 g/s.
- A stratified flow pattern was observed in all the experiments at the developed region.
- The liquid height at the bottom of the pipe increased from 1.9 to 5.2 mm when the mass flow rate increased from 2.1 to 23.4 g/s.
- All the experimental results were compared with the numerical simulation results, and reasonable agreement was observed. The difference between the experimental and numerical results was about 8 %.
- Empirical correlations were developed based on the experimental results to predict: (a) the expansion length at the bottom of the horizontal pipe; and (b) the void fraction in the developed region. Both correlations achieved R^2 values of 0.99.
- The CFD simulation results underestimated the expansion length and fully-developed liquid film height by about 8 % compared with the experimental observations.

9.2.2 Liquid separation efficiency in the flash tank before enhancement

- The highest value of the liquid separation efficiency was recorded with the VFT-V5 configuration which achieved 0.96 at 23.4 ±0.2 g/s.
- The inlet mass flow rate has a significant effect on the liquid separation efficiency in the vertical separator. The liquid separation efficiency of the VFT-V5 increased from 0.86 to 0.96 when the mass flow rate increased from 2.1 to 23.4 g/s.
- The highest value of the vapour quality at the gas outlet was recorded with the VFT-V5 which achieved 0.55 at 23.4 g/s.
- The liquid jet impingement on the inner side of the separator was increased when the inlet mass flow rate increased.
- The number of small liquid drops on the wall at the top portion of the separator was decreased when the volume of the separator increased.
- All the experimental results of the liquid separation efficiency using different sizes of the vertical separator were compared with the numerical results at the same operating condition, and differences between 1 % and 2 % were obtained.
- Using CFD, virtual experiments demonstrate that the d/D has a significant effect on the liquid separation efficiency. When $d/D = 1$, the simulated liquid separation efficiency decreased from 0.81 to 0.66 when the mass flow rate increased from 2.1 to 23.4 g/s. While for $d/D = 0.25$, the liquid separation efficiency is about 3.5 % higher than that for $d/D = 0.5$, for both $d/D = 0.25$ and $d/D = 0.5$, the efficiency increased when the mass flow rate increased from 2.1 to 23.4 g/s.
- An empirical correlation with $R^2 = 0.98$ was developed to predict the liquid separation efficiency based on the experimental data.
- The numerical results underestimated the liquid separation efficiency in the experiments with an average difference in the liquid separation efficiency of between 1 % and 2 %.

9.2.3 Enhancement of vertical separator

Separation enhancement options were investigated to improve the liquid separation efficiency of the VFT-V5 configuration.

- The highest value of the liquid separation efficiency was recorded with the VFT-V5-ODEXR configuration, achieving 0.99 at 23.4 ±0.2 g/s.
- The downward inlet flow orientation had a significant effect on the the liquid separation efficiency, causing an increase of about 8 % in efficiency.
- The extractor also increased the liquid separation efficiency, achieving a 2 % increase when the mass flow rate increased from 2.1 to 23.4 g/s.
- The enhancement design options also improve the vapour quality at the gas outlet and the highest value was recorded for the VFT-V5-ODEXR of 0.98.
- The impact of the incoming inlet jet on the wall was removed in the VFT-V5-ODEXR due to the downward inlet flow orientation.
- All the experimental and numerical results of the separation enhancement options were compared with the numerical and experimental results of the VFT-V5.
- The numerical and experimental results give the same trend of the liquid separation efficiency variation with the inlet mass velocity but the CFD underestimates the efficiency by between 1 % and 2 % across the range of conditions tested.

9.3 Summary of conclusions

In this thesis, experiments were performed to develop a data set on the two-phase flow development in a horizontal pipe and liquid separation efficiency in vertical flash tank separator using water as the working fluid. The experiments were performed over a range of operating conditions, but stratified flow was the developed pattern in all the experiments. The operating conditions in the experiments were used in the CFD simulations to assess the suitability of CFD in the design of the vertical flash tank separator. By comparing the experimental and CFD simulations results, it is demonstrated that liquid separation efficiency within about 2 % of the measured value can be simulated using CFD. Enhancement options to improve the separation efficiency were proposed, simulated, and experimentally tested. The CFD was again demonstrated to be a suitable design tool because liquid separation efficiency achieved with the enhancement options was simulated to within about 2 % of the measured values.

9.4 Future work

The primary limitation of the present conclusion regarding the viability of CFD as a design tool in vertical separator design is that the operating conditions produced only stratified flow at the inlet. Future work in which alternative inlet flow patterns are established would make a useful contribution.

References

Abdulkadir, M., Hernandez-Perez, V., Lowndes, I., Azzopardi, B. and Sam-Mbomah, E. 2016, 'Experimental study of the hydrodynamic behaviour of slug flow in a horizontal pipe', *Chemical Engineering Science* **156**, 147–161.

Abed, E. M. and Abdulkadhim, A. 2016, 'Modelling of phase change for two-phase refrigerant flow inside capillary tube under adiabatic conditions', *International Journal of Current Engineering and Technology* **6**(5), 1869–1872.

Acunha, I. C. and Schneider, P. S. 2013, 'Experimental assessment of heat transfer correlations for a small-scale evaporative condenser', *Heat transfer engineering* **34**(5-6), 532–540.

Ali, Z., Tucker, P. G. and Shahpar, S. 2017, 'Optimal mesh topology generation for cfd', *Computer Methods in Applied Mechanics and Engineering* **317**, 431–457.

Arnold, K. and Stewart, M. 1998, *Design of oil-handling systems and facilities*, Gulf Publishing Company.

Baker, O. et al. 1954, 'Design of pipe lines for simultaneous oil and gas flow', *Oil Gas Journal* **26**(13).

Bergman, T. L., Incropera, F. P., Lavine, A. S. and DeWitt, D. P. 2011, *Fundamentals of heat and mass transfer*, 6th edn, John Wiley & Sons.

Bothamley, M. et al. 2013, 'Gas/liquid separators: Quantifying separation performance-part 1', *Oil and Gas Facilities* **2**(04), 21–29.

Bottin, M., Berlandis, J., Hervieu, E., Lance, M., Marchand, M., Öztürk, O. and

Serre, G. 2014, 'Experimental investigation of a developing two-phase bubbly flow in horizontal pipe', *International Journal of Multiphase Flow* **60**, 161–179.

Bowers, C. D. 2009, Developing Adiabatic Two-Phase Flow, PhD thesis, Mechanical Engineering, University of Illinois at Urbana-Champaign.

Bowers, C. D. and Hrnjak, P. S. 2008, Developing two-phase R134a flow after an expansion valve in an 8.7 mm tube, International refrigeration and air conditioning conference, Purdue.

Brown, P. P. and Lawler, D. F. 2003, 'Sphere drag and settling velocity revisited', *Journal of environmental engineering* **129**(3), 222–231.

Campbell, J. 2014, *Gas Conditioning and Processing*, Vol. 2 of *The Equipment Modules*, 9th edn, Campbell Petroleum Series, Norman Oklahoma USA.

Cheng, L., Ribatski, G., Moreno Quibn, J. and Thome, J. R. 2008, 'New prediction methods for CO_2 evaporation inside tubes: Part I a two-phase flow pattern map and a flow pattern based phenomenological model for two-phase flow frictional pressure drops', *International Journal of Heat and Mass Transfer* **51**(12), 111–124.

Cioncolini, A. and Thome, J. R. 2017, 'Pressure drop prediction in annular two-phase flow in macroscale tubes and channels', *International Journal of Multiphase Flow* **89**, 321–330.

Coleman, H. W. and Steele, W. G. 2009, *Experimentation, validation, and uncertainty analysis for engineers*, John Wiley & Sons.

Collier, J. G. and Thome, J. R. 1994, *Convective boiling and condensation*, 3 edn, Oxford University Press.

Delgado, M. and Pichardo, C. 1999, 'Use of matlab and 20-sim to simulate a flash separator', *Simulation Practice and Theory* **7**(56), 515–530.

Dinaryanto, O., Widyatama, A., Majid, A. I. et al. 2016, Image processing analysis on the air-water slug two-phase flow in a horizontal pipe, Vol. 1737, AIP Publishing, pp. 4–11.

Dobson, M. K. 1994, Heat transfer and flow regimes during condensation in horizontal tubes, PhD thesis, University of Illinois at Urbana-Champaign.

El Hajal, J., Thome, J. R. and Cavallini, A. 2003, 'Condensation in horizontal tubes, part 1: two-phase flow pattern map', *International Journal of Heat and Mass Transfer* **46**(18), 3349–3363.

Elbel, S. and Hrnjak, P. 2004, 'Flash gas bypass for improving the performance of transcritical R744 systems that use microchannel evaporators', *International Journal of Refrigeration* **27**(7), 724–735.

Elbel, S. and Hrnjak, P. 2008, 'Experimental validation of a prototype ejector designed to reduce throttling losses encountered in transcritical R744 system operation', *International Journal of Refrigeration* **31**(3), 411–422.

Fair, G. and Geyer, J. 1954, *water supply and waste-water disposal*, Wiley New York.

Fei, P. 2004, Adiabatic Developing Two-phase Refrigerant Flow in Manifolds of Heat Exchangers, PhD thesis, College of Engineering. University of Illinois at Urbana-Champaign.

Feng, C., Kai, W., Shouguo, W., Ziwen, X. and Pengcheng, S. 2009, 'Investigation of the heat pump water heater using economizer vapor injection system and mixture of R22/R600a', *International Journal of Refrigeration* **32**(3), 509–514.

FLUENT, A. 2012, '14.5, theory guide; ansys', *Inc., Canonsburg, PA* .

Fu, C., Uddin, M., Robinson, C., Guzman, A. and Bailey, D. 2017, 'Turbulence models and model closure coefficients sensitivity of nascar racecar rans cfd aerodynamic predictions', *SAE International Journal of Passenger Cars-Mechanical Systems* **10**(2017-01-1547), 330–344.

Ghajar, A. J. and Bhagwat, S. M. 2013, 'Effect of void fraction and two phase dynamic viscosity models on prediction of hydrostatic and frictional pressure drop in vertical upward gas-liquid two phase flow', *Heat Transfer Engineering* **34**(13), 1044–1059.

Ghajar, A. J. and Tang, C. C. 2012, 'Void fraction and flow patterns of two-phase flow

in upward and downward vertical and horizontal pipes', *Advances in Multiphase Flow and Heat Transfer* **4**, 175–201.

GPSA 2004, *Engineering Data book*, Vol. I and II, Gas Processors and Suppliers Association.

Grodal, E. dal, E. and Realff, M. 1999, Optimal design of two-and three-phase separators: A mathematical programming formulation, *in* 'SPE Annual Technical Conference and Exhibition'.

Gruau, C. and Coupez, T. 2005, '3d tetrahedral, unstructured and anisotropic mesh generation with adaptation to natural and multidomain metric', *Computer Methods in Applied Mechanics and Engineering* **194**(48), 4951–4976.

Gu, B., Li, Y., Wang, Z. and Jing, B. 2003, 'Analysis on the adiabatic flow of r407c in capillary tube', *Applied thermal engineering* **23**(15), 1871–1880.

Hanfei, T. and Hrnjak, P. 2012, 'Experimental study of refrigerant two phase separation in a compact vertical T-junction', *ASHRAE Transactions* **118**(1), 672–680.

Heo, J., Jeong, M. W., Baek, C. and Kim, Y. 2011, 'Comparison of the heating performance of air-source heat pumps using various types of refrigerant injection', *International Journal of Refrigeration* **34**(2), 444–453.

Heo, J., Jeong, M. W. and Kim, Y. 2010, 'Effects of flash tank vapor injection on the heating performance of an inverter-driven heat pump for cold regions', *International Journal of Refrigeration* **33**(4), 848–855.

Heo, J., Kang, H. and Kim, Y. 2012, 'Optimum cycle control of a two-stage injection heat pump with a double expansion sub-cooler', *International Journal of Refrigeration* **35**(1), 58–67.

Hrnjak, P. 2004, 'Developing adiabatic two phase flow in headersdistribution issue in parallel flow microchannel heat exchangers', *Heat transfer engineering* **25**(3), 61–68.

Hrnjak, P. S. 2011, Flash gas bypass concept utilizing low pressure refrigerants, Master's thesis, Mechanical Science and Engineering, University of Illinois at Urbana-Champaign, United States.

Hu, H. and Cheng, Y. F. 2016, 'Modeling by computational fluid dynamics simulation of pipeline corrosion in co 2-containing oil-water two phase flow', *Journal of Petroleum Science and Engineering* **146**, 134–141.

Hwang, C.-Y. J. and Pal, R. 1997, 'Flow of two-phase oil/water mixtures through sudden expansions and contractions', *Chemical Engineering Journal* **68**(2), 157–163.

Hwang, Y., Xu, X., Radermacher, R. and Pham, H. 2010, Control strategy of vapor injection cycle, *in* 'International Refrigeration and Air Conditioning Conference', Purdue University School of Mechanical Engineering, United States.

Ishii, M. and Hibiki, T. 2011, *Thermo-fluid dynamics of two-phase flow*, Springer Science and Business Media.

Ishii, M. and Zuber, N. 1979, 'Drag coefficient and relative velocity in bubbly, droplet or particulate flows', *AIChE Journal* **25**(5), 843–855.

Jain, S., Jain, G. and Bullard, C. 2004, Vapor injection in scroll compressors, International Compressor Engineering Conference at Purdue.

Jang, Y., Lee, E., Chin, S. and Ha, S. 2010, Effect of flash and vapor injection on the air-to-air heat pump system, *in* 'International Refrigeration and Air Conditioning Conference', Purdue University School of Mechanical Engineering, United States.

Jekel, T. B. and Reindl, D. T. 2001, Gravity separation fundumentals and design, Ammonia refrigeration convention and exhibition, Ammonia Refrigeration Convention and Exhibition Long Beach, CA, Long Beach, CA.

Kalteh, M., Abbassi, A., Saffar-Avval, M. and Harting, J. 2011, 'Eulerian-eulerian two-phase numerical simulation of nanofluid laminar forced convection in a microchannel', *International Journal of Heat and Fluid Flow* **32**(1), 107 – 116.

Kanizawa, F. T. and Ribatski, G. 2012, 'Two-phase flow patterns and pressure drop inside horizontal tubes containing twisted-tape inserts', *International Journal of Multiphase Flow* **47**, 50–65.

Kattan, N., Thome, J. R. and Favrat, D. 1998, 'Flow boiling in horizontal tubes: Part

1development of a diabatic two-phase flow pattern map', *Journal of Heat Transfer* **120**(1), 140–147.

Kerdouss, F., Bannari, A. and Proulx, P. 2006, 'CFD modeling of gas dispersion and bubble size in a double turbine stirred tank', *Chemical engineering science* **61**(10), 3313–3322.

Kha, H. M., Phuong, N. N. and Nam, N. T. 2017, The effect of different geometrical configurations of the performances of gas-liquid cylindrical cyclone separators (glcc), *in* 'System Science and Engineering (ICSSE), 2017 International Conference on', IEEE, pp. 646–651.

Khorshidi, J. and Naderipour, I. 2012, 'Design of vertical gas-liquid separator and examination its effective parameters in sarkhoun & qeshm treating company', *Journal of Basic and Applied Scientific Research* **2**, 6986–6994.

Kilicarslan, A. and Müller, N. 2005, 'A comparative study of water as a refrigerant with some current refrigerants', *International journal of energy research* **29**(11), 947–959.

Lanzafame, R., Mauro, S. and Messina, M. 2013, 'Wind turbine cfd modeling using a correlation-based transitional model', *Renewable Energy* **52**, 31–39.

Li, Z., Spaulding, M., McCay, D. F., Crowley, D. and Payne, J. R. 2017, 'Development of a unified oil droplet size distribution model with application to surface breaking waves and subsea blowout releases considering dispersant effects', *Marine Pollution Bulletin* **114**(1), 247–257.

Ma, G.-Y. and Zhao, H.-X. 2008, 'Experimental study of a heat pump system with flash-tank coupled with scroll compressor', *Energy and Buildings* **40**(5), 697–701.

Ma, G. and Zhao, H. 2010, 'Performance prediction for heat pump system with flash tank coupled with scroll compressor', *International Journal of Ambient Energy* **31**(3), 153–160.

Maggioni, V., Sapiano, M. R. and Adler, R. F. 2016, 'Estimating uncertainties in high-resolution satellite precipitation products: Systematic or random error?', *Journal of Hydrometeorology* **17**(4), 1119–1129.

Main, A., Zeng, X., Avery, P. and Farhat, C. 2017, 'An enhanced fiver method for multi-material flow problems with second-order convergence rate', *Journal of Computational Physics* **329**, 141–172.

Mandhane, J., Gregory, G. and Aziz, K. 1974, 'A flow pattern map for gasliquid flow in horizontal pipes', *International Journal of Multiphase Flow* **1**(4), 537–553.

Mathison, M., Braun, J. and Groll, E. 2011, 'Performance limit for economized cycles with continuous refrigerant injection', *International Journal of Refrigeration* **34**(1), 234–242.

Messa, G. V., Malin, M. and Malavasi, S. 2014, 'Numerical prediction of fully-suspended slurry flow in horizontal pipes', *Powder Technology* **256**, 61–70.

Milkie, J. A., Garimella, S. and Macdonald, M. P. 2016, 'Flow regimes and void fractions during condensation of hydrocarbons in horizontal smooth tubes', *International Journal of Heat and Mass Transfer* **92**, 252–267.

Misiulia, D., Elsayed, K. and Andersson, A. G. 2017, 'Geometry optimization of a deswirler for cyclone separator in terms of pressure drop using cfd and artificial neural network', *Separation and Purification Technology* **185**, 10–23.

Misra, A., de Souza, L., Illner, M., Hohl, L., Kraume, M., Repke, J.-U. and Thévenin, D. 2017, 'Simulating separation of a multiphase liquid-liquid system in a horizontal settler by cfd', *Chemical Engineering Science* **167**, 242–250.

Mo, S., Chen, X., Chen, Y. and Yang, Z. 2014, 'Passive control of gas-liquid flow in a separator unit using an apertured baffle in a parallel-flow condenser', *Experimental Thermal and Fluid Science* **53**, 127 – 135.

Moffat, R. J. 1985, 'Using uncertainty analysis in the planning of an experiment', *Journal of Fluids Engineering* **107**(2), 173–178.

Moffat, R. J. 1988, 'Describing the uncertainties in experimental results', *Experimental thermal and fluid science* **1**(1), 3–17.

Mohanraj, M., Jayaraj, S. and Muraleedharan, C. 2009, 'Environment friendly alternatives to halogenated refrigerantsa review', *International Journal of Greenhouse Gas Control* **3**(1), 108–119.

Mokhatab, S., Poe, W. A., Zatzman, G. C., Islam, M. C. and Van Wassenhove, W. C. 2012, *Handbook of natural gas transmission and processing*, Gulf Professional Publishing.

Morrison, F. A. 2016, Data correlation for drag coefficient for sphere, Michigan Technological University, Houghton, MI.

Naderipour, J. K. I. 2012, 'Design of vertical gas-liquid separator and examination its effective parameters in sarkhoun & qeshm treating company', *Journal of Basic and Applied Scientific Research* **2**(7), 6986–6994.

Pichardo, C. and Delgado, M. 2003, 'Pseudo-bond graph model and simulation of an industrial flash separator', *Simulation Modelling Practice and Theory* **11**(2), 125–150.

Pointon, A., Mills, T., Seil, G. and Zhang, Q. 2009, 'Computational fluid dynamic techniques for validating geothermal separator sizing', *GRC Transactions* **33**, 943–948.

Rafiee, S. E., Ayenehpour, S. and Sadeghiazad, M. 2016, 'A study on the optimization of the angle of curvature for a ranque–hilsch vortex tube, using both experimental and full reynolds stress turbulence numerical modelling', *Heat and Mass Transfer* **52**(2), 337–350.

Ramezani, L., Karney, B. and Malekpour, A. 2016, 'Encouraging effective air management in water pipelines: A critical review', *Journal of Water Resources Planning and Management* **142**(12).

Rasmussen, B. P. 2011, 'Dynamic modeling for vapor compression systemspart I: Literature review', *HVAC and Research* **18**(5), 934–955.

Rasmussen, B. P. and Shenoy, B. 2011, 'Dynamic modeling for vapor compression systemspart II: Simulation tutorial', *HVAC and Research* **18**(5), 956–973.

Rhodes, M. J. 2008, *Introduction to particle technology*, John Wiley & Sons.

Roman, A. J., Kreitzer, P. J., Ervin, J. S., Hanchak, M. S. and Byrd, L. W. 2016, 'Flow pattern identification of horizontal two-phase refrigerant flow using neural networks', *International Communications in Heat and Mass Transfer* **71**, 254–264.

Rouhani, S. Z. and Axelsson, E. 1970, 'Calculation of void volume fraction in the subcooled and quality boiling regions', *International Journal of Heat and Mass Transfer* **13**(2), 383–393.

Roul, M. K. and Sahoo, L. K. 2012, 'CFD modeling of pressure drop caused by two-phase flow of oil/water emulsions through sudden expansions', *International Journal of Engineering Research and Applications* **2**(6), 1047–1054.

Rudolf, P. 2009, 'Connection between inlet velocity field and diffuser flow instability', *Journal of Applied and Computational Mechanics.* **3**, 177–184.

Saisorn, S. and Wongwises, S. 2015, 'Adiabatic two-phase gas–liquid flow behaviors during upward flow in a vertical circular micro-channel', *Experimental Thermal and Fluid Science* **69**, 158–168.

Šarevski, M. and Šarevski, V. 2012, 'Characteristics of water vapor turbocompressors applied in refrigeration and heat pump systems', *International Journal of Refrigeration* **35**(5), 1484–1496.

Schiller, L., N. Z. 1935, 'Drag coefficient correlation', *Z. Ver. Deutsch. Ing* **77**, 318–323.

Seader, J. D., Henley, E. J. and Roper, D. K. 1998, *Separation process principles*, 2 edn, Wiley New York.

Setyawan, A. et al. 2016, 'The effect of the fluid properties on the wave velocity and wave frequency of gas–liquid annular two-phase flow in a horizontal pipe', *Experimental Thermal and Fluid Science* **71**, 25–41.

Shelley, S. 2007, 'Computational fluid dynamic power to the people', *Chem. Eng. Prog* **103**(4), 10–13.

Shoukri, M, H. I. P. F. 2002, 'Steam-water stratified flow in t-junctions - experiments and modelling', *Transactions of The Canadian Society for Mechanical Engineering* **26**(2), 241–259.

Shuxue, X. and Guoyuan, M. 2014, 'Experimental study on two-stage compression refrigeration/heat pump system with dual-cylinder rolling piston compressor', *Applied Thermal Engineering* **62**(2), 803–808.

Sirwan, R., Alghoul, M. A., Sopian, K., Ali, Y. and Abdulateef, J. 2013, 'Evaluation of adding flash tank to solar combined ejectorabsorption refrigeration system', *Solar Energy* **91**, 283–296.

Souders, M. and Brown, G. G. 1934, 'Design of fractionating columns i. entrainment and capacity', *Industrial & Engineering Chemistry* **26**(1), 98–103.

Srisomba, R., Mahian, O., Dalkilic, A. S. and Wongwises, S. 2014, 'Measurement of the void fraction of r-134a flowing through a horizontal tube', *International Communications in Heat and Mass Transfer* **56**, 8–14.

Stanly, W. and Walas, E. 1990, *Chemical Process Equipment-Selection and Design*, Butterman-Heinemam Series.

Steiner, D. 1993, 'Heat transfer to boiling saturated liquids, VDI-warmeatlas VDI heat atlas), verein deutscher ingenieure VDI, gessellschaft verfahrenstechnik und chemieingenieurwesen GCV', *trans., Düsseldorf* .

Stern, E., Newville, M., Ravel, B., Yacoby, Y. and Haskel, D. 1995, 'The uwxafs analysis package: philosophy and details', *Physica B: Condensed Matter* **208**, 117–120.

Svrcek, Y. and Monnery, D. 1993, 'Design two-phase separators within the right limits', *Chemical engineering progress* **89**(10), 53–60.

Terzuoli, F., Galassi, M., Mazzini, D. and D'Auria, F. 2008, 'Cfd code validation against stratified air-water flow experimental data', *Science and Technology of Nuclear Installations* .

Thome, J. R. and Hajal, J. E. 2003, 'Two-phase flow pattern map for evaporation in horizontal tubes: latest version', *Heat transfer engineering* **24**(6), 3–10.

Triplett, K., Ghiaasiaan, S., Abdel-Khalik, S. and Sadowski, D. 1999, 'Gas–liquid two-phase flow in microchannels part i: two-phase flow patterns', *International Journal of Multiphase Flow* **25**(3), 377–394.

Tuo, H. 2014, Flash gas bypass-a way to improve distribution of adiabatic two-phase refrigerant flow in headers of microchannel evaporators, PhD thesis, University of Illinois at Urbana-Champaign.

Tuo, H. and Hrnjak, P. 2012, 'Flash gas bypass in mobile air conditioning system with R134a', *International Journal of Refrigeration* **35**(7), 1869–1877.

Tuo, H. and Hrnjak, P. 2013, 'New approach to improve performance by venting periodic reverse vapor flow in microchannel evaporator', *International Journal of Refrigeration* **36**(8), 2187–2195.

Tuo, H. and Hrnjak, P. 2014*a*, 'Enhancement of vapor–liquid separation in vertical impact T-junctions for vapor compression systems with flash gas bypass', *International Journal of Refrigeration* **40**, 43–50.

Tuo, H. and Hrnjak, P. 2014*b*, 'Vapor–liquid separation in a vertical impact T-junction for vapor compression systems with flash gas bypass', *International Journal of Refrigeration* **40**, 189–200.

Vallée, C., Höhne, T., Prasser, H.-M. and Sühnel, T. 2008, 'Experimental investigation and CFD simulation of horizontal stratified two-phase flow phenomena', *Nuclear Engineering and Design* **238**(3), 637–646.

Vasquez, V. R. and Whiting, W. B. 2005, 'Accounting for both random errors and systematic errors in uncertainty propagation analysis of computer models involving experimental measurements with monte carlo methods', *Risk analysis* **25**(6), 1669–1681.

Villermaux, E. and Bossa, B. 2009, 'Single-drop fragmentation determines size distribution of raindrops', *Nature Physics* **5**(9), 697–702.

Volk, A., Ghia, U. and Stoltz, C. 2017, 'Effect of grid type and refinement method on CFD-DEM solution trend with grid size', *Powder Technology* **311**, 137–146.

Walvekar, R. G., Choong, T. S., Hussain, S., Khalid, M. and Chuah, T. 2009, 'Numerical study of dispersed oilwater turbulent flow in horizontal tube', *Journal of Petroleum Science and Engineering* **65**(3), 123–128.

Wang, B., Shi, W., Han, L. and Li, X. 2009, 'Optimization of refrigeration system with gas-injected scroll compressor', *International Journal of Refrigeration* **32**(7), 1544–1554.

Wang, S., Mohan, R. S., Shoham, O., Marrelli, J. D. and Kouba, G. E. 2000, 'Performance improvement of gas liquid cylindrical cyclone separators using integrated level and pressure control systems', *Journal of energy resources technology* **122**(4), 185–192.

White, F. 1991, *Viscous Fluid Flow*, McGraw-Hill, New York.

Wiencke, B. 2011, 'Fundamental principles for sizing and design of gravity separators for industrial refrigeration', *International Journal of Refrigeration* **34**(8), 2092–2108.

Wika 2011, *Pressure transmitter model A-10*, Wika Alexander Wiegand SE & Co.Kg, Alexander Wiegand -StraBe 30 63911 Klingenberg / Germany.

Wojtan, L., Ursenbacher, T. and Thome, J. R. 2005, 'Investigation of flow boiling in horizontal tubes: Part ia new diabatic two-phase flow pattern map', *International Journal of Heat and Mass Transfer* **48**(14), 2955–2969.

Wu, F. 1984, 'Drum separator design: a new approach', *Chemical Engineering* **91**(7), 74–80.

Xiong, Z., Lu, M., Wang, M., Gu, H. and Cheng, X. 2014, 'Study on flow pattern and separation performance of air–water swirl-vane separator', *Annals of Nuclear Energy* **63**, 138–145.

Xu, Hhwang, R. and Pham 2012, Performance measurement of R32 in vapor injection heat pump system, *in* 'International Refrigeration and Air conditioning Conference', United States.

Xu, X., Hwang, Y. and Radermacher, R. 2011*a*, 'Refrigerant injection for heat pumping/air conditioning systems: Literature review and challenges discussions', *International Journal of Refrigeration* **34**(2), 402–415.

Xu, X., Hwang, Y. and Radermacher, R. 2011*b*, 'Transient and steady-state experimental investigation of flash tank vapor injection heat pump cycle control strategy', *International Journal of Refrigeration* **34**(8), 1922–1933.

Xu, Y. and Fang, X. 2013, 'A new correlation of two-phase frictional pressure drop for condensing flow in pipes', *Nuclear Engineering and Design* **263**, 87–96.

Xue, Y., Li, H., Hao, C. and Yao, C. 2016, 'Investigation on the void fraction of gas–liquid two-phase flows in vertically-downward pipes', *International Communications in Heat and Mass Transfer* **77**, 1–8.

Yan, X., Jia, Y., Wang, L. and Cao, Y. 2017, 'Drag coefficient fluctuation prediction of a single bubble rising in water', *Chemical Engineering Journal* **316**, 553–562.

Yang, J., Reichert, P., Abbaspour, K. C., Xia, J. and Yang, H. 2008, 'Comparing uncertainty analysis techniques for a swat application to the chaohe basin in china', *Journal of Hydrology* **358**(1-2), 1–23.

York, O. H. 1954, 'Performance of wire-mesh demisters', *Chemical Engineering Progress* **50**(8), 421–424.

Yuling, L., Limin, H., Guodong, W. et al. 2008, 'Numerical simulation of flow field inside gravitational separator with different internals', *China Petroleum Machinery* **2**, 005.

Zarrouk, S. J. and Purnanto, M. H. 2015, 'Geothermal steam-water separators: Design overview', *Geothermics* **53**, 236–254.

Zhai, L.-S., Jin, N.-D., Zong, Y.-B., Hao, Q.-Y. and Gao, Z.-K. 2015, 'Experimental flow pattern map, slippage and time–frequency representation of oil–water two-phase flow in horizontal small diameter pipes', *International Journal of Multiphase Flow* **76**, 168–186.

Zheng, N., Zhao, L., Hwang, Y., Zhang, J. and Yang, X. 2016, 'Experimental study on two-phase separation performance of impacting T-junction', *International Journal of Multiphase Flow* **83**, 172–182.

Zhou, Y. H. 2013, Experimental and simulation studies on performance of a compact gas/liquid separation system, PhD thesis, School of engineering process system engineering, Cranfield University.

Zhuang, X., Gong, M., Chen, G., Zou, X. and Shen, J. 2016, 'Two-phase flow pattern map for R170 in a horizontal smooth tube', *International Journal of Heat and Mass Transfer* **102**, 1141–1149.

Appendix A

Drawings and design of apparatus

A.1 Condenser design and assembly

A vacuum condenser was developed for this work. The condenser consisted of two pipes: an inner brass pipe and an outer PVC shell which are connected and sealed by a combination of flanges. The inner brass pipe was connected to a vacuum pump through a set of flanges, while the outer PVC shell was connected to a cooling water circulation system using flexible hoses. Figure A.1 illustrates the configuration of the vacuum condenser and its connection details.

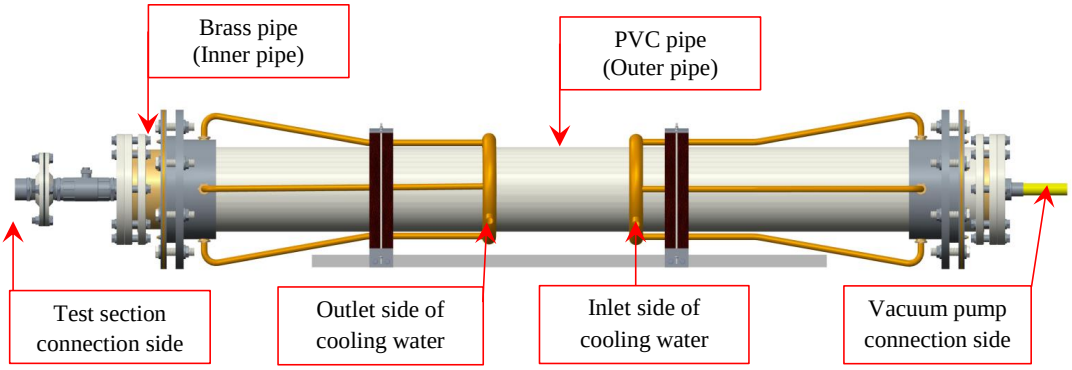

Figure A.1: Configuration of the vacuum condenser and its connections.

The vacuum condenser was mounted horizontally. The test section was connected with the inner brass tube by using a combination of fittings. The cooling water pump was connected between the cooling water tank and the PVC pipe to circulate a cooling water.

To ensure that the ends of the condenser were sealed, a special flange was designed to use an O-Rings on the inner and side faces. Figure A.2 presents the design of the O-Ring flange and Figure A.3 shows the location of the O-Ring flange and flange combination.

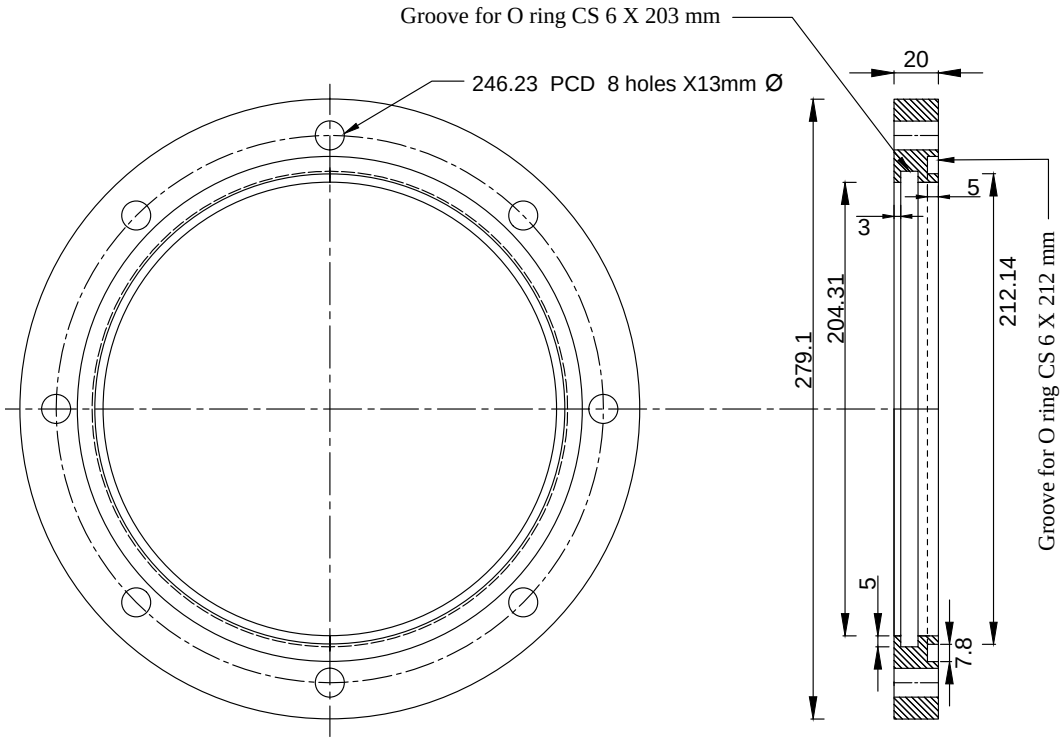

Figure A.2: Schematic diagram of the O-ring flange.

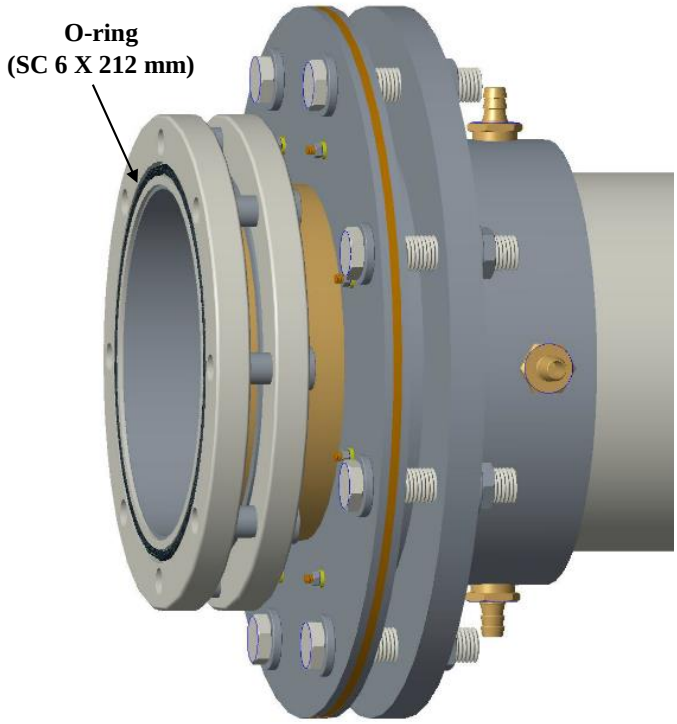

Figure A.3: Condenser vacuum side showing the location of the O-ring and flange combination.

Then the end of the condenser was closed by the end flange. Figure A.4 shows the end flange configuration and its dimensions. The end flange was seated on the side face of the O-ring flange and connected to it by bolts. In order to hold all the flanges and provide sealing, a retaining flange was designed and fabricated. Figure A.5 shows the retaining flange configuration and its dimensions. All the flanges were connected with each other to seal the brass pipe properly. Figure A.6 presents the connection details of the combination of the flanges that were used to seal the brass pipe.

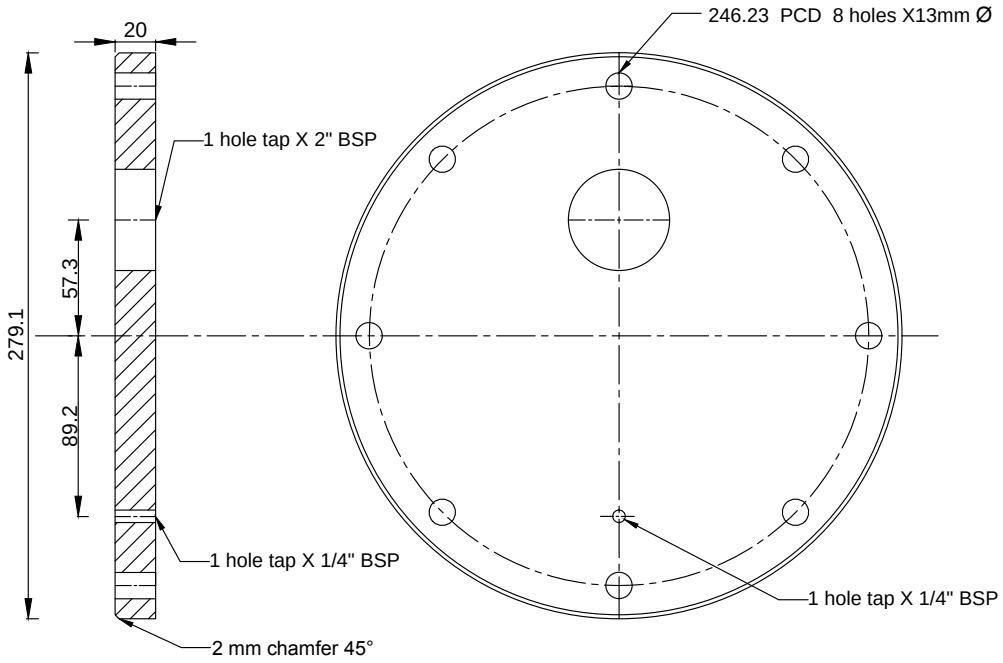

Figure A.4: Schematic diagram of the end plate flange and its dimensions.

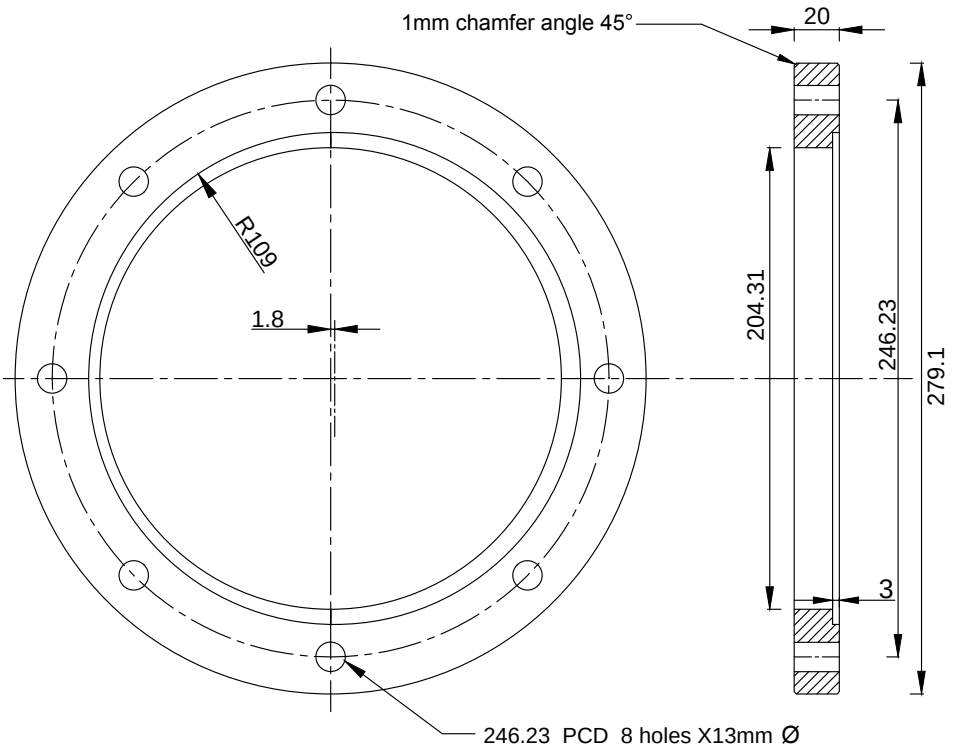

Figure A.5: Schematic diagram of the retaining flange and its dimensions.

Aluminium flanges were designed to connect the brass pipe and its sealing flange combination to the PVC pipe. The aluminium flanges seal the outer surface of the

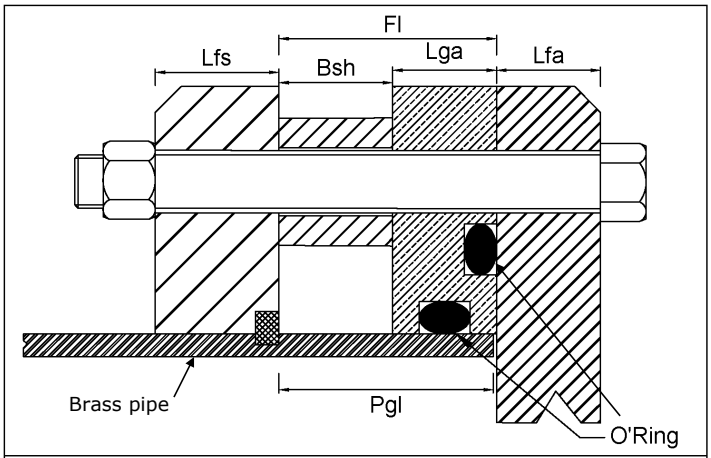

Flange Connection Details

Bsh	13.5 mm (Bush)	Pgl	33 mm
Lfs	20 mm (Steel Flange)	Fl	33.5 mm
Lfa	20 mm (Aluminum Flange)		
Lga	20 mm (Aluminum Grooved Flange)		

Figure A.6: Combination of the flange connection around the brass pipe.

brass pipe to prevent water leaking out of the PVC shell. Figure A.7 and Figure A.8 show the design and a photo of the aluminium flanges. The aluminium flanges centralise the PVC pipe. Figure A.9 presents the details of the flange combination and its connection to hold and seal the PVC and brass pipes.

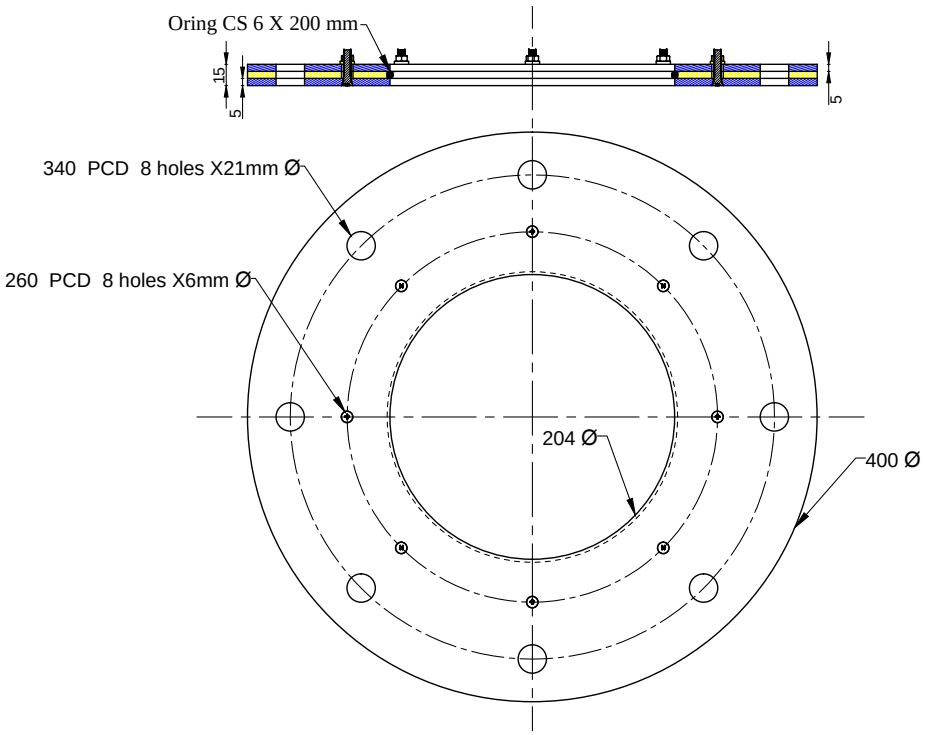

Figure A.7: Dimensions of the aluminium sealing flanges to connect to the PVC pipe.

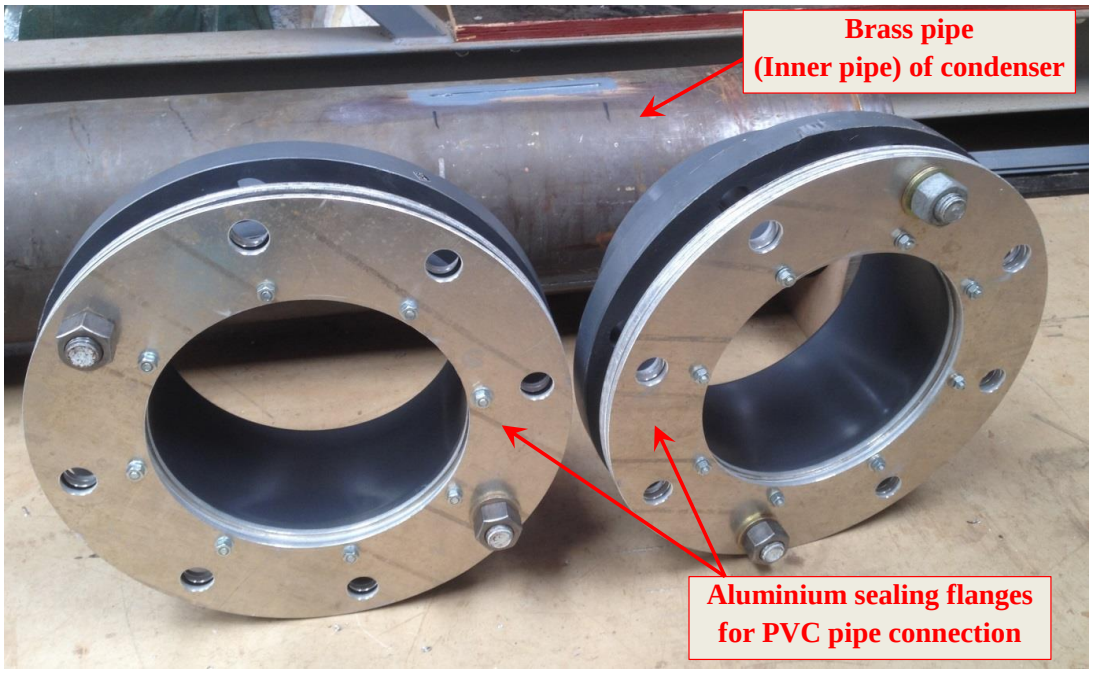

Figure A.8: Aluminium sealing flanges to connect the PVC pipe and the brass pipe.

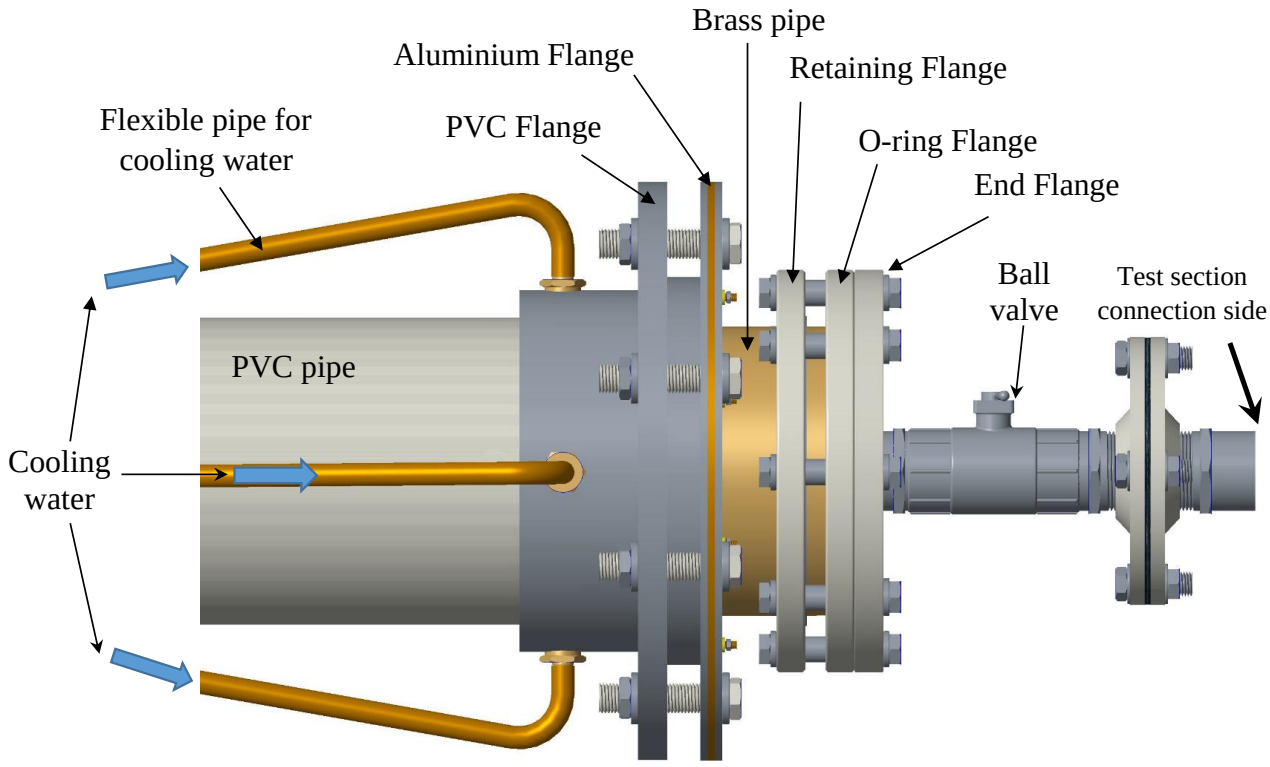

Figure A.9: Details of the flange combination connection to hold and seal the PVC and brass pipes on the test section connection side.

The path of the cooling water in the PVC pipe is completely separated from the vacuum side and there is nothing inside the brass pipe. Figure A.10 presents a section view of the upstream of the vacuum condenser presenting the inside configuration of the condenser and cooling water path.

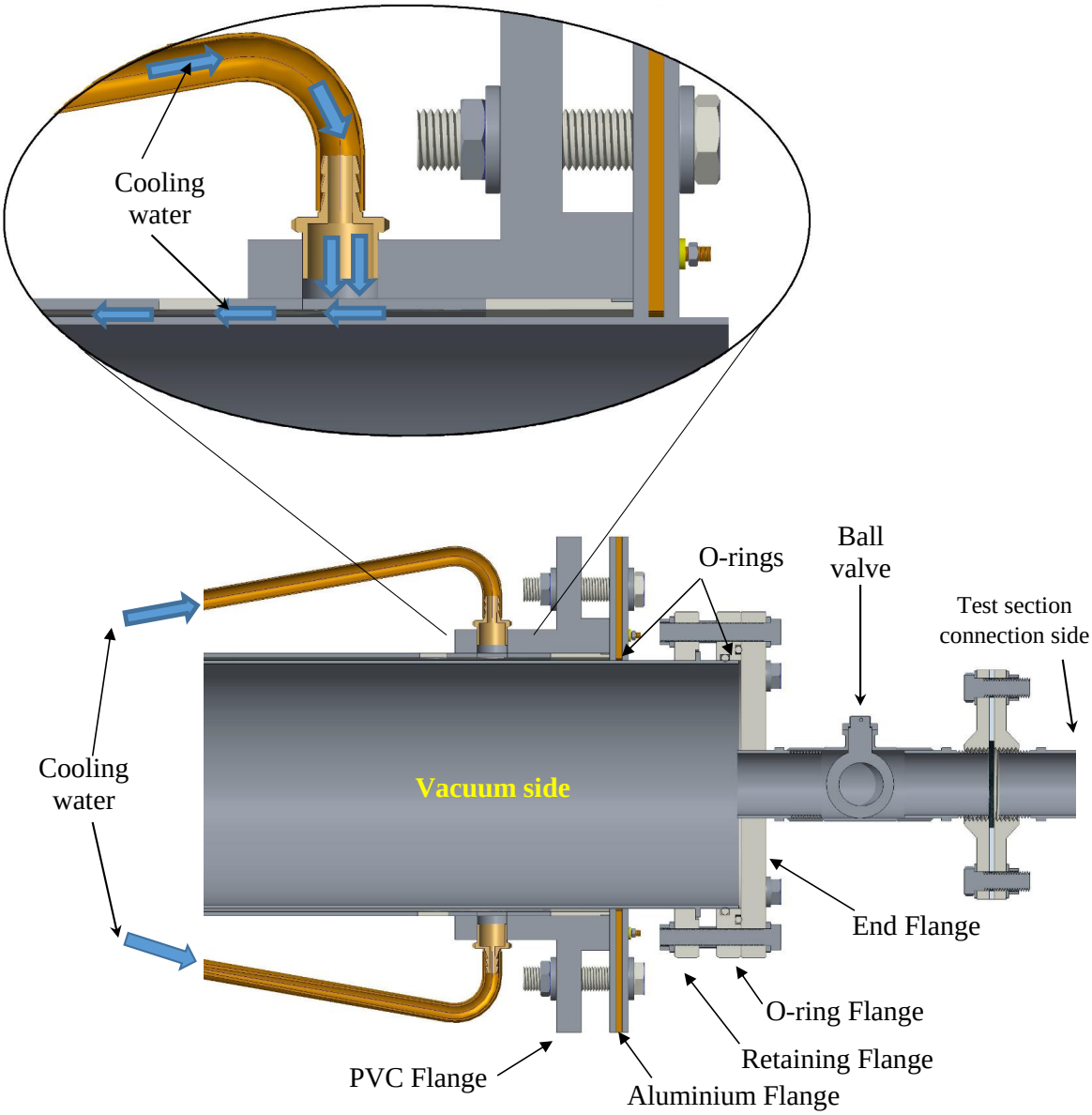

Figure A.10: Section view of the condenser on the upstream test section connection side.

A.2 Expansion device design

A.2.1 Description of expansion device design

An expansion device was fabricated at the University of Southern Queensland using a 3D printer. The expansion device provided a pressure drop across a flow length of 65 mm and supplied a uniform distribution of the two-phase flow through 400 × 0.3 mm diameter holes. Figure A.11 present the details of the expansion device

through a section view and a photo of the 3D printed expansion device. VisiJet crystal (EX 200 plastic material) was used to fabricate the expansion device. The VisiJet crystal has physical and chemical properties which are presented in Table A.1. The VisiJet is chemically stable under normal conditions of handling, use and transportation. However, it should not be exposed to heat, sunlight and UV light.

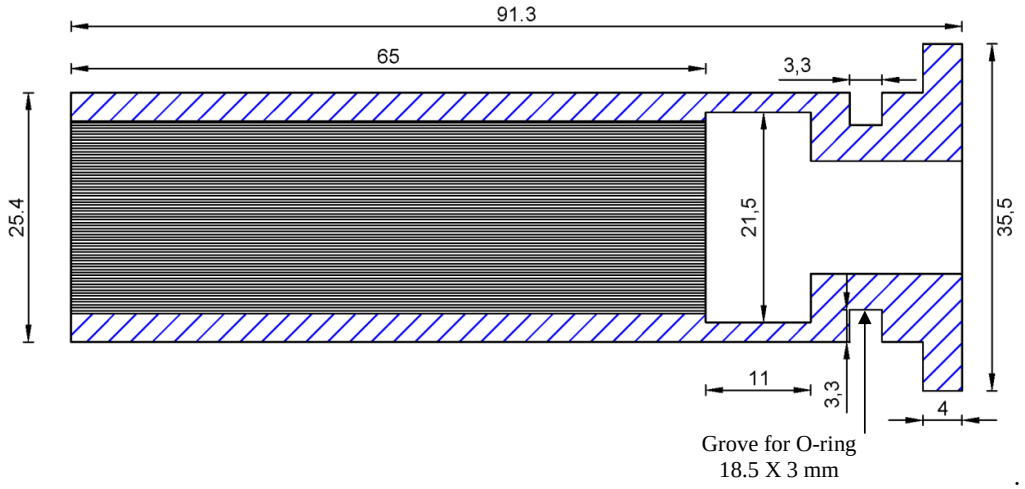

(a)

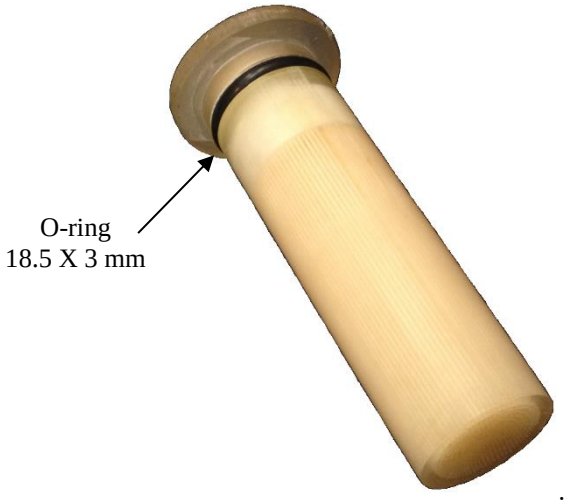

(b)

Figure A.11: Expansion device (a) section view of the expansion device, (b) photo of 3D printed device.

Table A.1: Data on the VisiJet crystal plastic material.

Physical and chemical properties	
Appearance .....Natural	Odor .....Mild
Physical State .....Soft solid to paste	PH ..... 6-7 at 1:1 in Water
Vapour Pressure .....2Pa at 20 ℃	
Boiling Point .....200 ℃	Melting/Freezing Point .....55-65 ℃
Solubility (H2O) .....Insoluble at 20 ℃	Specific Gravity .....1.1 g/m^3 at 25 ℃

A.2.2 Connection of the expansion device

The expansion device was connected with an acrylic transparent pipe and a needle valve. An O-ring 18.5 × 3 mm was used around the expansion device for sealing. Figure A.12 shows the configuration of the expansion device connection in the horizontal tube experiments. A PVC end cup with a downward direction outlet was used at the end of the horizontal tube to ensure that the flow at the downstream end discharged to the condensing receiver in a uniform manner.

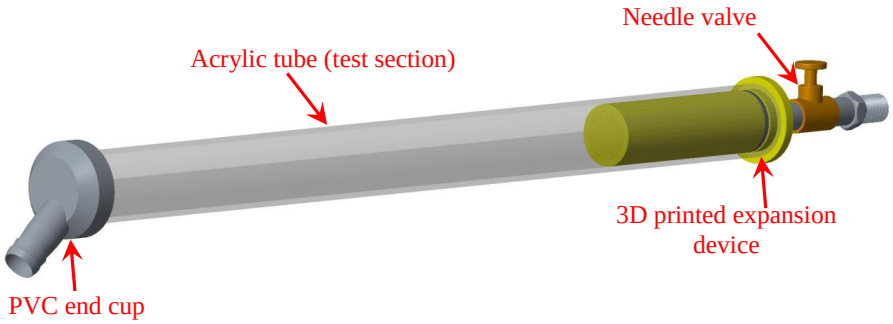

Figure A.12: Assembly of the horizontal test section tube, expansion device and needle valve with PVC end cup.

A.2.3 Pipe supporter clamp

In order to set up the horizontal pipe in a horizontal position precisely, a special clamp was designed. The clamp was printed using the 3D printer and VisiJet crystal material. Two clamps were located along the horizontal pipe. The clamp includes four grooves,defining the vertical and horizontal planes. These grooves were used to level the horizontal tube. Figure A.13 shows the details of the clamp.

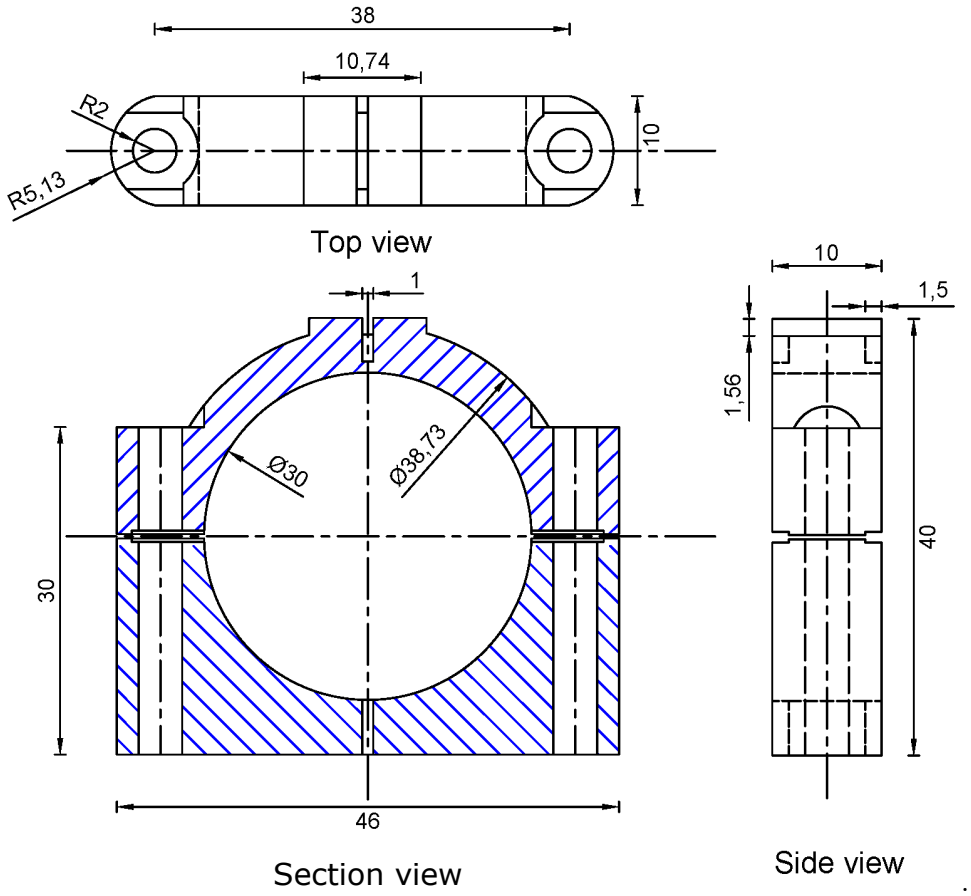

(a)

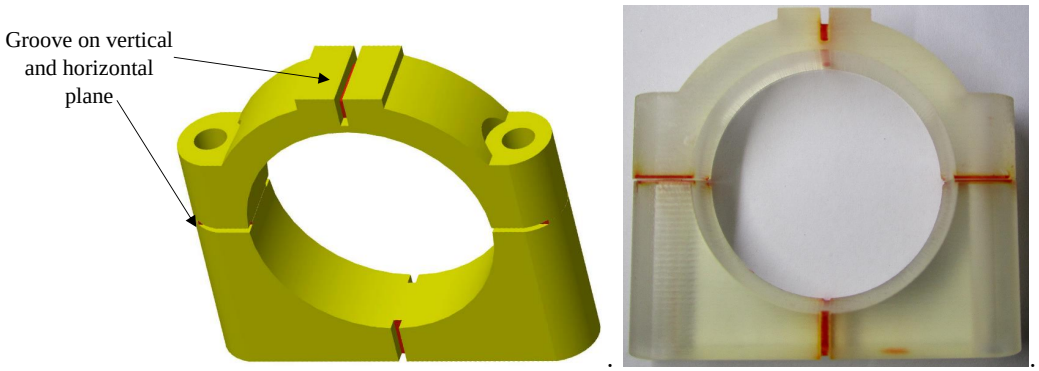

(b) (c)

Figure A.13: Special supporter clamp (a) views of the supporter clamp, (b) 3D view, (c) photo of 3D printed clamp.

A.3 Vertical flash tank separator

The vertical flash tank separators were built in five different volumes from transparent acrylic material. In order to obtain flexibility for the geometry to change the body volume, aluminium flanges were designed to provide the liquid and gas outlets. These flanges seal the top and bottom of the separator through O-rings (CS 3 X ID 44.2 mm). Figure A.14 presents the configuration of the vertical flash tank separator model VFT-V3.

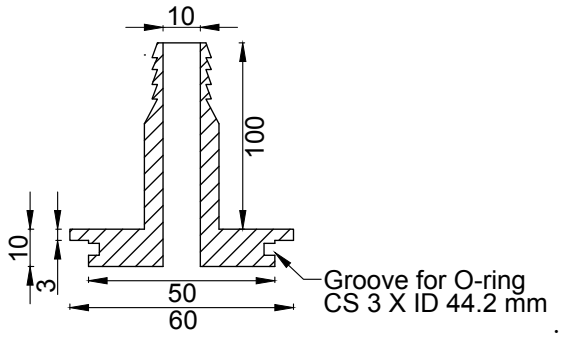

(a)

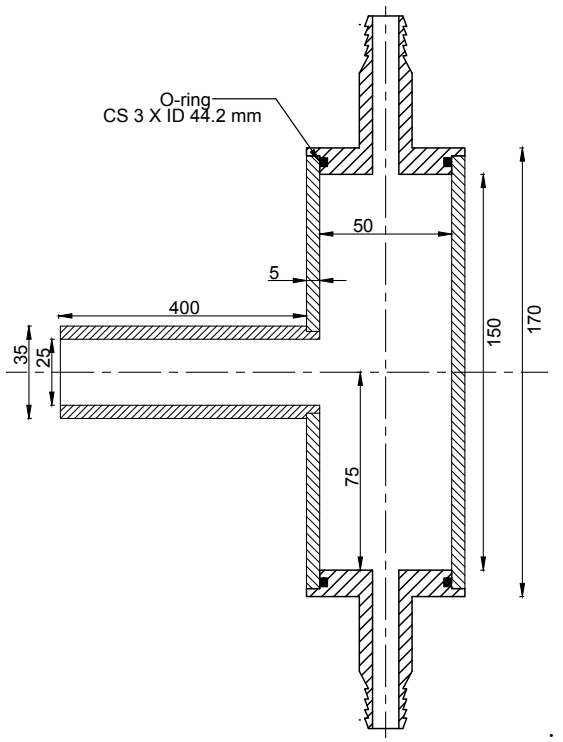

(b)

Figure A.14: Vertical flash tank separator (a) Aluminium flange for top and bottom of the tank, (b) illustration of the VFT-V3 separator.

A.4 Experiment of a vertical separator

The main parts of the experimental apparatus were arranged and connected to investigate the performance of the vertical separator. Figure A.15 presents the arrangements of the main parts in the experiments of the vertical separator.

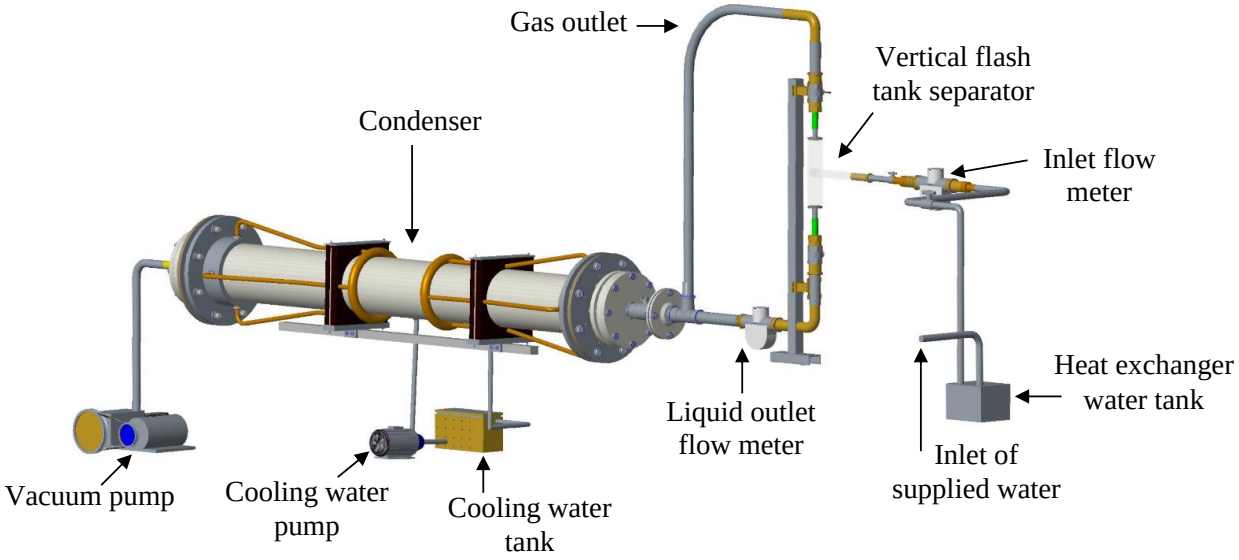

Figure A.15: Arrangement of the main parts of the experiment on the vertical separator.

Appendix B

Instrument calibration

B.1 Pressure Transducer

A hydraulic dead-weight tester, Budenberg model 580 was used to calibrate the pressure transducer (Wika A-10) which was used to measure the absolute pressure on the delivery pipe to the expansion device. Figure B.1 shows a photo of the hydraulic dead weight tester. Transducers with a lower operating pressure were also used, but because these were newly acquired from the manufacture for these experiments, the calibration provided by the manufacture were used. Table B.1 presents the calibration equations for each of the pressure transducers.

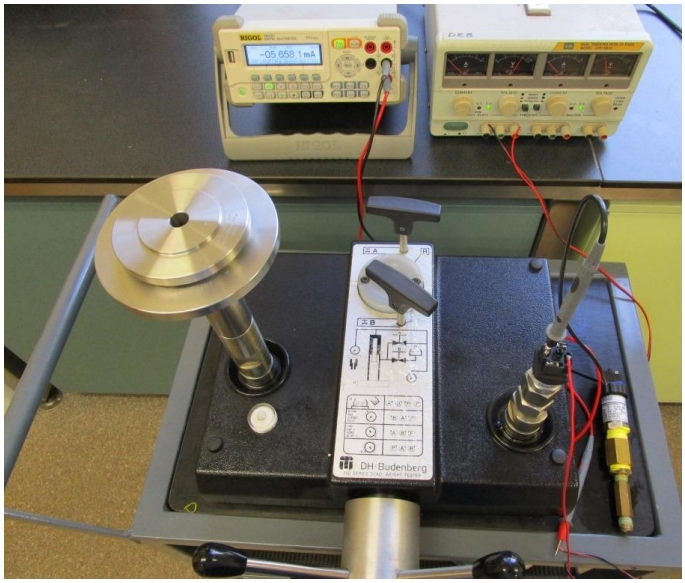

Figure B.1: Photograph of the hydraulic dead-weight tester Budenberg model 580.

Table B.1: Calibration of Wika pressure transducers. V_{meas}= measured voltage, L.P. lower pressure, and H.P. high pressure.

	Serial Number	Type	Pressure	Equation
1	1A007IB5HO	Wika	L.P.	Pa=0.2005V_{meas}-1.0037+Patm
2	1A0077IAZIH	Wika	L.P.	Pa=0.2005V_{meas}-1.0034+Patm
3	1A0077ICLI5	Wika	L.P.	Pa= 0.2004V_{meas}-1.0036+Patm
4	1A0077I80HG	Wika	L.P.	Pa= 0.2005V_{meas}-1.0038+Patm
5	1A0077I9O24	Wika	L.P.	Pa= 0.2004V_{meas}-1.0034+Patm
6	1A005U813IM	Wika	H.P.	Pa =0.3208V_{meas}-0.0056

B.2 RTD calibration check

Resistance temperature detectors (RTD) were used to measure the temperature in the experiments of the the present work. The RTD platinum resistor (PT100) produces a more linear response than thermocouples or thermistors and in order to ensure that RTD works properly a small test was completed by using a mercury thermometer to measure the temperature in different range. The differences between the RTD temperature sensor and mercury thermometer were less than 0.1 ℃. Figure B.2 shows a comparison of temperature reading between the mercury thermometer and RTD temperature sensor in different range of temperature.

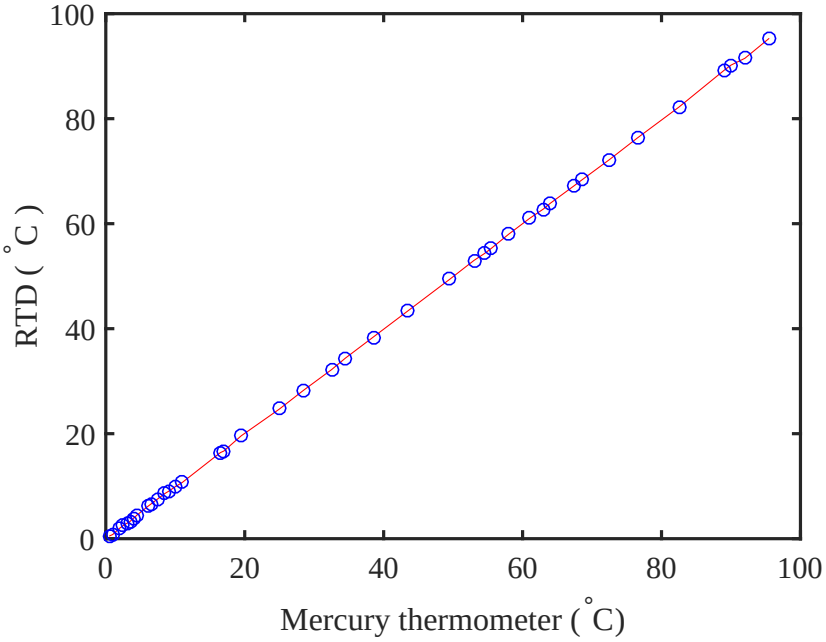

Figure B.2: Comparison of temperature reading between the mercury thermometer and RTD temperature sensor.

B.3 Mass flow rate calibration

The Yokogwa mass flow meter, which consists of transmitter model RCCF31 and sensor model RCCS32, and the Siemens flow meter, which consists of a transmitter model FCT030 and sensor model FCS400, were used to measure the flow rate in the horizontal pipe and vertical flash tank separator experiments. These two meters were calibrated using a timer and certain volume of water and results were in good agreement with the manufacture's calibration.

Appendix C

Experimental procedures

C.1 Procedures for horizontal pipe

In the horizontal pipe experiment the arrangement is presented in Figure C.1. The operating steps are:

1. Close the ball valve 1.
2. Close the ball valve 2.
3. Close the liquid drain valve 4.
4. Run the vacuum pump after ensuring the ball valve 3 is open.
5. While the vacuum pump is running, turn on the water pump to cool down the condenser. Ice is used to maintain a low temperature in the cooling water tank.
6. Turn on the 3.5 kW electrical immersion element heaters used to raise the temperature of the water in the heat exchanger. The immersion heater is electronically controlled to maintain the required temperature. Water is sourced from a mains water supply.
7. Open the ball valve 2. Upon reaching about 1 kPa in the condenser, open and adjust the ball valve 1 that is located between the heat exchanger and the flow meter to set the required flow according to operation condition of the experiment.

8. Keep both the vacuum pump and water pump running during the experiment operating time.

9. Record, the two-phase flow behaviour at the two positions: directly after the expansion device and at the developed region (1665 mm from the inlet). A digital camera (Sony model SLT-A57) was used and simultaneously the pressure is recorded using pressure transducers during the experiment operating time.

10. All the above steps were repeated in every experiment.

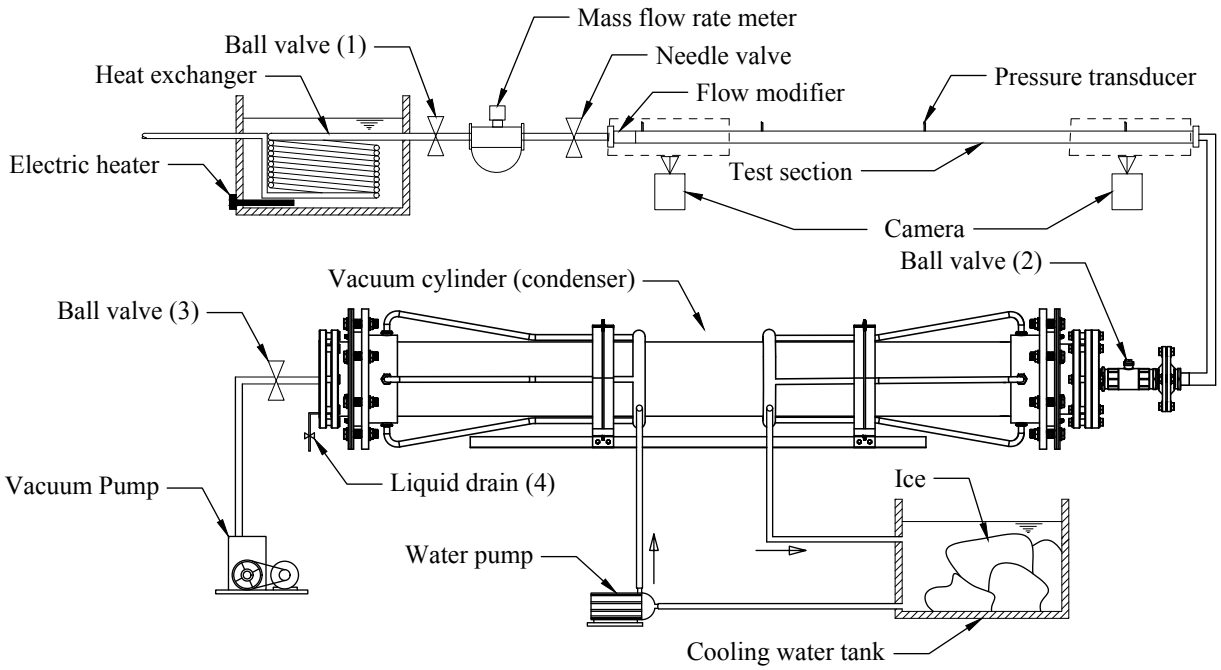

Figure C.1: Experimental arrangement for the horizontal pipe experiment.

C.2 Procedures for flash tank

In the vertical flash tank separator experiment the arrangement is presented in Figure C.2. The operating steps are similar to that in the horizontal pipe experiment except there was an additional mass flow meter that was set up to measure the separated liquid at the liquid outlet.

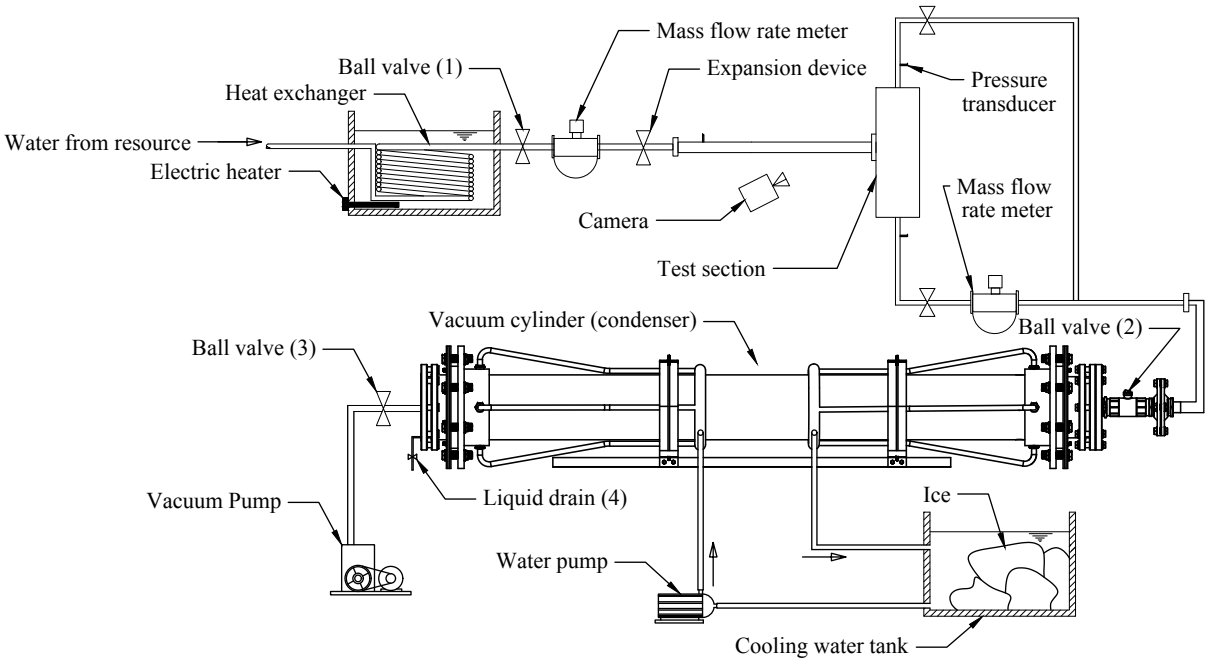

Figure C.2: Experimental arrangement for the vertical flash tank experiment.

Appendix D

Vapour quality calculation

The vapour quality at the inlet of the horizontal tube directly after the expansion device can be calculated on the assumption of adiabatic conditions in the expansion device based on the measured inlet temperature and measured pressure downstream. For example, at the operating condition of 8.1 g/s, the temperature of the water at the inlet of the expansion device was 55.6 ℃ and the pressure drop across the expansion device was 24.7 kPa. From the thermodynamic property tables for the saturated water, the enthalpy at the inlet can be found, h_i=232.77 kJ/kg. At the outlet of the expansion device, the absolute pressure was 2.64 kPa, so from the property tables the enthalpy of the liquid and vapour can be found, since h_f=91.9 kJ/kg and h_{fg}=2449.0 kJ/kg. The vapour quality can be calculated on the assumption that the process in the expansion device is adiabatic, because under these conditions the enthalpy across the expansion device is constant, giving the outlet enthalpy as $h_o = h_i$, and since the quality can be written as

$x = (h_o - h_f)/h_{fg}$

the numerical value can now be calculated

$x = (232.77 - 91.9)/2449.0 = 0.0576.$

For each operating condition, the flow quality is obtained in the manner outlined above.

Appendix E

Calculation for flow pattern map

The two-phase flow pattern map for water using the transition curve equations that were adopted from the literature was developed as shown below.

```
close all;
clear all;
clc;
NFS = 14;
NLW = 1.5;
NMS = 10;
=======================
Constant input section
=======================
Gt =150;          % Mass velocity or Mass flux (kg/s.m^2)
D =0.026;         %Tube Diameter (m)
q=0;              % Heat flux
hlv = 2446.2        % Latent heat of evaporation (kJ/kg)
Rl =985.09;         % Liquid density (kg/m^3)
Rv =0.554;          % Vapour density (kg/m^3)
ul =0.001003;         % Liquid viscosity (kg/m.s)
uv =0.0000134;        % Vapour viscosity (kg/m.s)
SL =0.00071;          %Liquid Surface Tension (N/m)
```

xvec=0:0.01:0.95;

for itr=1:length(xvec)

x=xvec(1,itr);

==========

Calculated parameter section

==========

A=(pi*D^2)/4;

XIA=((0.2914*(Rv/Rl)$^{(-1/1.175)}$*(ul/uv)$^{(-1/7))}$+1)$^{-1}$;

X_{tt}=(((1-x)/x)$^{0.875}$)*((Rv/Rl)$^{0.5}$)*((ul/uv)^0.125);

e=(x/Rv)*((1+0.12*(1-x))*((x/Rv)+((1-x)/Rl))+(1.18*(1-x)*(9.81*SL*(Rl-Rv))$^{0.25}$)/(Gt*Rl^0.5))$^{-1}$;

Al=A*(1-e);

Av=A*e;

ALD=Al/D^2;

Avd=Av/D^2;

i=1;

for theta=1:0.0001:10

Ald=(1/8)*[(2*pi-theta)-sin(2*pi-theta)];

mat(i,1)=theta;

mat(i,2)=Ald-ALD;

if abs(Ald-ALD) <10^{-5}

rad=100

break

end

end

hld=0.5*(1-cos((2*pi-theta)/2));

Pid=sin((2*pi-theta)/2);

WF=(9.81*D^2*Rl)/SL;

Z=(1.138+2*log(pi/(1.5*Ald)))$^{-2}$;

qc=0.131*(Rv$^{0.5}$)*hlv*(9.81*(Rl-Rv)*SL)$^{0.25}$;

Fq1=646*((q/2)/qc)^2+(64.8*((q/2)/qc));

Fq2=18.8*((q/2)/qc)+1.023;

h=hld*D;

==========

Transition curves calculation section

==========

Mass velocity in wavy flow regime

G_{wavy}(1,itr)=(((16*(Avd^3)*9.81*D*Rl*Rv)/((x^2)*(pi^2)*(1-((2*hld)-1)^2)$^{0.5}$))*

((((pi^2)/(25*(hld^2)))*(1-x)$^{(-Fq1)}$)*((WF)$^{(-Fq2)}$)+1))$^{0.5}$+50-(75*exp(-(x$^{2-0.97}$)^2/

(x*(1-x)))); Mass velocity in mist flow regime

G_{mist}(1,itr)=((7680*Avd^2*9.81*D*Rl*Rv*(1/WF))/(x^2*pi^2*Z))$^{0.5}$; Mass Velocity in stratified flow regime

G_{start}(1,itr)=(((226.3^2)*Ald*(Avd^2)*Rv*ul*9.81*(Rl-Rv))/(x^2*(1-x)*pi^3))$^{(1/3)}$+20*x;

Mass Velocity in bubbly flow regime

G_{bubbly}(1,itr)=((256*Avd*(Ald^2)*(D$^{1.25}$)*Rl*(Rl-Rv)*9.81)/(0.3164*((1-x)$^{1.75}$)*pi^2*

Pid*ul$^{0.25}$))$^{(1/1.75)}$;

==========

Plotting the transition curves of two-phase map section

==========

plot(xvec(6:end)*100,G_{wavy}(6:end),'k-','LineWidth',NLW);hold on;

plot(xvec(6:end)*100,G_{start}(6:end),'k-','LineWidth',NLW);hold on;grid on;

plot(xvec(6:end)*100,G_{mist}(6:end),'k-','LineWidth',NLW);hold on;

plot(xvec(6:end)*100,XIA(6:end),'k-');

Appendix F

Uncertainty analysis

F.1 Quantification of random errors — horizontal pipe

Table F.1 illustrates an example of the random errors associated with the horizontal pipe flow experiment in determining the liquid height in the fully developed region. In the Table F.1, S1, S1, S3, S4, S5, ..., S10 are 10 different measurements of the liquid height in each experiment. Ave is the mean of the ten liquid height measurements in each experiment and 2σ is twice the standard deviation.

Table F.1: Measurements of liquid height in the fully developed region for the range of mass flow rates.

Flow rate (g/s)	S1 (mm)	S1 (mm)	S3 (mm)	S4 (mm)	S5 (mm)	S6 (mm)	S7 (mm)	S8 (mm)	S9 (mm)	S10 (mm)	Ave (mm)	2σ (mm)
2.1	1.7	1.8	1.7	1.7	2.1	2.1	2.1	1.9	2.2	2.1	1.94	0.20
5.1	1.9	2.1	2	2	2.2	2.2	2.4	2.3	2.4	2.7	2.22	0.23
8.18	3	3	2.3	2.2	2.8	2.4	2.7	3.5	2.5	2.4	2.68	0.40
10.21	3.2	3	3.1	2.5	3.2	3	3	3.1	2.8	3.1	3.00	0.21
13.1	3.5	3	3.7	3.5	3.2	3.8	3.3	2.7	3.4	3.8	3.39	0.35
23.4	4.9	5	5.2	5.3	5.7	5.3	5.2	5.5	5.1	4.9	5.21	0.25

F.2 Quantification of random errors — flash tank

For the vertical flash tank separator experiments, Tables F.2 and F.3 present an example of the random errors in the mass flow rates. In these tables, m1, m2, m3, ..., m7 are 7 different measurements of the mass flow rate at the inlet ($\dot{m}_{total}$) and liquid outlet ($\dot{m}_{L,out}$) of the vertical flash tank separator. Ave is the mean, and 2σ is twice the standard deviation of the seven mass flow rate measurements in each experiment.

Table F.2: Measurements of mass flow rates of vertical flash tank VFT-V1 at operating condition 2.1 g/s.

Flow rate (g/s)	m1	m2	m3	m4	m5	m6	m7	Ave	2σ
$\dot{m}_{total}$	2.1	2.0	2.3	2.0	2.3	2.0	2.0	2.1	0.11
$\dot{m}_{L,out}$	1.54	1.74	1.4	1.8	1.54	1.5	1.8	1.62	0.11

Table F.3: Measurements of mass flow rates of vertical flash tank VFT-V3 at operating condition 8.1 g/s.

Flow rate (g/s)	m1	m2	m3	m4	m5	m6	m7	Ave	2σ
$\dot{m}_{total}$	8.1	8.0	7.9	8.3	8.3	7.9	8.2	8.1	0.14
$\dot{m}_{L,out}$	7.1	7.3	6.8	7.5	7.3	7.2	7.4	7.2	0.13

F.3 Uncertainty in measured parameters — horizontal pipe

In order to illustrate the calculation of experimental uncertainty, an example calculation is presented for the inlet pressure measurement in the horizontal pipe experiments. At the inlet mass flow rate of 5.1 g/s, the inlet pressure was measured several times using a pressure transducer which was connected to the data acquisition system. The data acquisition system was set to record at 100 samples per second, so a range of the inlet pressure was recorded.

From the measured inlet pressure, P_{inlet}=(2.39, 2.21,..., 2.43), all in kPa, the mean of the inlet pressure was obtained and was equal to 2.39 kPa. In order to present the uncertainty of the measured inlet pressure, the double standard deviation (2σ) was determined to be 0.23 kPa, which represents the random component of the measurement uncertainty. A systematic uncertainty component arises from the pressure transducer calibration of ±0.5 kPa, see Section 4.10.3. Assuming the components of uncertainty are statistically independent, the total experimental uncertainty is $\sqrt{(0.23)^2 + (0.5)^2} = 0.55$, so the inlet pressure has an uncertainty of ± 0.55 kPa in this study. Similar calculations were applied to the temperature measurement, outlet pressure and mass flow rate, and the results are presented in Table F.4.

Table F.4: Sample of experimental uncertainty calculation of measured quantity in the horizontal pipe experiments for case 1.

Quantity	Mean	2σ	Uncertainty of instrument ±	Total uncertainty ±
Inlet mass flow rate (g/s)	2.1	0.11	0.2	0.21
Inlet temperature (℃)	20.2	1.62	0.1	1.62
Inlet pressure (kPa)	2.36	0.21	0.5	0.55
Outlet pressure (kPa)	2.06	0.18	0.5	0.53
Vapour quality(%)	5.8	-	-	0.006

F.4 Uncertainty in vapour quality — horizontal pipe

The calculation of flow quality produced by the expansion device is sensitive to both the inlet flow temperature (T_i) and the outlet pressure (P_o) as described in Appendix D. For representative operating conditions in the present experiments, $\frac{\partial x}{\partial T_i} = 0.0617$ units/℃, $\frac{\partial x}{\partial P_o}$ = -0.0103 units/kPa.

From Table F.4, for the 2.1 g/s flow rate case, the combined (systematic plus random) uncertainty in the temperature is 1.6℃ and the combined (systematic plus random) uncertainty in the pressure is 0.55 kPa. Therefore, the overall uncertainty of the vapour quality can be calculated as $\left[(\frac{\partial x}{\partial T_i}1.6)^2 + (\frac{\partial x}{\partial P_o}0.55)^2\right]^{1/2} = 0.006$.

Therefore, in the 2.1 g/s flow rate case, the flow quality is specified as $x = 0.058 \pm 0.006$.

F.5 Uncertainty in void fraction — horizontal pipe

In the void fraction (α) uncertainty calculation, the area occupied by the vapour (A_V) was estimated by subtracting the area occupied by liquid (A_L) from the total area of the pipe, $A_V = A_t - A_L$. A_L is a function of the measured liquid height L_H. So, by taking the mean values of L_H and A_L, A_V can be calculated. The void fraction was calculated by dividing A_V by the total area $A_L + A_V$. The accuracy interval (u_A) for each area occupied by liquid and vapour was estimated by double standard deviation (2σ). The experimental uncertainty of the void fraction is presented in Table F.5.

Table F.5: Sample of void fraction uncertainty calculation for 2.1 g/s.

A_t (mm^2)	A_V (mm^2)	α
490 ± 2	474 ± 5	0.97 ± 0.01

F.6 Uncertainty in separation efficiency and quality — flash tank

Liquid separation efficiency (η_L) of the vertical flash tank separator is a derived quantity that is calculated from the measured mass flow rates, it is the ratio between the mass flow rate at the liquid outlet ($\dot{m}_{L,outlet}$) and the liquid mass flow rate at the inlet ($\dot{m}_{L,inlet}$). In the experiment, the total mass flow rate was measured at the inlet of the separator ($\dot{m}_{total}$) and the mass flow rate at the liquid outlet ($\dot{m}_{L,outlet}$) was also measured. In order to calculate the overall uncertainty of the mass flow rate, the random error needs to be combined with the systematic error which was obtained from the calibration of the mass flow rate sensors. Section F.2 presented an example showing the identification of the random errors for the inlet mass flow rate and liquid outlet mass flow rate of the vertical flash tank separator (as represented by 2σ). Table 4.5 presented the systematic uncertainty of the mass flow rate sensors, so the overall uncer-

tainty for the inlet mass flow rate can be obtained from $u_{m,total} = ((u_{mt})^2 + (u_{mf}^2))^{1/2}$, where u_{mt} is the random uncertainty of the inlet mass flow rate and u_{mf} is the systematic uncertainty of the flow meter device. Similar calculations were applied to the mass flow rate at the outlet of the vertical separator giving the quantity $u_{mL,outlet}$, and results are shown in Table F.6.

Vapour quality x_3 at the gas outlet of the vertical flash tank separator is a derived quantity that is calculated based on the measured mass flow rates, so the uncertainty of the vapour quality can also be calculated based on the uncertainty of the mass flow rates. The vapour quality at the gas outlet is a ratio between the vapour mass flow rate $\dot{m}_g$ and the total mass flow rate at the gas outlet $\dot{m}_{t,Gout}$. In the experiment, the total mass flow rate was measured at the inlet of the separator $\dot{m}_{total}$ and the mass flow rate at the liquid outlet was also measured $\dot{m}_{L,outlet}$. Therefore, $\dot{m}_{t,Gout}$ can be obtained by $\dot{m}_{t,Gout} = \dot{m}_{total} - \dot{m}_{L,outlet}$. So, the uncertainty of mass flow rate at the gas outlet ($u_{mt,Gout}$) can be obtained by combining the uncertainty of the total mass flow rate at the inlet ($u_{m,total}$) with the uncertainty of the liquid mass flow rate at the liquid outlet ($u_{mL,outlet}$). The total uncertainty of the vapour quality can then also be obtained. Results of the uncertainty of the vapour quality are summarized in the Table F.6.

Table F.6: Sample of results for vapour quality uncertainty calculation for the gas outlet of the vertical flash tank separator.

$\dot{m}_{total}$ g/s	$\dot{m}_{L,outlet}$ g/s	$\dot{m}_{t,Gout}$ g/s	$\dot{m}_g$ g/s	x_3
23.5 ± 0.2	21.4 ± 0.1	2.1 ± 0.1	1.2 ± 0.1	0.2 ± 0.1

Similar calculations were applied to calculate the uncertainty of the separation efficiency which are summarized in the Table F.7.

Table F.7: Sample of separation efficiency uncertainty calculation for the vertical flash tank separator.

$\dot{m}_{total}$ g/s	$\dot{m}_{L,outlet}$ g/s	$\dot{m}_{t,Gout}$ g/s	$\dot{m}_{L,inlet}$ g/s	η_L
23.5 ± 0.2	21.4 ± 0.1	2.1 ± 0.1	22.3 ± 0.2	0.95 ± 0.05

Uncertainties in the vertical flash tank separator experiments for the measured quantities: temperature, inlet mass flow rate, mass flow rate at liquid outlet, and pressure at the outlet and inlet are presented in Table F.8.

Table F.8: Sample of experimental uncertainty of measured quantities in the vertical flash tank separator experiments for case 1.

Quantity	Mean	2σ	Uncertainty of instrument $\pm$	Total uncertainty $\pm$
Inlet mass flow rate (g/s)	2.1	0.11	0.2	0.21
Mass flow rate at liquid outlet (g/s)	1.7	0.11	0.1	0.15
Inlet temperature (℃)	20.2	1.6	0.1	1.6
Inlet pressure (kPa)	2.54	0.25	0.5	0.55
Pressure at liquid outlet (kPa)	2.05	0.17	0.5	0.52
Pressure at gas outlet (kPa)	2.05	0.17	0.5	0.52
Vapour quality	0.058	n/a	n/a	0.006

Appendix G

Flash tank sizing calculation

Settling theory is used here to illustrate the theoretical size of a vertical flash tank. The equations of the settling theory were described in Section 2.5, so these equations can be used to calculate the theoretical size of a vertical flash tank separator. The drag coefficient (C_D) was obtained from the correlation that presented by White (1991) as it covers wide range of the Reynolds number, see Table 2.1. Then, terminal velocity, diameter, and height of the vertical flash tank separator can be obtained as follows,

$$U_T = \sqrt{\frac{4.g.d_d^*.(\rho_l - \rho_g)}{3.\rho_g.C_D}} \tag{G.1}$$

$$D = \sqrt{\frac{4\dot{V}}{\pi U_T}} \tag{G.2}$$

$$H = \frac{4\dot{V}}{\pi D U_T} \tag{G.3}$$

The operating condition of case 6, as shown in Table 4.7, was used to illustrate the vertical flash tank separator sizing. Based on the expansion device design, which has a large number of 0.3 mm diameter tubes as presented in Section 4.4, the liquid droplets were assumed to be spherical with a diameter of 0.3 mm. The density and viscosity of vapour and liquid of water were obtained from the properties tables at 23.1 ℃.
For these case 6 conditions, the combination of U_T, Re and C_D that satisfies Equation G.1 and the Re-C_D relationship (Section 2.5) is U_T = 3.97 m/s, Re = 2.73, and

$C_D = 11.49$. The diameter and height of the vertical flash tank can then be calculated directly from Equations G.2 and G.3. In this case, the diameter and height of the vertical flash tank were obtained, 175.6 mm and 175.6 mm. This sizing calculation gives a separator height that is comparable to the largest size used in the present experiments (250 mm, Table 4.1), although the separator diameter from sizing calculation is about three times larger than used in the present experiments (50 mm, Table 4.1).

Appendix H

Fluent 17.1 key equations

In the CFD simulations, Fluent 17.1 was used to simulate the two-phase flow in a horizontal tube and vertical flash tank separator. A summary of the key equations that are solved by Fluent is presented in this section.

H.0.1 Governing two-phase equations solved by fluent

In order to present two-phase flow equations, q and p will be used to describe liquid and gas phases respectively. The volume fraction of phase q represents the space that occupied by phase q. (Bowers, 2009) defined the volume fraction for the individual phase as the volume that occupied by that phase. So the volume of the phase (q) can be given by.

$$V_q = \int \alpha_q dV \tag{H.1}$$

where

$$\sum_{q=1}^{n} \alpha_q = 1 \tag{H.2}$$

So, the volume fraction of the gas phase can be given by.

$$\alpha_q = \frac{Q_q}{Q_t} = \frac{V_q}{V_t} \tag{H.3}$$

Therefore, the effective density of the phase q can be given by,

$$\bar{\rho_q} = \alpha_q \rho_q \tag{H.4}$$

where ρ_q is the physical density of the fluid (kg/m^3). The subscripts q and p refer to the gas and liquid phase.

Multiphase equation of fluid-fluid two-phase flow are presented in this section. These equations for the general case of n-phase flow are solved by fluent.

- Continuity equation.

  The volume fraction of each phase is calculated from a continuity equation as

  $$\frac{1}{\rho_q}\Big(\frac{\partial}{\partial t}(\alpha_q \rho_q) + \nabla.(\alpha_q \rho_q \vec{v}_q) = \sum_{p=1}^{n}(\dot{m}_{pq} - \dot{m}_{qp}) + S_{\alpha q}\Big) \tag{H.5}$$

  Where $S_{\alpha q}$, $\dot{m}_{pq}$ and $\dot{m}_{qp}$ are the mass source term, mass transfer from phase p to phase q and the mass transfer from phase to phase and the mass transfer from phase p to phase q, respectively. According to Fluent user guide FLUENT 2012 the source term on the right-hand side of the Equation H.5 is by default set to zero. Therefore, the solution of the above equation for each secondary phase should match with the equation H.2, which presents the summation of volume fraction equal to one.

- Fluid-Fluid momentum equation.

  From fluid-fluid momentum equation, the conservation of momentum for fluid phase q can be presented as following.

  $$\frac{\partial}{\partial t}(\alpha_q \rho_q \vec{v}_q) + \nabla.(\alpha_q \rho_q \vec{v}_q \vec{v}_q) = -\alpha q \nabla p + \nabla.\vec{\tau}_q + \alpha_q \rho_q \vec{g} + \sum_{p=1}^{n}\Big(K_{pq}(\vec{v}_p - \vec{v}_q) + \dot{m}_{pq}\vec{v}_{pq} - \dot{m}_{qp}\vec{v}_{qp}\Big) + (\vec{F}_q + \vec{F}_{lift,q} + \vec{F}_{vm,q}) \tag{H.6}$$

  Where $\vec{g}$ is the acceleration due to gravity, while $\vec{\tau}_q, \vec{F}_q, \vec{F}_{lift,q}, and \vec{F}_{vm,q}$ are defined in Equation 6.6.

- Fluid-Fluid exchange.

  Fluid-Fluid exchange coefficient influences on the momentum exchange between the phases as shown in Equation H.6. In fluid-fluid flow, usually the secondary phase assumed to be bubble or droplet form, so the exchange coefficient for gas-liquid two-phase flow can be written in general form as following.

$$K_{pq} = \frac{\alpha_q \alpha_p \rho_p f}{\tau_p} \tag{H.7}$$

  Where f is the drag coefficient, and its definition depends on the exchange coefficient model. τ_p is the particulate relaxation time which can be defined as below.

$$\tau_p = \frac{\rho_p d_p^2}{18\mu_q} \tag{H.8}$$

  Where the d_p is the diameter of the secondary phase (bubble or droplet).

In order to define drag function f, drag coefficient C_D should be included. The drag coefficient baseds on the relative Reynolds number. Therefore, there are different exchange coefficient models resulting of different drag coefficient.
In FLUENT there are three common models to determine the drag coefficient; Schiller and Naumann model, Morsi and Alexander model and finally Symmetric model.

- Schiller and Naumann model

  It is a default model for all fluid-fluid two-phase flow, it is acceptable for general use.

$$f = \frac{C_D Re}{24} \tag{H.9}$$

  where C_D can be determined as following.

$$C_D = \begin{cases} 24(1 + 0.15Re^{0.687})/Re & Re \leq 1000 \\ 0.44 & Re > 1000 \end{cases} \tag{H.10}$$

  For the relative Reynolds number for primary and secondary phases, it can be determined respectively as following.

$$Re = \frac{\rho_q(\vec{v}_p - \vec{v}_q)d_p}{\mu_q} \tag{H.11}$$

$$Re = \frac{\rho_{rp}(\vec{v}_r - \vec{v}_p)d_{rp}}{\mu_{rp}} \tag{H.12}$$

Where μ_{rp} is a mixture viscosity of phase p and r, it can be obtained by.

$$\mu_{rp} = \alpha_p\mu_p + \alpha_r\mu_r \tag{H.13}$$

- Morsi and Alexander Calculation in this model may be less stable that other models, but it is most complete and adjusting the function definition over a large range of Reynolds numbers. So, drag function is obtained as following.

$$f = \frac{C_D Re}{24} \tag{H.14}$$

Where C_D is

$$C_D = a_1 + \frac{a_2}{Re} + \frac{a_3}{Re^2} \tag{H.15}$$

Here Re is defined as presented in Equation H.11 or H.12. While the a_1, a_2 and a_3 are constant that can be obtained as following.

$$a_1, a_2, a_3 = \begin{cases} 0, 24, 0 & 0 < Re < 0.1 \\ 3.690, 22.73, 0.0903 & 0.1 < Re < 1000 \\ 1.222, 29.1667, -3.8889 & 1 < Re < 10 \\ 0.6167, 46.50, -116.67 & 10 < Re < 100 \\ 0.3644, 98.33, -2778 & 100 < Re < 1000 \\ 0.357, 148.62, -47500 & 1000 < Re < 5000 \\ 0.46, -490.546, 578700 & 5000 < Re < 10000 \\ 0.5191, -1662.5, 5416700 & Re \geq 10000 \end{cases} \tag{H.16}$$

- Symmetric model.

When the secondary phase (dispersed) in one regime becomes primary (continuous) phase, the symmetric model is then recommended. In this model all the properties; density and viscosity are obtained from volume average properties.

$$\rho_{pq} = \alpha_p\rho_p + \alpha_q\rho_q \tag{H.17}$$

$$\mu_{pq} = \alpha_p\mu_p + \alpha_q\mu_q \tag{H.18}$$

And the diameter is equal to

$$d_{pq} = 0.5(d_p - d_q) \tag{H.19}$$

Therefore, the exchange coefficient can be calculated by

$$K_{pq} = \frac{\alpha_p \alpha_q \rho_{pq} f}{\tau_{pq}} \tag{H.20}$$

$$\tau_{pq} = \frac{\rho_{pq}(d_{pq})^2}{18\mu_{pq}} \tag{H.21}$$

$$Re = \frac{\rho_{pq}(\vec{v}_p - \vec{v}_q)d_{pq}}{\mu_{pq}} \tag{H.22}$$

And finally, drag function can be obtained from.

$$f = \frac{C_D Re}{24} \tag{H.23}$$

Here, C_D is determined from Equation H.10.

H.0.2 Turbulence model

There are various types of turbulent models such as, k-ϵ and k-ω to describe the effect of turbulent fluctuation of velocities and scalar quantities in single phase and two-phase flow (Fu et al., 2017). However, the number of terms in the momentum equations of the two-phase flow which needs to be modelled is larger than that in single phase. Therefore, the modelling of turbulence in the two-phase flow is complex (Main et al., 2017). In the two-phase flow simulation using FLUENT, three methods for turbulence simulation with context of the k-ϵ and k-ω model and two turbulence options within the context of the Reynolds stress model (RSM) are provided.

- k-ϵ and k-ω turbulence options model.

    1. mixture turbulence model (default model).
    2. dispersed turbulence model.
    3. turbulence model per each phase.

- RSM turbulence model options.

    1. mixture turbulence model (default model).
    2. dispersed turbulence model.

Choosing of turbulent model method depends on the importance of secondary-phase turbulence in actual flow (FLUENT, 2012). By comparing the turbulent methods in CFD simulation, the k-ϵ per each phase is appropriate choice because turbulence transfer of two-phase flow after expansion valve among the phases plays a dominant role, and it also compatible with the Eulerian two-phase flow model which provide an accurate prediction (Hrnjak, 2004; Kalteh et al., 2011). Therefore, k-ϵ per each phase was used in the simulation of the present work.

H.0.2.1 k-ϵ turbulence per each phase

Set of K and ϵ transport equations are solved for each phase in two-phase turbulence model. k-ϵ turbulence per each phase model is appropriate choice when the turbulence transfer among the phases plays a dominant role (FLUENT, 2012). Per-phase turbulence model also is more computationally intensive than other turbulence models.
Reynolds stress tensor and turbulent viscosity can be computed by using a following form.

$$\bar{\bar{\tau}}_q = -\frac{2}{3}\Big(\rho_q k_q + \rho_q \mu_{t,q} \nabla . \vec{U}_q\Big)\bar{\bar{I}} + \rho_q \mu_{t,q}\Big(\nabla \vec{U}_q + \nabla \vec{U}_q^T\Big) \tag{H.24}$$

Where $\vec{U}_q$ is the phase weighted velocity and $\mu_{t,q}$ is the turbulent viscosity which can be determined by.

$$\mu_{t,q} = \rho_q 0.09 \frac{k_q^2}{\varepsilon_q} \tag{H.25}$$

Where k_q is the kienetic energy for phase q. ε_q is the dissipation rate for phase q. Therefore,, FLUENT predict the turbulence by.

$$\frac{\partial}{\partial t}(\alpha_q\rho_q k_q) + \nabla.(\alpha_q\rho_q\vec{U}_q k_q) = \nabla.\Big(\alpha_q\Big(\mu_q + \frac{\mu_{t,q}}{\sigma_k}\Big)\nabla k_q\Big) + (\alpha_q G_{k,q} - \alpha_q\rho_q\varepsilon_q) + \sum_{l=1}^{N} K_{lq}\Big(C_{lq}k_l - C_{ql}k_q\Big) - \sum_{l=1}^{N} K_{lq}\Big(\vec{U}_l - \vec{U}_q\Big).\frac{\mu_{t,l}}{\alpha_q\sigma_q}\nabla\alpha_l + \sum_{l=1}^{N} K_{lq}\Big(\vec{U}_l - \vec{U}_q\Big).\frac{\mu_{t,l}}{\alpha_q\sigma_q}\nabla\alpha_q \tag{H.26}$$

and

$$\frac{\partial}{\partial t}(\alpha_q\rho_q\varepsilon_q) + \nabla.(\alpha_q\rho_q\vec{U}_q\varepsilon_q) = \nabla.\Big(\alpha_q\frac{\mu_{t,q}}{\sigma_k}\nabla\varepsilon_q\Big) + \frac{\varepsilon_q}{k_q}\Big[C_{1,\varepsilon}\alpha_q G_{k,q} - C_{2,\varepsilon}\alpha_q\rho_q\varepsilon_q + C_{3,\varepsilon}\Big(\sum_{l=1}^{N} K_{lq}\Big(C_{lq}k_l - C_{ql}k_q\Big) - \sum_{l=1}^{N} K_{lq}\Big(\vec{U}_l - \vec{U}_q\Big).\frac{\mu_{t,l}}{\alpha_q\sigma_q}\nabla\alpha_l + \sum_{l=1}^{N} K_{lq}\Big(\vec{U}_l - \vec{U}_q\Big).\frac{\mu_{t,q}}{\alpha_q\sigma_q}\nabla\alpha_q\Big)\Big] \tag{H.27}$$

where $C_{l,q}$ and $C_{q,l}$ can be obtained by.

$$\begin{aligned} C_{l,q} &= 2 \\ C_{q,l} &= 2\Big[\frac{\tau_{l,q}}{1+\tau_{l,q}}\Big] \end{aligned} \tag{H.28}$$

while $C_{1,\varepsilon}, C_{2,\varepsilon}, C_{3,\varepsilon}, \sigma_k$ and σ_ε are constant numbers. $C_{k,q}$ is the production of turbulent kinetic energy. The (q) and (p) represent the primary phase and secondary phase respectively in two-phase flow case. In the Equations H.26, H.27 and H.28, the l=p and $\tau_{l,q} = \tau_{pq}$ can be defined as a ratio between two characteristic times that can be obtained as following.

$$\tau_{pq} = \frac{\tau_{t,pq}}{\tau_{F,pq}} \tag{H.29}$$

where $\tau_{t,pq}$ is Lagrangian integral time scale which is effected by the crossing trajectory effect, this term can be obtained from.

$$\tau_{t,pq} = \frac{\tau_{t,q}}{\sqrt{(1 + C_\beta\xi^2)}} \tag{H.30}$$

where ξ equal to.

$$\xi = \frac{|\vec{v}_{pq}|\tau_{t,q}}{L_{t,q}} \tag{H.31}$$

$$C_\beta = 1.8 - 1.35cos^2\theta \tag{H.32}$$

θ is the angle between mean relative velocity and mean particle velocity.

$$\tau_{t,q} = \frac{3}{2}C_\mu \frac{k_q}{\varepsilon_q} \tag{H.33}$$

$\tau_{F,pq}$ is the characteristic particle relaxation time which is connected with inertial effects acting on a dispersed phase (p), this term can be determined as following.

$$\tau_{F,pq} = \alpha_p \rho_p k_{pq}^{-1} \left[\frac{\rho_p}{\rho_q} + 0.5\right] \tag{H.34}$$

There is a modification on the Equation 6.8 due to interphase turbulent momentum, this modification can be presented as following.

$$\sum_{p=1}^{N} K_{pq}\Big(\vec{v}_p - \vec{v}_q\Big) \tag{H.35}$$

In order to present this term in general form , use l insted of p as the dispersed phase and q still for continuous phase.

$$\sum_{l=1}^{n} K_{lq}\Big(\vec{v}_l - \vec{v}_q\Big) = \sum_{l=1}^{n} K_{lq}\Big(\vec{U}_l - \vec{U}_q\Big) - \sum_{l=1}^{n} K_{lq}\vec{v}_{dr,lq} \tag{H.36}$$

Where $\vec{U}_l$ and $\vec{U}_q$ are the phase-weighted velocities. While $\vec{v}_{dr,lq}$ is the drift velocity for the dispersed phase.

$$\vec{v}_{dr,pq} = -\Big[\frac{D_p}{\sigma_{pq}\alpha_p}\nabla\alpha_p - \frac{D_q}{\sigma_{pq}\alpha_q}\nabla\alpha_q\Big] \tag{H.37}$$

Here, D_p and D_q are diffusivities, these are computed by FLUENT from the transport equations. Meanwhile, FLUENT will set σ_{pq} to be equal to 0.67. Therefore, the turbulence model for each phase is accounted the effect of turbulence field by using above set of equations.

Appendix I

Experimental results

Experimental results for the horizontal pipe experiments, vertical flash tank separator and the enhancement design options of the vertical flash tank separator are provided in this appendix.

I.1 Horizontal pipe experiments

Table I.1: Experimental result from the horizontal pipe experiments for the range of mass flow rates.

Flow rate (g/s)	Expansion length (mm)	Liquid height at developed region (mm)	Void fraction at developed region	Slip ratio
2.1± 0.2	30.70± 4.31	1.94± 0.34	0.966± 0.010	3.136
5.1± 0.2	90.00± 9.76	2.22± 0.23	0.959± 0.007	4.203
8.1± 0.2	126.70± 9.69	2.68± 0.24	0.945± 0.011	5.258
10.2± 0.2	136.30± 14.07	3.00± 0.21	0.936± 0.007	5.44
13.1± 0.2	153.60± 2.97	3.39±0.35	0.922± 0.008	6.507
23.4± 0.2	180.05± 3.92	5.21± 0.25	0.857± 0.008	7.528

Table I.2: Dimensionless parameters from the horizontal pipe experiments for the range of mass flow rates.

Flow rate (g/s)	Re_{TP}	We_{TP}	Fr_{TP}
2.1± 0.2	450.45	0.0055	0.0602
5.1± 0.2	1188.81	0.0341	0.3698
8.18± 0.2	1841.70	0.0901	0.9785
10.21± 0.2	2099.9	0.1396	1.5158
13.1± 0.2	2638.9	0.2306	2.5031
23.4± 0.2	3246	0.7242	7.8621

I.2 Vertical flash tank experiments

Table I.3: Experimental liquid separation efficiency from the vertical flash tank separator experiments for the range of mass flow rates.

Flow rate (g/s)	VFT-V1	VFT-V2	VFT-V3	VFT-V4	VFT-V5
2.1± 0.2	0.81 ± 0.022	0.83± 0.024	0.84± 0.025	0.85± 0.023	0.86± 0.027
5.1± 0.2	0.83 ± 0.021	0.85± 0.022	0.86± 0.028	0.87± 0.027	0.88± 0.027
8.18± 0.2	0.86 ± 0.031	0.87± 0.03	0.88± 0.023	0.9± 0.024	0.92± 0.022
10.21± 0.2	0.87 ± 0.044	0.88± 0.051	0.89± 0.048	0.92± 0.038	0.93± 0.039
13.1± 0.2	0.89 ± 0.051	0.9± 0.028	0.91± 0.051	0.93± 0.030	0.94± 0.047
23.4± 0.2	0.9 ± 0.044	0.92± 0.024	0.93± 0.058	0.95± 0.032	0.96± 0.054

Table I.4: Experimental vapour quality at the gas outlet from the vertical flash tank separator experiments for the range of mass flow rates.

Flow rate (g/s)	VFT-V1	VFT-V2	VFT-V3	VFT-V4	VFT-V5
2.1± 0.2	0.218± 0.021	0.233± 0.019	0.245± 0.022	0.258± 0.023	0.276± 0.020
5.1± 0.2	0.239± 0.013	0.258± 0.028	0.269± 0.019	0.288± 0.051	0.312± 0.041
8.18± 0.2	0.271± 0.022	0.289± 0.024	0.3± 0.053	0.341± 0.061	0.393± 0.030
10.21± 0.2	0.292± 0.023	0.308± 0.022	0.331± 0.065	0.393± 0.029	0.432± 0.021
13.1± 0.2	0.304± 0.051	0.342± 0.042	0.371± 0.042	0.415± 0.038	0.475± 0.042
23.4± 0.2	0.351± 0.034	0.379± 0.024	0.425± 0.036	0.498± 0.041	0.562± 0.039

I.3 Enhancement design options of the vertical flash tank experiments

Table I.5: Experimental liquid separation efficiency from the vertical flash tank separator (enhancement design options) experiments for the range of mass flow rates.

Flow rate (g/s)	VFT-V5-EXR	VFT-V5-INT	VFT-V5-OD	VFT-V5-ODEXR
2.1± 0.2	0.879± 0.023	0.871± 0.029	0.941± 0.023	0.956± 0.022
5.1± 0.2	0.902± 0.028	0.892± 0.045	0.950± 0.034	0.968± 0.023
8.18± 0.2	0.937± 0.031	0.931± 0.039	0.962± 0.025	0.978± 0.032
10.21± 0.2	0.951± 0.036	0.942± 0.060	0.971± 0.037	0.987± 0.031
13.1± 0.2	0.961± 0.022	0.950± 0.042	0.980± 0.022	0.997± 0.032
23.4± 0.2	0.978± 0.012	0.971± 0.028	0.991± 0.011	0.999± 0.012

Table I.6: Experimental vapour quality at the gas outlet from the vertical flash tank separator (enhancement design options) experiments for the range of mass flow rates.

Flow rate (g/s)	VFT-V5-EXR	VFT-V5-INT	VFT-V5-OD	VFT-V5-ODEXR
2.1± 0.2	0.335± 0.013	0.309± 0.011	0.556± 0.029	0.631± 0.021
5.1± 0.2	0.393± 0.010	0.346± 0.057	0.601± 0.046	0.701± 0.024
8.18± 0.2	0.491± 0.021	0.454± 0.025	0.652± 0.025	0.773± 0.019
10.21± 0.2	0.538± 0.036	0.492± 0.038	0.715± 0.021	0.852± 0.011
13.1± 0.2	0.593± 0.022	0.538± 0.019	0.791± 0.010	0.974± 0.012
23.4± 0.2	0.726± 0.023	0.661± 0.020	0.881± 0.001	0.986± 0.018